UNIVERSITAT DE BARCELONA

Geophysical and geological characterization of fault-controlled geothermal systems: The Vallès Basin case of study

Gemma Mitjanas Colls

Doctoral dissertation

Geophysical and geological characterization of fault-controlled geothermal systems

The Vallès Basin case of study

Gemma Mitjanas

Doctoral program in Earth Science
Department of Earth and Ocean Dynamics

Universitat de Barcelona
2023

UNIVERSITAT DE BARCELONA

Institut de Recerca Geomodels
UNIVERSITAT DE BARCELONA

Doctoral Dissertation

Doctoral Program in Earth Science, Universitat de Barcelona

Department of Earth and Ocean Dynamics

Geophysical and geological characterization of fault-controlled geothermal systems: The Vallès Basin case of study

by

Gemma Mitjanas Colls

Supervisors:

Prof. P. Queralt, *Universitat de Barcelona*

Prof. J. Ledo, *Universidad Complutense de Madrid*

2023

This thesis has been carried out with the support of the APIF predoctoral fellowship (2019).

The research was also funded by the GEO-URBAN project (ERANET-GEOTHERMICA project no.73117 and PCI2018-092943 Spanish Government – Ministerio de Ciencia, Innovación y Universidades), and the PIXIL project (project no. EFA362/19, co-financed by the INTERREG POCTEFA program of the European Regional Development Fund, and the University of Barcelona).

Hoy he salido fuera,
hace un sol que no es de invierno.
No hay sombras en el suelo,
no parece un día cualquiera.

Cala Vento

AGRAÏMENTS

Segurament aquest apartat és dels que se m'ha fet més complicats d'escriure. Suposo que és difícil pensar en qui agrair la realització de la tesis quan provablement has estat influenciat per tanta gent, des de la família, amics, i tots els professors que t'han acompanyat en aquesta etapa.
En les properes línies intentaré resumir la gent que ha tingut una implicació més directa en la realització d'aquesta tesis, però espero que tothom que hagi format part de la meva vida personal i professional, així com la gent que dediqui un cert temps a fullejar aquesta tesis, es senti lliure d'identificar-se i emportar-se una part d'aquests agraïments.

Primer de tot, m'agradaria agrair als meus supervisors Juanjo Ledo i Pilar Queralt el seu suport des de que vaig començar a col·laborar amb ells durant el meu any de màster, i en particular, per aquests anys de doctorat. No només m'han format en els seus camps d'expertesa sinó que també m'han donat la llibertat de portar aquest treball cap on el meu perfil d'investigació em demanava. Per suposat, també n'han format part cada un dels membres del grup d'electromagnètica-geofísica, Anna, Alex i Perla. També a la gent que ha anat passant pel grup, des de doctorands, post-doctorands, estudiants de màster, de grau, i tècnics que han col·laborat directament en l'elaboració d'aquests estudis, ja sigui acompanyant-me a les campanyes de camp, com revisant les dades.

Per donar-me suport en l'àmbit geològic, estic molt agraïda a la Gemma Alías, qui sempre ha tingut la porta oberta del seu despatx, des del primer moment en què es va iniciar aquesta investigació. Espero poder-ho celebrar aviat entre forquilles.

To John Walsh, being a guide me through a structural vision and invite me to collaborate. Your point of view was definitely a turning point in the study. Moreover, I will be proud to share a paper with you.

To Jana Börner, for dedicating all the necessary time to me, and making the stay possible despite the inconveniences of the pandemic. I am grateful that you fight for open the doors of your lab despite the administrative inconveniences. But above all, thank you for always having time to solve my doubts and supporting me in the petrophysical part of the research.

Al grup de Tècniques Geofísiques de l'ICGC, per cedir-me les dades, i pel suport i acompanyament durant aquests anys en el projecte GEO-URBAN, on la integració de idees han fet evolucionar aquest treball.

Als membres de *Seequent* que sempre han posat a la meva disposició llicència i formació en *Leapfrog*, i m'han permès compartir la meva experiència amb altres usuaris.

Gràcies a tots els membres de la facultat de Ciències de la Terra, del primer al últim formador, investigador, becaris, administratius i gent de serveis, per haver-me fet sentir com a casa aquests últims 9 anys.

I per últim, a la família, als amics, i a l'Alex. És la prova que necessitàveu per saber que treballava...

TABLE OF CONTENTS

PART 2

PART 3

PART 5

LIST OF TABLES

LIST OF FIGURES

Summary

Geothermal energy is a renewable source of energy that harnesses heat from the Earth's interior. Temperature increases with depth, defining the geothermal gradient, which can be variable depending on the geological context.

The geological setting of western Europe favors a relatively high geothermal gradient that could be exploited to generate electricity or for its direct use, for example, for its application in industry, greenhouses, or heating systems. In each of these cases, geothermal could favor the community's energy independence and reduce the use of polluting energy sources.

To appropriately exploit areas with a significant geothermal gradient, it is essential to know the origin of the temperature anomaly and the system's functioning. In this context, developing appropriate exploration methodologies and techniques is essential for its adequate and efficient use.

This thesis develops a methodology focused on a geothermal system type characterized by being located in highly fractured zones. These fractures connect the surface with great depths, allowing the rapid ascent of deep fluids at high temperatures without giving them time to cool down. Specifically, this thesis applies this methodology to a study case located in the Vallès Basin, close to Barcelona city (NE Iberian Peninsula), where some localities, such as La Garriga and Caldes de Montbui towns, have thermal hot springs (60ºC and 70ºC, respectively).

In particular, the methodology applied to study the Vallès Basin geothermal fractured system, is focused on two main cores, geophysical and geological techniques.

Geophysical methods allow the characterization of the subsurface physical properties, reaching great depths without having to drill. For example, if the physical characteristics of the subsurface have enough contrast, they could allow distinguishing between different types of rocks, fractured zones, or if there is any fluid circulation. However, the geophysical results have to be complemented with other geoscientific studies in order to make a proper interpretation. In this case, this thesis includes a characterization of the area's geology, fracturing, and hydrology. Finally, the integration of the applied techniques has allowed the understanding of the origin and system's functioning, which is presented in the form of a 3D conceptual model, geological model, and temperature model.

This innovative methodology, which integrates different geoscientific techniques at different scales, combining traditional techniques with novel digital tools, has facilitated the characterization of a geothermal system controlled by geological structures. Therefore, it is established as a methodical option to characterize systems of similar origin.

Resumen

La ***Geotermia*** es una fuente renovable de energía que aprovecha el calor del interior de la Tierra. La temperatura del interior de la Tierra aumenta con la profundidad, y este aumento, definido como gradiente geotérmico, puede ser variable según el contexto geológico.

El contexto geológico del oeste del continente europeo favorece un gradiente geotérmico relativamente alto que podría ser aprovechado para generar electricidad o para su uso directo, como es el caso de aplicaciones en industria, invernaderos o sistemas de calefacción. En cualquier caso, la geotermia podría favorecer la independencia energética y una disminución del uso de fuentes de energía contaminantes.

Para un apropiado aprovechamiento de estas zonas con un gradiente geotérmico significativo, es esencial conocer su origen y funcionamiento. En este contexto, es necesario un avance en el desarrollo de metodologías de exploración que sean adecuadas y eficientes.

Esta tesis desarrolla una metodología aplicada a un tipo de sistema geotérmico caracterizado por estar ubicado en zonas muy fracturadas. Estas fracturas conectan la superficie con grandes profundidades, permitiendo el ascenso rápido de fluidos profundos que se encuentran a altas temperaturas sin que les dé tiempo a enfriarse. Geográficamente, esta zona de estudio se encuentra en la Cuenca del Vallès, cerca de Barcelona (NE Península Ibérica), donde algunas localidades como La Garriga y Caldes de Montbui, tienen surgencias de agua termal (60ºC y 70ºC, respectivamente).

Concretamente, esta metodología se puede separar en dos partes principales, la exploración geofísica y la geológica. Los métodos geofísicos nos permiten conocer las propiedades físicas del subsuelo, llegando a grandes profundidades, sin tener que hacer perforaciones. Si las características físicas del terreno presentan un contraste suficiente, nos pueden permitir, por ejemplo, distinguir entre tipos de rocas, zonas fracturadas, o si hay circulación de algún fluido. Aun así, los resultados geofísicos tienen que complementarse con otros estudios geocientíficos para poder hacer una apropiada interpretación. Esta tesis incluye una caracterización de la geología, la fracturación y la hidrología de la zona, cuya integración final ha permitido entender el origen y funcionamiento de este sistema. Los resultados finales se presentan en forma de un modelo 3D conceptual, geológico y de temperaturas.

Esta metodología innovadora integra distintas técnicas geocientíficas a distinta escala, combinando técnicas tradicionales con herramientas digitales novedosas, facilitando la caracterización de un sistema geotérmico controlado por estructuras geológicas. Por lo tanto, se establece como una opción metódica a seguir para la caracterización de sistemas de origen similar.

Resum

La ***Geotèrmia*** és una font renovable d'energia que aprofita la temperatura de l'interior de la Terra. El grau en què aquesta temperatura augmenta en profunditat, ve definint pel gradient geotèrmic, el qual pot ser variable segons el context geològic.

La geologia de la regió oest del continent europeu afavoreix un gradient geotèrmic relativament alt que podria ser aprofitat per generar electricitat o per a ús directe, com és el cas d'aplicacions en indústria, hivernacles o sistemes de calefacció. En qualsevol cas, la geotèrmia podria afavorir la independència energètica i una disminució en l'ús de fonts d'energia contaminants.

Per a un aprofitament d'aquestes zones amb un gradient geotèrmic significatiu, és essencial conèixer-ne l'origen i el funcionament. En aquest context, és basic desenvolupar metodologies d'exploració que siguin adequades i eficients.

Aquesta tesis desenvolupa una metodologia aplicada a un exemple de sistema geotèrmic caracteritzat per estar ubicat en una zona molt fracturada. Aquestes fractures connecten la superfície amb grans profunditats, permetent l'ascens ràpid de fluids profunds que es troben a temperatures altes, sense que els doni temps a refredar-se. Concretament, aquesta zona d'estudi es situa a la Conca del Vallès (NE Península Ibèrica), on algunes localitats com La Garriga i Caldes de Montbui, tenen surgències d'aigua termal (60ºC i 70ºC, respectivament).

Concretament, la metodologia aplicada es basa en dues parts principals: l'exploració geofísica i la geològica. Els mètodes geofísics ens permeten conèixer les propietats físiques del subsol arribant a grans profunditats sense haver de fer perforacions. Si les característiques físiques del terreny presenten un contrast suficient, poden permetre, per exemple, distingir entre tipus de roques, zones fracturades, o si hi ha circulació d'algun fluid. Tot i així, els resultats geofísics s'han de complementar amb altres estudis geocientífics per una correcta interpretació dels resultats. En aquest cas, aquesta tesis inclou una caracterització de la geologia, la fracturació i la hidrologia de la zona. La integració final de totes les dades ha permès entendre l'origen i el funcionament d'aquest sistema, resultat del qual es presenta en forma d'un model 3D conceptual, geològic i de temperatures.

Aquesta metodologia innovadora, que integra diferents tècniques geocientífiques a escala diferent, ha combinat tècniques tradicionals amb eines digitals noves, facilitant la caracterització d'un sistema geotèrmic controlat per estructures geològiques. Per tant, s'estableix com una opció metòdica a seguir per a la caracterització de sistemes d'origen similar.

Part 1

Chapter I

Thesis introduction

Chapter II

Geothermal exploration in non-magmatic convective systems: The Vallès Basin case of study

Chapter I

Thesis introduction

1.1. Motivation and background

Geothermal energy is a clean and efficient energy source that harnesses the earth's inner heat. Electricity production from geothermal energy is usually restricted to high-temperature areas, such as volcanic regions; however, other geological contexts with multiple energy applications should be considered.

Since the dawn of civilization, geothermal energy has already been used directly for thermal baths or washing clothes. Nowadays, its direct application can involve various end uses, such as space heating and cooling, industry, greenhouses, fish farming, or touristic/service sectors. These applications have the advantage that they can use all-temperature geothermal resources, and therefore, they are much more widespread worldwide than the resources exploitable for electricity production. Moreover, these applications could also reduce our dependence on external energy sources, reducing the consumption of non-renewable energy of fossil origin, and ensuring a constant supply without depending on external factors.

Within this framework, the Iberian Peninsula has significant potential for geothermal resources, which, through appropriate development of the sector, could bring this area closer to the levels of exploitation of other European regions. Nevertheless, development associated with more excellent scientific knowledge and a significant technological evolution is essential.

The Vallès Basin geothermal system, in the NE of the Iberian Peninsula, presents thermal anomalies evidence in the form of hot springs in two localities, Caldes de Montbui (70ºC) and La Garriga (60ºC) towns. Although these thermal waters located in highly-fractured geological units are only used for tourist purposes in spas, a better knowledge of the system functioning could contribute to advising other applications to benefit the community and the natural environment.

1.2. Objectives

In the frame of two international projects, GEO-URBAN[1] and PIXIL[2] projects, this thesis aims to explore the potential of a mid-enthalpy geothermal system located in an urban area with a vital farming and industrial sectors, the Vallès Basin (NE of Spain). Moreover, it presents a practical and efficient exploration methodology that could be extrapolated to other areas of similar geological context.

These goals are addressed through the following specific aims:

- The review and analysis of the study area's previous geological and geothermal data.
- The development of an integrated methodology considering previous and newly acquired data, and applying different geoscience techniques.
- The geophysical characterization of fault zones and geothermal interpretation of their physical properties.
- The geological characterization of the geothermal units and their hydraulic properties.
- The understanding of the geological structural complexity role in the geothermal system's functioning.
- The creation of geological and geothermal models to image the results and represent the system's functioning.

1.3. Methodology

The Vallès Basin case study is an example of a fault-controlled geothermal system in which the knowledge of the geological structures that dominate the area is of great importance to understanding the system's functioning.

This geothermal system had already been an area of interest in the 80s; therefore, geological and geophysical data are already available, although these have never been reviewed in detail. Based on this information, the acquisition of data has been completed to describe the system and be able to extrapolate this methodology to other geothermal investigations of similar origin.

Specifically, geophysical, geological, petrophysical, and hydrogeological studies have been carried out to characterize the Vallès Basin geothermal system. The exploration methods applied are mainly focused on identifying and characterizing the geological structure of the area, which seems to have great relevance in the circulation of fluids. Each of these methodologies will be described in detail in the corresponding chapters.

[1] Project subsidized through the ERANET Cofund GEOTHERMICA (Project no. 731117) and Spanish Government – Ministerio de Ciencia, Innovación y Universidades (PCI2018-092943).
[2] Project EFA362/19, co-financed by the European Regional Development Fund (FEDER) through the Interreg V-A Spain-France-Andorra Program (POCTEFA 2014-2020) and the University of Barcelona.

1.4. Thesis outline

The thesis is organized into five main parts. The 1st part (Chapter I and II) includes the introduction to the thesis and the area of study; the 2nd part (Chapter III) is focused on the geophysical methodology; the 3rd part (Chapters IV, V, VI) is focused on the hydrogeological characterization; the 4th part (Chapter VII and VIII) presents the main results and discussions, including the final geological and geothermal models. And finally, the 5th part includes the article's manuscripts and the appendix.

The information presented in each chapter is detailed below.

After this opening section, ***Chapter II*** puts in a social background of the current situation of geothermal exploration and presents the classification of geothermal systems. It also introduces the main study area, the Vallès Basin, including its geological and geothermal bibliographic background.

Chapter III highlights the potential of applying different geophysical techniques based on different physical parameters to characterize fault-controlled geothermal systems. This case study presents the application of magnetotellurics, gravity, passive seismic, electrical resistivity tomography, and induced polarization methods. The resulting physical parameters characterization (electrical resistivity, density, acoustic impedance, and chargeability) have resulted in the appropriate starting point for the exploration of the system since they have allowed the identification of the main geological structures of the area.

The paper by *Mitjanas et al. (2021)* published in *Geothermics* [Scientific Papers (1)] presents part of this geophysical integration methodology applied to the eastern Vallès Basin, in the La Garriga-Samalús area. This paper is the result of the collaboration of the University of Barcelona (UB) and the *Institut Cartogràfic i Geològic de Catalunya* (ICGC).

Chapter IV includes the multi-scale geological methodology. Due to the geothermal classification of this system as fault-controlled, the characterization of fracturing has been essential. Fieldwork and the later microscopic analysis have been used to define and characterize the fault zones related to the main structures of the study area. Moreover, the availability of some borehole samples has allowed the correlation of the surface results with deep geological data.

Some of the results, which enhance the relevance of structurally complex zones in geothermal exploration, are ready to be submitted in *Geothermics* [Scientific Papers (2)]. This paper is the result of the collaboration with Dr. John Walsh from the iCRAG center of the University of Dublin.

This PhD originally included an international stay at the Technical University of Freiberg under the supervision of Dr. Jana H. Börner (*TU Bergakademie Freiberg*). However, this stay had to be

postponed several times due to the global pandemic situation. Finally, in May 2021, it was possible to carry out the stay even though the duration was shorter than desired. ***Chapter V*** presents this laboratory work on the petrophysical study of outcrop and borehole samples. This characterization included fault zone samples from which density, porosity, and induced polarization were parameterized.

Chapter VI reviews previous hydrological data, mainly related to the composition and temperature of the thermal fluid. This data analysis, together with the interpretation of new hydrological parameters, allows an imaging of the thermal fluid circulation and the maximum temperature zones. This reviewed data, together with the published multidisciplinary works of the Vallès Basin area, is being prepared to be submitted as a scientific paper.

Chapter VII combines all the previous results to represent them in a conceptual model that explains the geothermal system's functioning. From this conceptual model, 3D geological and temperature models have been created using *Leapfrog Geothermal®* (Seequent) software. Therefore, this chapter represent the first part of the main discussions and conclusions of the thesis.

Finally, ***Chapter VIII*** presents the final discussions which integrate all the previous results, and consider further structural considerations of the study area. The conclusions are also presented in this chapter, where the fulfillment of the main objectives of the thesis is confirmed.

* The manuscripts of the *Scientific Papers* and the appended data are available at the end of the thesis.

Chapter II

The geothermal exploration in non-magmatic convective systems: The Vallès Basin case of study

This chapter provides a social background to the state of play in geothermal energy and the classification of the different geothermal systems types. The study area is also introduced by reviewing the geological and geothermal bibliographic background.

2.1. Geothermal energy overview

In the global warming context, great efforts are made to control greenhouse gas emissions with the goal of the Paris agreement to limit the atmospheric temperature increase (COP-21, 2015). In this context, the use of renewable energies is a crucial factor in climate control and economics. Moreover, favoring the energy independence of countries could prevent economic inflation in cases of war conflicts, as in the case of the 2022 Russian conflict (Johannesson & Clowes, 2022). This subtle improvement in political consideration, together with the technological evolution, is allowing the growth in electricity production from renewable resources, which includes the growth in the production of electricity-heat using geothermal energy.

Compared with other renewable energies, geothermal is an inexhaustible source of thermal and electrical energy on a human-time scale. Moreover, its energy is supplied 24 hours per day, seven days a week, not depending on the weather. Therefore, it could have an essential role in the future of our energy supply systems, which is moving toward Smarts Cities and Smart Rural Communities (Poggi et al., 2015). In this context, the integration of combined technologies using renewable energy sources would reduce the environmental impact and offer citizens a better life quality (Dumas, 2016).

During the last decades, population growth and increasing concentration in cities have turned these areas into substantial commercial, industrial, and residential energy consumers (Ramos-Escudero et al., 2021). For example, the industrial sector is one of the world's largest greenhouse

gas dispatchers, and geothermal energy can significantly contribute to this challenge. Specifically, in Spain, almost 85% of the industrial processes could be carried out with very low, low, and medium geothermal systems, thus, avoiding CO_2 emissions to the atmosphere by more than 80 million tons per year (Palomo-Torrejón et al., 2021).

The utilization of geothermal energy is commonly divided into two categories, electricity production and heat (direct application). These two categories are directly related to the exploited reservoir's temperature and the structural setting. Europe has significant geothermal resources with a spectrum that varies from high enthalpy resources for power production (e.g., Iceland, Italy, or Greece) to direct use of hydrothermal resources in sedimentary basins (e.g., France, Germany, or Romania) (Antics & Sanner, 2007). Nevertheless, the European Union remains the world's largest energy importer, relying on imports for 50% of its energy needs (Maltby, 2013).

2.2. Classification of geothermal systems

Different types of geothermal systems and their characteristics condition how this energy can be harnessed. However, the same four elements, which are comparable to the components that constitute an oil-gas reservoir, can be identified (Haklidir et al., 2010):

- The **heat source**, which can be related to magmatic intrusions, implying very high temperatures; or related to the Earth's temperature gradient.
- The **reservoir** is the rock volume that contains and allows the circulation of fluids that transport the heat. It is usually overlined by an impermeable layer, known as the seal.
- The geothermal **fluid** is water, in most cases, meteoric water in the liquid or vapor phase. This fluid typically carries chemicals and gases such as CO_2, H_2S, H_2, and CH_4.
- The **recharge** is the input of the geothermal system. The input of fluid, which can be natural or artificial, will condition the final usable fluid volume.

There are many ways of classifying the geothermal systems and resources, which can be based on the different presented element's characteristics. In this work, two different parameters will be considered, the temperature-based and the "play"-based; as both can greatly condition the exploration procedure and the technics.

The temperature-based classification is the most used one, although there is no general agreement on the temperature ranges (Table 1). Moreover, the schemes based on temperature say no specific about the reservoir itself and, therefore, cannot be directly related to explicit development practice.

Table 1.Examples of classification of geothermal resources by temperature (Benderitter & Cormy, 1990).

Temp.	(Muffler, 1978)	(Hochstein, 1988)	(Benderitter & Cormy, 1990)	(Haenel et al., 1988)
Low-	< 90 ºC	< 125 ºC	< 100 ºC	< 150 ºC
Mid-	90-150 ºC	125-255 ºC	100-200 ºC	-
High-	> 150 ºC	> 225 ºC	> 200 ºC	> 150 ºC

Although temperature is a key parameter in the definition of a geothermal system, it should be combined with other classification types. In this case, the classification defined by Moeck (2014) has been considered the most suitable to complete the information about the geothermal system. This classification, based on geological controls, is summarized in two main groups, the convection- and the conduction-dominated geothermal plays. Figure 1 presents a summary of these two main group classifications with their related tectonic contexts and reservoir locations.

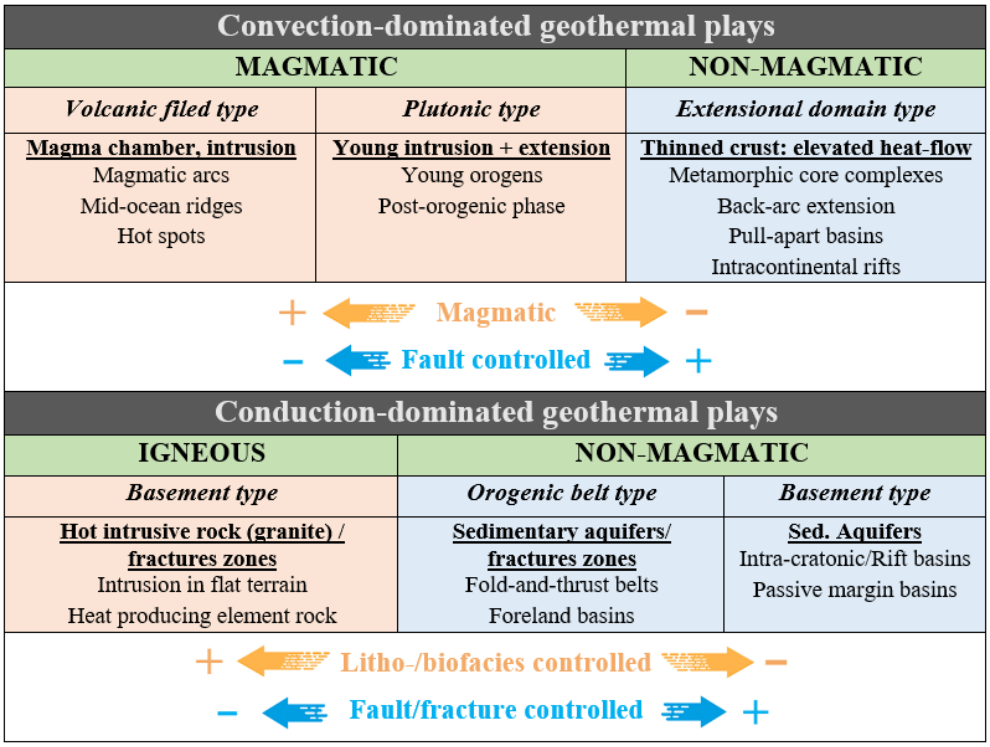

Figure 1. Geothermal play types classified in the two main groups: convection- and conduction-types. Every group has 3 different play types with different plate tectonic settings and geologic habitat of potential reservoirs (modified from Moeck, 2014).

The **conduction-dominated** geothermal plays (passive geothermal) host low to medium enthalpy resources not related to significant recent tectonism or volcanism, and therefore, the geothermal gradient is the mean gradient.

The **convection-dominated** geothermal plays (active geothermal) imply heat transport from deeper levels to the surface, in which structure controls fluid flow pathways. These systems include the vast majority of operating geothermal power plants worldwide and are related to areas of active tectonism, active volcanism, young plutonism (<3 Ma), and elevated heat flow caused by extensional tectonics.

The following description is focused on the non-magmatic convective systems group, which corresponds to the case of the study.

2.2.1. Non-magmatic convection-dominated geothermal plays

In the non-magmatic convection-dominated geothermal play systems, the heat source is the Earth's natural temperature gradient, although it is altered due to an extensional tectonic setting. The extensional setup favors crustal thinning, resulting in a higher temperature gradient.

These systems are controlled by either faulting or leakage, depending on whether convection occurs entirely along a fault zone (Figure 2, borehole 1) or if the fluid previously leaks through a permeable layer (Figure 2, boreholes 2a & 2b). In borehole 1, located inside a fault zone, the temperature would constantly increase along the fault plane. In boreholes 2a and 2b, the temperature would be conditioned by the location of the permeable layer.

Considering the previously presented four elements that characterize a geothermal system; in non-magmatic convection-dominated plays, they can be defined as follows:

- The **heat source** is the Earth's natural gradient, which can be increased due to the thin crust in extensive contexts.
- The **reservoir** may be related to various types of rock (volcanic, plutonic, or sedimentary rocks), which are fractured. The typical targets are dilatational and shear-dilatational faulting regimes, fault intersections, or extensional domains in convergence settings.
- The geothermal **fluids** composition will be conditioned by the reservoir rock lithology and the circulation temperature.
- The **recharge** area will be conditioned by its permeability (fracturing) and needs to present enough hydraulic gradient, favoring a high degree of water infiltration. Mountain ranges nearby where meteoric water infiltrates are typical recharge areas.

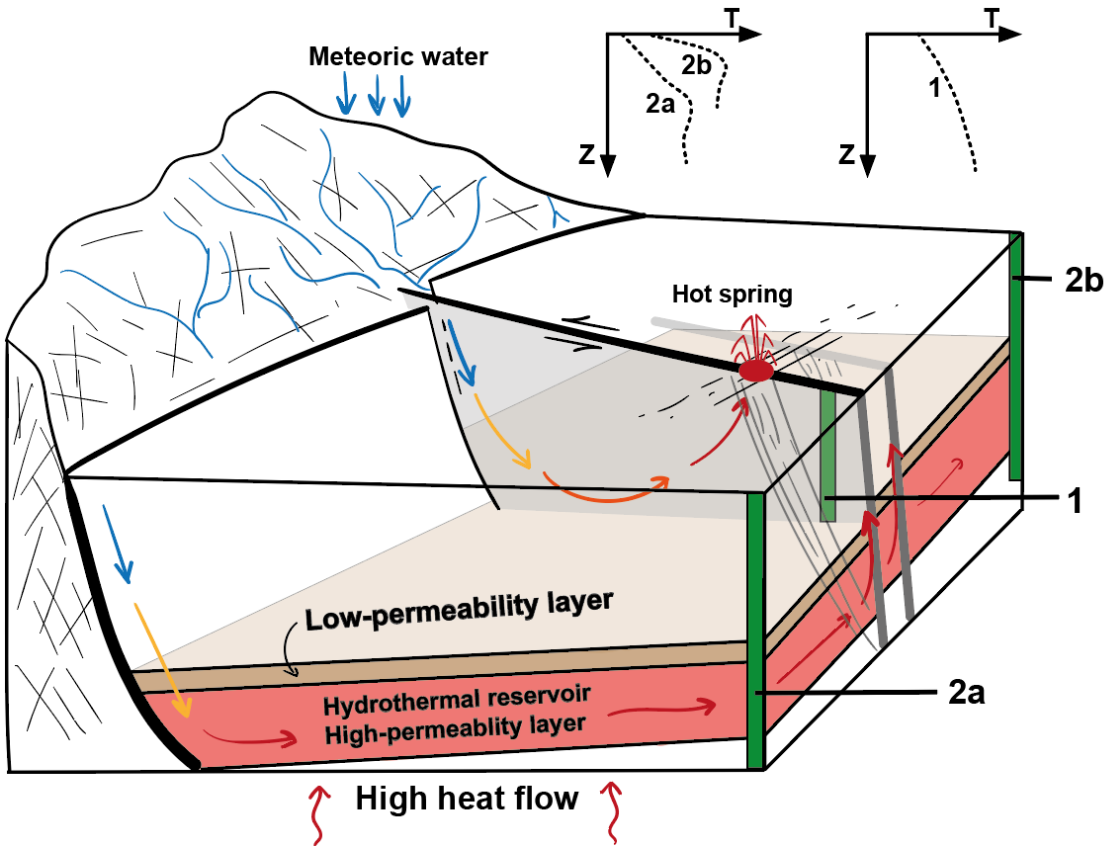

Figure 2. Non-magmatic active geothermal play system in active extensional terrains with different types of reservoirs and their temperature gradient of a drilling well. Type (1), creates a convection cell from infiltration to discharge along one fault plane. Type (2) are fault leakage-controlled plays, in which the temperature gradient rises to the permeable layer and drops below the layer (modified from Moeck, 2014).

2.3. The study area: Vallès Basin

The northern part of Europe is relatively structurally stable, characterized mainly by the presence of granitic massifs, large sedimentary intracratonic basins, and some rifting phenomena. On the other hand, the southern part can be described by the presence of orogenic systems of the arch-trench type, extending marginal back-arc basins, volcanic island areas, subduction zones, continental rifts, and recent volcanism (Haenel & Staroste, 1988). The distribution of the geothermal heat flux outlines these main macrotectonic features of the continent, localizing most of the geothermal resources in the western part (Figure 3).

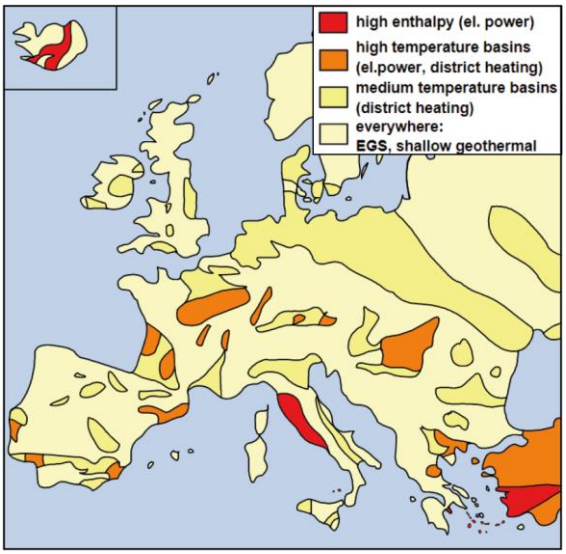

Figure 3. Main basins and geothermal resources of Europe. The distribution of the temperature resources outlines the main structural complex areas of the southern part of Europe. The area of study, in the Catalan Coastal Ranges (NE Iberian Peninsula), shows a basin classified as a "High-temperature basin" (Antics & Sanner, 2007).

The Cenozoic grabens related to the West European Rift system (WER) are the main features to consider in geothermal exploration (Boissavy et al., 2016). In this continental extension setting, the main targets for high-temperature geothermal drillings are the fault zones in graben basement rocks (Bertrand et al., 2021). In the western Mediterranean, between the Iberian Peninsula and the Balearic Islands, the Valencia Trough is the southern expression of the WER, where the Catalan-Valencian domain is characterized by extensional tectonics. The Vallès-Penedès Basin, in the Catalan Coastal Ranges (CCR), stands out due to thermal anomalies along a major crustal fault trace, the Vallès-Penedès Fault (Roca & Guimerà, 1992).

This thesis presents a complete procedure of exploring a non-magmatic convective system related to the extensive tectonic context of the CCR. Specifically, at the northeastern limit of the CCR, in the Vallès region, two main towns along the Vallès-Penedès Fault present geothermal surface evidence, La Garriga and Caldes de Montbui towns, which will focus the study due to the previously confirmed geothermal anomaly (Fernàndez & Banda, 1990; IGME, 1986b).

2.3.1. Structural context

The overall basement of the WER-related grabens is composed of different tectonic domains stuck together during the large-scale Hercynian orogeny of the Paleozoic Era up to 300 Ma (Matte, 2001; Nance et al., 2010). Since the end of the Hercynian orogeny and the subsequent collapse of the mountain belts in the Carboniferous and Permian periods, these litho-tectonic domains were subjected to several tectonic events that reactivated the primary structures (Schumacher, 2002;

Ziegler & Dèzes, 2006). The timing and influence of this reactivation were directly related to the location and characteristics of the fault network. In the case of the study, the Catalan-Valencian extensional domain of the Valencia trough was developed and superimposed on previous compressional structures (Bartrina et al., 1992). These previous structures were formed during the Late Cretaceous-Early Oligocene due to overall N-S compression caused by the collision of the Iberian and European plates (Guimerà, 1984).

The CCR constitutes the onshore expression of the northeastern sector of the Catalan margin, which separates the Valencia trough's thinned continental crust from the Iberian plate's thickened crust (Gallart et al., 1990; Vidal et al., 1995). In this sector, the crust displays a well-developed horst and graben structure, composed of several NE-SW to ENE-WSW striking blocks (Figure 4) related to listric faults with a detachment level at 12-16 km depth, as a result of the last Neogene deformation (Gaspar-Escribano et al., 2004; Roca, 1992).

The current configuration in the northeastern part of the CCR is formed by two longitudinal mountainous chains: the Prelitoral and Litoral ranges, which are separated by the Vallès-Penedès (V-P) Basin. The V-P Fault is the crustal listric fault that limits the Prelitoral Range from the V-P Basin. This 100 km-length major fault has an average displacement of at least 4.7 km in the center of the basin (Gaspar-Escribano et al., 2004), which produced crustal thinning of about 30-35% (Bartrina et al., 1992; Roca, 1996).

The area of study is located in the northeastern part of the V-P Basin, in the Vallès region (Figure 4 and Figure 5). Therefore, during this thesis, the V-P Fault and Basin will be referred to as the Vallès Fault (VF) and Basin (eastern segment).

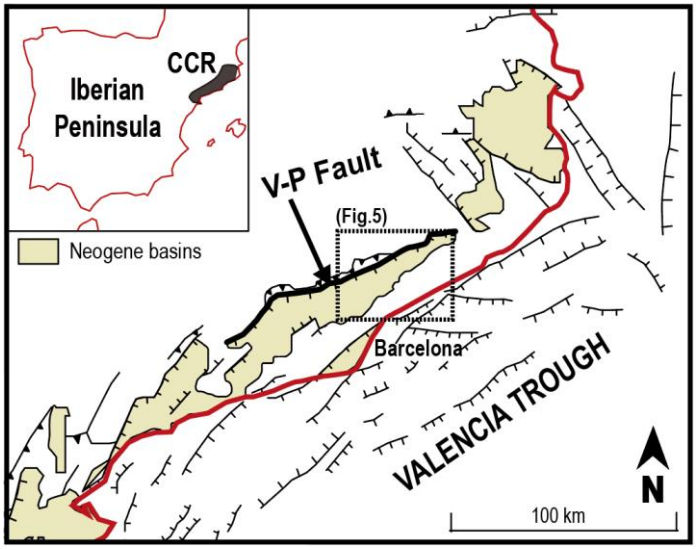

Figure 4. Structural map of the Valencia trough, showing the Catalan-Valencian domain. The dashed square shows the area of study, located in the Vallès region. This map shows an ENE-WSE trend in the center of the study area, close to the Barcelona area. Towards the SW, this trend bends, having a rather NE-SW orientation. Towards the NE, the trend of the V-P Basin is truncated by perpendicular structures with NW-SE orientations (modified from Roca & Desegaulx, 1992).

2.3.2. Local geology in the northeastern limit of the Vallès-Penedès (V-P) Basin

The area of study is located in the eastern part of the V-P Basin, in the Vallès region. This zone involves two main structures: the Paleogene/Alpine Thrust (AT) and the Vallès Fault (VF); and four geological units: The Metamorphic Paleozoic, the Triassic, the Post-Variscan/Hercynian intrusive unit, and the Miocene Basin (Figure 5).

The VF footwall forms a mountain range up to 1700 m high (the Prelitoral Range), resulting from the fault block isostatic uplift (2 km) that occurred during the Neogene extensional movement of the fault (Gaspar-Escribano, 2003). In the study area, this footwall is formed by an NNW-directed granodioritic Paleogene thrust sheet which overthrusts the Cambro-Ordovician to Carboniferous metamorphic series towards the NNE, and a Triassic series towards the NW, with an arched shape. This Paleogene AT is identified as a major reverse fault with a sinistral horizontal displacement fault system, oblique to the direction of maximum shortening of the Pyrenean zone (Anadón et al., 1985; Gaspar-Escribano et al., 2004; Guimerà, 1984; Roca, 1996; Roca et al., 1999).

The granodioritic thrust sheet is a post-Variscan intrusive unit formed by granodiorites later intruded by E-W aplite, pegmatite, and granitic porphyry dykes (ICGC, 2006). The Paleozoic metamorphic rocks of the NNE are integrated mainly by slates and minor limestones, sandstones, and quartzite intercalations (ICGC, 2006; IGME, 1974). The NW Triassic rocks are mainly formed in the base by the Buntsandstein conglomerates, followed by layers of silicic sandstones and clays. The later Muschelkalk facies are formed by the alternation of dolomites, limestones, sandstones, and clays.

The VF has an average of 060º strike orientation and separates the previously described Variscan basement from the Miocene sediments of the Vallès Basin. This Miocene unit constitutes the VF hanging wall block, formed by conglomerates, arkosic sandstones, and mudstones. These sediments are interpreted as syn-tectonic alluvial fans, which are close to the fault trace and include big boulders from the Prelitoral Range igneous and metamorphic rocks (ICGC, 2002, 2006; IGME, 1974). For this sector of the CCR, the basin thickness is still widely unknown, as demonstrated by the different proposed geological cross sections (Fernàndez & Banda, 1988, 1990; Fontboté, 1954; IGME, 1977; Mitjanas et al., 2021; Roca, 1992).

Although far from our study area, previous seismic profiles image the VF in depth (Gaspar-Escribano et al., 2004; Roca et al., 1999; Santanach et al., 2011). In these seismic interpretations, the VF is characterized by a listric geometry with the consequent roll-over in the Pliocene-Miocene hanging wall (Roca et al., 1999; Sàbat et al., 1995). Moreover, it is also characterized by a detachment depth located in the lower/upper crust boundary (13-15 km) (Bartrina et al., 1992; Roca & Guimerà, 1992). These authors identified the Miocene maximum thickness next to the fault, which in some areas reached up to 3000 m. However, later works extrapolated this

geometry from the center of the Vallès-Penedès Basin to the Vallès northeastern limit, near our study area (Canals et al., 1990; Cardellach et al., 2002; Fernàndez & Banda, 1988, 1990).

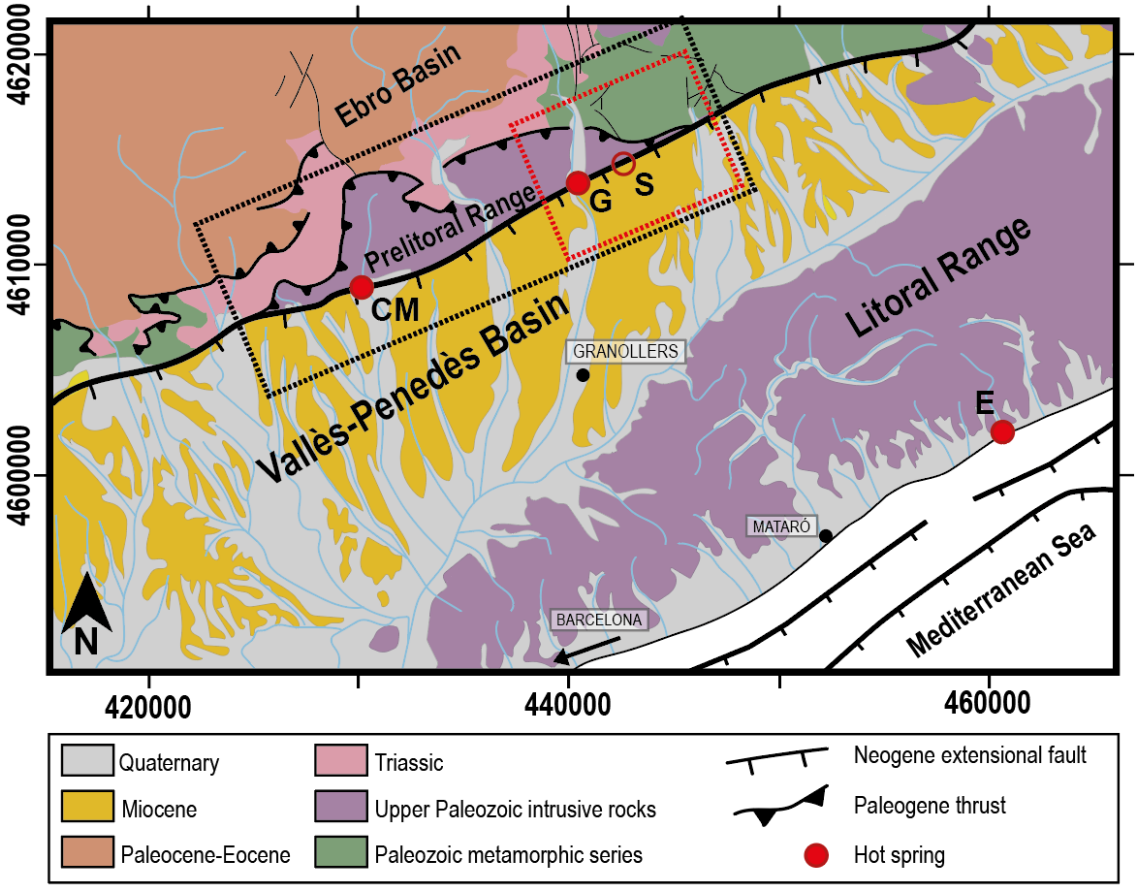

Figure 5. Geological map (UTM coordinates) of the central to the eastern part of the Catalan Coastal Ranges, highlighting the Valles-Penedès Basin and its bounding southward-dipping Valles-Penedès Fault. Hot springs along the Vallès Fault are located where the footwall rocks are Upper Paleozoic granitic intrusive in the hanging wall of a southward dipping Paleogene thrust study area. Location of the towns with thermal hot springs: CM - Caldes de Montbui (hot springs at 70ºC); G - La Garriga (hot springs at 60ºC); E - Caldes d'Estrac (hot springs at 38ºC); and other indicators of thermal activity: S - Samalús (90ºC at 1000 m depth). The study area is indicated by the black outlined square, and the red square locates the main acquired data location for this study. Modified from ICGC (2002) and Martí et al. (1992).

2.3.3. Geothermal context of the study area

The growing interest in potential geothermal areas of Catalonia in the 1980s encouraged IGME (*Instituto Geológico y Minero de España* - Geological Survey of Spain) to start several studies on the Vallès region, where upwelling springs temperatures are between 60°C (in La Garriga town) and 70 ºC (in Caldes de Montbui town) (Compañía General de Sondeos S.A., 1977, 1978).

The first phase of the IGME exploration survey in the CCR consisted of a preliminary study in the Vallès region which included geological, geophysical, hydrological, and temperature studies to choose the area where the exploration boreholes could be made (Compañía General de Sondeos S.A., 1977, 1978, 1979b, 1979c, 1979a). Finally, two surveys were carried out, first in Samalús (La Garriga area) and later in Caldes de Montbui towns (Figure 6A).

La Garriga-Samalús exploration project

Samalús town was chosen due to three main reasons:

(1) It is next to La Garriga town, where the water temperature at the surface is 60ºC.
(2) The temperature readings in private wells in Samalús town showed a surface temperature of around 18ºC, above the average of 14-15ºC (Compañía General de Sondeos S.A., 1977).
(3) It was an accessible area for the construction of exploration wells.

The first completed geothermal exploration well in Samalús, S1, confirmed the presence of a thermal anomaly and allowed the characterization of the geological units (IGME, 1982). After that, IGME conducted a more exhaustive exploration report, which mainly included an improvement of the geohydrological characterization of the area and the building of four more geothermal exploration boreholes along the VF in Samalús town (IGME, 1984b, 1984a). Finally, they built the S6 borehole, of 1000 m depth, which reached 90ºC (IGME, 1986b). All these boreholes and geoscientific reports allowed the characterization of the geological units and temperature at depth (Figure 6C).

In these boreholes' reports, the Miocene sedimentary rocks of the Vallès Basin were defined as intercalations of arkosic sandstones, shales, and discordant conglomerates. The basement rock was mainly constituted by a granitic column with a high degree of permeability, which caused some inconveniences during the drilling due to rock losses. The VF zone was intersected in five of the six boreholes, which helped to define a fault plane dip between 73 and 75 degrees.

After these investigations, other authors studied the geothermal anomaly of Samalús, including its convective origin (Fernàndez & Banda, 1988, 1990), the chemical characterization of the geothermal water, and the geothermal history of the area (Albert, 1988; Albert et al., 1979; Baqués et al., 2012; Canals et al., 1990; Cantarero et al., 2014).

Caldes de Montbui project

The Caldes de Montbui project started after the confirmation of the first temperature anomalies (CM-1) (Compañía General de Sondeos S.A., 1978) and also due to the promising results in the characterization of the La Garriga-Samalús thermal anomaly. This project included three reconnaissance soundings: CM-2, CM-3, and CM-4 (IGME, 1986) (Figure 6B).

The main goals of this project were localizing the thermal anomaly in the western limit of the granodioritic thrust sheet, studying the role of the main faults in the circulation of fluids, and analyzing the granodioritic unit as the potential reservoir.

The results showed that the main stream in Caldes de Montbui might follow a perpendicular fault that breaks the VF into two segments, resulting in an elevated block towards the west (with higher temperatures) and a downthrown block towards the east. The high permeability zone in the intersection between faults would act as a vertical pipe, generating the hot springs.

On the other hand, the permeability generated by the AT would cause the infiltration of meteoric waters. So, the proximity towards the thrust would be conditioning the mixing of waters and, therefore, the temperature gradient.

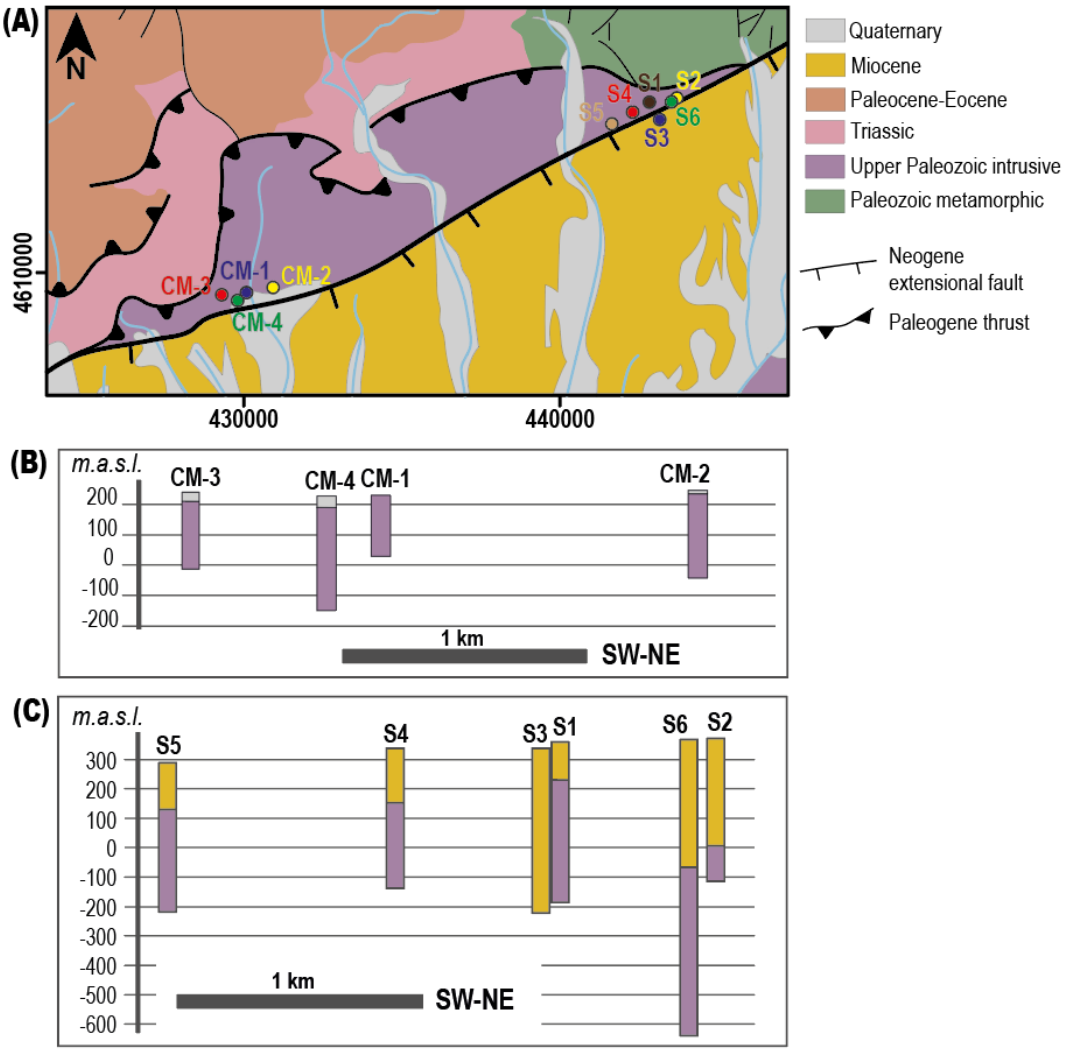

Figure 6. A) Geological map with the location of the geothermal exploration boreholes in the Vallès region. The boreholes were located close to the Vallès Fault trace and in the two main locations with surface thermal evidence: Caldes de Montbui (CM) (70ºC) and La Garriga-Samalús (S) (60ºC) towns. B) Geothermal exploration boreholes (IGME, 1982, 1984a, 1986b) plot in an SW-NE profile, between La Garriga and Cànoves towns. The Miocene Basin – Basement limit is a structural limit set by the Vallès Fault plane. Borehole S3 did not reach the main fault. C) Geothermal exploration boreholes (IGME, 1986a) plot in an SW-NE profile in Caldes de Montbui town. In this case, the boreholes were located in the granodioritic sheet, so the only sedimentary rocks crossed were the Quaternary sediments.

Vallès Basin geothermal system

The results obtained in previous works allowed the definition of two geothermal systems whose functioning and whether they are part of the same system is still not known. However, both subsystems studies have some conclusions in common: (1) The appearance of thermal waters on the surface always takes place in the horst-graben boundary, so on the VF trace. (2) Specifically, the hot springs are located where the granodioritic thrust sheet outcrops in the Prelitoral Range. (3) There is the possibility of perpendicular NNW-SSE structures close to the hot springs, which would condition the permeability of the area.

In the following chapters, an integrated methodology is presented to improve the knowledge of the Vallès Basin area and confirm the main causes and characteristics of this geothermal system.

Part 2

Chapter III

Geophysical exploration.
An integrated methodology

Chapter III

Geophysical exploration. An integrated methodology

Geophysical exploration methods can be used to characterize the physical properties of the Earth's crust, measuring the parameters connected to the geological structure and the properties of the geothermal system. However, it should be noted that no particular technique can be universally applicable, so the chosen methods should suit each geological context. Therefore, geophysical exploration is meaningless if a surface geological survey, hydrological study, and preferably drilling do not complement it.

This chapter presents the geophysical methodology applied for geothermal exploration, including a geophysical background for every method, the details of the survey, and the results. The methods used, magnetotellurics (MT), ambient seismic noise (HVSR), gravity, electrical resistivity tomography (ERT), and induced polarization (IP), are presented by order of relevance in the system characterization.

For the application of the geophysical methods, members from the *Institut Cartogràfic i Geològic de Catalunya* (ICGC) and from the University of Barcelona have been involved, mainly as part of the previously mentioned GEO-URBAN project.

Some of the results are already published by *Mitjanas et al., 2021*, and the manuscript can be consulted in the *Scientific Papers (1)* (Appendix).

3.1. Geophysical exploration in geothermal sites

Geophysical methods play a crucial role in geothermal exploration since they can achieve many objectives of the preliminary phases. Although most geophysical methods have been developed for the oil and gas industry, geothermal exploration has benefited from some of these advances.

In the context of geothermal resources, geophysical exploration is mainly focused on physical parameters which characterize the system, such as temperature, permeability, or fluid content, or on parameters that may reveal structures that influence the geothermal system's functioning (Georgsson, 2009). The application of particular methods will be conditioned by the geothermal

system type, the study goals, but also by the access to the methods or even depending on the country in which particular methods may be popularized.

In this study case, affordable geophysical methods were chosen to define the area's main structures, the VF and AT, which have been previously considered the key parameters in the functioning of the geothermal system. In this structural context, the integration of geophysical methods based on different physical parameters has been chosen. This combined methodology can be advantageous in the early stages of exploration, especially when there are many geological and geothermal uncertainties. Moreover, it is an appropriate practice in urban areas, as different noise sources can affect particular methods and distort the results.

Specifically, the methods used are based on electrical resistivity (*Magnetotellurics* and *Electrical Resistivity Tomography*), chargeability (*Induced Polarization*), density (*Gravity),* and acoustic impedance (*Horizontal-to-Vertical Spectral Ratio*).

3.1.1. Electrical properties

The magnetotelluric (MT) and the electrical resistivity tomography (ERT) methods allow the characterization of the subsurface electrical resistivity. However, the scale of the investigated targets varies for each method. Whereas the ERT method is applied to shallow investigations, MT is the only method capable of providing information about the subsurface characteristics up to several kilometers deep.

The electrical resistivity is sensitive to minor changes in the rock volume; therefore, it is strongly influenced by several factors, such as the nature and composition of the rock, the rock's alteration, the porosity, the proportion of saturated pores, the characteristics of the saturation fluid, the pressure, or the temperature (Schön, 2015).

The main examples of the application of electrical and electromagnetic methods in geothermal exploration are related to the products resulting from hydrothermal alteration, usually related to high-temperature systems (Árnason et al., 2000; Pellerin et al., 1992; Piña-Varas, 2014). In contrast, the fluid temperature is not high enough to affect the rock volume in the exploration of medium or low-temperature systems. Therefore, it is mainly used to characterize the intrinsic rock characteristics (such as rock type or porosity), which condition the geothermal system's functioning but are not sufficiently affected by the hydrothermal circulation.

In this study, the electrical resistivity results will be used to differentiate between different geothermal. First, as the resistivity in the Earth is in the range of many orders of magnitude (Figure 7), the Vallès Basin sediments and the basement electrical responses should be different enough. Furthermore, due to the presence of faults, some fractured zones with particular permeabilities and water saturation could also be imaged and characterized.

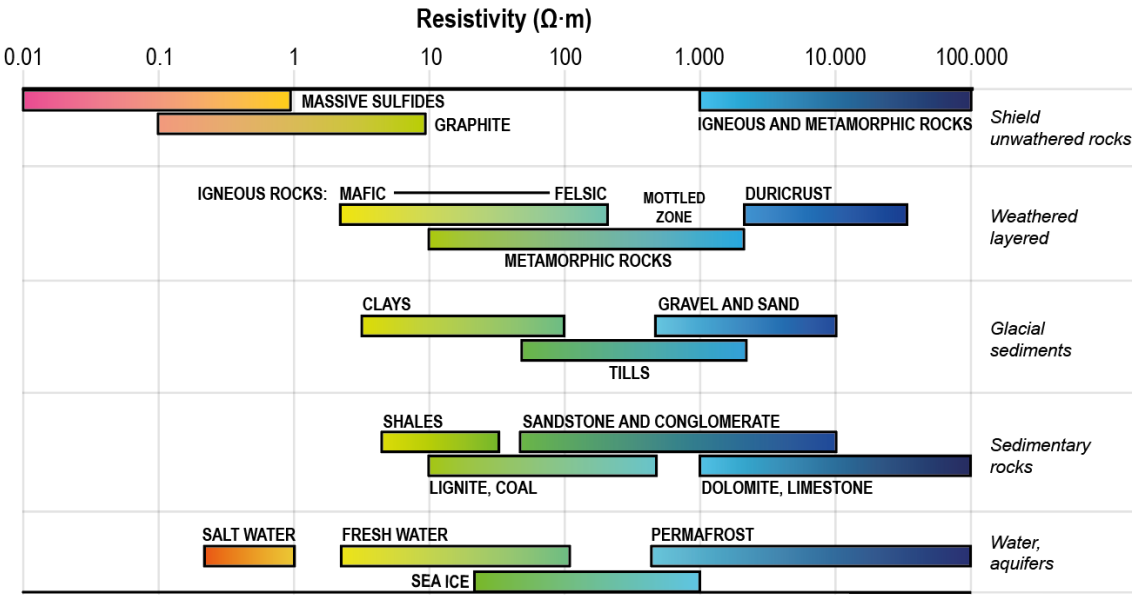

Figure 7. Electrical resistivity (Ωm) range of some geological materials (created from Palacky, 1987).

A combined ERT-Induced Polarization survey is also presented; therefore, another parameter will define the electrical properties of the subsurface: the chargeability.

In the time domain, chargeability is usually presented in milliseconds and indicates the time the residual voltage decreases to the equilibrium state after the cutoff of the current injection in the subsurface (Schön, 2015; Telford et al., 1990). In simple terms, the chargeability reflects the degree to which the subsurface can store electric charge, analogous to a leaky capacitor. Therefore, it will depend on the polarization capacities of the subsurface, which is usually related to multiple and complex electric phenomena, mainly influenced by the mineralogy or the water content (Burtman & Zhdanov, 2015).

The induced polarization method is widely used in the exploration of ore bodies, environmental investigations, and groundwater studies (Revil et al., 2012; Seigel et al., 2007); however, it could also be useful in geothermal exploration. The main target would be clay formations, which in geothermal sites are usually related to the development of self-hydrothermal clay caps (Raguenel et al., 2019; Revil & Gresse, 2021), but also clay formations in fault zones (i.e., fault gouge). Moreover, it can also detect massive sulfide minerals, which are sometimes related with hydrothermal minerals deposition, and which have high chargeability capacities (Telford et al., 1990). Besides that, recent studies state that this technique could be used to characterize the hydraulic and mechanical properties of volcanoes and geothermal systems; however, some developments still have to be made (Revil & Gresse, 2021).

3.1.2. Density

Gravity surveys are a quick and inexpensive way to obtain a rough picture of the density distribution, which is strongly influenced by the nature of the rock units rather than other geological factors. However, as the gravity method is limited due to the ambiguity that an infinite number of density distributions fit a given gravity field, other information is needed to be able to fix some parameters (Georgsson, 2009).

The main applications of density models in geothermal exploration are focused on the basement depth variations in sedimentary areas, intrusive rocks and heat sources, fault or dyke systems, and alteration or cementation due to thermal effects (Georgsson, 2009; Manzella, 1973; Mariita, 2012). However, in a minor sense, other factors such as temperature, pressure, or porosity (Figure 8) could also affect the results (Schön, 2015). The resolution used in this work will only allow the identification of rock units, specifically to limit the Vallès Basin from the basement units.

A *(Sharma, 1997)*

Rock type	Density (wet)
Sand	1.62-2 *(g/cm³)*
Sandstones (Mesozoic)	2.15-2.4
Sandstones (Paleozoic and older)	2.35-2.65
Quartzite	2.60-2.70
Limestone	2.5-2.75
Shales (younger)	2.1-2.6 (2.4)
Shales (older)	2.65-2.75 (2.7)
Gneiss	2.6-2.9 (2.7)
Basalt	2.7-3.3 (2.98)
Gypsium	2.3
Rocksalt	2.1-2.4 (2.2)
Granite	2.52-2.81 (2.67)
Granodiorite	2.67-2.79 (2.72)
Peridotite	3.15-3.28 (3.23)
Eclogite	3.34-3.45 (3.39)

B *(Sari, 2018)*

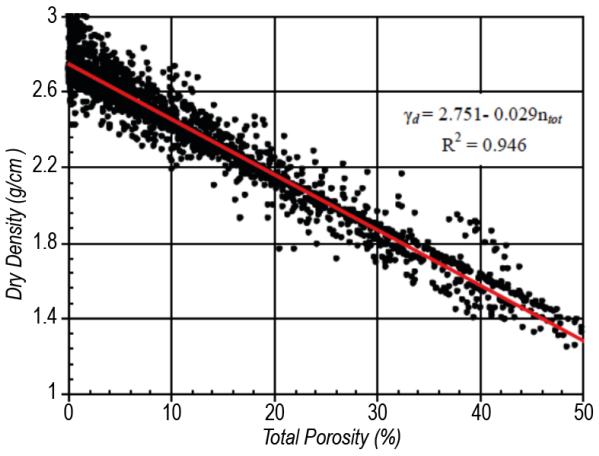

Figure 8. A) Density values of typical rocks. Figures in parentheses are taken to be average values (Sharma, 1997) B) Relationship between total porosity and dry density (excluding coal and evaporate rocks) (Sari, 2018).

3.1.3. Acoustic impedance

Acoustic impedance is a physical property that describes how much resistance an ultrasound beam encounters as it passes through a material. It is the product of the porous media density through which the sound wave travels per the velocity of the sound wave, which varies among the different rock layers (Andreassen et al., 2007; Schlumberger, 1998).

Although the acoustic impedance can give us some information about gas saturation, porosity, or shalyness (Schön, 2015), in this study, it will be used to delimitate different geological units. Specifically, the density contrast between the sediments of the basin and the underlying hard bedrock can allow us to draw the Vallès Basin geometry.

3.2. Magnetotelluric method

The magnetotelluric method (MT) is an electromagnetic method of natural source which allows the electrical resistivity characterization of the subsurface by measuring the electromagnetic (EM) field variations of the ionosphere. From the ionosphere, the electrical fluctuations propagate without considerable attenuation, and when they reach the Earth's surface, given its conductive nature, they are attenuated. Beneath the Earth, the waves propagate diffusively, and their penetration depends on both their frequency of oscillation and the conductivity of the subsurface in which they propagate (Everett, 2013).

MT is based on the simultaneous measurement, at the surface, of the time variations of the electric and magnetic fields. In every MT site, this method measures the variations with the frequency of five components of the electromagnetic field: the horizontal electric (E_x and E_y) and magnetic (B_x and B_y) components, and the vertical magnetic component (B_z) (Figure 9). The resulting time variations are transformed to the frequency domain using the Fourier transform functions. Then, the electric and magnetic field components will be used to calculate the impedance tensor, which will relate both fields to finally determine the distribution of the electrical resistivity of the subsurface in depth (Chave & Jones, 2012).

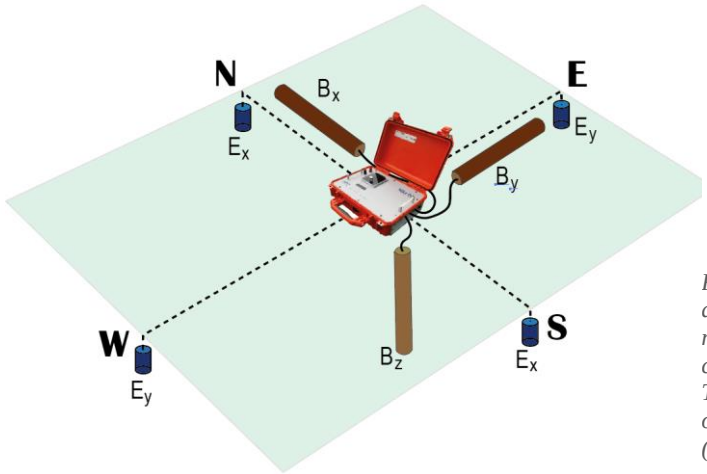

Figure 9. Typical setup for MT data acquisition. Three induction coils or magnetometers measure the orthogonal components of the magnetic field ($B_x B_x B_x$). Two pairs of electrodes measure the orthogonal components of the electric field ($E_x E_y$).

A) Fundamentals[3]

The MT method is based in the fundamental Maxwell equations, which describe the electric and magnetic fields behavior and how they interact. These are: the Faraday's law ($Eq.$ III. 1), the Ampère's law ($Eq.$ III. 2), and the Gauss' laws for the electric ($Eq.$ III. 3) and magnetic fields ($Eq.$ III. 4):

[3] From Cagniard (1953), Chave & Jones (2012), and Vozoff (1991).

$$\vec{\nabla} \times \vec{E} = -\frac{\partial \vec{B}}{\partial t}, \qquad (Eq.\ \text{III.}1)$$

$$\vec{\nabla} \times \vec{H} = \vec{j} + \frac{\partial \vec{D}}{\partial t}, \qquad (Eq.\ \text{III.}2)$$

$$\vec{\nabla} \cdot \vec{D} = \rho_v, \qquad (Eq.\ \text{III.}3)$$

$$\vec{\nabla} \cdot \vec{B} = 0, \qquad (Eq.\ \text{III.}4)$$

where, $\vec{E}\ (V/m)$ and $\vec{H}\ (A/m)$ are the electric and magnetic fields intensities; $\vec{B}\ (T)$ is the magnetic induction; $\vec{D}\ (C/m^2)$ is the electric displacement, $\vec{j}\ (A/m^2)$ is the current density, and $\rho_v\ (C/m^3)$ is the charge density.

The vector quantities presented in these equations are related through the constitutive equations of the medium:

$$\vec{j} = \sigma \vec{E}, \qquad (Eq.\ \text{III.}5)$$

$$\vec{D} = \varepsilon \vec{E}, \qquad (Eq.\ \text{III.}6)$$

$$\vec{B} = \mu \vec{H}, \qquad (Eq.\ \text{III.}7)$$

where, $\sigma\ (S/m)$ is the electrical conductivity; $\varepsilon\ (As/Vm)$ is the dielectric permittivity, and $\mu\ (Vs/Am)$ is the magnetic permeability. All these factors describe the intrinsic properties of the materials through which electromagnetic fields propagate.

All these previous equations describe the propagation of the electromagnetic waves through the inner Earth when the source of energy is at the surface. When the electromagnetic wave penetrates into the interior, it is attenuated, and its amplitude decreases.

The *skin depth* parameter indicates how a wave of a given frequency is attenuated in a given subsurface medium. It is defined as the distance at which the amplitude of the electric field has been attenuated by a factor $\boldsymbol{e}$ from the Earth's surface value, so it allows the definition of the investigation depth: high-frequency waves will penetrate short distances, while low-frequency waves may reach, in some cases, even the boundary between the lithosphere and the asthenosphere.

These time-varying electric and magnetic fields are recorded for a long time, depending on the project's objective (from hours to months). With longer acquisition time, longer period range, and *skin depth.*

B) Magnetotelluric transfer functions[4]

Processing the acquired data consists of converting the EM fields into the frequency domain through the Fourier transform, to calculate the transfer functions. The MT transfer functions are tensor relationships between the electric and magnetic field orthogonal components as a function of the frequency. The most common transfer functions that are going to be used in this thesis are: the impedance tensor and the geomagnetic transfer function (*tipper*).

The *impedance tensor* $\boldsymbol{Z}(\boldsymbol{\omega})$ links the horizontal components of E and B (Eq. III.8). The $\boldsymbol{Z}$ components are determined for a frequency range, and can be decomposed into two scalar magnitudes, the modulus (apparent resistivity, ρ_a) and the phase (φ). Both are fundamental MT measurements for data interpretation, as ρ_a ($\Omega \cdot \mathrm{m}$) is the average resistivity of the equivalent uniform half-space (Eq. III.9), and φ (º) changes according to the increasing or decreasing resistivity with depth (Eq. III.10).

$$\begin{pmatrix} E_x(\omega) \\ E_y(\omega) \end{pmatrix} = \begin{pmatrix} Z_{xx} & Z_{xy} \\ Z_{yx} & Z_{yy} \end{pmatrix} \cdot \begin{pmatrix} B_x(\omega)/\mu_0 \\ B_y(\omega)/\mu_0 \end{pmatrix} \qquad \text{(Eq. III.8)}$$

$$\rho_{a_{ij}} = \frac{1}{2\pi\mu\omega} \left| Z_{ij}(\omega) \right|^2 \qquad \text{(Eq. III.9)}$$

$$\varphi_{ij}(\omega) = tan^{-1}\left[\frac{Im\, Z_{ij}(\omega)}{Re\, Z_{ij}(\omega)}\right] \qquad \text{(Eq. III.10)}$$

The impedance tensor will be represented as apparent resistivity and phase graphs as function of period. This morphology varies according to the geoelectrical structures, whose distribution condition the geoelectric dimensionality, which can be set as 1D, 2D or 3D.

The *geomagnetic transfer function* (*tipper* vector, $\boldsymbol{T}(\boldsymbol{\omega})$), relates the vertical component of the magnetic field to its two horizontal components. This tipper vector can be decomposed into its real and imaginary vectors, representing the projection of B_z into the horizontal plane. The graphical representation of the real vectors, by means of the induction arrows, are useful to infer the presence of lateral variations of the electrical resistivity. Therefore, it will be a crucial parameter in the dimensionality analysis.

$$B_z(\omega) = \left(T_x(\omega), T_y(\omega)\right) \cdot \begin{pmatrix} B_x(\omega) \\ B_y(\omega) \end{pmatrix} \qquad (Eq.\ \text{III.11})$$

[4] From Chave & Jones (2012), Parkinson (1959), and Weise (1962).

C) Dimensionality analysis[5]

The dimensionality analysis is fundamental to understand how to interpret the MT and correctly perform the modeling or inversion. The spatial distribution of the geoelectrical structures condition the dimensionality, which can be 1D, 2D or 3D. To simplify the methodology applied in this thesis, only the bidimensional cases are described.

In an ideal 2D case, the electrical resistivity is constant along one horizontal direction, which is defined as the *strike*, and varies in the other two directions (one horizontal and the vertical) (Figure 10). The impedance tensor response is decoupled into two independent modes, the Transverse Electric (**TE**) mode and the Transverse Magnetic (**TM**) mode. TE describes currents flowing parallel to the strike while TM describes currents flowing perpendicular to the strike. The final representation of the impedance tensor can be simplified in the strike direction, resulting the diagonals to 0, and the anti-diagonals to the modes TM and TE ($Eq.$ III. 12).

To retrieve the strike of the regional structures and the regional impedance tensor, the scheme of McNeice and Jones (2002) based on the Groom and Bailey decomposition method (Groom and Bailey, 1989) has been followed.

$$Z_{2D} = \begin{pmatrix} Z_{xx} & Z_{xy} \\ Z_{yx} & Z_{yy} \end{pmatrix} = \begin{pmatrix} 0 & Z_{xy} \\ Z_{yx} & 0 \end{pmatrix} = \begin{pmatrix} 0 & Z_{TE} \\ Z_{TM} & 0 \end{pmatrix} \qquad (Eq.\ \text{III. 12})$$

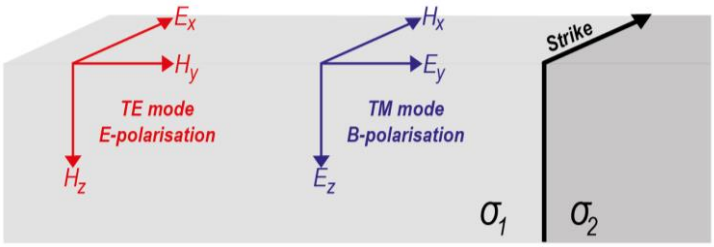

Figure 10. Example of 2D Earth's model with a vertical contact which separates two bodies with different conductivities (σ) (modified from F. Simpson & Bahr, 2005).

D) Distortion evaluation[6]

The dimensionality analysis can also be used to understand whether the data are affected or not by galvanic distortion, also called *static shift*. The static shift is a non-inductive change of the MT apparent resistivity response that severally impairs the interpretation of data, caused by near-surface resistivities close to the receivers. It is not a time-dependent effect and does not disturb the phase or transfer functions. However, it shifts the apparent resistivity curve to higher or lower values by a constant, real scaling factor. Therefore, it preserves the same shape of the recorded apparent resistivity curve.

[5] From Chave & Jones (2012) and F. Simpson & Bahr (2005).
[6] From Chave & Jones (2012), Ledo et al., 1998; F. Simpson & Bahr (2005), and Spitzer (2001).

The static shift correction is one of the significant drawbacks of the MT analysis since it requires invoking either other geophysical methods less affected by distortion or geological information. Some techniques are reviewed in Chave and Jones (2002) or Simpson and Bahr (2005).

Following the primary procedure and the elements described above, the MT survey of this thesis is presented in the succeeding chapters.

3.2.1. Magnetotelluric survey

Since the electrical resistivity may be affected by changes in temperature and permeability which are key parameters for geothermal exploration; and considering the Vallès Fault (VF), which involves great depths, the MT method seems to be the most appropriate exploration method.

The data acquisition was done in two field campaigns (Figure 11). The first campaign (MT-Samalús) aims to acquire a profile next to the previous boreholes (IGME, 1982, 1984a, 1986b) to characterize the VF. The second campaign (MT-Vilamajor) aims to characterize the VF out of the granodioritic thrust sheet, where there are no thermal manifestations.

3.2.2. Data acquisition

For both MT profiles (MT-Samalús and MT-Vilamajor) measurements were carried out using the multichannel geophysical measurement system Metronix-ADU06 and Metronix-ADU07, two induction coil magnetometers MFS-06 (horizontal measurements), and four non-polarizable electrodes forming two dipoles in two orthogonal directions (N-S and E-W). The electrode distances were 50 m for the MT-Samalús stations, and 20 m for the MT-Vilamajor stations. Natural electromagnetic field fluctuations were recorded between 3 and 12 hours at each site, using sampling frequencies of 128 Hz, 256 Hz, and 4096 Hz.

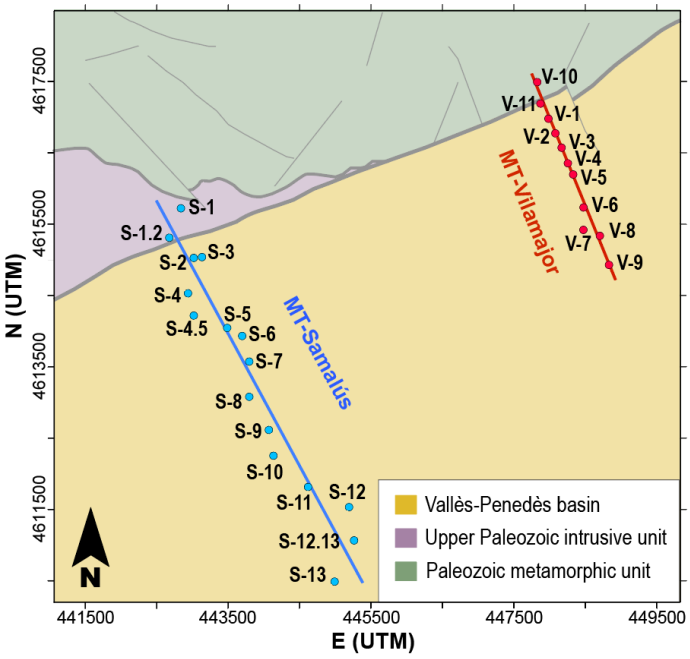

Figure 11. Geological map focused on the location of the MT profiles: MT-Samalús and MT-Vilamajor.
The MT-Samalús profile which go from Samalús to Cardedeu town, and it is located in the eastern edge of the granodioritic sheet. The MT-Vilamajor include stations made in a single campaign and it is localized in Sant Pere de Vilamajor town. It is located out of the granodioritic thrust sheet, so it only crosses the Vallès Fault.

3.2.3. Data processing

The acquired MT data is located close to an urban area with industrial and farming activity, which induces cultural noise. Furthermore, both MT profiles cross power lines and stations, one of the most common noise sources (Szarka, 1988).

Using a Wavelet Transform-based scheme (Escalas et al., 2013), the time and frequency intervals affected mainly by cultural noise have been selected to reduce their effect. Figure 12 compares the acquired data during the day and night for the S-3 station. While the same site shows higher amplitudes of the electric field for all the frequencies during the day hours, the amplitudes are clearly reduced at night. The exception of a high-frequency cyclic signal is related to the cathodic protection of pipe systems characteristic of this area (50 Hz in Europe).

After selecting the time intervals with lower noise effect, more detailed quality controls were carried out on time series. This process consists of selecting the time segments identified as noisy due to the presence of peaks or disturbances, which will not be used later in the processing stage.

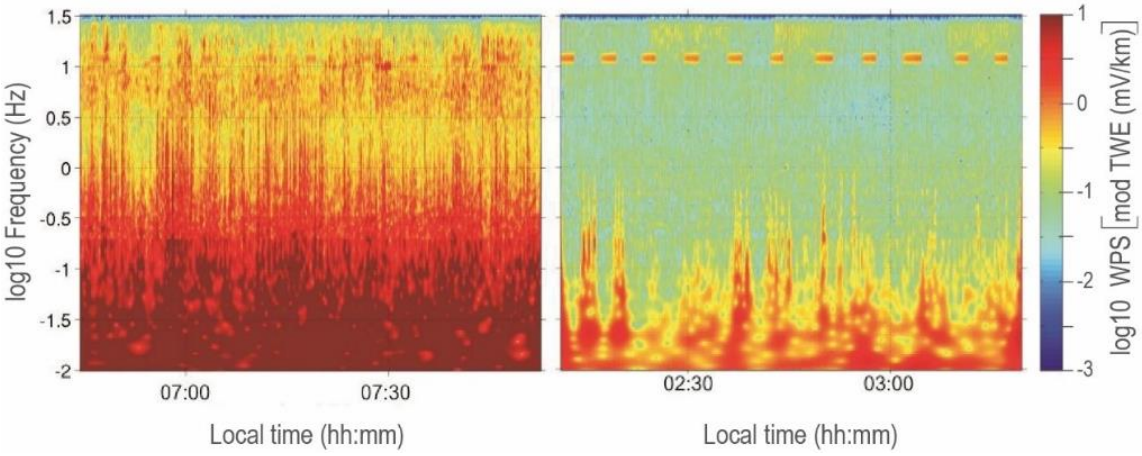

Figure 12. Left: scalogram of the electric field of the site S-3 during day hours. Right: scalogram of the electric field of site S-3 during night hours.

During data processing, the remote reference technique was applied (Gamble et al., 1979). This methodology consists of locating a marginal MT station (UTM 31N ETRS89; X: 447527.550m, Y: 4605737.162m) less affected by cultural noise, or that its cultural noise is not related to the measuring station's noise. The basis of the method is that the magnetic field does not change significantly, unlike the electric field. Therefore, correlating the remote and measuring signals, is possible to get an increment in the signal-to-noise ratio.

From later converting the selected segments of the time series to the frequency domain, power spectra have been obtained for a total of twenty frequencies for each logarithmic decade of periods. First, every frequency is processed separately using different parameters and, later, smoothed by using different mathematic functions. At the end of the processing stage, MT

responses for every site were obtained, which included the apparent resistivity curves and the phase for the *xy* and *yx* polarizations. Figure 13 shows an example of using the data before after removing the noisy segments. The transfer functions obtained using all the data have a more scattered behavior and bigger error bars than those using only clean time series.

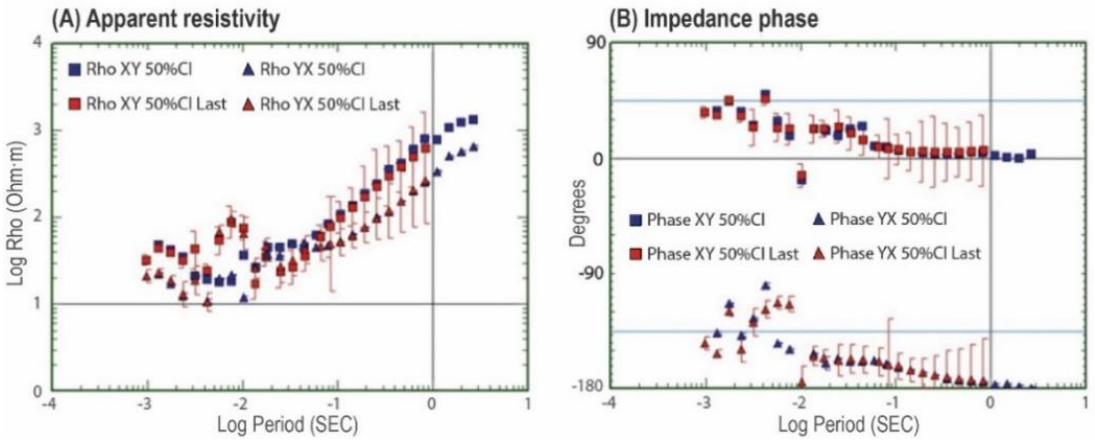

Figure 13. Comparison between the apparent resistivities (A) and phases (B) for site S-3 using all the data (red) and cleaned time series (blue).

3.2.4. Data analysis

After completing the processing, the data was subjected to stringent quality control, removing low-quality points which will not be included in the inversion process. Secondly, the D+ method (Beamish & Travassos, 1992) was used to check the causal relationship between the apparent resistivity and the phase curves, and obtain interpolated points that replace those eliminated due to their low quality. The smoothed data are the ones used for the inversion. Figure 14 shows an example of smoothed curves for stations S-8 and S-9.

Previous to the modelization, is important to analyze the dimensionality of the magnetotelluric data, setting the geometry of the geoelectrical strike. Considering an error floor for the impedance components of 5%, the obtained regional strike was 060N for the MT-Samalús profile, and 070N for MT-Vilamajor. The values agree the main geological strike of the studied zone, the ENE-WSW Catalan Coastal Ranges.

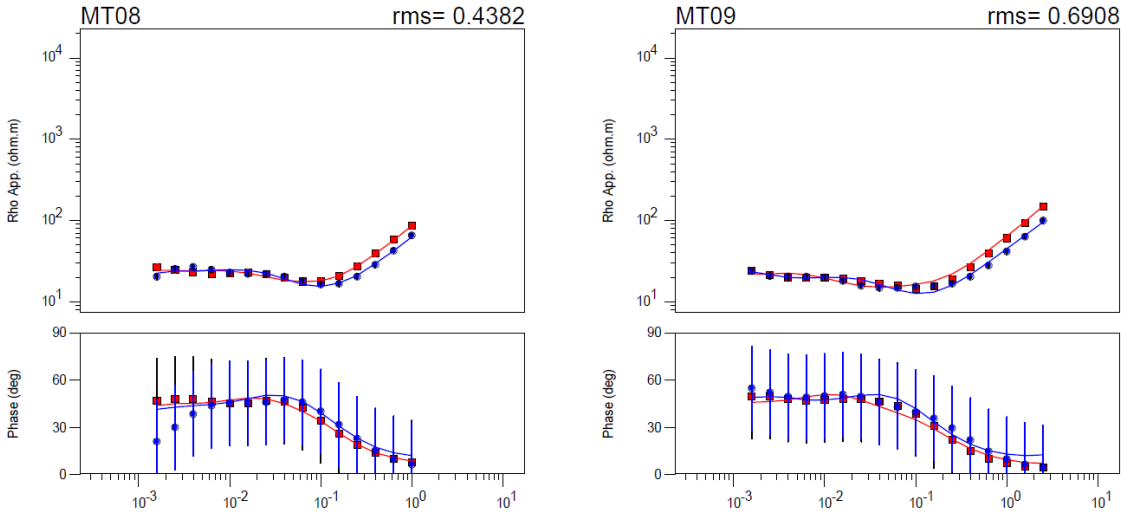

Figure 14. Apparent resistivity and phase curves for two stations of the MT-Samalús profile (S-8 and S-9). This data has been smoothed using the method D+ from (Beamish & Travassos, 1992).

3.2.5. 2D inversion

The goal of the inversion of the processed data is to obtain the resistivity distribution in the subsurface of the studied area.

After rotating the MT data, the TE and TM modes were assigned to the main impedance components and the related apparent resistivities and phases. Then, simultaneous 2D inversions of TM and TE apparent resistivities and phases were undertaken using the nonlinear conjugate-gradient algorithm of Rodi and Mackie (2001), implemented in the *Winglink*® (Geosystem SRL) software. This algorithm, simultaneously searches for the model which trades off the lowest overall RMS misfit with the smallest lateral and vertical conductivity gradients in a regularized manner. On average, the logarithm of the apparent resistivity data was fit to within 10%, and the phases to within 2.9º.

3.2.6. MT-Samalús

Finally, the MT-Samalús was made up of 15 sites (station S-2 was discarded because of its proximity to station S-3) along an NNW-SSE profile of approximately 6 km in length, from the granodioritic unit of the Prelitoral Range and across the Vallès Basin. The sites spacing ranged between 100 and 600 m.

The initial model was a homogeneous half-space of 100 Ωm, with a mesh of 89 horizontal and 134 vertical cells. Neither structural features nor conductivity discontinuities were imposed, and a final RMS 1.2 was achieved. The comparation between the raw data and the model response curves are plot in the *Appendix* (A.1.).

The resulting final model is shown in Figure 15, where the results of HVSR (which will be detailed in chapter 3.4.) and the borehole's information (IGME, 1986, 1984a, 1982) are also plotted. The boreholes horizontal lines indicate the limit between the basin and the basement, and the HVSR vertical lines indicate the limits of the bedrock depth considering the standard deviation. In the following lines, the description of the geoelectrical bodies and a general interpretation for these units are presented:

- **R1:** In the north-northwestern part of the model, there is a geoelectrical unit that presents the highest resistivity values (>3000 Ωm). These values can be observed from the shallow to the deeper parts of the model. This high resistivity unit corresponds to the outcropping granitic materials of the Prelitoral range.

- **C1:** To the SE of R1, there is a sub-vertical band with lower resistivity values. The resistivity values increase gradually with depth, from 100 Ωm to 500 Ωm. This unit is assumed to be the VF plane and its associated fractured zone.

- **C2:** The model presents a near-surface conductive geoelectrical unit. This unit has a wedge geometry, with its thickness increasing towards the SSE (from 500 m of thickness in the north-northwestern part to 1250 m in the southeastern part). The resistivity values vary from 1 Ωm to 200 Ωm. This upper unit is associated with the Miocene sediments filling the basin (alluvial fans of shales, sandstones, and conglomerates).

- **R2:** Below the C2 unit, there is a resistive zone with values between 500 Ωm and 3000 Ωm, associated to the basement unit. In this case, the high conductivity values of the C2 unit could affect the determination of the resistivity value underneath.

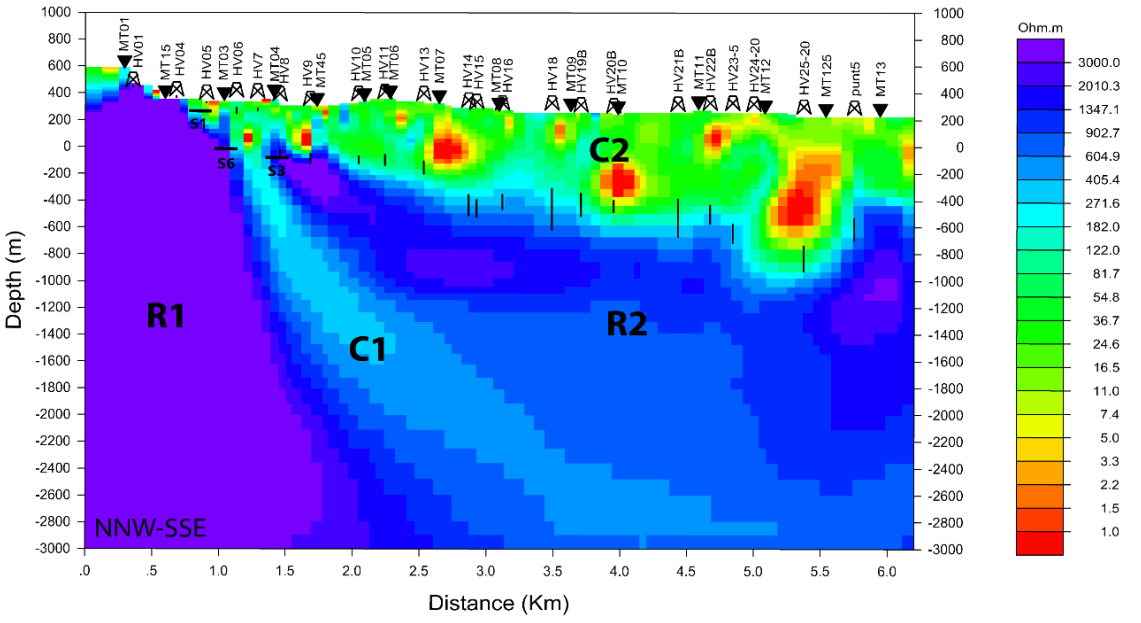

Figure 15. MT-Samalús resistivity model with the location of basin depth considering boreholes and HVSR sites. This NW-SE profile goes from the Prelitoral Range, inside the granodioritic thrust sheet, and across the Vallès Basin.

3.2.7. MT-Vilamajor

The goal of this profile was the delimitation of the geothermal system in the eastern part of the Vallès Basin. Considering the previous works in the area, which indicate that the granodioritic unit controls the geothermal system anomaly, the profile has been strategically localized outside of the thrust sheet, in order to compare the results with the MT-Samalús.

The MT-Vilamajor profile includes 10 sites (V-4 was not include due to its low quality) along an NNW-SSE profile of 4 km long, which extends from the Paleozoic metamorphic rocks towards the Vallès Basin. The distance between sites ranges between 250 and 400 m approximately. As the acquisition of the sites was interrupted due to the COVID-19 crisis, the first nine stations were measured in February (2020), and the V-10 and V-11 stations were acquired in June (2020).

The resulting final model is shown in Figure 16, and the comparation between the raw data and the model response curves are plot in the *Appendix* (A.2.). The description of the main geoelectrical bodies in comparison to the MT-Samalús resistivity model are presented below:

- **R1 & R2:** At both edges of the deepest part of the model, and surrounding C1, there is a geoelectrical unit that presents the highest resistivity values (>5000 Ωm). This high resistivity unit corresponds to the basement, which is the Paleozoic metamorphic unit in this area.

- **C1:** Same sub-vertical band with lower resistivity values as the one presented in MT-Samalús. The resistivity values increase gradually with depth, from 10 Ωm to 1000 Ωm. Unlike the MT-Samalús profile, this unit, attributed to the VF zone, has a rectilinear morphology with a dip around 60º.

- **C2:** The near-surface conductive geoelectrical unit presents the same stepwise morphology, increasing its thickness towards the SSE. This unit is also associated with the same Vallès Basin Miocene sediments.

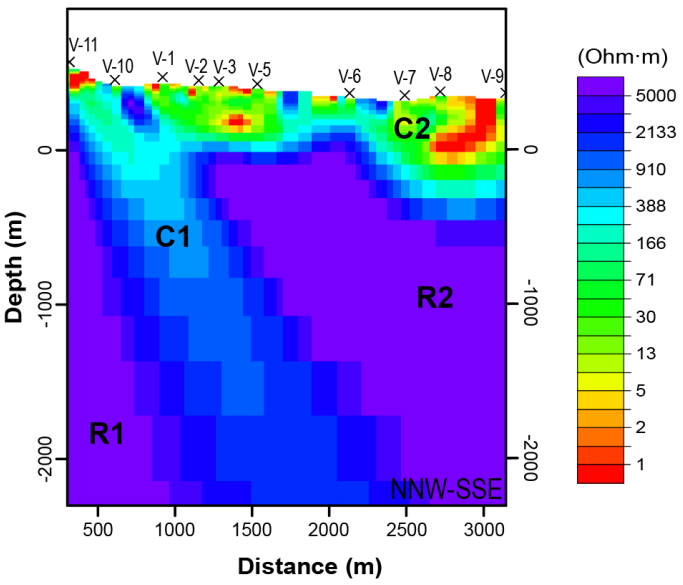

Figure 16. MT-Vilamajor resistivity model. The model finally uses 10 sites located close to Vilamajor town, and cover an NNW-SSE profile which goes from the Prelitoral Range and across the Vallès Basin.

3.2.8. Resistivity models discussion overview

The MT-Samalús and MT-Vilamajor resistivity models have allowed the definition of the deep geometry of the VF and the Miocene Vallès Basin. However, although the models are similar, the VF zone has a slightly different geometry.

On the one hand, the Miocene geoelectrical unit shows the step-wise morphology in both resistivity models. The base of syn-kinematic deposits at the hanging wall, shows a gradual deepening towards the SSE, towards the center of the Vallès Basin. Specifically, the model set the base of the basin at a maximum point of 1200 m, which differs from the models of the Vallès-Penedès Basin center, which mainly draw 3 km of normal slip (Bartrina et al., 1992; Gallart et al., 1997; Gaspar-Escribano et al., 2004; Gómez & Guimerà, 1999; Juez-Larré & Andriessen, 2006; Roca & Guimerà, 1992; Sàbat et al., 1995; Vidal et al., 1995). Some offshore profiles parallel to the Vallès-Penedès Basin (Roca, 1992) evidence this decrease in the basement depth towards the northeastern boundary. This base shallowing would be related to an increase in uplift towards the NE margin, implying a higher erosion rate. In fact, at the northeastern limit of the Vallès Basin, near Campins town, the basement unit of the hanging wall block outcrops, what would validate this hypothesis (see the granodioritic outcrop in the middle of the V-P Basin, in Figure 5).

On the other hand, the VF zone unit in MT-Vilamajor is a sub-vertical band of around 70º dip, keeping its uprightness with depth. Still, in the MT-Samalús profile, it is a listric fault whose geometry changes from 70ºC to 45º. This new outcome suggests a dilemma with the VF geometry which needs other data input to be solved. Therefore, it will be discussed in later chapters.

3.3. Gravity method

Gravity surveying measures variations in the Earth's gravitational field caused by differences in the density of subsurface rocks (Reynolds, 1997). A subsurface zone whose density differs from the surroundings causes a localized perturbation in the gravitational field known as gravity anomaly.

Gravimeters measure the difference in gravity between a base station, where the absolute value of gravity is known, and a series of other stations that cover the study area. At the same time, the theoretical gravity is calculated, which depends on latitude, elevation, and the surrounding topography. The difference between the observed gravity and the theoretical gravity is known as the Bouguer anomaly, which will be affected by the subsurface densities (Hinze et al., 2012; Mariita, 2012).

A) Method theory[7]

The gravity method has its base in two laws derived by Newton, the Universal Law of Gravitation (Eq. III.13), and the Second Law of motion (Eq. III.14):

$$F = G\frac{m_1 \cdot m_2}{R^2} \qquad \text{(Eq. III.13)}$$

, where F is the gravitational force, which is proportional to the object's mass (m_1, m_2) and the gravitational constant G; and decreases with distance (R); and,

$$F = m \cdot a \qquad \text{(Eq. III.14)}$$

, where the force is proportional to the mass and the acceleration (a).

There are different ways to calculate the acceleration of gravity, but the most commonly used and attributed to the gravimeters uses a spring. This system is based on Hooke's Law (Eq. III.15), and considers that if a mass hangs on a spring, a force on the mass will stretch the spring. Therefore, the spring's displacement will be proportional to the applied force.

$$F_{spring} = -k \cdot x \qquad \text{(Eq. III.15)}$$

, where k is a constant factor characteristic of the spring, and x is the displacement or change in length.

The unit of gravity acceleration is the Gal, which equals to 1 cm/sec^2. The Earth's gravity field is typically around 980 Gal; however, the gravimeters can detect differences between 1 µGal and 0.1 Gal, which allows the detection of anomalies controlled by the subsurface density

B) Correction formulas[8]

The application of this method, which varies in an extensive range of scales, can involve the measurement of the absolute gravity acceleration or the relative gravity acceleration. Since there is a network of gravity stations worldwide where absolute gravity values are available (Morelli et al., 1972), it is usually not necessary to determine the absolute value. In contrast, the relative variation in relation to one of these official stations is used.

After acquiring the relative gravity data with the gravimeter, it must be corrected for further processing and interpretation. The gravity correction formulas used are based on the *Oasis Montaj*® (Geosoft, Seequent) software guide:

- **Instrument scale factor:** Corrects a reading to a relative mGal value based on the instrument calibration. Depending on the range of gravity readings, a specific scale factor is applied.

[7] From Hinze et al. (2012), Kearey et al. (2002), Lowrie (2007), and Telford et al. (1990).
[8] From Geosoft Inc. (2015)

$$r_c = r_t \cdot S\,(r) \qquad \text{(Eq. III. 16)}$$

r_c: $scale\ corrected\ reading\ (mGal)$

r: $instrument\ reading\ (mGal)$

$S(r)$: $scale\ factor$

- **Tide correction**: All readings are corrected for earth tides due to the position of the sun and the moon at the time and location of the observation. The software used for the tide data has been *solid.exe* (Milbert, 2010), which implements the International Earth Rotation Service Conventions (McCarthy & Petit, 2004) to calculate the solid Earth's tide.

$$r_t = r_c + g_{tide} \qquad \text{(Eq. III. 17)}$$

r_t: $tide\ corrected\ reading\ (mGal)$

r_c: $scale\ corrected\ reading\ (mGal)$

g_{tide}: $tide\ correction\ (mGal)$

- **Instrument height:** each reading should be corrected for the height of the instrument above the base at which the reading is measured.

$$r_h = r_t + 0.308596 \cdot h_i \qquad \text{(Eq. III. 18)}$$

r_h: $instrument\ height\ corrected\ reading\ (mGal)$

r_c: $tide\ corrected\ reading\ (mGal)$

h_i: $instrument\ height\ (m)$

- **Instrument drift:** Gravimeter readings change with time as a result of elastic creep in the springs, which cause an apparent change in gravity in a given station. In order to determine this change, in every field campaign, the gravity was measured in the same station (base station) at the start and the end of the day. The differences between the measurements at the base station are plotted to produce a drift curve and correct the intermediate readings (Figure 17).

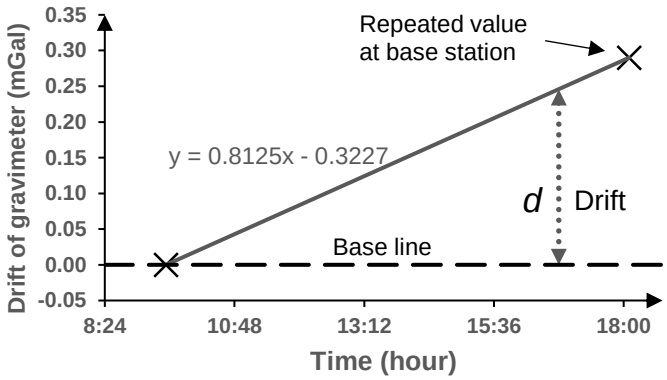

Figure 17. Example of the instrumental drift for the gravity field campaign 4/2/2020.

- **Absolute gravity:** the base station used has a known absolute gravity value, which is used to calculate the absolute gravity in the rest of the stations considering the relative gravity readings differences. In this case, the base employed belongs to the Fundamental Gravimetric Network of Spain (Casas et al., 1987), originated from the International Gravity Standardization Network (IGSN71) (Morelli et al., 1972).

$$g_a = g_{B1} + (r_h - r_{B1}) - (t - t_{B1})d \qquad \text{(Eq. III. 19)}$$

g_a: $absolute\ gravity\ (mGal)$; g_{B1}: $base\ 1\ absolute\ G\ (mGal)$
r_h: $instrument\ height\ corrected\ station\ reading\ (mGal)$; r_{B1}: $base\ 1\ reading\ (mGal)$
t: $reading\ time\ (hour)$; t_{B1}: $base\ 1\ reading\ time\ (hour)$
d: $drift\ \left(\frac{mGal}{hour}\right)$

- **Latitude correction:** the latitude correction consists in subtracting the theoretical gravity calculated using the International Gravity Formula from the observed value. In this case, the formula used is the 1980 International Gravity Formula (Moritz, 1980):

$$g_\phi(1980) = 9.78032.7 \cdot\ (1 + 0.0053024\ \sin^2\phi - 0.0000058\ \sin^2\ 2\phi) \text{ (Eq. III. 20)}$$

g_ϕ: $theoretical\ gravity\ (mGal)$
ϕ: $latitude\ of\ the\ station\ (decimal\ degrees)$

- **Free Air anomaly:** the free-air correction is the difference between gravity measured at sea level and at an elevation with no rock in between. The value considered for this correction is: 3.086 g.u./m:

$$g_{fa} = g_a - g_\phi + 0.3086 \cdot h_s \qquad \text{(Eq. III. 21)}$$

g_{fa}: $free - air\ anomaly\ (mGal)$
g_a: $absolute\ gravity\ (mGal)$
g_ϕ: $latitude\ correction\ (mGal)$
h_s: $station\ elevation\ (m)$

- **Bouguer anomaly:** the Bouguer anomaly corrects the free-air anomaly for the mass of rock that exists between the station elevation and the spheroid.

$$g_{ba} = g_{fa} - 0.4191 \cdot \rho \cdot h_s \qquad \text{(Eq. III. 22)}$$

g_{ba}: $bouguer\ anomaly\ (mGal)$
g_{fa}: $free - air\ anomaly\ (mGal)$
d: $mean\ density\ of\ the\ upper\ crust\ \left(2.67\frac{g}{cm^3}\right)$ (Simpson & Jachens, 1989)
h_s: $station\ elevation\ (m)$

- **Terrain correction**: the elevation correction combining the free-air and Bouguer corrections usually is adequate to cope with slight topographic effects. However, a particular terrain correction must be applied in areas with considerable elevation variations.

The Bouguer correction assumes an approximation to a semi-infinite horizontal slab of rock between the measuring station and sea level. Therefore, when there are close hills or valleys, there is a mass excess or deficiency, which results in the measurement of $\boldsymbol{g}$ being over- or underestimated (Reynolds, 1997). This correction procedure is based on the Hammer chart (Hammer, 1939), although the *Gravity and Terrain Correction* extension of *Geosoft Oasis Montaj Programs* (2006) has been applied. For the computation, the software only needs a coarse regional Digital Elevation Model (DEM) draped over a more finely sampled local DEM model that covers the survey area. The correction is calculated based on near zone, intermediate zone, and far zone topography contributions for every station (details for every zone in Kane, 1962 and Nagy, 1966).

The total terrain grid should cover a large area depending on the terrain's severity and the detail of anomalies under investigation. In this case the recommended distance was 165 km from the station's limits (Nowell, 1999).

C) Processing of the Bouguer anomaly

After applying the corrections, the final Bouguer Anomaly values are obtained from the g_{ba} with the applied the terrain correction. These values consider the effects caused by large-scale regional structures, and also the local structures. For a good interpretation of local structures, the regional effect has to be subtracted. The applied process will be explained in chapter 3.3.3, using the study case.

3.3.1. Gravity survey

Due to the area's geological characteristics, which presents a horst and graben system with different rock densities, the gravity method could help understand the basin's geometry and detect the basement-basin limit, related to the VF trace.

In order to obtain a map of gravity anomalies, a bibliographic compilation of data previously acquired by the *Instituto Geológico y Minero de España* (IGME), the *Institut Cartogràfic i Geològic de Catalunya* (ICGC), and the University of Barcelona (UB) has been carried out, complemented with new data. In total, there are 1121 points distributed around the granodioritic thrust sheet and the surrounding area, covering the Vallès Basin (Figure 18).

3.3.2. Data acquisition

The new gravity data were acquired between 2019 and 2021 using a Lacoste & Romberg gravimeter, and the base station located in the Faculty of Physics of the University of Barcelona

(Casas et al., 1987; Morelli et al., 1972). There is a kindly irregular distribution of the stations, with distances between 50 and 200 m, caused by access difficulties. However, the sampling is good enough in where the temperature anomalies are identified, and where other geophysical methods can be integrated.

Specifically, most of the newly acquired gravity sites are located in the eastern part of the Vallès Basin, to have a more detailed model and to be able to integrate it with the MT models (MT-Samalús and MT-Vilamajor); and in Caldes de Montbui surrounds.

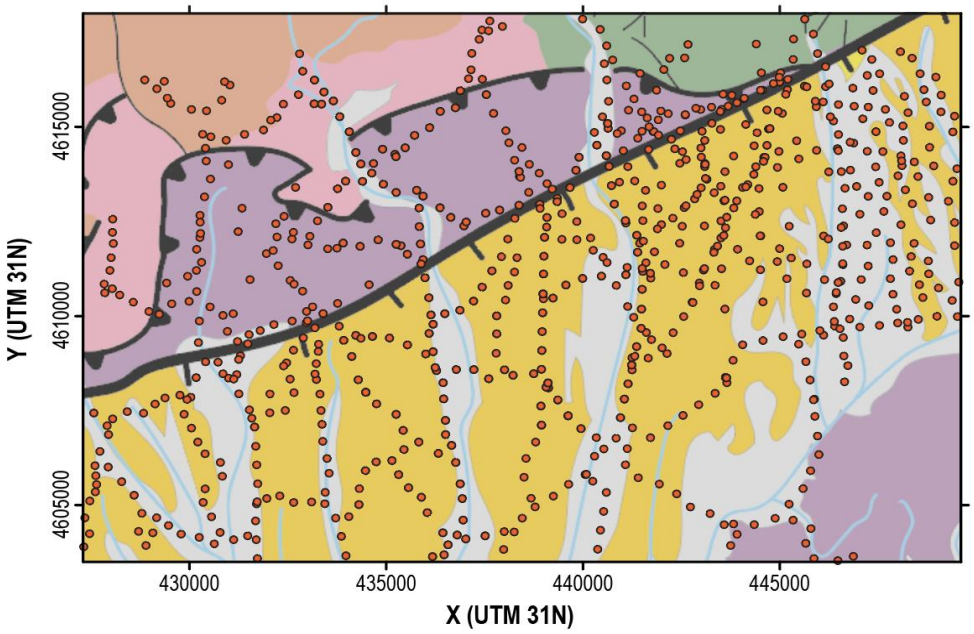

Figure 18. Gravity sites used for the creation of the residual anomaly map and the density model. Most of the sites are well distributed, with a higher density area located in La Garriga-Samalús region (eastern part of the granodioritic thrust sheet). For the geological unit's legend, see Figure 5.

3.3.3. Data processing and results

After applying the corrections, the final Bouguer Anomaly values are obtained from the g_{ba} with the applied terrain correction. Then, the Bouguer anomaly map is interpolated from every site's corrected Bouguer anomaly value. The resulting map (Figure 19A) contains all the gravity anomaly effects generated by the crustal structure and other effects generated by shallower local structures with enough density contrast. As our objective in this survey was defining the near-surface structure, the Bouguer anomaly was decomposed into a regional component and a residual component. This separation was carried out by assimilating the regional anomaly to a first-degree polynomial surface (Figure 19B), assuming the ENE-WSW trending of the Catalan Coastal Ranges.

The Residual Anomaly map (Figure 19C) illustrates a sizable negative anomaly with an ENE-WSW direction. This anomaly reaches –8 mGal over the center of the Vallès Basin. Towards the NNW, a high slope with higher values reaches 10 mGal. These increasing values would be related

to the Prelitoral range, which is characterized by denser materials (igneous and metamorphic Paleozoic rocks). The VF, which separates the Prelitoral range and the Vallès Basin, should be traced in the steeper parts of the map, where the contour lines are close together.

In contrast, towards the SSE, where the contour lines are widely separated, the contact between the Vallès Basin and the Litoral Range is more gradual. Figure 19C also shows SW-NE variations in the negative anomaly within the basin, which can be associated with lateral changes in basement depth. The lower values, and therefore, the basin's maximum thickness, are located close to La Garriga town.

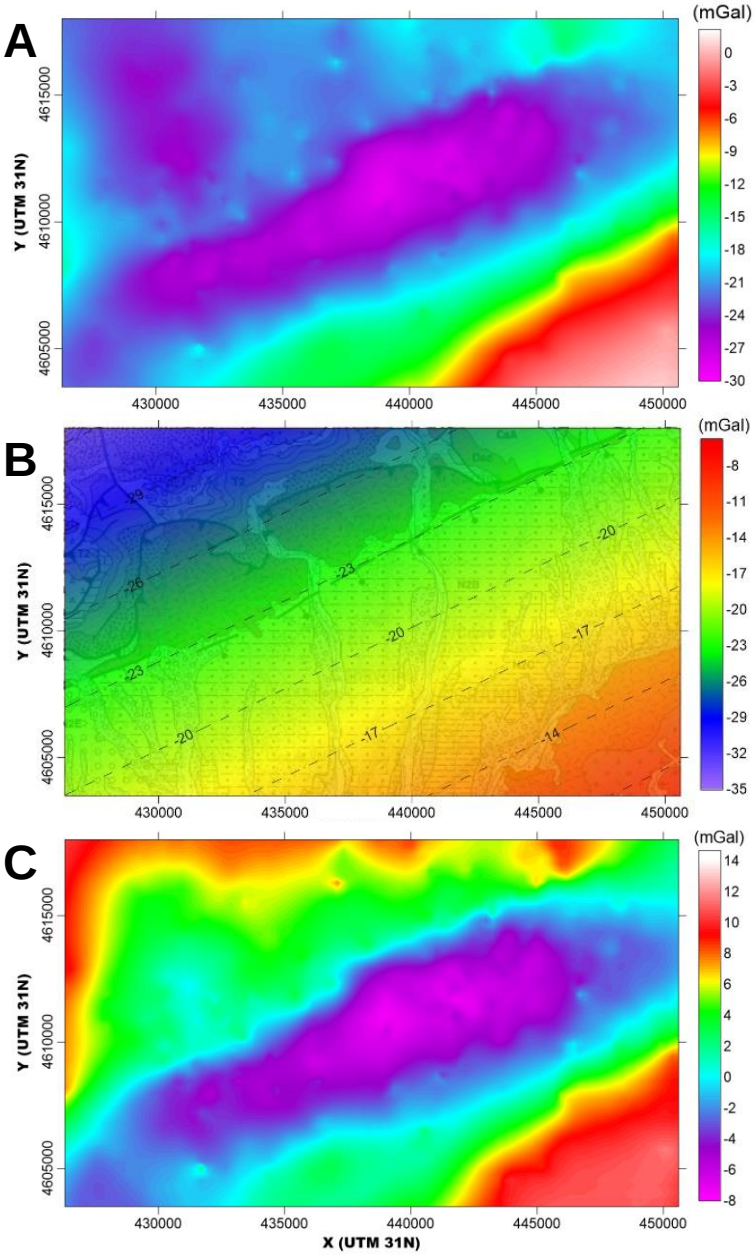

Figure 19. A) Bouguer anomaly map. This map follows the ENE-WSW trend, and is it possible to identify a lowest anomaly in the Vallès Basin location. This map contains the gravity anomaly effects generated by the crustal and shallower structures. B) Regional anomaly map. Considering the geologic map underneath, the regional anomaly map clearly follows the trend of the Catalan Coastal Ranges (ENE-WSE trend), so it contains the gravity effects generated by the crustal geological structure. C) Residual anomaly map which presents the gravity anomaly caused by the shallower density contrasts. The result clearly images the Vallès Basin and the granodioritic sheet limit.

3.3.4. Gravity gradient

The gravity data has been analyzed to identify the limit between the Vallès Basin and the Prelitoral Range, which corresponds to the VF trace. By taking the horizontal derivative of the residual anomaly data, this enhancement aims to detail the basin boundary by comparing the gravity contours. Therefore, it images the slope or rate of change of gradient with horizontal displacement (Kusumah et al., 2010). To compute the horizontal derivative, the *Gradient Operator* plugin in *Surfer*® (Golden Software LLC, 2016), which generates a grid of the steepest slopes at any point on the surface, has been used.

The final map presented in Figure 20 shows the most significant changes in density along the VF trace. The most important outcome is that the interpreted geometry for the VF trace is linear but not continuous. In other words, the highest density changes, attributed to the fault trace, present a constant ENE-WSW orientation, but it is divided in different segments.

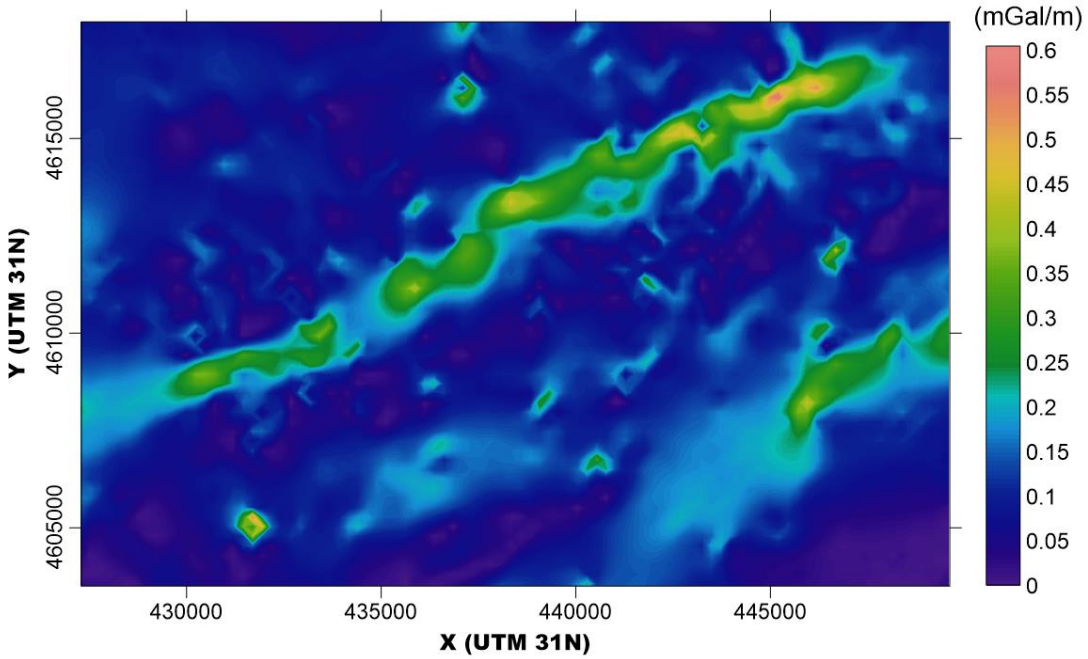

Figure 20. Gravity slope map represented by the horizontal derivative of the residual anomaly map. The major changes in density would be related to the limit between the basin and the basement, represented by the Vallès Fault. This limit presents a linear but not continuous geometry.

3.4. HVSR method

The Horizontal-to-Vertical Spectral Ratio (HVSR) methodology is a passive seismic technique that uses the environmental noise to obtain the fundamental frequency of the ground. It detects frequency peaks related to an impedance contrast that can be interpreted as contrasts between sediments and underlying bedrock. Therefore, it is an indicator of the bedrock geometry (Bard, 1985, 1998; Nakamura, 1989).

The acquisition and processing of these data has been carried out by the ICGC.

A) Method theory[9]

HVSR definition is proposed as the ratio of the Fourier amplitude spectra of the horizontal and the vertical components of the ambient noise vibrations, which is recorded at one single station by a sensor on the free surface (Figure 21):

$$HVSR_S = \frac{H_S}{V_S} \qquad \text{(Eq. III. 23)}$$

, where H_S is the horizontal component of Fourier spectrum recording at surface; and V_S is the vertical component of Fourier spectrum recording at the surface.

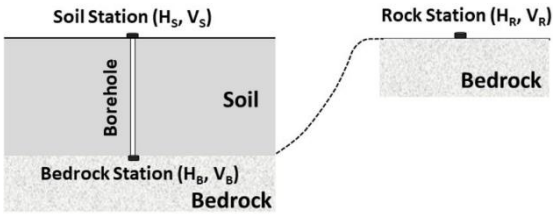

Figure 21. Schematic diagram of soil, reference rock, and bedrock recordings (Xu & Wang, 2021).

The HVSR method is based on two assumptions. First, the H/V Fourier spectral ratio at the bedrock ($HVSR_B$) is 1, so the horizontal and vertical waves travel equally on bedrock. And second, after the seismic wave propagates from the basement to the surface, the vertical component is not amplified, therefore, the vertical transfer function (TF_V) is 1.

$$HVSR_B = \frac{H_B}{V_B} = 1 \qquad \text{(Eq. III. 24)} \qquad\qquad TF_V = \frac{V_S}{V_B} = 1 \qquad \text{(Eq. III. 25)}$$

Considering the horizontal transfer function and previous formulas:

$$TF_H = \frac{H_S}{H_B} = \frac{H_S}{V_B} \cdot \frac{V_S}{V_B} \cdot \frac{V_B}{H_B} = \frac{H_S}{V_S} = HVSR_S \qquad \text{(Eq. III. 26)}$$

TF_H is the same as $HVSR_S$. Moreover, there is an agreement that the HVSR is similar to the result of empirical transfer function, and thus, it can be used to reveal the fundamental frequency.

These formulas can be summarized as if the site can be assumed to be relatively hard and flat, it will not amplify the site effect horizontally or vertically within a specific frequency band, so the horizontal and vertical vibrations should be the same within a certain frequency range. However, for specific sites with overburdened or softer soil, the horizontal ground motion amplification is relatively significant in a particular band range. In contrast, the corresponding vertical ground motion does not significantly magnify within this band range. Then, estimating site predominating frequency and site amplification, can be realized through the Fourier amplitude spectrum ratio of horizontal and vertical ground motion.

Thus, it is possible to determine the transfer function and the fundamental frequency (f_0) by realizing a unique measurement at the surface. The main requirement in applying the HVSR method to calculate the sediment's fundamental frequency (f_0^{sed}) is that there must exist a sharp

[9] From Nakamura (1989), Xu & Wang (2021), Bard 1985 and 1999)

acoustic impedance contrast between sediments and bedrock, being the basement rock acoustic impedance at least twice the sedimentary one (Fäh et al., 2001; Lachet & Bard, 1994). The processing and inversion procedure will be explained in the following chapters, with the case study example.

3.4.1. HVSR survey

The HVSR survey is focused on determining the geometry of the basement in the eastern part of the Vallès Basin. The data acquisition and processing is a collaborative geophysical acquisition work of the *Unitat Tècniques Geofísiques* of the ICGC and the University of Barcelona, as part of the GEO-URBAN project.

The data was acquired during three major campaigns: the HVSR-Samalús profile survey, which coincides with the trace of the MT-Samalús magnetotelluric profile; the eastern survey HVSR-Vilamajor, to correlate the data with the MT-Vilamajor profile and identify the southern basin limit; and the western survey HVSR-La Garriga, to finally widely cover the surroundings of La Garriga town. Therefore, the sites are distributed between La Sagrera and Sant Pere de Vilamajor towns (west-eastern limits), and they cover the entire Vallès Basin, from the Montseny massif to the Litoral Range (north-southern limits).

3.4.2. Data acquisition

The HVSR survey includes 205 sites in the three campaigns. The average spacing in the western survey (HVSR-La Garriga) is 500 m, in the eastern (HVSR-Vilamajor) is 1000 m, and in the profile (HVSR-Samalús) is 200 m. Their distribution is also influenced by the high-noise anthropogenic sectors, such as roads, industrial parks, or railways, which were tried to be avoided.

The HVSR sites were recorded using a SARA SL06 data logger connected to Lennartz 0.2 Hz LE-3D/5s three-component seismometer. The data was acquired with a sampling rate of 200 Hz and a variable recording length depending on the expected basement depth (between 20 and 120 minutes).

3.4.3. Data processing

The H/V curves were calculated using the *Geopsy*® software (http://www.geopsy.org), which follows this expression:

$$\frac{H}{V} = \frac{\sqrt{\frac{S_{NS}^2 + S_{EW}^2}{2}}}{S_v} \qquad \text{(Eq. III.27)}$$

, where S_{NS} and S_{EW} are the magnitudes of the spectrum Fourier method of north–south, east–west and vertical components, respectively. The Fourier spectrum for each component was

smoothed in overlapped windows by 50 %. Anthropogenic noise was removed using a STA/LTA antitrigger algorithm (Lee & Stewart, 1981).

Figure 22 shows an example of the H/V spectra represented as a function of frequency. The significant peak represents the soil fundamental frequency. According to the SESAME project criteria, for a peak to be considered significant, its H/V amplitude must be greater than 2 (Bard & SESAME-Team, 2005). Therefore, the sites where the H/V spectral ratio shows a flat curve without any significant peak, indicate that the basement is outcropping or very shallow.

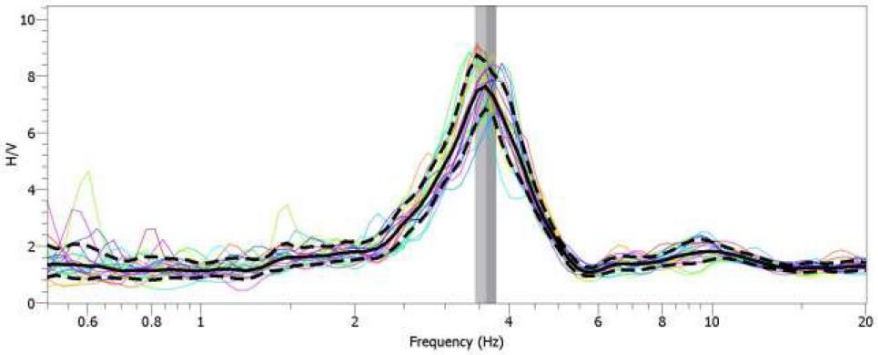

Figure 22. Example of the H/V spectral ratios obtained for sites located above basin sediments. Color lines represent the different ratios for each calculation window, and the black line represents the mean of the values with the error margin (dashed black lines) (Macau et al., 2021).

3.4.4. Data inversion and results

The first draft of the sediments-basement boundary geometry is based on the fundamental frequency values, which shows that the deepest basement would be in the center of the basin, and the shallowest would appear near the VF (Figure 23).

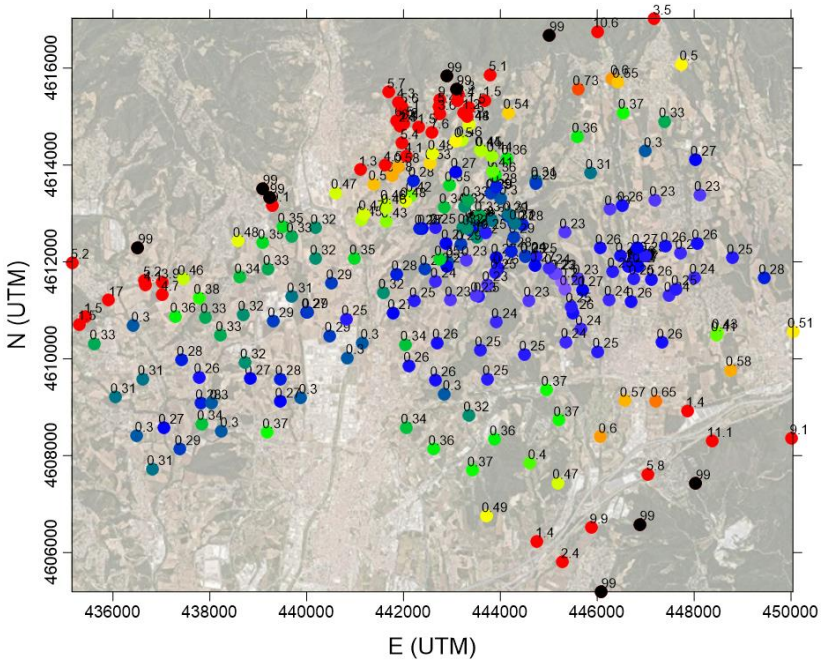

Figure 23. Distribution of the sediment's fundamental frequency at the studied sites. Black dots (99 Hz) correspond to points located on the outcropping basement, where no significant peak is detected. Data from Macau et al. (2021).

The calculated depth can be obtained using an empirical relationship between the basement depth and the fundamental frequency (Ibs-Von Seht & Wohlenberg, 1999):

$$H = a \cdot f_0^b \qquad \text{(Eq. III. 28)}$$

, where a and b are empirical parameters strongly dependent on geological conditions, specifically on shear-wave velocity profiles. In most cases, bedrock depth was directly measured from boreholes, but it could also be calculated from the geophysical methods. The bibliography shows different empirical laws fitted in different geological environment: Ibs-Von Seht and Wohlenberg (1999) estimated in a deep Tertiary basin; Delgado et al. (2000) computed in a thin Quaternary deposit, or Benjumea et al. (2011) calculated in a weathered granitic area.

In this case, in order to do a proper estimation of the real depths, the unit of the *Unitat Tècniques Geofísiques* (ICGC) is building an empirical relation for the Neogene basins of Catalunya, by the comparison of between different geophysical methods results (HVSR, magnetotelluric method, seismic refraction technology, seismic noise array technique) and deep boreholes which reached the basin-basement contact (i.e. Benjumea et al., 2014, 2011; Gabàs et al., 2016; Macau et al., 2018) (Figure 24). They have obtained the following empirical relation named GICE-2014-pous:

$$H = 164.65 \cdot f_0^{-1.33} \qquad \text{(Eq. III. 29)}$$

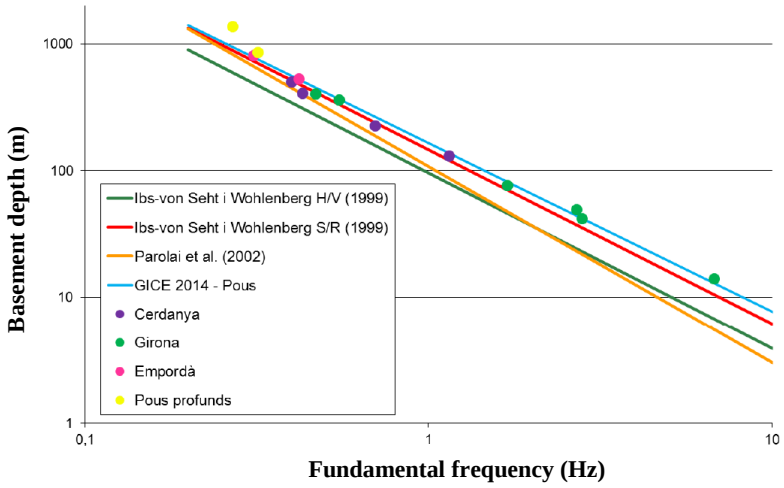

Figure 24. Comparison between different empiric relations, including GICE-2014-pous, and the relation between basement depth and fundamental frequency in cases of study, using the Array technique, HVSR and borehole's information (Macau et al., 2021).

3.4.5. Basin-basement limit

Considering the empirical relation GICE-2014-pous, the Neogene basin thickness has been calculated. Figure 25 shows the final basin-basement limit surface geometry and the basin thickness. Before the map's interpretation, it is important to notice that the edges of the surface should not be considered because of the interpolation method and because the surface could have intersected the topography.

This final surface in presents an ENE-WSW basin geometry with lateral variations. The depocenter changes laterally with its maximum depth, 1200 m.a.s.l., in the eastern part of the survey. Specifically, the basin is deeper from the Congost river valley towards the east. Between La Garriga and Samalús towns, the -200 and -400 m.a.s.l. contour lines also present some irregularities, whereas other parts are linear.

The lateral changes in the basin thickness map are even more marked, and the depocenter lines vary laterally. This change in the depocenter position is visible in the Congost valley, in the La Garriga town (close to x:44000 UTM). Towards the east, the basin depocenter is located southern, while towards the west of the valley, the basin is located northern. Further to the west, there could also be another change in the depocenter line position. However, it is not as clear due to the lack of data on this part of the area.

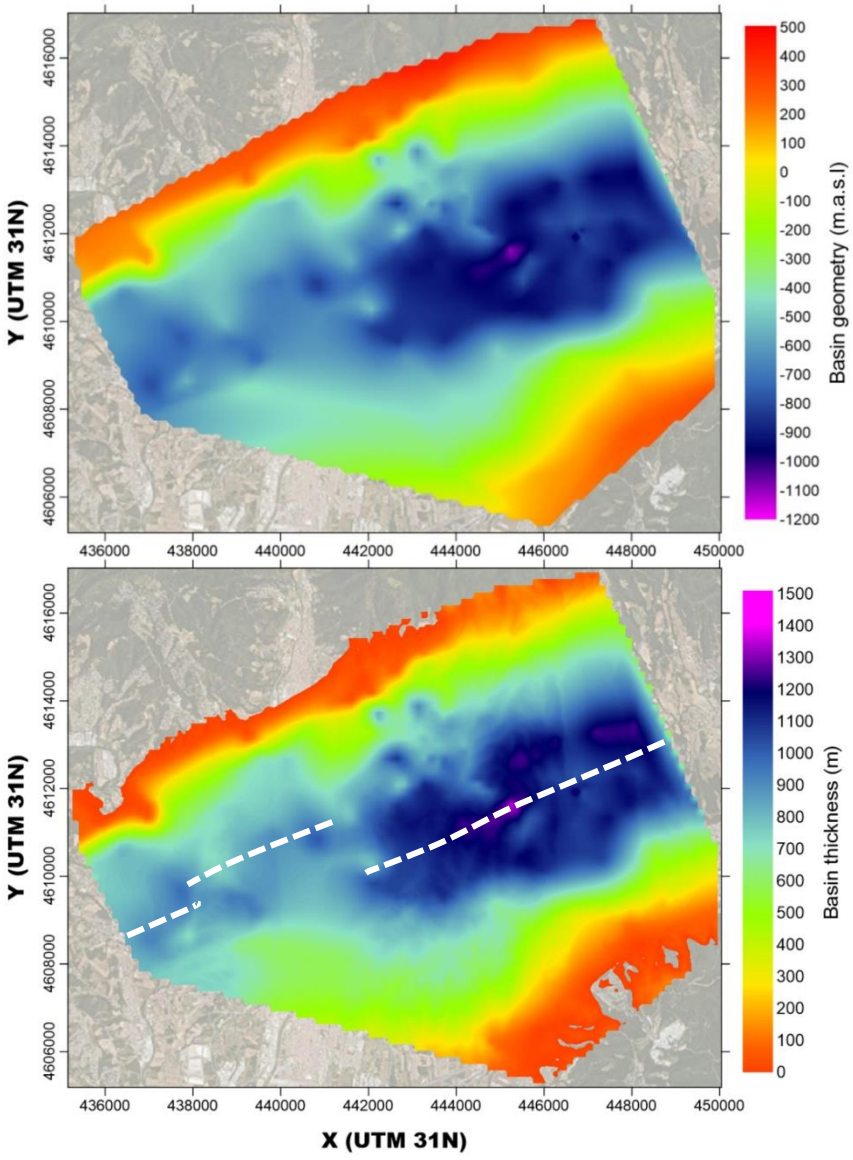

Figure 25. Up) Vallès Basin geometry map from HVSR data. Down) Vallès Basin thickness map from HVSR data. The white dashed lines indicate an approximate position of the depocenter of the basin. The geometry of the Vallès Basin changes laterally its position and depth.

3.5. Electrical resistivity tomography survey (ERT)

The electrical resistivity tomography (ERT) method detects and localizes resistivity anomalies in the subsurface by injecting an electrical current. In this case study, this method aims to get a 2-D section of resistivities to identify the location of the fault traces and characterize the subsurface fault zone.

This near-surface method is based on introducing a low-frequency electrical current into the subsurface through two surface electrodes and simultaneously measuring the induced potential gradient with other surface electrodes (at least two). When an electric field is created in the ground, the electric voltage will vary depending on the electric resistance of subsurface materials. So, each potential measurement gives insight into the electrical properties of the subsurface materials (Everett, 2013). Finally, to obtain the resistivity distribution, an inverse problem should be resolved.

A) Electrodes configuration

Modern instruments can simultaneously produce large datasets of resistance or apparent resistivity data using several tens to hundreds of electrodes. The greater the number of electrodes permanently attached to multi-core cable, the higher the investigation capabilities and the less time is spent in the field.

For 2D imaging using a multi-electrode system, the multiple electrodes are fixed for the entire survey, and measurements are taken sequentially using different sets of four electrodes controlled by a switching device. Thus, any survey is based on a four-electrodes system (two injecting current (**C**) and two measuring voltage (**P**)) and their relative position (configurations or array). Their position, the profile length, and physical parameters of the materials underlying the area of interest will condition the depth of investigation. Every configuration or array defines the geometric factor (k), which is used, together with the voltage-to-current (R), to get the apparent resistivity values:

$$\rho_a = k \cdot R \quad \text{(Eq. III.30)}$$

To obtain efficient coverage in an ERT survey using conventional electrical imaging techniques that use a limited number of electrodes, large electrode spacings must be used. However, information from the near surface of the surveyed area could be missed. In this context, a multiscale survey technique is an efficient option, in which information from various depth levels is gained by conducting a series of measurements using different electrode spacings over the same survey line (Abdul Nassir, 1997).

The description of two different configurations of a four-electrode array applying the multiscale survey technique is presented below. These two configurations are used in this case study, the profiles of which will be presented in the following chapters.

a) Schlumberger reciprocal configuration (S_R): In the Schlumberger configuration, the potential electrodes P_1P_2 are kept centered at a fixed location with constant separation. The current electrodes C_1C_2 are centered at the exact location, but voltage readings are made as the separation between them is expanded about the common midpoint (Everett, 2013). The **reciprocal** configuration consists of exchanging the current and potential electrodes. So, as it is shown in Figure 26, the current electrodes are in the middle of the array.

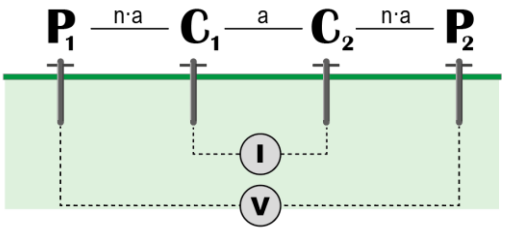

Figure 26. Four-electrode configuration for the Schlumberger reciprocal array. C: current electrodes, where the electric current is injected. P: potential electrodes, where the electric voltage is measured.

The electrode layout of the first level, in which the minimum electrode spacing (a) is used, is the same as in the Wenner array. In order to increase the depth of investigation, the outer potential electrodes are moved out gradually. In contrast, the spacing between the central current electrodes remains fixed for several layers (multiple lengths, n) before it is increased for a new profile over the same survey line (Abdul Nassir et al., 2000). The measured point position (x, z) varies with the position of the four-electrode system and the electrodes spacing (n, a). For example, considering Eq. III. 31.2, with bigger electrode spacing, more profound depths are reached. Figure 27 shows an example of the data survey points in a 220 m long profile, which reached 110 m depth.

$$x = \frac{x_{C_1} + x_{C_2}}{2} \quad \text{(Eq. III. 31.1)} \qquad z = \frac{x_{P_2} - x_{P_1}}{2} \quad \text{(Eq. III. 31.2)}$$

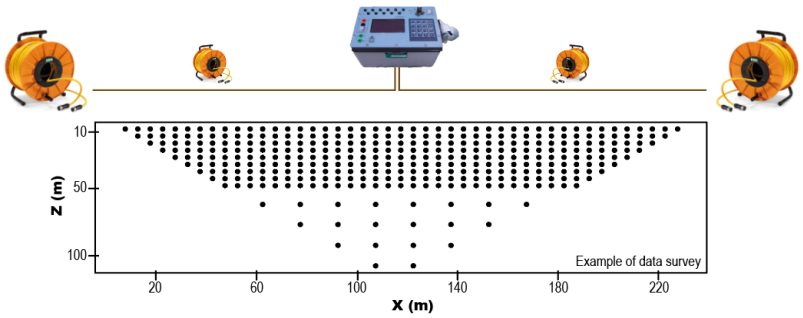

Figure 27. Data survey with the measurement sequences for building up a 2D resistivity section using a multiscale technique with the Reciprocal Schlumberger array. The resistivity measurements for a certain depth can be collected from different levels with different spacings between the potential electrodes, i.e. the deeper separated points are related to a double-spacing technique.

The Reciprocal Schlumberger configuration was chosen because it can be optimized to maximize the number of potential electrode pairs measured by signal current injection, and to assess the assurance and control of quality data compared to the Schlumberger array (Santoso et al., 2019; Stanton et al., 2007). However, it would not influence the measured apparent resistivity if the positions of the potential and current electrodes were interchanged (AL-Hameedawi & Thabit, 2017; Keller & Frischknecht, 1966; van Nostrand & Cook, 1966).

b) Dipole-dipole configuration (D-D): in this array, the current electrodes (***C₁C₂***) and the potential electrodes (***P₁P₂***) have the same spacing ***a***, but the two pairs are widely separated by a distance ***n·a***, where ***n***>>1 (Figure 28).

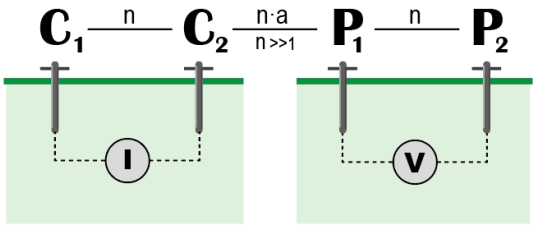

Figure 28. Four-electrode configuration for the Dipole-Dipole array. C: current electrodes, where the electric current is injected. P: potential electrodes, where the electric voltage is measured.

This D-D array is good at vertical structure mappings, such as dykes, cavities, or faults. It is comparatively insensitive to vertical variations in the resistivity distribution but much more sensitive to the difference in horizontal distribution (Loke, 2000). However, the signal-to-noise ratio deteriorates for large values of ***n***, and voltage measurements can be distorted if small-scale, near-surface heterogeneities are present (Everett, 2013).

Figure 29 shows an example of the data survey points in a 220 m long profile, which reached 200 m depth. The density of the points can also vary depending on the programmed survey.

$$x = \frac{x_{C_1} + x_{P_1}}{2} \quad \text{(Eq. III.32.1)} \qquad z = \frac{x_{P_2} - x_{C_2}}{2} \quad \text{(Eq. III.32.2)}$$

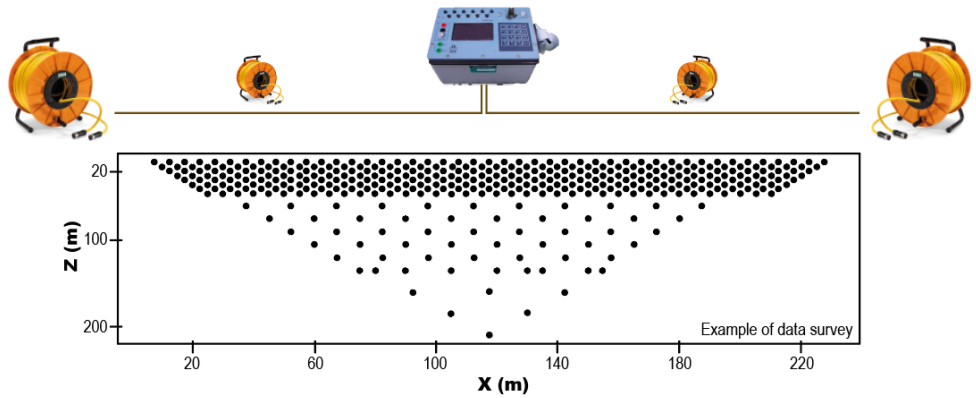

Figure 29. Data survey with the measurement sequences for building up a 2D resistivity pseudosection using a multiscale technique with the Dipole-Dipole array. The resistivity measurements for a certain depth can be collected from different levels with different spacings between the potential electrodes, i.e. the deeper separated points are related to a double-spacing technique.

3.5.1. ERT survey

We carried out two ERT surveys, the first focused on the characterization of the Vallès Fault (ERT-VF), and the other located close to the Alpine Thrust (ERT-AT). The location of profiles has been strategically selected, trying to locate the fault planes in the middle of the profile. So, evidence of the presence of the fault traces, such as a high fracture density, the presence of cataclastic rocks, or even abrupt terrain slope changes (especially in the case of the VF), have played an essential role in choosing the position of the profiles.

Figure 30 shows the position of the two selected profiles with the geological map presented in the introduction. Both profiles are located on the eastern edge of the granodioritic thrust sheet, close to La Garriga town.

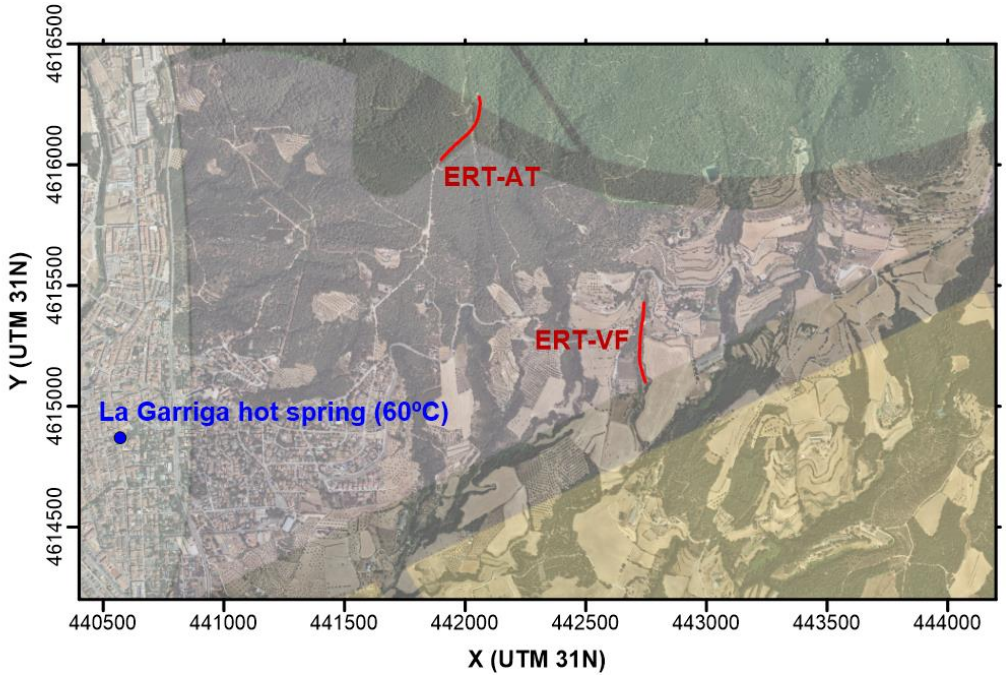

Figure 30. Location of the ERT profiles (red) in relation to the La Garriga town, and the main hot spring (60ºC). The location of both profiles has been chosen considering the geological map presented in Figure 4, but subsequently cross-checking this information with the outcrops. So, although the ERT-VF does not cross the Vallès Fault map trace, there were some outcrop indications that the profile would cross the fault.

3.5.2. Data acquisition, processing and inversion

The ERT profiles were acquired using an SYSCAL, four multi-core cable rolls connected in series, 72 metal electrodes, connection forceps, and a standard battery as a power source.

The ERT-VF profile is 355 meters long, with 5 meters of electrode spacing. This profile orientation (N-S) is conditioned by a dirt road that intersects the fault cartographic trace. Thus, it is not perpendicular to the fault, which must be considered if apparent dips are interpreted. The array used in ERT-VF has been the Schlumberger Reciprocal.

The ERT-AT profile is 355 meters long, with 5 meters of electrode spacing. This profile changes its orientation due to road constraints. Two different arrays were used, the Schlumberger reciprocal and the Dipole-Dipole, and separated and joint inversions were tried.

The electrode configurations were arranged before the fieldwork using *Electre Pro®* (IRIS Instruments) software. After the acquisition, the data were first processed using software *Prosys-II®* (IRIS Instruments) and *EarthImager®* (AGI, Advanced Geoscience, Inc.) for the inversion model. Before the inversion, the wrong data points were eliminated. Then, the *model refinement* option was used due to the presence of significant resistivity variations near the surface, setting the width of the cells to be half the unit electrode spacing.

3.5.3. Vallès Fault ERT profile (ERT-VF)

The ERT-VF resistivity profile obtained is presented in Figure 31. The results show four geoelectrical units.

- The southwestern margin unit (x:0-200m) is characterized by the lowest resistivity values, between 1-40 Ωm. This unit is assigned to the Miocene sediments of the Vallès Basin.
- The northeastern margin unit (x: 200-350m) is characterized by the highest resistivity values, between 70-230 Ωm. This unit is assigned to the basement rocks of the footwall unit, which in this location is the granodioritic unit. Although this unit presents the maximum values, these are low compared with the expected for a granodiorite. The main explanation would be related to the degree of rock fracturing, which could be observed during the data acquisition.
- The intermediate unit is a vertical band separating the previous units, characterized by a resistivity around 50 Ωm. This unit is related to the fault core of the VF.
- The shallower surface unit, parallel to the topography, covers the first few meters underground. It is characterized by a resistivity of about 50-60 Ωm. This unit is related to the Quaternary sedimentary cover.

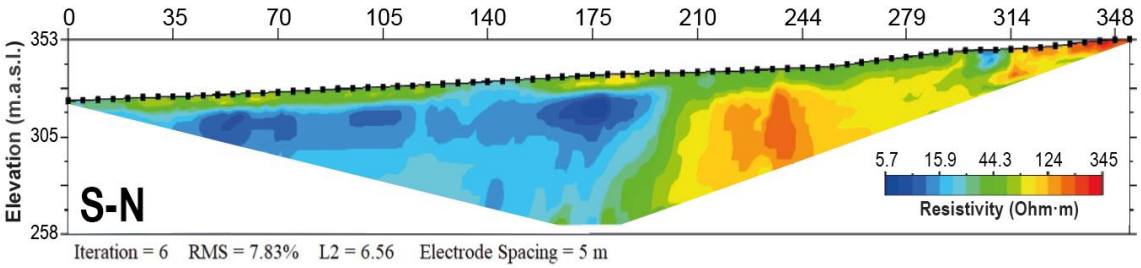

Figure 31. S-N resistivity model for the Vallès Fault. This section crosses the Vallès Fault trace and it clearly shows the contact between the granodioritic unit (resistive unit of the NNE margin) and the Miocene sediments of the Vallès Basin (conductive unit of the SSW margin).

3.5.4. Alpine Thrust ERT profile (ERT-AT)

In this case, two different configurations were used, which were inverted separately and in a joint inversion (Figure 32). Unlike the ERT-VF profile, in these resistivity models it is more difficult to describe geoelectrical units, although some interesting results can be discussed.

One the one hand, the W-S model evidence the shallower changes on resistivity. On the other hand, the D-D model images the deeper lateral changes. However, the joint inversion model represents accurately the main geoelectrical structures from both models.

The most evident geoelectrical body is presented as a vertical band in the middle of the D-D and joint models. This high resistivity unit (600-2000 Ωm) is located in the AT trace, therefore is interpreted as the fault core. In the W-S profile, the shallower units show high conductivities (20-100 Ωm), mainly at each side of the AT trace.

The rest of the profile shows a homogeneous resistivity which does not allow to differentiate between the units affected by the AT, the granodioritic unit of the thrust sheet and the metamorphic rocks.

3.5.5. ERT resistivity model's discussion

In the ERT-VF, the fault core is imaged as the division between two units with considerable resistivity differences (Miocene sediments of the Vallès Basin and the granodioritic unit); in contrast, in the ERT-AT profile, the basement units have similar resistivity values (granodioritic unit and metamorphic series).

Considering the expected protolith rock theoretical resistivities (Figure 7), the fault zone presents low resistivities. These low values could be related to its fracture degree, with the potential development of clays, like in a fault gouge; and the water content between fractures.

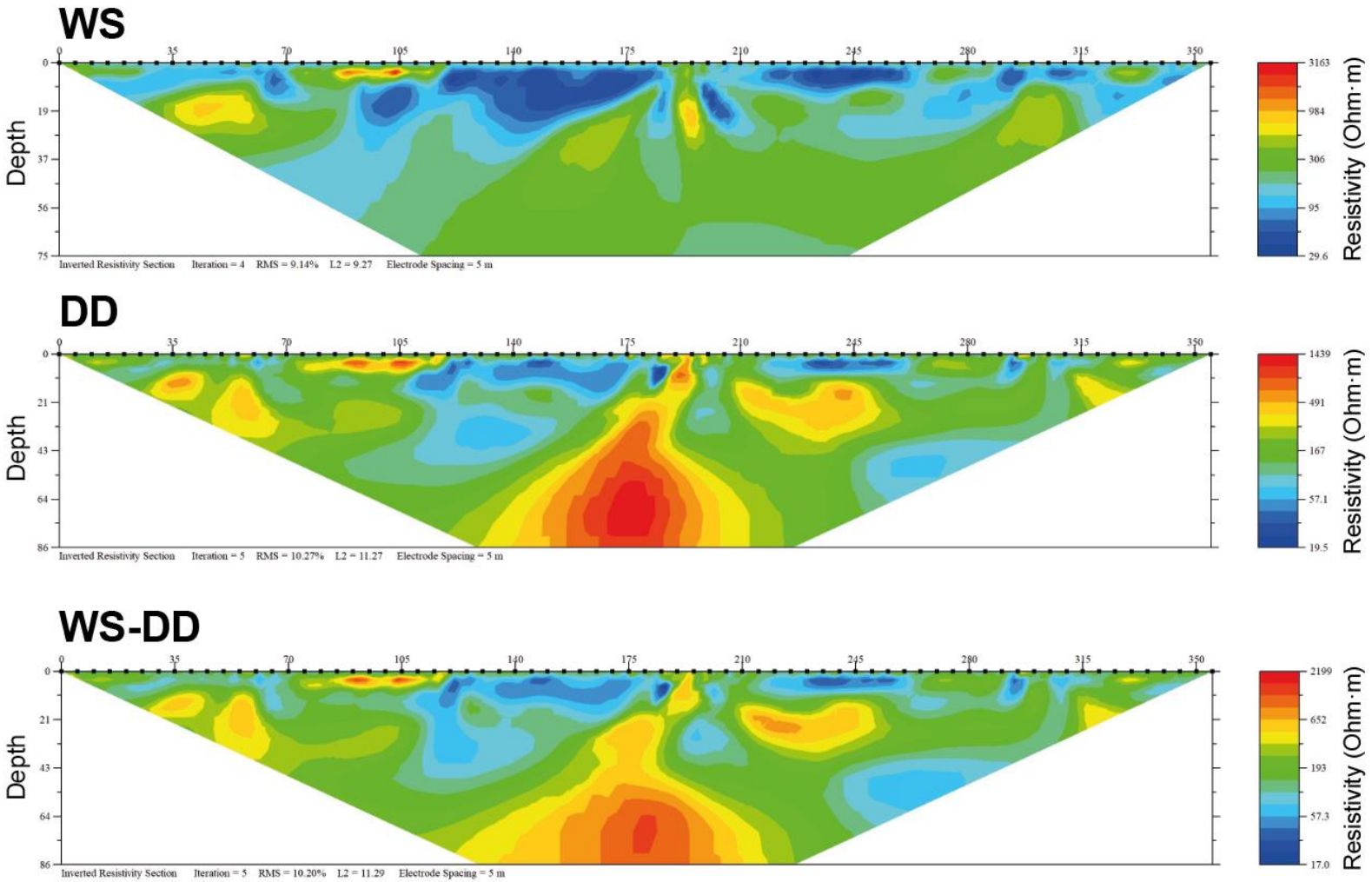

Figure 32. SW-NE resistivity pseudosections for the Alpine Thrust profile, with an electrode spacing of 5m (EarthImager® software, from AGI INC.). WS) Wenner-Schlumberger reciprocal array; DD) Dipole-Dipole array. WS-DD) Joint inversion Wenner-Schlumberger and Dipole-Dipole arrays.

3.6. Induced Polarization (IP)

The Induced Polarization (IP) method characterizes the ability of media to store electric charges under the action of an external electrical field (Vinegar & Waxman, 1984).

Although IP techniques are widely used in ore exploration (Horo et al., 2020; Moret et al., 2006), it is not as well established in geothermal prospections. In a geothermal context, the IP could be sensitive to the electrical properties of the clay units (i.e., fault gouge or hydrothermal clay cap), the saturation of the water phase, or the density and orientation of fractures (Okay et al., 2013; Revil et al., 2019; Slater & Lesmes, 2002).

A) Method theory

When injecting an electrical current through the subsurface, certain geoelectrical units may become electrically polarized. Once this external current is removed, the ground gradually discharges until the initial equilibrium. The study of decaying potential differences as a function of time is known as time-domain IP. The physical property measured by IP is the chargeability (Summer, 1976), which will be mainly related to subsurface contents of disseminated metallic, clays, or graphite particles (Telford et al., 1990).

When the current is turned off, the measured potential does not fall to zero immediately but dies away over a few seconds. There are several different ways to express the information contained in this decreasing curve (Slater & Lesmes, 2002), and Eq. III.33 shows an example:

$$M = \frac{1}{V_c} \cdot \frac{\int_{t_1}^{t_2} V \, dt}{\int_{t_1}^{t_2} dt} \qquad \text{(Eq. III. 33)}$$

, where M is chargeability, V is the measured voltage, V_c is the voltage attributed to injected current, and t_1 and t_2 define the time period during which the voltage is measured (Figure 33).

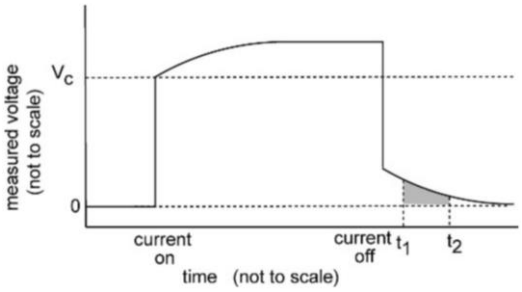

Figure 33. Diagram of an IP signal measured in the time domain. When the electrical current is turned off, the voltage drops, but due to the charge on the metallic particles, decays slowly. The area of this decay is the chargeability (M) (Moret et al., 2006; Summer, 1976).

3.6.1. IP survey

Time-domain IP measurements have been collected in conjunction with the ERT-AT survey, measuring the decay of the overvoltage. The same electrode arrangements have been used, the Dipole-Dipole and the reciprocal Wenner-Schlumberger.

Figure 34 shows the inversion results of the time-domain IP data performed with the software *EarthImager*® (AGI, INC.), which includes the two electrode arrangements and joint inversions.

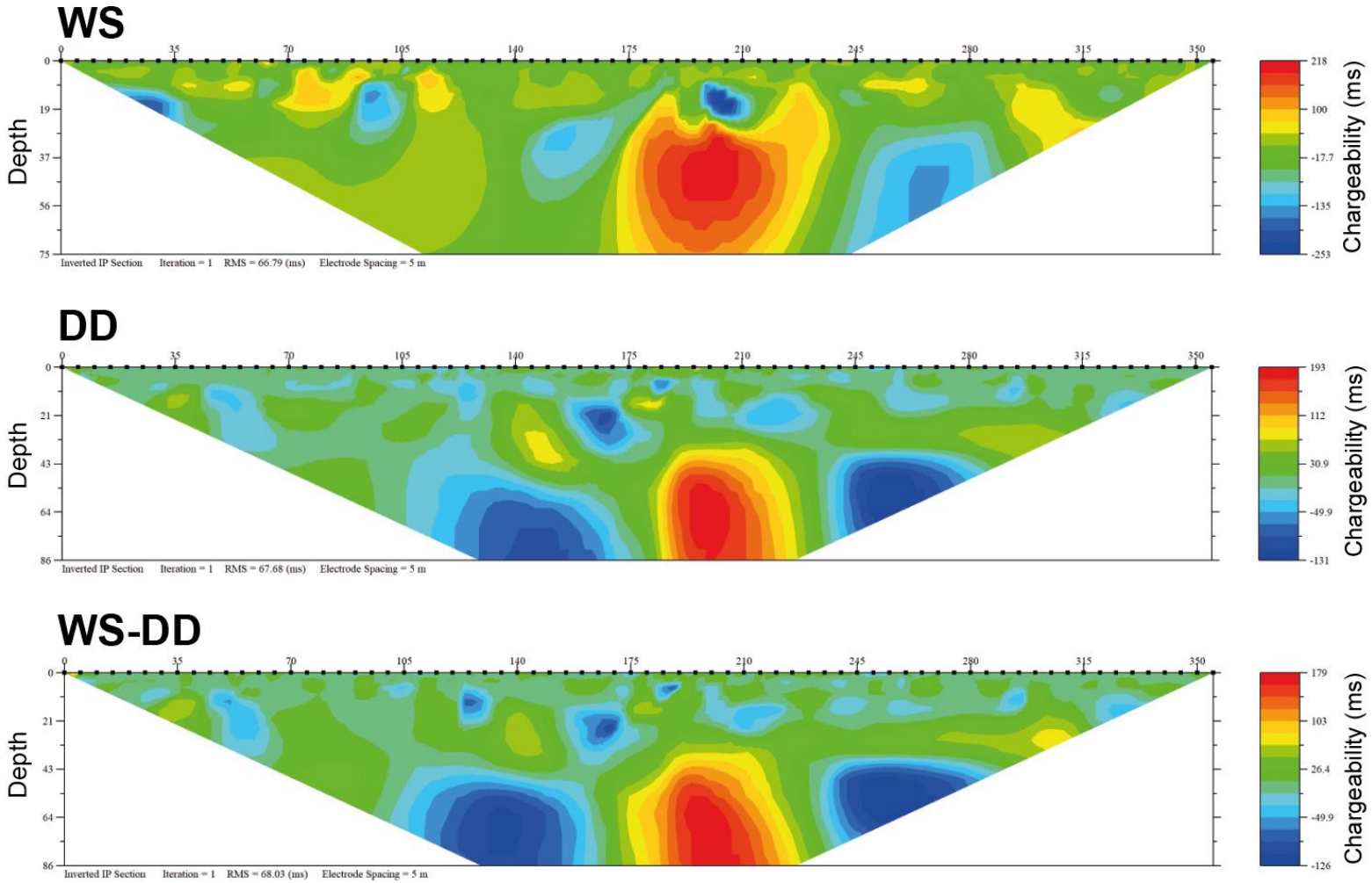

Figure 34. SW-NE chargeability pseudosections for the Alpine Thrust profile (EarthImager® software, from AGI, INC.). WS) Wenner-Schlumberger reciprocal array; DD) Dipole-Dipole array. WS-DD) Joint inversion Wenner-Schlumberger and Dipole-Dipole arrays. All the profiles show similar results with an anomaly at the center of the profile, coinciding with the Alpine Thrust trace.

3.6.2. Chargeability models

Unlike the resistivity models, in this case, the different electrode arrangements show similar chargeability results. A 150-200 ms anomaly stands out in the center of the profile, coinciding with the trace of the AT. While low chargeability values are expected for the Paleozoic metamorphic unit, the presence of clays and fracture-filling sulfides are usually related to high chargeability anomalies (Telford et al., 1990).

On the one hand, the outcropping formation evidences the presence of clays in the AT core; and, far from the study area, the metamorphic Paleozoic unit shows its great capacity to form fault gouges (Ribes Blaves fault gouge outcrop will be described in later chapters). On the other hand, the IGME drilling reports (IGME, 1982, 1984a, 1986b) identify sulfides that fill the microfractures in the VF cataclastic zones. However, there is no information about the zones affected by the AT.

In the following chapters, the geological study will provide more information for a better characterization of the AT fault core and the interpretation of the chargeability anomaly.

3.7. Discussion and conclusions for the geophysical methods used

The different geophysical methods applied in the study area have allowed the characterization of the main geological features involved in the geothermal system's functioning. The primary outcomes can be summarized by identifying and characterizing the main faults, AT and VF, and the characterization of the Vallès Basin geometry.

A) Vallès Basin geometry

The MT resistivity models establish a stepwise morphology for the Vallès Basin, which increases its thickness towards the SE.

The gravity also has allowed a qualitative evaluation of the Vallès Basin geometry, defining the maximum thickness, which is related to the minimum values for the gravity anomaly, in the eastern half of the granodioritic thrust sheet, close to the La Garriga town area. Towards the lateral margins of the study area, so outside the area influenced by the AT, the Vallès Basin seems to become deeper.

The HVSR data provides quantitative data on the Vallès Basin geometry. Results show that the most profound basin-basement limit is located east of La Garriga town, matching the gravity results and confirming some apparent lateral changes along the basin. These lateral changes involve basin depth variations, including in the position of the depocenter, probably related also to changes in the position of the VF trace.

B) Vallès Fault geometry

The horizontal derivative of the residual anomaly map suggests variations in the VF trace position, which would be presented as a segmented fault instead of following a continuous line. The most significant segment shift would be located in La Garriga town, following the Congost river N-S valley.

Figure 35 shows the intersection between the basin surface (from HVSR) and the topography, which would be related to the geometry of the VF trace. This geometry also confirms the non-linearity of the VF trace, with an important step close to La Garriga and Samalús towns.

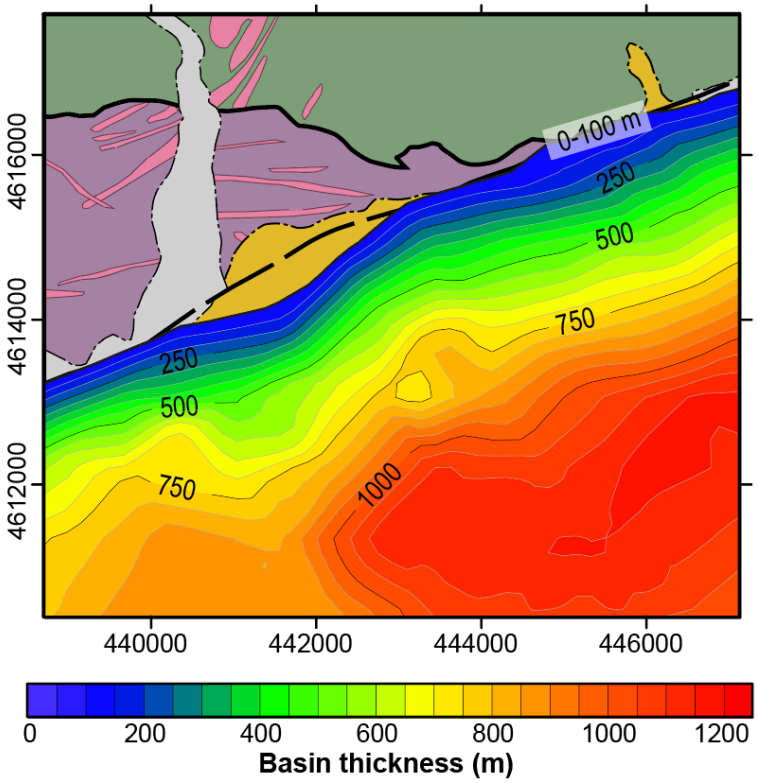

Figure 35. Sediment thickness along the region of study, between La Garriga and Cànoves towns. The first contour (0-100 m) is set as a range since the accuracy of the final extrapolation from the measurement points does not allow to obtain an accurate limit this close to the topographic surface. Its thickness is up to a maximum of 1200 m towards the center of the basin (SE), and the intersection of the presented surface and the topography seems to represent the Vallès fault trace.

The geometry of the VF in depth cannot be determined with certainty. The most likely option would be that the VF in its first 3 km is a constant dip plane. However, at deeper depths, it would show the listric geometry described in previous seismic profiles carried out in other areas of the CCR (Gaspar-Escribano et al., 2004; Roca et al., 1999). Therefore, the listric geometry shown in the MT-Samalús model would be an artifact of the inversion and modeling. The location of the MT-Samalús profile in a VF segment could have caused this effect, so the geoelectrical units could not be well-resolved with the 2D resistivity inversion followed.

However, the VF zone can be preliminary described. The resistivity models of MT and ERT methods identify a fault damage zone of 200-300 meters in the first 500 meters in depth, characterized by low resistivities (considering the theoretical resistivity for the protolith); and a high-conductive fault core of around 10 meters.

C) Alpine Thrust geometry

On the other hand, the AT fault zone has been imaged using the ERT resistivity and IP chargeability models, so only in the shallow subsurface. In both profiles, the AT is imaged, and the IP method has proven useful when resistivity anomalies are sometimes not detected (see results with the Wenner-Schlumberger reciprocal arrangement). Moreover, critical units in the functioning of a geothermal system, such as a hydrothermal clay cap, a fault gouge in a fault zone, fracture zones, precipitation of hydrothermal minerals (sulfides), or water saturation, could be detected using both methods. Nevertheless, integration with the geological information will be needed to reach any conclusion.

D) Conclusions

Therefore, all the geophysical methods have been essential for a primary characterization of the study area. Furthermore, combining the methods (based on different physical properties) has been the best option to support the different hypotheses. Though, a geological and hydrological characterization will be essential to reasonably interpret these faults' role in the geothermal system functioning. As will be discussed in later chapters, although both fault zones have similar resistivity values, their lithology, fluid saturation, and, in general, their role in the system will be completely different.

Part 3

Chapter IV
Fracture and geological characterization
The role of structural complexity

Chapter V
Petrophysical measurements

Chapter VI
Hidrogeological characterization

Chapter IV

Fracture and geological characterization. The role of structural complexity

Understanding the geology is the backbone of any geothermal project since the properties and the arrangement of lithological units strongly control the hydraulic parameters and temperature anomalies.

Based on the bibliographical background presented in Chapter II and considering the geophysical results and discussions of Chapter III, a multi-scale geological and fracture characterization will be carried out in the study area. The main objective of this chapter consists of a better understanding of the geological structure, which includes the fracture system, the fault zones, and an analysis of their role in the geothermal system's functioning. This characterization methodology goes from the big-scale topography analysis through the outcrop scale fractures characterization and the outcrop and borehole samples micro-characterization.

4.1. Fault zones overview

A fault is a zone of rupture that allows the release of local stress, along which two rock blocks move relative to each other. It is represented by a plane in 3D or a map line, indicating where the deformation linked to the rupture is located (Bertrand, 2017).

The upper-crustal fault zones can be defined by a volume of rock with three primary components:

- The ***fault core*** is the lithologic and morphologic portion of a fault zone where most displacement is accommodated. Fault cores may include single slip surfaces, unconsolidated clay-rich gouge zones, brecciated and geochemically altered zones, or highly indurated, cataclastic zones (Bistacchi et al., 2010; Jefferies, Holdsworth, Shimamoto, et al., 2006; Jefferies, Holdsworth, Wibberley, et al., 2006).
- The ***damage zone*** is the network of subsidiary structures that bound the fault core, including minor faults, veins, fractures, cleavage, and folds that cause heterogeneity and anisotropy in

the permeability structure and elastic properties of the fault (Odling et al., 2004; Uehara & Shimamoto, 2004).

- The ***protolith*** represents the volume of rock that is not affected by the stresses and, therefore, does not present significant deformation evidence (Caine et al., 1996).

However, the fundamental architecture of a fault is usually much more complex. For example, faults may contain several fault cores, different degrees of deformation in the damage zone, and different hydraulic properties; therefore, the different identified components have particular effects on permeability and fluid flow circulation. Figure 36 shows a simplified scheme of example cases relating the fault zone characteristics with their hydraulic behavior.

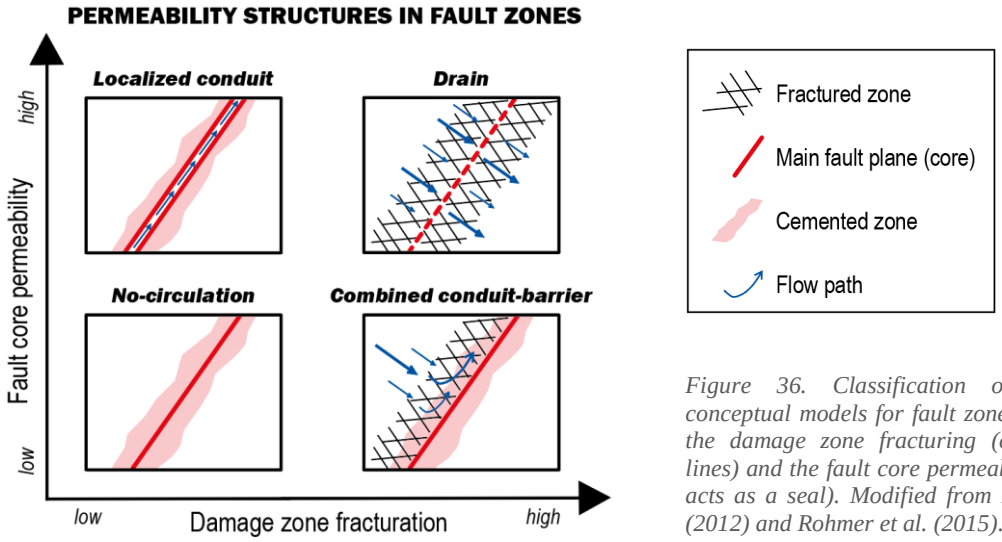

Figure 36. Classification of the main conceptual models for fault zones considering the damage zone fracturing (crossed black lines) and the fault core permeability (red line acts as a seal). Modified from Matonti et al. (2012) and Rohmer et al. (2015).

At the regional scale, faults and fractures play a crucial role in localizing permeability in intermediate-temperature to high-temperature convective geothermal systems (Glyn-Morris et al., 2011). Most permeable structures are located in extensional or transtensional settings and usually in complex interaction zones, such as fault terminations, fault intersections, step-overs, or relay ramps. Figure 37 shows the main structural settings involving fault zones related to the presence of geothermal systems.

For a good understanding of the geothermal system's potential and functioning, we need to know about the structural history of the area, but also the recent and current stress field. The active forces are critical for defining which structures are most likely to channel fluids and be capable of breaking previous hydrothermal seals. At the same time, it can provide critical information for modeling the risk of induced seismic events of potential economic and social concern. Also, the lithological heterogeneities, such as formation boundaries or dyke intrusions, can modify the local stress conditions simultaneously as they interact in the fluid circulation.

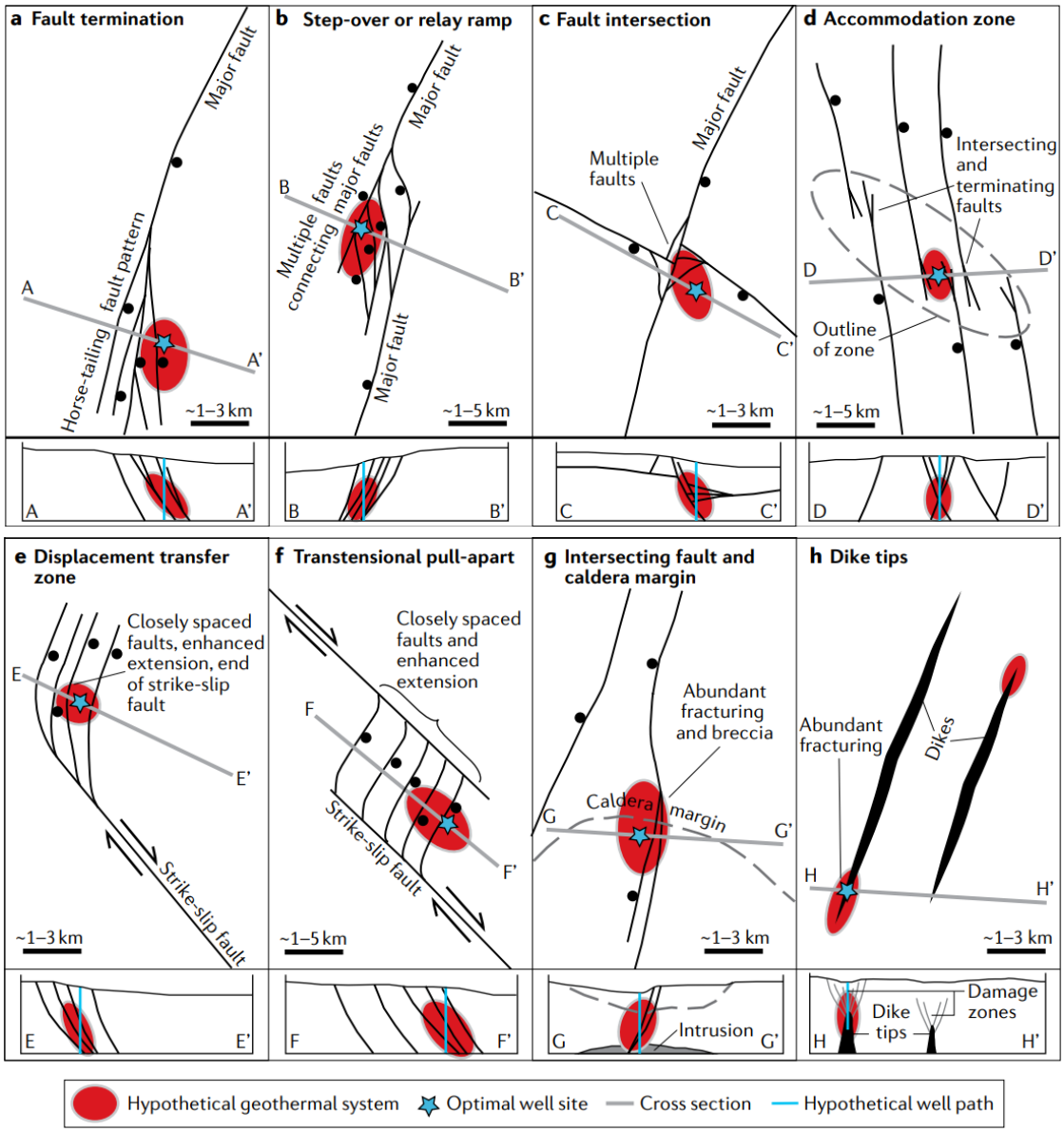

Figure 37. Favorable structural settings for geothermal exploitation. A) Fault tip showing a horse-tailing pattern of closely spaced faults at the termination of a major normal fault. B) Step-over or breached relay ramp showing abundant minor faults connecting overlapping strands of a major normal fault zone. C) Fault intersection with abundant minor faults proximal to the intersection. D) Accommodation zone (marked by an ellipse) encompassing a belt of terminating, overlapping, and intersecting normal faults. E) Displacement transfer zone whereby a major strike-slip fault terminates in an array of normal faults. F) Transtensional pull-apart incorporating multiple closely spaced normal faults connecting a releasing step in a major strike-slip fault. G) Intersecting normal fault and caldera margin (thick dashed gray line). H) Dike tip or termination, whereby abundant fracturing characterizes the damage zone proximal to the tip of a dike (Jolie et al., 2021).

In this chapter, the main structures and minor fracture sets have been identified and characterized in a major-scale (topography analysis), mid-scale (outcrop fracture analysis), and small/micro-scale (borehole samples characterization and microscopic analysis of the granodioritic unit). The main objectives are having a well-defined geometry of the principal structure's traces and identifying the potential reservoir and its petro-structural characteristics. In turn, a good characterization of the historical activity of the different fracture sets can help to understand the location of the most significant temperature anomalies and the presence of hot springs.

4.2. Topography analysis

Digital elevation models (DEM) record the topographic surface expression of any area. This topographic mesh and some derived attributes, such as terrain derivative maps (slope, aspect, and curvatures) or shaded relief images, have previously demonstrated their usefulness for lineaments and fault investigations (Abdullah et al., 2010; Tchalenko & Ambraseys, 1970). Therefore, the extraction and analysis of lineaments from DEMs and the analysis of topographic attributes, can provide valuable sources for regional structural and tectonic characterization of this geothermal investigation (Ekren et al., 1976; Seleem, 2013).

4.2.1. Methodology

Topography has been analyzed to get information about the geological unit limits and the regional fracture system of the studied area.

A) Topography and slope maps analysis

The main structures of the study area, the Vallès Fault (VF) and the Alpine Thrust (AT) limit geological units with different hardness: the Miocene unit of the Vallès Basin, the granodioritic thrust sheet, and the Paleozoic metamorphic unit. This hardness property, which is linked to the nature of the rock and its fracture degree and alteration, will influence the area's topography.

We have used a digital terrain model based on the altimetric information of the topographic base of Catalunya region 1:5.000 (BT-5M v2.0) with an altimetric accuracy of 0.9 m mean square error (ICGC, 2011). Complementary, we have created a terrain slope map for the studied area using *Surfer*® software (Golden Software LLC, 2016). The *Terrain Slope* plugin allows the calculation of the slope at any grid node on the surface, getting the result in degrees (from 0 to 90º). Both maps are presented in Figure 38.

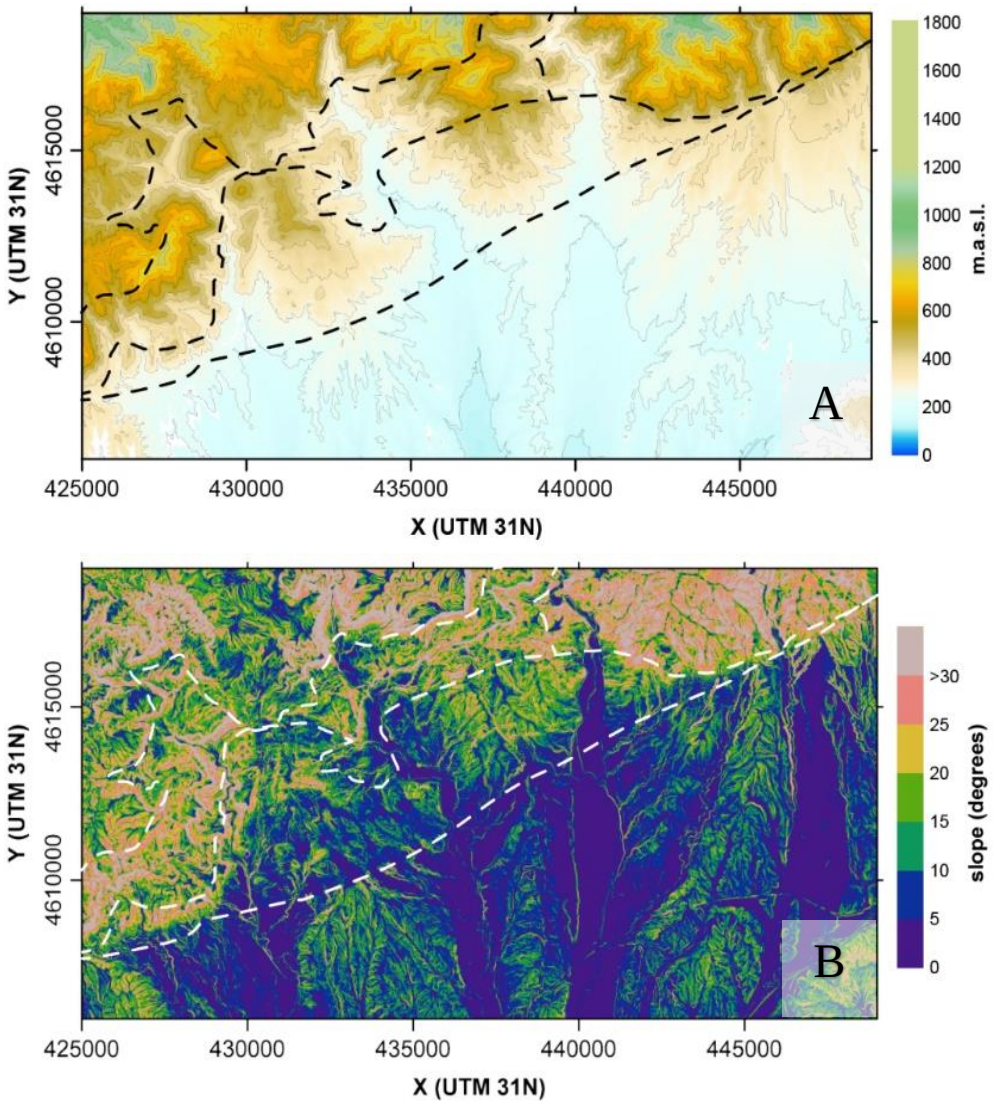

Figure 38. Topography analysis maps with the main expected hardness limits given by the Vallès Fault, the Alpine Thrust, and the Triassic-Eocene limit. A) Topographic map created from the topographic base of Catalunya 1:5.000 (ICGC, 2011). B) Slope map created using the Terrain Slope plugin from Surfer® software (Golden Software).

B) Lineaments analysis

We use the term lineament for a linear or curvilinear feature, which is identified by remote sensing methods and is believed to represent the trace of intersection between a planar or sub-planar structural inhomogeneity and the surface of the Earth (O'Leary et al., 1978). Faults are usually detectable in the landscape because they often locate breaks in the slope and partially control the hydrographic network (Bertrand, 2017). Therefore, the analysis of lineaments could also be applied in fault and fracture-controlled geothermal prospect areas (Soengkono, 1999).

In this topographic analysis context, and related to the lineaments, the drainage network can also be a reliable indicator of tectonic activity. However, it is essential to note that stream-long profiles are sensitive to forces other than tectonics, such as lithology, climate, or bed load (Grohmann et al., 2011).

For the extraction and analysis of lineaments, we have used an elevation model of the high-definition terrain, with a 2x2m regular mesh, based on LIDAR data, with an estimated altimetric error of 0.15 m. The processing method had the advantage of setting up different azimuths of the illumination source, which can benefit the later interpretation of multiple orientation structures. In the present study, the structural lineaments were extracted using DEM with the sun azimuth values: 0, 45, 90, 135, 180, 225, 270, 315, and a sun height of 45º. Moreover, we have evaluated different topographic and slope maps with different rendering parameters to better analyze the lineaments.

The lineaments have been drawn manually in the basement and in the basin using the free and open-source geographic information system application *QGIS* (QGIS.org, 2021). Complementary, the plug-in *GeoTrace* (Thiele et al., 2017) has been used to extract and analyze the orientations of the lineaments.

4.2.2. Results

A relation between the slope and the rocks involved in faulting can be observed. Therefore, this method can be used to draw the traces coherently in regions with insufficient outcrop information. However, the geophysical and geological data acquired in the field campaigns must be prioritized.

Figure 39 shows the slope map with the interpreted traces. The VF causes a change in the slope, probably due to the different erodability between the Miocene sedimentary unit and the hanging wall's Paleozoic basement. Apart from the previous geometry for the VF trace (ICGC, 2002, 2006; IGME, 1974), the inflection points of valleys orientation and river courses have also been considered to delineate the new trace geometry.

The metamorphic series shows a more evident slope contrast between the granodioritic unit and the Miocene sediments. This significant hardness contrast between the VF footwall units is likely related to the granodioritic unit's high fracturing degree and weathering, which increases its erodibility. Finally, the resulting lineament for the VF confirms the hypothesis of a segmented fault suggested in the geophysical chapter.

The detailed analysis of lineaments using DEM and slope maps shows the main strike for the lineaments, which in Figure 40 has been separated considering if they are located in the basement, in the hanging wall of the VF, or the Vallès Basin. The final results show a clear N-S/NNW-SSE trend and a variety of orientations, mainly NE-SW, E-W, and SE-NW. Although all these orientations can be identified in basement and basin units, their prevalence differs. Within the basement, the mentioned lineament orientations have similar intensities, whereas, within the basin, the N-S/NNW-SSE direction is the most significant. This observation would suggest that

the N-S lineaments are related to the latest deformation event, although another explanation relating to river course and catchments is also considered possible.

The statistical analysis of lineaments can be followed up by a detailed examination of their cause. Near La Garriga town and following a river valley (Congost river), there is a major N-S lineament, filled with recent sediments, which transects the VF. Near the Congost lineament, minor linking lineaments are perpendicular within the footwall, with a tendency to be more NNE- to NE-trending in the hanging wall and have the appearance of tributary river channels. Therefore, the significance of these lineaments requires consideration of other issues discussed in the following sections.

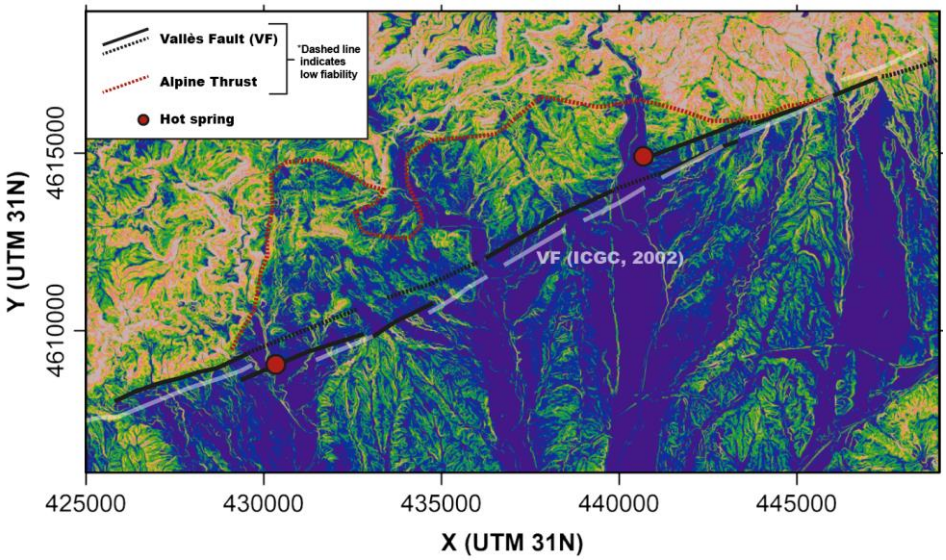

Figure 39. Slope map with the interpreted traces for the Vallès Fault (VF) and the Alpine Thrust (AT). The slope differences, but also the inflection points on valleys orientations and river courses, have been used to interpret the position of the VF and AT traces. VF trace shows different segments which sometimes overlap, with the main hot springs located above these segments.

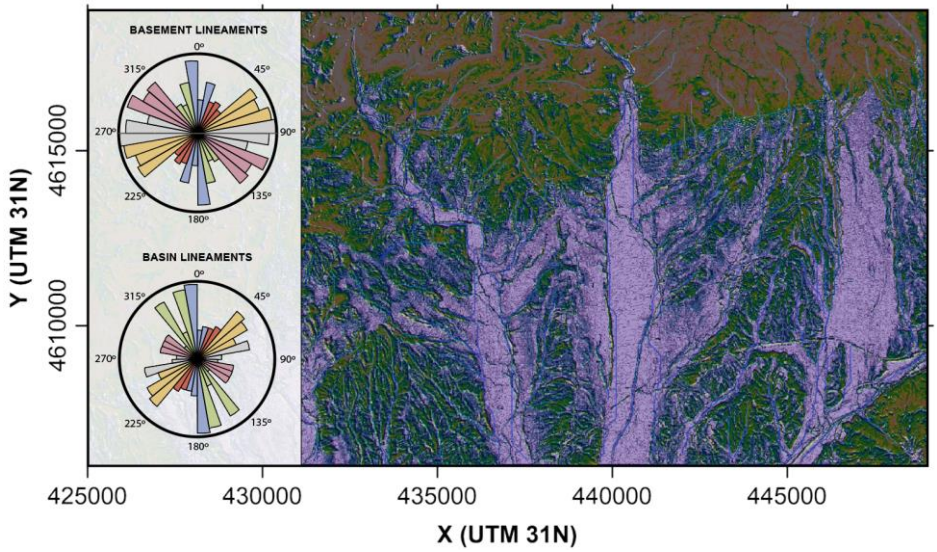

Figure 40. Lineament analysis using an image that merges a black-white band slope map figure, and a three-color band topographic map figure. The strike of lines is analyzed by considering if they are located in the VF hanging wall or footwall, so in the basement or in the basin.

4.3. Fractures characterization – outcrop scale

Although the topography analysis can give us an idea of the structural trends of the area, in order to better characterize the fracturing and confirm the results of the topography analysis, fieldwork and borehole characterization must be done.

Due to the scarcity of borehole data, outcrop studies are useful for analyzing the fault zone architecture and thereby increase the predictability of fluid flow behavior through and across fault zones in the corresponding deep reservoir (Bauer et al., 2015; Chesnaux et al., 2009). For this reason, active or inactive faults occurring in fault zones are considered of strategic interest for geothermal and ore deposit exploration.

This multiscale fracture study has been focused on the eastern part of the study area, in the La Garriga-Samalús surrounds. This area has been chosen for four main reasons:

(1) In La Garriga town, geothermal evidence is on the surface.
(2) Both main faults, the VF and the AT, outcrop nearby La Garriga town.
(3) Most of the geophysical data is located in the area
(4) There is fault segmentation evidence (from geophysical and topography analysis results), which is considered relevant for the functioning of the geothermal system and the presence of hot springs.

4.3.1. Methodology

For the study of fracturing, we have applied the Linear scanline sampling method (Priest, 1993; Priest and Hudson, 1981; Schön, 2015; Watkins et al., 2015), which allows a fast recording of a wide range of fracture attributes. However, it should be noted that the results can be susceptible to orientation bias when multiple orientation fractures are sampled in a single scanline (Park and West, 2002).

Due to a large amount of vegetated and private areas, this methodology has only been applied in 55 thrust sheet outcrops. This constrained number of outcrops makes it challenging to obtain a more solid statistical result. Therefore, the results will also be compared with the topography analysis and the historical structural knowledge of the area.

Figure 41 shows an example of applying the Linear scanline sampling method in a granodioritic outcrop. The white dashed lines indicate the main fractures, and the horizontal yellow scale is the reference used for the fractures counting. Therefore, in this 5-meter example, 23 white dashed lines cross the horizontal reference, resulting in a fracture density of 4.6 fracture/meter.

Figure 41. Example of fracture/discontinuity identification in a granodioritic outcrop, using the scanline method. Dashed white lines highlight main fractures.

Samalús to Cànoves road. Left: Gemma Mitjanas; Right: Gemma Alías.

4.3.2. Fracture sets – outcrop scale

Fracture plane exposures are very limited; thus, slickenlines or other displacement indicators are almost undetectable and negligible. In the same sense, the length and the spacing between fractures made it hard to establish crosscutting relations.

Finally, we have identified six sets of fractures at the outcrop scale in the granodioritic unit and the fault zone, which characteristics are summarized in Table 2.

Table 2. Fracture sets that have been identified in the granodioritic unit of the Prelitoral thrust sheet.

ID	Strike	Dip	Aperture	Infillings
$\mathbf{F_A}$	NE-SW	50º – 88º	1 mm – 4 cm	Mostly unfilled (not-determined)
$\mathbf{F_B}$	N-S to NNE-SSW	66º – 90º	4 mm – 2 cm	Unfilled
$\mathbf{F_C}$	N-S	16º – 55º	0 mm – 2 mm	Filled (kaolin)
$\mathbf{F_D}$	E-W	28º – 84º	2 mm – 1 cm	Filled (not-determined)
$\mathbf{F_E}$	NW-SE to NNW-SSE	57º – 89º	1 mm – 3 mm	Mostly unfilled (carbonated)
$\mathbf{F_F}$	WNW-ESE	73º – 86º	0 mm – 2 mm	Unfilled

The F_A fractures are characterized by a NE-SW strike, which corresponds to the same direction of the horst and graben structures generated during the Neogene deformation in the CCR. Main fractures dip between 50º and nearly vertical toward the SE, and subsidiary NW-dipping planes are considered conjugated structures. In most outcrops, these fractures are persistent and show different apertures ranging from 1 mm to 4 cm. Although some fractures show carbonated infillings, most are unfilled, with an average aperture of 3 mm. In some outcrops, slickenlines can be perceived. About the cross-cut relationship, the F_A fracture set cuts F_B, F_C, and F_E fracture sets.

The F_B fractures have an N-S to NNE-SSW strike direction. These fractures are nearly vertical and could be related to some strike-slip movements. Most outcrops show open fractures with

widths between 4 mm and 2 cm. In some locations, the fractures are filled with carbonated infillings.

The F_C fractures have an N-S direction with an average dip of around 30º indistinctly towards the E and W. This set of fractures is rather underrepresented, except for very localized zones. The fractures are barely or not at all open, and in some cases, kaolin filling is observed. The cross-cut relationship between F_B and F_C changes in different outcrops. That is, there is a mutual-cut relationship.

The F_D fractures are E-W faults with dips between 45 and 80º towards the south. These fractures have apertures of 2-4 mm and, punctually, centimetric. These fractures are usually located close to the intrusive dykes, and are presented in high-density groups. In most outcrops, this set is filled, eventually with a dark-colored filling whose composition has not been determined. About the cross-cut relationship, the F_D fracture set cuts the F_E fracture set.

The F_E fracture group is pervasive and is characterized by sub-vertical planes with NW-SE to NNW-SSE direction. This set is strongly represented, with fracture openings between 1 and 3 mm. These fractures are generally unfilled, although in some cases, patinas or precipitated carbonates are observed. About the cross-cut relationship, the F_E fracture set cuts the F_F fracture set and is cut by F_D and F_A fracture sets.

The F_F fracture group is characterized by a WNW-ESE strike and low dips towards the NE. In most outcrops, these fractures are barely open, without any filling. About the cross-cut relationship, the F_F fracture set is cut by the F_E fracture set.

Figure 42 presents the fractures measured in outcrops in rose diagrams and Schmidt stereonets, grouped considering the main orientations and dip.

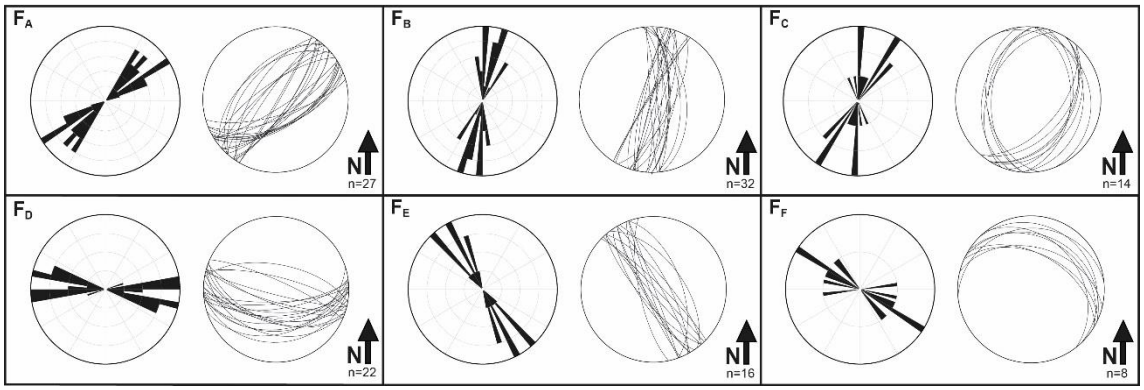

Figure 42. Lower-hemisphere Schmidt stereonet and rose diagrams of the measured fractures grouped in the 6 fracture families distinguished in the granodiorite of the Prelitoral thrust sheet.

4.3.3. Fracture density

Quantitative characterization of the VF damage zone has been performed by measuring fracture density as a function of distance from the VF core east of La Garriga town, within the footwall granodioritic unit. The resulting data has been plotted as fracture density using the Natural Neighbour gridding method within *Surfer*® software (Golden Software LLC, 2016).

The resulting map (Figure 43a) highlights an increase in fracture density towards the VF trace. However, the increase of fracture density towards the AT trace appears less significant. Specifically, a maximum is observed in the northern limit of the fracture density profile (dashed white line), which is related to an outcrop where the thrust plane is observed. This maximum represents only 50% of the fracturing maxima detected near the VF trace.

The fracture density NNW-oriented profile (Figure 43b) also images how fracturing varies in the thrust sheet, which is influenced by the proximity to the AT and, above all, by the VF.

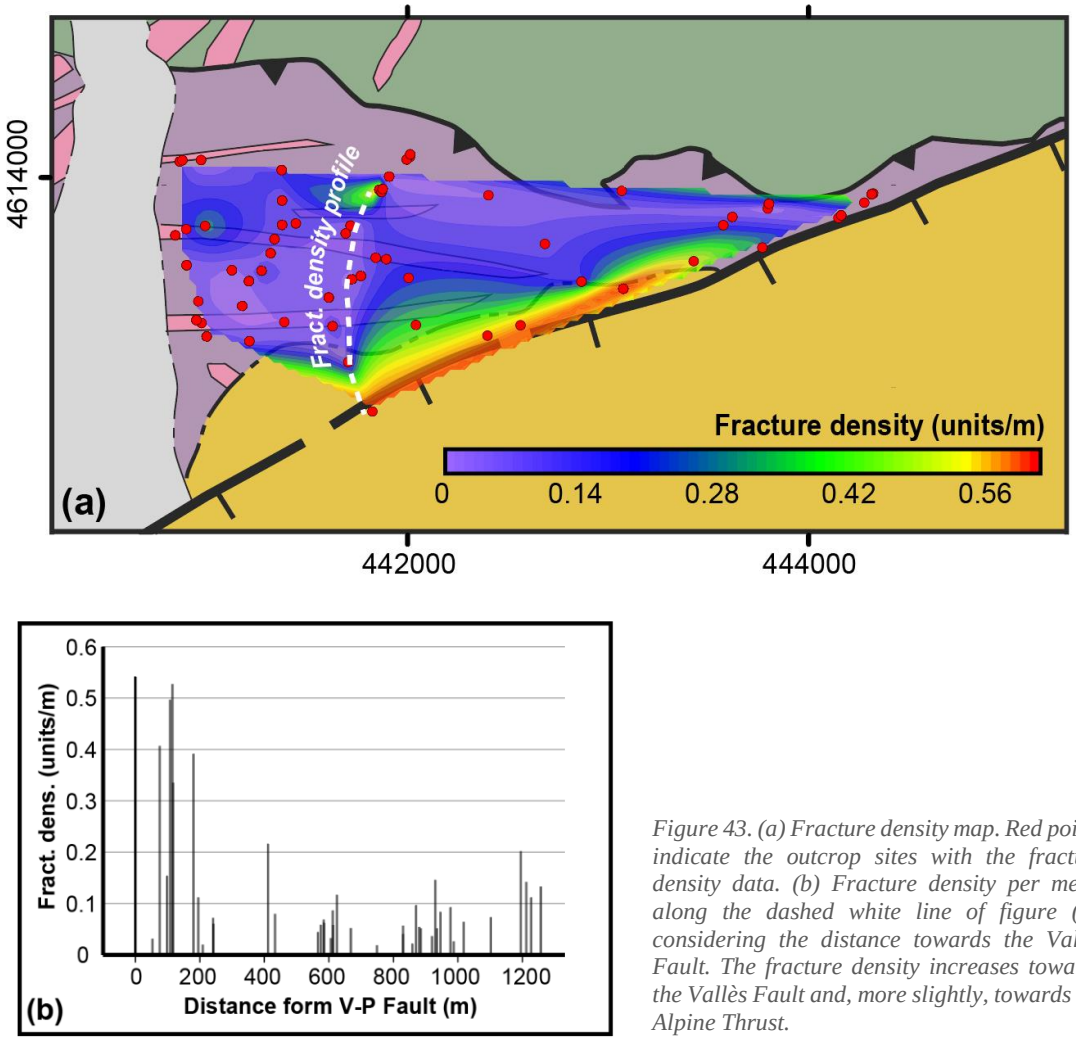

Figure 43. (a) Fracture density map. Red points indicate the outcrop sites with the fracture density data. (b) Fracture density per meter along the dashed white line of figure (a), considering the distance towards the Vallès Fault. The fracture density increases towards the Vallès Fault and, more slightly, towards the Alpine Thrust.

4.4. Microscopical characterization

Mineralogical transformations play an important role in developing the pore network in altered zones linked to fault zones and supergene alteration (Bertrand, 2017). The analysis of thin sections can give us a qualitative image of the main minerals and their degree of fracturing and alteration, allowing a better characterization of the fault zone and protolith facies and, therefore, a more accurate characterization of the geothermal reservoir.

Moreover, the mineral's hydrothermal alteration degree can provide information about the past and actual geothermal system functioning in addition to the hydrochemical properties (and temperature) of the fluid (Cantarero, 2013).

4.4.1. Methodology

For the microscopical petrological study, 20 thin sections from the granodioritic thrust sheet unit were prepared and analyzed using an optical microscope. Due to the degree of fracturing and alteration, most samples had to be saturated with a polyester resin to consolidate them before cutting thin sections.

The main objectives of this section are the mineral characterization of the host rock and the analysis of the crystal's fracturing, deformation, and alteration in function to the proximity of the major structures. In order to characterize the degree of alteration, the primary mineralogy of the granodioritic unit and the notes by Velde and Meunier (2008) have been followed:

- For the plagioclase and feldspars, the degree of alteration has been determined by the argillic alteration percentage, classified as non-existent, weak, strong, or total.
- For the biotite and amphibole, the degree of alteration has been determined by the chloritization percentage.
- For the quartz crystals, which are relatively inalterable, its description has been focused on fracture density, the presence of subgrain recrystallization, or undulant extinction.

4.4.2. Results

The granodiorite unit has a granular texture, with a crystals size of 1-2 mm, except for some bigger mafic minerals up to 5 mm. It generally shows different degrees of alteration and fractures depending on the distance from the VF and the AT. However, its composition remains relatively consistent in all the outcrops, being the essential minerals, quartz (25%), potassic feldspar (20%), plagioclase (40%), and biotite (10%) (+5% accessory minerals).

The granodiorite characteristics are relatively constant along the entire thrust sheet, except close to the major faults. A highly-fractured granodiorite predominates, where the average fracture network represents 20% of the rock. It presents a moderate degree of replacement of orthose and

plagioclase by kaolinite and sericite. The biotite crystals are deformed, showing an incipient alteration to chlorite, some kink folds, and an interstratified texture with calcite cement (Figure 44F). Depending on the sample, fractures are anastomotic, although, in most of them, two preferred orientations are observed (the orientations of these fractures have not been determined). Fracture apertures vary from 0.05 to 2 mm and are sometimes filled with calcite and iron oxides.

In the VF plane and its vicinity outcrops, the granodioritic rock is characterized by a high degree of hardness and compaction. It is even more difficult to sample a rock than in other outcrops. Nevertheless, under the optical microscope, a high degree of fracturing with large proportions of cement is observed, allowing the definition of these samples as a protocataclasite and assigning them as the VF core unit.

The protocataclasite samples of the fault core are completely crushed rocks with an aphanitic silicic and calcitic cement matrix (Figure 44E). The matrix percentage is usually lower than 50%. In these samples, crystals are highly deformed, rounded to angular boundaries, and moderate to total alteration of feldspars. In addition, quartz crystals show undulate extinctions and subgrains.

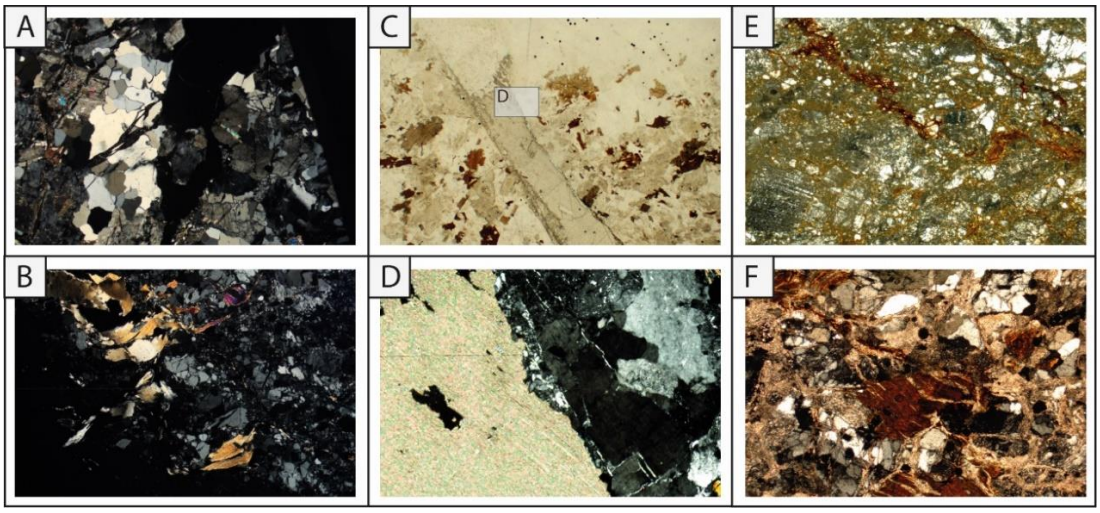

Figure 44. A & B) Fractured granodiorite with open fractures, undulant extinction, biotite deformation, and subgrain recrystallization (XP). C) Carbonate vein infills and quartz grains in contact with the vein (PP and XP) the D) figure zooms in the contact between the carbonate vein and the quartz subgrains. E & F) Protocataclasite and highly fractured rock in which it is possible to identify an associated matrix (XP).

4.4.3. Borehole's microscopic review

The microscopical characterization of borehole samples summarized in the reports of Samalús and Caldes de Montbui (IGME, 1982, 1984a, 1986b, 1986a) match the results presented above. The mineralogical series of the granodioritic unit in the boreholes can be generalized with the following characteristics:

- Texture: holocrystalline, granular, cataclastic.
- Principal minerals: Quartz, K-feldspar, plagioclase and biotite.

- Secondary minerals: chlorite, epidote, prehnite, saussurite, and opaque (pyrite).
- Philonian minerals: calcite, cryptocrystalline hydrothermal silica, quartz, epidote, prehnite, fluorite, adularia, zeolites.
- Alteration: plagioclase to sericite, prehnite, saussurite[10], and epidote. Biotite is altered to chlorite and epidote, sometimes with opaque minerals.

Apart from that, the original texture is modified to cataclastic at some zones of the borehole core. This texture induces deformation and breaking of minerals which show undulant extinction and deformed crystal twinning.

Fracturing in the borehole samples is characterized by different hydrothermal infills: monocrystalline silica, quartz, calcite, fluorite, epidote, chlorite, prehnite, and adularia. In many of the samples, it is possible to establish precipitation timings. For example, in adularia-quartz mixed infills, adularia corresponds to older generations and, therefore, to older fluids.

In most of the optical microscope images from borehole samples, there is evidence that hydrothermal minerals (which are in equilibrium with the water – Chapter VI - Hydrological characterization) have been later affected by deformation (Figure 45). Some examples are hydrothermal infill break and displacement, different generations of infills, cataclastic hydrothermal infills, or undulant extinction in hydrothermal quartz crystals.

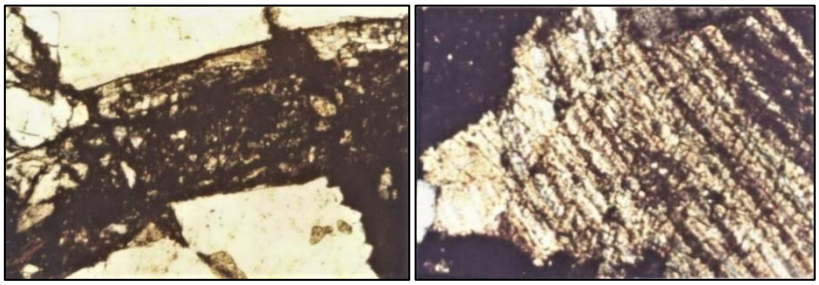

Figure 45. Left: Borehole CM-3. Fracture displacement with cataclastic zeolites (x100 XP). Right: Borehole S-5. Hydrothermal calcite twins, bent due to the deformation in the cataclastic zone (x250 XP) (IGME, 1986b).

4.5. Borehole samples characterization by photogrammetry

In the La Garriga and Samalús area, six exploration drillings were carried out during the ‘80s (IGME, 1982, 1984a, 1986b). Although it has not been possible to access the continuous core samples from the boreholes, some isolated samples from the S1 borehole have been made available (IGME, 1982). Since these samples were scarce, and we wanted to perform some destructive analysis later, we decided to digitize them as 3D digital models so they could be accessed when necessary.

[10] Mineral aggregate formed as a hydrothermal alteration and composed of a microscopic mixture of other minerals: zoisite, epidote, sericite, and albite (Le Maitre et al., 2002).

In this context, applying full-sample photogrammetry produces a comprehensive visual record of (surface) conditions. Identifiable features can be digitally measured, assessed, and integrated with 3D modeling and reverse engineering processes long after the loss of the original (Betlem et al., 2020). Compared with other traditional close-range photogrammetry methods, Structure-from-motion Photogrammetry (SfM) automatic feature-matching algorithm has many advantages, such as high efficiency, flexible workflows, and no expert supervision.

The SfM method has been previously applied on different scales, from outcrops to centimeters-sample scale, but mainly in archeological (Ashton et al., 2014; Barazzetti et al., 2011) and paleontological studies (Haug et al., 2009; Kordić et al., 2019). For geological applications, this methodology is mainly used on bigger scales for stratigraphic, structural, and sedimentological characterization or *in situ* geotechnical applications (Lin et al., 2019; Li et al., 2021; Nesbit et al., 2018). The improvement of drone technologies during the last decade has also influenced the increasing use of this methodology on bigger scales, not only for purely scientific purposes but also for information and dissemination (Mezghani et al., 2018; Spector et al., 2020).

The SfM method also enables the cost-effective digital characterization of geoscientific samples. Unwrapping cores using 3D software tools allow analytical opportunities, like accurate structural and sedimentological characterization, density calculation (from volume), and digital storage for samples needed for destructive analysis (Betlem et al., 2020; Holmes, 2020).

Several free tools and commercial software have recently been developed to process various images taken from different camera sensors. Among these software packages, *Metashape*® (Agisoft) is a simple and popular solution for photogrammetric applications, through which inexperienced users can obtain accurate 3D models in only a few steps (An et al., 2021).

4.5.1. Methodology

We have applied SfM two five borehole samples to analyze fractures at great depths and to have them accessible after destruction for the thin sections and petrophysical analysis.

Digital images were acquired using a remote-controlled system camera Lumix G7 coupled with a 14-42 mm Lumix lens. The acquisition was carried out by placing the camera in front of a turntable with a uniform white background (Figure 46). The turntable included several markers named coded targets, which can be used to define the model's local coordinate system, scale, and accurate matches to improve the photo-alignment procedure (Agisoft Metashape, 2019). In this case, the software used includes automatic detection and matching of coded targets on source photos, which allows benefiting from marker implementation in the project while saving time on manual marker placement.

For every sample, we took 24 photos, rotating the turntable 15º every time. The same procedure was made by changing the camera position two or three times (depending on the shape of the sample and the area covered) and the sample's position. Finally, 250-300 photos for every sample were used to have reliable results without shadows effects or points without information.

The SfM processing started with the photos import, their classification into different chunks, the alignment of the photos of every chunk, and defining the bounding box or region of interest. First, in order to align the photos, semi-automated marker detection and masking sequence tool was used, which needs the use of the Metashape 12-bit coded targets during the image acquisition. Secondly, the preliminary dense cloud can be built, adding manual markers for better photo alignment and merging the different chunks. After merging the chunks, the final texture of the 3D model will be built, adding a scale and orientation for their final interpretation.

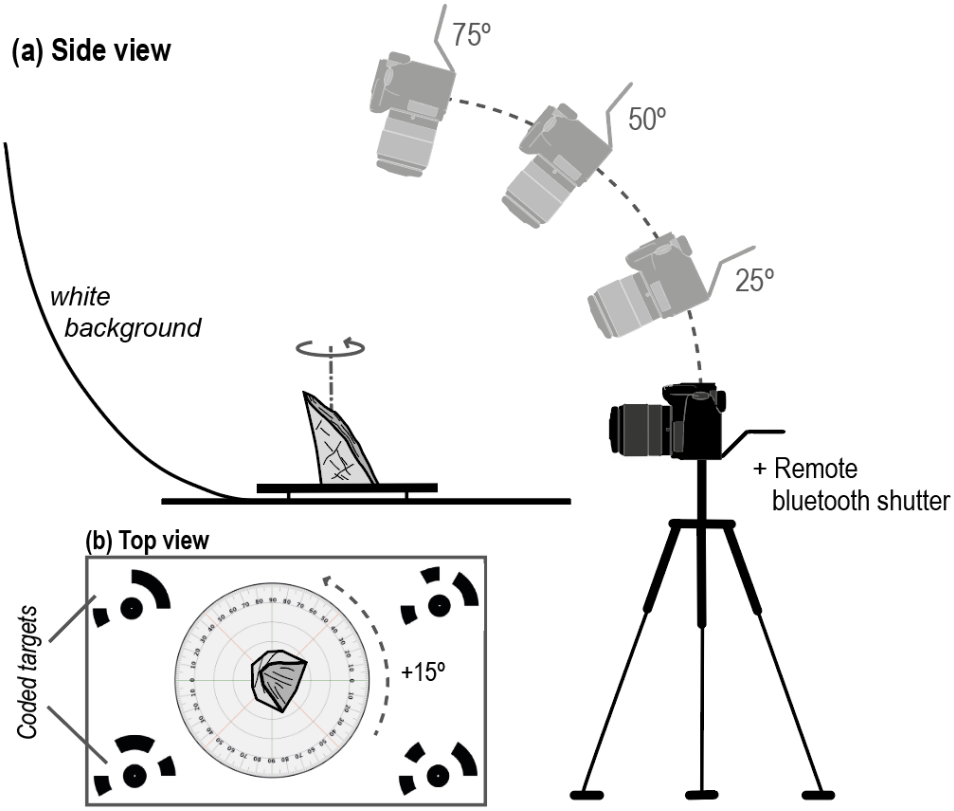

Figure 46. Schematic diagram of fixed camera capturing mode, with the side (a) and top (b) view.

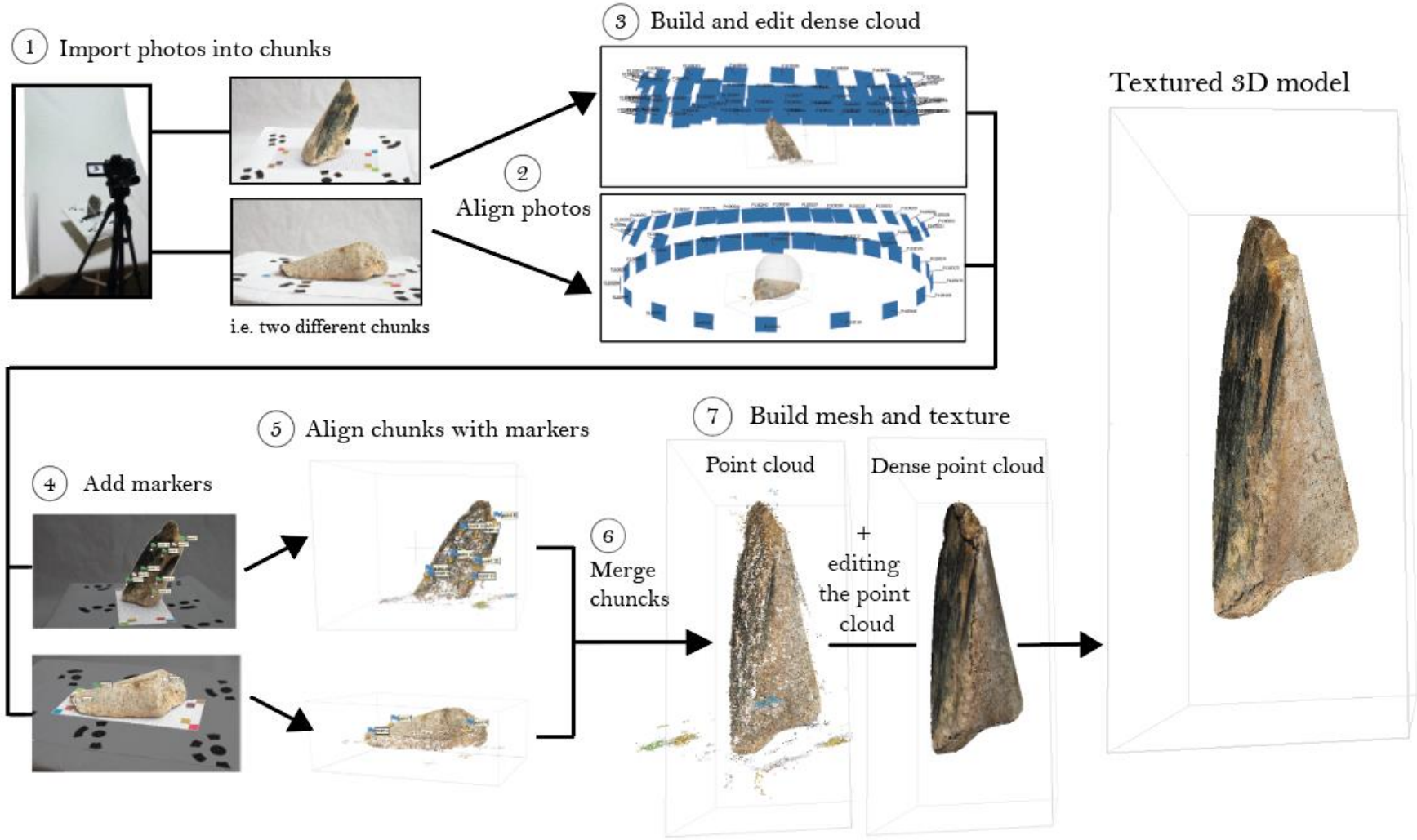

Figure 47. Flowchart of the developed workflow to generate digital sample models using Agisoft Metashape software.

The resulting textured model and the point cloud can provide a non-destructive calculation of volumes and, therefore, an estimate of derived bulk densities. However, in this study, the main objective is the documentation of samples that will be digitally stored and their structural characterization. With the resulting point cloud, the different fractures and lineaments have been analyzed with the open-source software *CloudCompare* (*www.danielgm.net/cc/*) and the *FACETS* plugin (Dewez et al., 2016).

FACETS plugin allows to perform planar facet extraction, calculate their dip and dip direction, and report the extracted data in interactive stereograms (Dewez et al., 2016). First, fractures can be automatically detected by clicking on lines (Figure 48-Left) or planes that offer a contrast in the point cloud. For detecting planes, different parts of the plane were selected to get a more representative result (Figure 48-Right). Moreover, from the fracture lines we can get plane orientation. Finally, all these data are plotted together in a stereoplot.

The main drawback of this methodology is that most of the available samples were not oriented, so the only way to correlate the fractures with the sets defined at the surface is by rotating the stereoplots until they match. However, other fracture characteristics such as the aperture, mineralization, or movement marks could also be helpful.

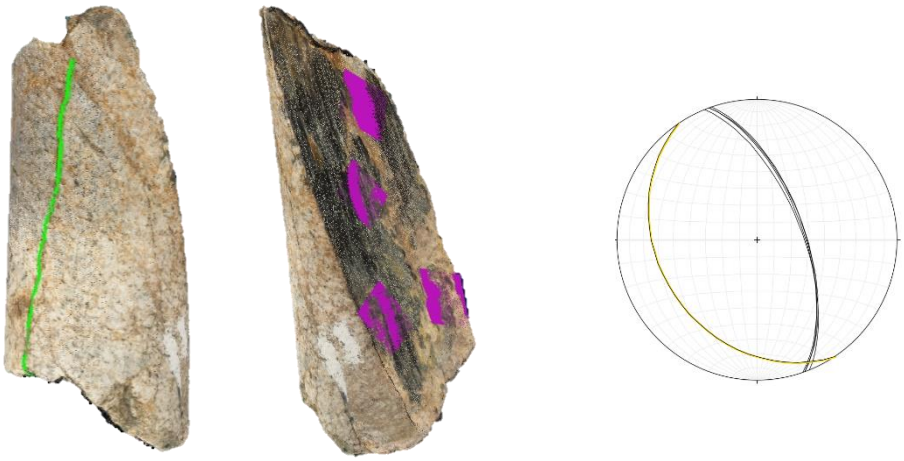

Figure 48. Point clouds of two sample orientations. Left: automatic line detection of a fracture. Right: Multiple plane set in order to have a representative average dip. The not-oriented stereoplot shows in yellow the line on the left.

4.5.2. Results

This methodology's primary outcome has been storing the samples in high-quality 3D models (Figure 49). However, the structural analysis of the point cloud also offers some significant good results.

Figure 49. Examples of zoomed screenshots of the textured 3D model of three different borehole samples.

The main orientations of fractures in boreholes match those sets of fractures defined in the outcrops (see Table 2), with the most common fractures being F_A, followed by N-S steep (F_B) and shallow dipping (F_C) fractures. Although it has not been possible to determine the orientation of all the borehole samples, they have contributed to characterizing the fractures in depth without surface weathering. Notably, most borehole samples show significant open and connected fractures of 2-4 cm (Figure 50).

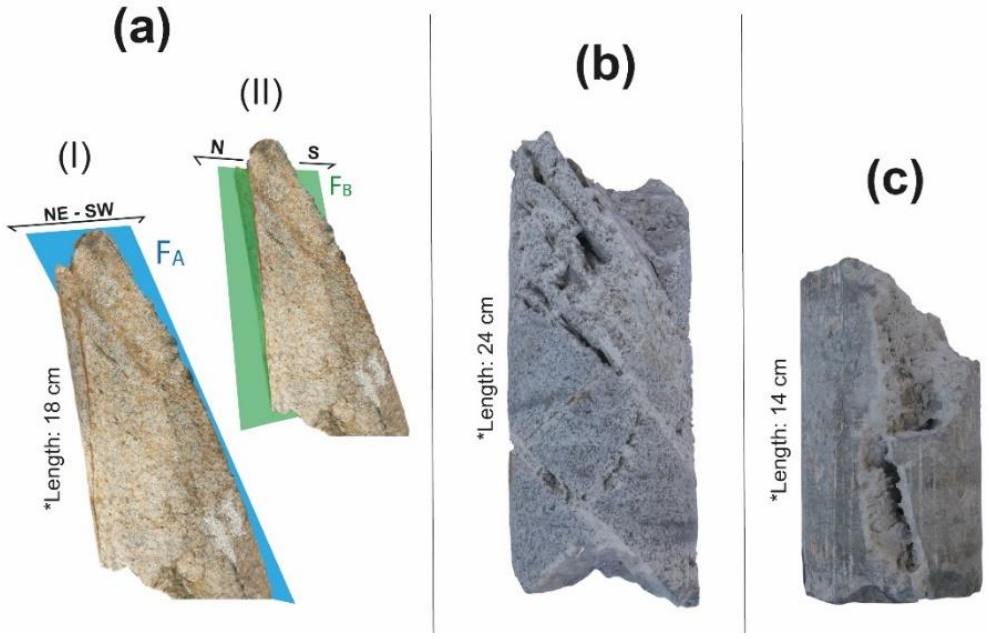

Figure 50. S1 borehole core samples. (a) Oriented sample used to relate the family sets described in outcrops with the deep fractures. (b & c) Not oriented samples of a granodiorite (left) and a leucogranite (right) with open fractures partially filled by hydrothermal carbonated precipitates.

4.6. Discussion and conclusions

The present-day structure of the CCR reflects the Neogene extensional tectonics, which cuts the Paleogene structure formed during the compressional Alpine stage (Marcén et al., 2018). Previous authors who focused the study on the structural evolution of the CCR state that the VF is the result of the negative inversion that occurred during the Neogene (e.g., Anadón et al., 1979; Fontboté, 1954; Roca et al., 1999). However, there is no consensus on the relationship between the AT and the VF, and their geometry is still a question mark.

In this background context, based on the results obtained in this chapter and also considering the previous information and the geophysical results, we propose a structural model discussing the geometrical arrangement of the major faults. In addition, the deformation characteristics associated with the related fault zones will also be discussed.

4.6.1. La Garriga-Samalús (G-S) area and its local structural analysis

The G-S area has focused most of the investigations performed during this thesis. The presence of all the newly acquired geophysical data and the study of outcrops and boreholes makes it the best objective to preliminary understand the presence of the geothermal system and the hot springs.

We have characterized the thrust sheet unit, formed mainly by granodioritic rocks, which corresponds to the VF footwall block. Only fragile deformation structures are observed along the thrust sheet, such as open fractures or fractures filled with intrusive rocks or cement; no medium or small-scale ductile deformation structures have been detected. A variation in the mineralogy and texture of the granodioritic samples has also been observed following a similar tendency. Throughout the thrust sheet, the granodiorite unit is highly fractured, although their characteristics change due to the high-stress conditions in the vicinity of the faults. The fracture grading at the surface is an image of what happens in-depth, with the granodioritic column of the borehole showing fracturing conditioned by the proximity to the VF plane.

Figure 51 presents the new trace drawn for the VF and the AT in the La Garriga-Samalús area. These new traces have been defined using fieldwork geological mapping, topography analysis, and geophysical data. The primary outcomes are the slight change in the AT geometry; and the confirmation of the segmented VF geometry, which had already been suggested in the geophysical discussion. The fault segments in this area form a relay zone, which geometry will be described in the regional analysis of faults.

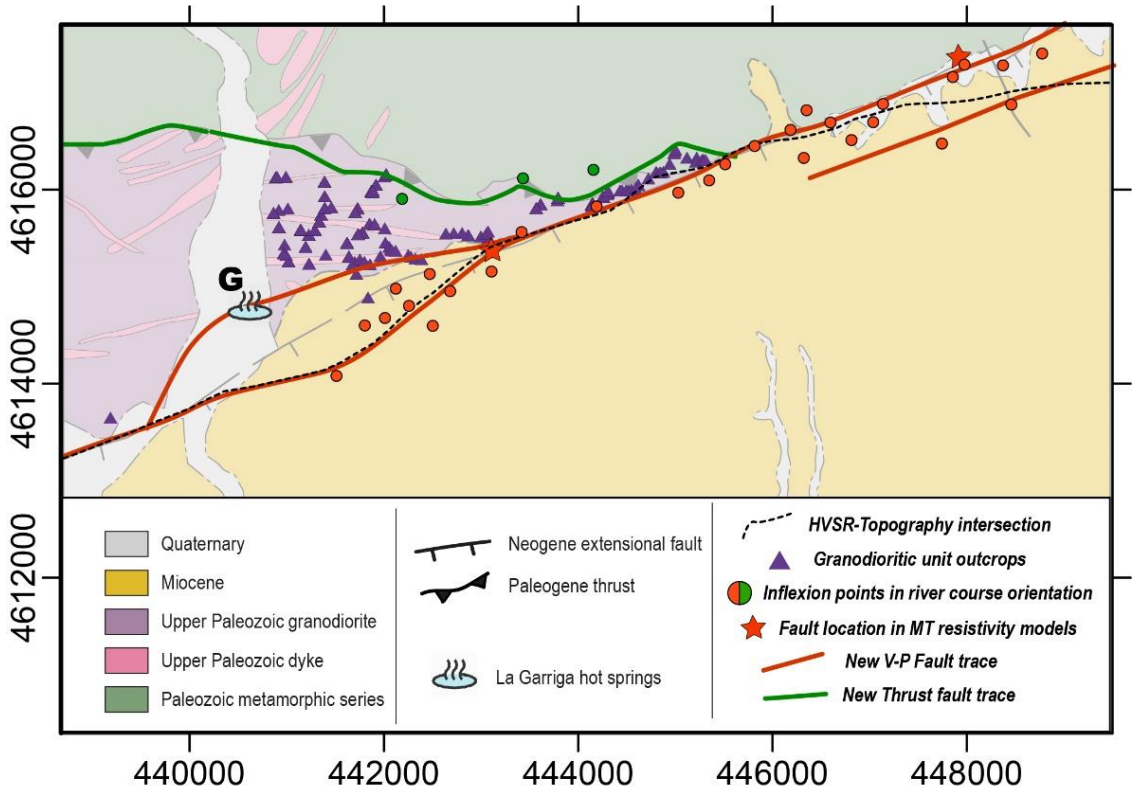

Figure 51. Location of the conditions used for the new Vallès Fault and Alpine Thrust traces, above the old geological map (modified from ICGC, 2016). The main new feature lies in the segmentation of the Vallès Fault at the eastern part of La Garriga town (G).

4.6.2. Paleogene Alpine Thrust geometry

The granodioritic unit is placed in the studied area as a thrust sheet above Paleozoic metamorphic rocks, which are more or less deformed, and affected by contact and regional metamorphism. From Caldes de Montbui and towards La Garriga, this Paleogene thrust draws a line that changes the direction from SW-NE to NW-SE, and its dip varies between 15º and 50º (cartographically calculated). The western and eastern margins of the thrust sheet generate a *branch point* close to Castellar del Vallès and Cànoves town, respectively.

The available geophysical data does not allow the characterization of the AT in depth. However, previous exploration boreholes in Samalús town did not cross the granodioritic unit-metamorphic series limit, which implies that considering the S6 borehole (IGME, 1986), the thrust must be at least 1000 m depth (which is the maximum depth of the borehole).

It has not been possible to well-characterize an outcropping AT plane. However, close to La Garriga town, there is a 2-5m long outcrop of unconsolidated, small grain size rock, which suggests the presence of a fault gouge, and the IP results would validate this hypothesis. This fault gouge is located between the granodiorite and Ordovician slates of the footwall outcrops. The

fracturing, close to the fault gouge, disappears rapidly towards the north, towards the Ordovician slates. However, towards the south, the granodioritic unit keeps an almost high fracturing degree.

As there are no more outcrops of the metamorphic series in contact with the AT, the area's surroundings have been considered to understand the rheology of the metamorphic materials.

Following the VF towards the SW, at 20 km from Caldes de Montbui and 35 km from La Garriga, there is a well-studied outcrop of these Paleozoic metamorphic materials in contact with a fault. This site, Ribes Blaves, is known for the erosional morphologies that form badlands resulting from the erosion of bluish-colored fault gouges (Figure 52). This fault rock is the result of crushing the Paleozoic metamorphic rocks in contact with the VF. This fault gouge is characterized by millimetric to decametric size grains of generally quarzitic composition. Previous works in this area are mainly focused on rock's characterization and its structural history (Aldega et al., 2019; Cantarero et al., 2012; Marcén et al., 2018).

Ribes Blaves fault gouge presents the deformation characteristics of the Paleozoic metamorphic series affected by the VF. However, in the area of study, this unit is mainly affected by the AT. Nevertheless, although no information can be extracted from the outcrops of la Garriga town (Figure 53), similar deformation results are expected, which will have the same relevance in the hydraulic functioning of the system, so being characterized as an impermeable unit.

Figure 52. Fault gouge outcrop in Ribes Blaves. This formation is the result of the Paleozoic metamorphic unit affected by the Vallès Fault. Although this formation outcrops far from the study area, it shows an example of the fragile behavior of the metamorphic series in contact with a major fault.

Figure 53. Outcrop of the Alpine Thrust in the La Garriga town. The high degree of weathering of this outcrop complicates its surface characterization.

4.6.3. Vallès Fault geometry

On a regional scale, from Caldes de Montbui and towards the eastern limit of the Vallès Basin, the VF does not completely keep the same rectilinear orientation. However, it forms non-aligned linear segments connected by fault trace bends. In the La Garriga-Samalús area, we locate one of the most significant segment steps, the La Garriga relay zone.

The La Garriga dextral relay zone, with a width of 650 m and a length of 2000 m, is set on average of a well-defined relationship between relay width and relay length (fault overlap) for large faults (Fossen and Rotevatn, 2016), and therefore, is structurally coherent. Moreover, the kilometric displacement set for the VF in previous works is consistent with the fault zone, which can be defined in the granodioritic thrust sheet (Figure 54D). Internally, this ramp develops a complex area of subsidiary faults and fractures. Fractures from sets F_A, F_B, and F_c are predominant in this area, although other structures like F_E are present. F_A structures are mainly located close to the major fault trace, and F_B and F_C predominate in the ramp area.

The internal deformation of relay ramps results from displacement accumulation (Figure 54A). Further growth leads to breaching of the relay ramp and linkage of the segments, often with breaching occurring in the upper ramp (Figure 54B). In this case, breaching is inevitable given the mechanical properties of the granodiorites, principally because of VF's large displacements compared to the separation of the segments and the likely length of the overlap. Preserving an intact relay within those internal deformations in granodiorites is practically impossible (Childs et al., 2009). Even so, the Quaternary and Miocene deposits over the top of the basement granodiorites could retain an intact relay because they could accommodate higher ramp rotations before breaching. The branch may not be evident on the surface, but in-depth, leading to the relay structure maturation downward the syn-rift sequence (Fossen and Rotevatn, 2016; Giba et al., 2012). The ramp rotations and the high degree of deformation in the relay zone could also favor the development of other major structures (Figure 54C) or act as a potential area for developing cross-fault river systems. However, in all such cases, it will act as a site for both deformation and up-fault flow (Walsh et al., 2018).

The topography analysis results suggest that in the other location with hot springs, Caldes de Montbui, there is the same geometry of overlapping VF segments and relay zone. Moreover, both areas have important N-S lineaments that cross-cut the VF trace. These lineaments would be related to the later N-S structures with relevant presence in Vallès Basin, and the F_B defined in the outcrop studies. The high permeability zone caused by the high deformation and stress degree in the relay zones would favor the presence of a geothermal reservoir, and the later structures would act as a recent hydrothermal seal-breaker, causing the upwelling of hot water in these particular areas.

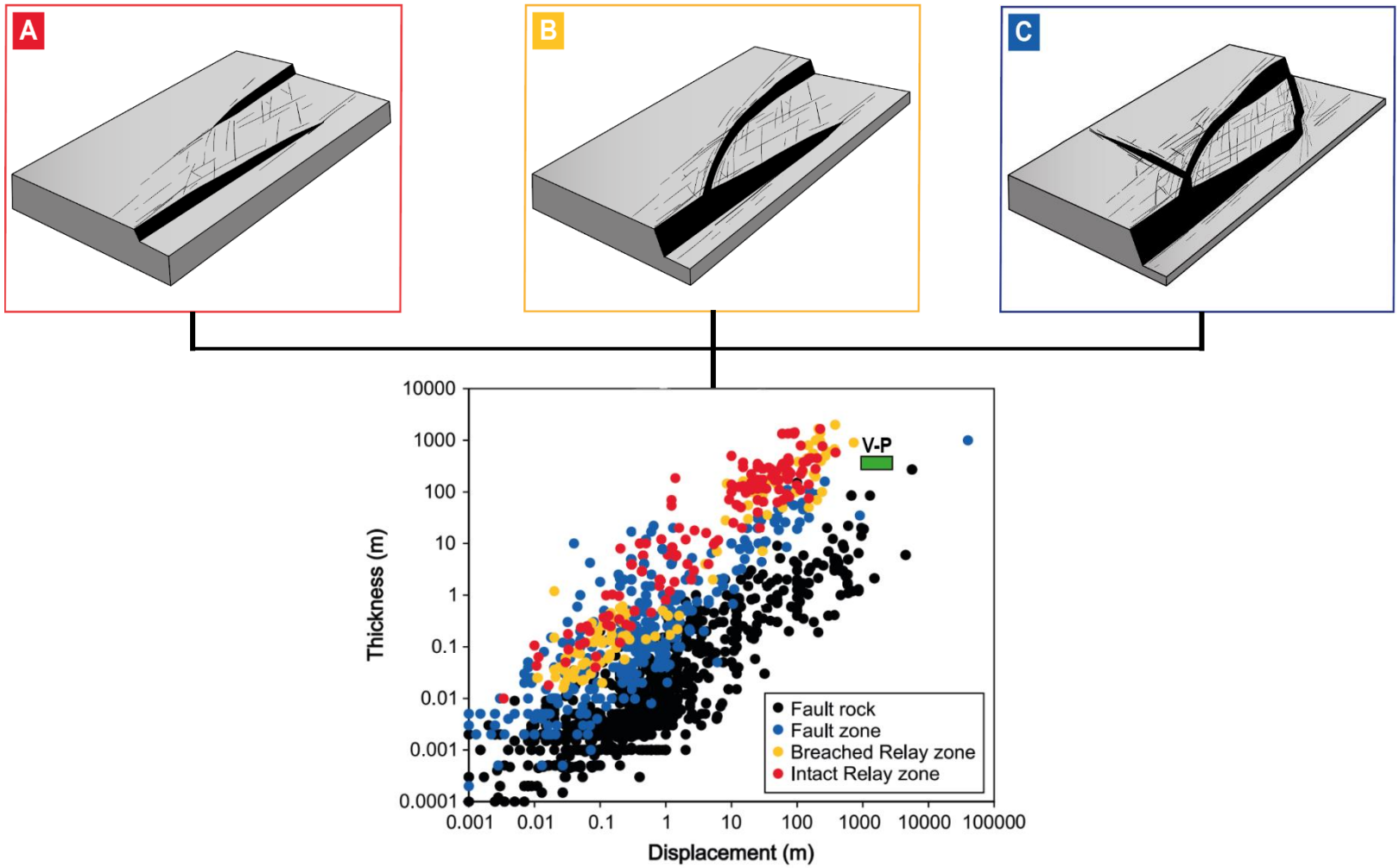

Figure 54. A) Unbreached relay ramp displaying ramp-related fracturing and deformation. The thickness or segment perpendicular separation, is shown. B) Breached relay ramp in which continuous (i.e., ramp-related) deformations still accommodate much displacement transfer between segments. C) Doubly-breached relay ramp with strongly deformed fault lens. D) Displacement vs thickness plot for different components of fault zones, including intact relay zones (red), breached relay zones (orange), fault zones (blue; including intact relays through to fault lenses), and fault rock (black) (modified from Childs et al., 2009). The scaling of the Vallès fault zone at La Garriga is consistent with strongly fractured host rock and fault rock.

4.6.4. Fault zones and fracturing pattern

According to the results, the granodioritic zone shows sustained fracturing throughout the intrusive body. Moreover, this fracturing is presented in different degrees depending on the proximity to the major structures, the VF and the AT.

Although the fracture characterization has been focused on the granodioritic unit (footwall of the VF and hanging wall of the AT), fracturing in Paleozoic metamorphic materials should not be underestimated.

The AT core is described as a 3-4 m impermeable fault gouge. This type of rock has also been previously identified in other parts of the CCR (i.e., Ribes Blaves fault gouge (Marcén et al., 2018)). The Prelitoral damage zone in the footwall is highly concentrated close to the fault core and does not exceed 50 meters.

The VF core in its footwall is defined as a ten meters-thick band along the fault plane. The associated fault core rocks are protocataclasites with no open fractures, generating a fault rock that is both hard and impermeable. The studied borehole samples show this particular fracturing corresponding to the VF's impermeable core, with clear slicklines and developing high-pressure alteration minerals.

The VF damage zone is identified immediately adjacent to the previously described fault core and covers a variable extension, which reaches approximately 300 meters away from the fault plane. This area provides the most permeable rock volume, with a significant density fracturing. In addition, the density map highlights a more fractured part of the damage zone close to the La Garriga relay ramp. This step, described below, represents one of the most direct pathways for hot fluids.

The potential presence of N-S structures favored by the weak relay zones should not be underestimated. These structures, which have been defined as the last to form, could act as seal breakers, maintaining the hydrothermal activity and the hot springs at the principal thermal localities.

4.6.5. Structural evolution and fracture development in the La Garriga-Samalús area

As no radiometric ages of veins are available in this area, an attempt to correlate family fractures with the main tectonic events has been made according to the dip and azimuth of fractures and the comparison with other works in adjacent areas. However, the scarcity and bad quality of the outcrops cause uncertainty in some of these groups.

We consider the F_D, F_E, and F_F fractures the oldest fracture sets developed during the later stages of magma cooling related to the Variscan Orogeny. Cooling joints in magmatic intrusions are

persistently displaying a characteristic pattern of vertical (F_E) and subhorizontal fractures (F_F) (Cloos, 1922; Mattsson et al., 2020; Price and Cosgrove, 1989). Moreover, F_D fractures have the same orientation as the E-W dyke swarm of aplites and pegmatites, suggesting that cooling fractures favour the late intrusions ascend.

Following the Variscan Orogeny, fractures related to Mesozoic deformation have been previously described in the western part of the Vallès Basin (Cantarero et al., 2014). However, no similar structures attributable to this deformation have been found in this case.

During the Alpine orogeny (Eocene-Oligocene), the main directions of compression vary between NW-SE and N-S in the first phase and NE-SW in the second phase (Guimerá and Santanach, 1978). The primary Alpine expression in the study area would be the AT. The minor structures resulted in strike-slip fractures with NW-SE and E-W orientations (Guimerá, 1984; Guimerá and Santanach, 1978), which, therefore, could imply the reactivation of the previous fracture sets.

Following the Alpine deformation, the VF has been set as the main expression of the Neogene rifting event (Bartrina et al., 1992; Cabrera and Calvet, 1996; Fontboté et al., 1990; Roca and Guimerà, 1992). In our model, we propose that the AT, characterized by an oblique plane, is reactivated as an extensive ramp during the Neogene. However, instead of being reactivated, new faults of steeper dips are created in the area of study. These upper panels of 70º dip would be rooted to the original AT. Similar orientation fractures have been defined in outcrops (F_A), especially close to the fault trace, but also in the borehole samples, characterized by clear slickenlines.

The ages of formation for the F_B and F_C fracture sets have not been determined. However, both are N-S structures located around the studied area and densely localized close to the VF trace in the La Garriga town (west margin of the study area), so in the branch point between the AT and the VF. Therefore, these fracture sets could have taken advantage of zones of high deformation and weakness, such as relay ramps.

While the Paleogene and Neogene tectonic evolution of the CCR have been well studied, there needs to be more information about the Pliocene and Quaternary structural activity (Masana, 1996). Small faults within the Pliocene and Lower Quaternary are sparse, attesting to the decreased intensity and activity of normal faulting in that period. Some works in southern parts of the CCR showed that this area has been active. Specifically, associated seismicity within the CCR is considered to be low (Masana, 1994, 1996), with several earthquakes of M<4 every year, and two historical earthquakes with intensities of VII and VII-VIII (corresponding to M~6.0-6.8) have occurred on or adjacent to the V-P Fault (Sanz de Galdeano et al., 2020). In the study area, the main epicenter earthquakes are located in the eastern margin, where an evident topographic shoulder acts as a watershed and may be linked to an N-S structure. There are also two earthquakes

close to the two main hot springs (M~1.2), and the biggest one is close to an intersection between an N-S fault and the AT (M~3.3) (Figure 55).

Despite this relatively low level of activity, these earthquakes and the protracted history of the V-P Fault provide support for fault reactivation and associated fluid circulation, a scenario we consider later in the context of the geothermal systems of La Garriga and Caldes de Montbui.

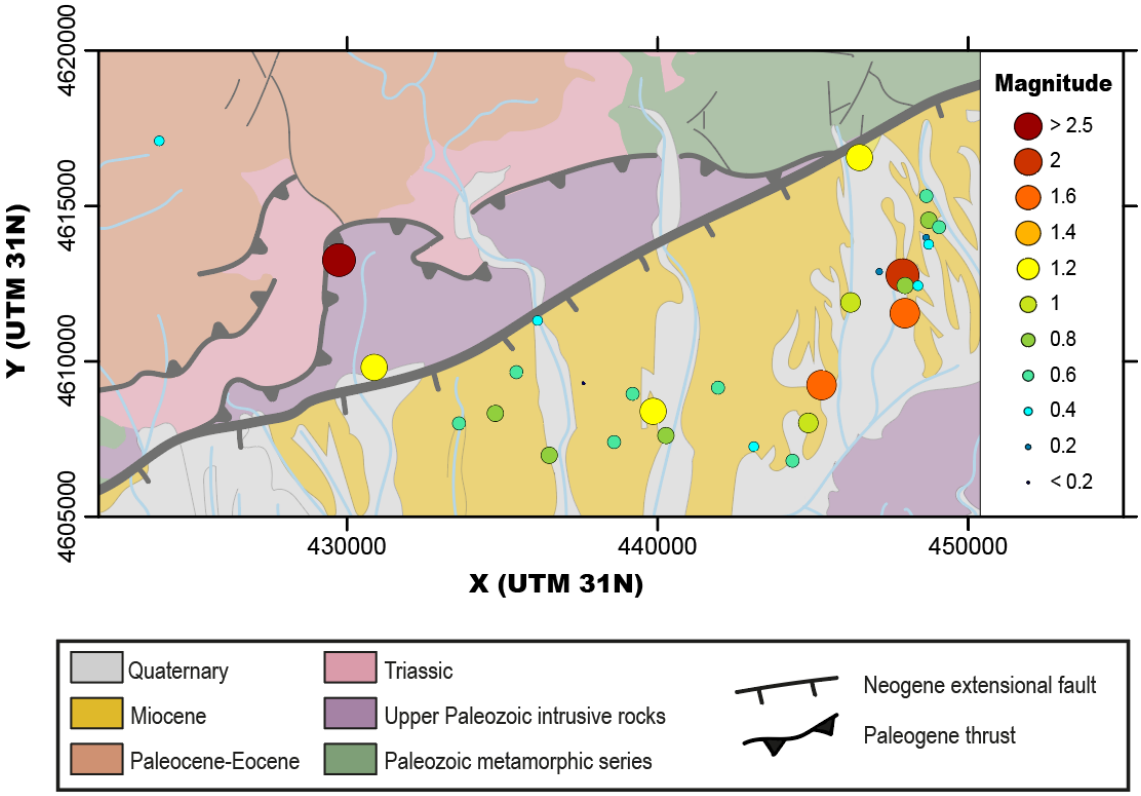

Figure 55. Earthquakes recorded in the study area from 1984 to September 2002, on the 1:250.000 geological map (ICGC, 2002). The size of the symbol and the color refer to the magnitude of the earthquake. ICGC database and epicenters locations from IGN (ICGC, 2022).

Chapter V

Petrophysical measurements

Petrophysical rock properties are fundamental parameters for subsurface characterization in geothermal exploration, as they are commonly used for the interpretation of geophysical data and the quantification of physical parameters related to the hydraulic properties of the different geothermal units.

In this chapter, we present density measurements, porosity calculations, and the spectral induced polarization method (SIP), which acquisition and analysis were conducted at the *Institute of Geophysics and Geoinformatics* of the *Technical University of Bergakademie Freiberg* (Germany) under the supervision of Dr. Jana H. Börner. These laboratory analyses have been carried out to characterize each geothermal unit and quantify some of its hydraulic properties to support the interpretation of the system's functioning. Moreover, if necessary, the density and SIP results could be used to re-evaluate the geophysical model interpretation.

The samples used for the petrophysical analysis include 12 samples from outcrops and the borehole S1 (IGME, 1982).

The surface samples (Figure 56) are mainly from the thrust sheet unit, including granodioritic rocks and later-dyke intrusions. Specifically, these samples include slates from the Paleozoic metamorphic unit (M7), samples from both block sides of the Alpine Thrust (AT) (M6 and M6.2), and a cataclastic rock from the Vallès Fault (VF) core (M0).

On the other hand, the S1 borehole samples are fractured granodiorites with big cavities whose exact depth has not been determined.

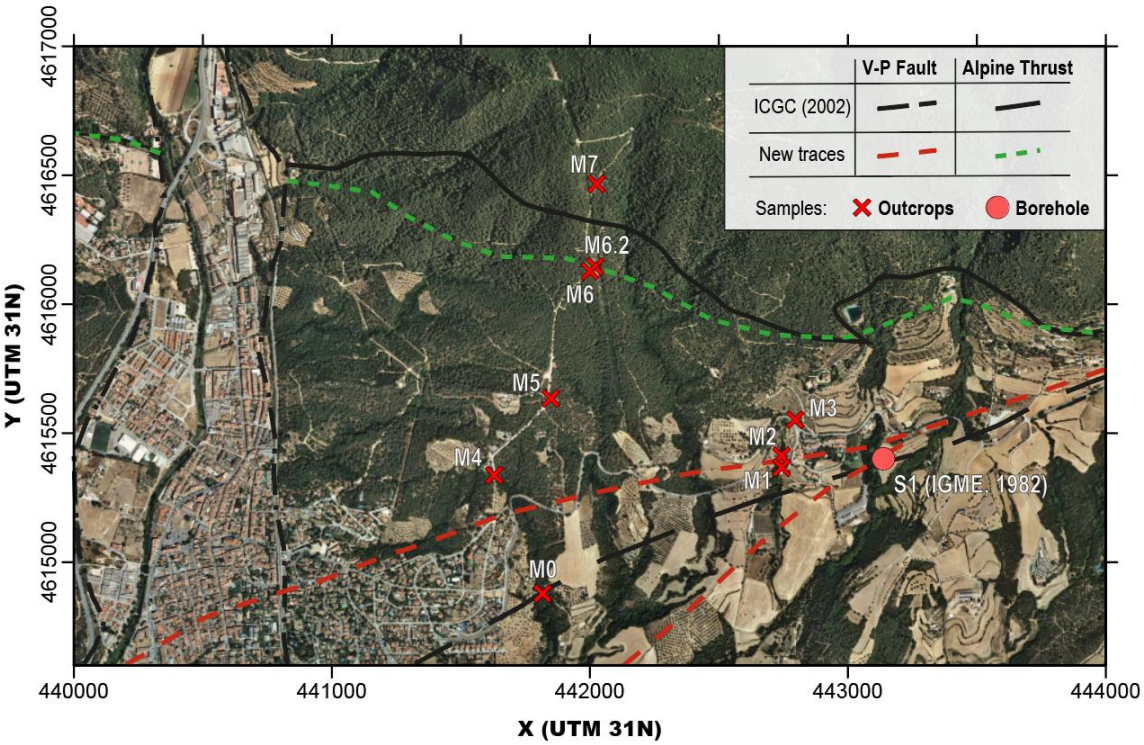

Figure 56. Location of the samples used in the petrophysical analysis. The fault traces include the ones from the previous geological map 1:250.000 (ICGC, 2022), and the new traces after the Chapter IV discussion.

5.1. Density

The bulk density of rocks depends on the mineral composition (mineral densities and volume fractions), porosity (pores and fractures), and the density of pore fluids (Schön, 2015). Its value can be used for the gravity data inversion review and for further petrophysical calculations.

Furthermore, previous work focused on geothermal reservoir characterization has shown that density can directly be related to other important parameters, such as thermal conductivity (Jorand et al., 2015; Rybach & Bunterbarth, 1982; Sundberg et al., 2009).

5.1.1. Methodology

The solid phase density has been calculated using the *AccuPyc 1330* helium pycnometer (*Micromeritics Instrument Corporation*) (Figure 57A). This device determines the sample volume by measuring the pressure change of helium in a calibrated volume. It uses two volumes (one with the added sample) connected by a valve (Figure 57B). Employing different pressure conditions and based on the Ideal Gas Law equation, the volume of the sample can finally be obtained (Micrometrics Instrument Corporation, 2005).

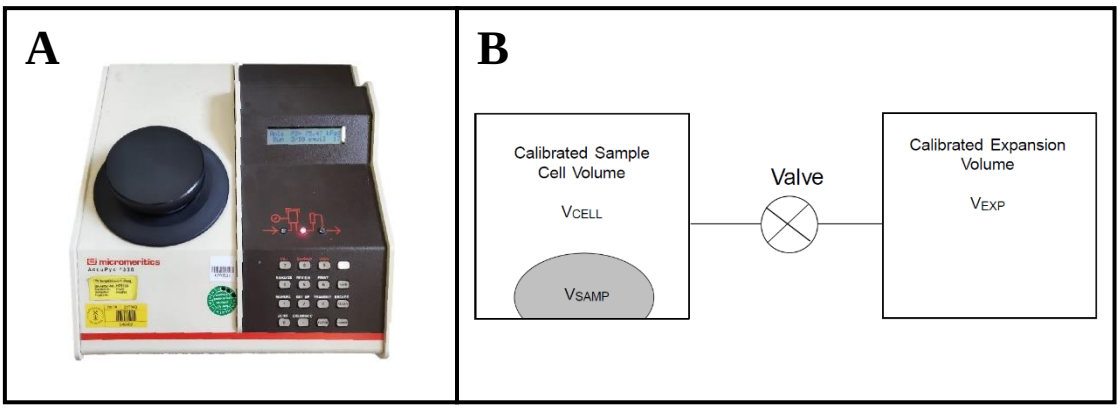

Figure 57. (A) AccuPyc device (photography from the Freiberg lab) and a (B) simplified block diagram of the inner system functioning (Micrometrics Instrument Corporation, 2005).

The V_{CELL} is where the sample is located, which in the first phase is filled by helium gas at pressure P_1. The Ideal Gas Law varies for both volumes, the Cell $_{(CELL)}$ (Eq. V.1) and the Expansion $_{(EXP)}$ (Eq. V.2) volumes:

$$P_1 \cdot \left(V_{CELL} - V_{Sample}\right) = n_{CELL} \cdot R \cdot T_a \qquad \text{(Eq. V.1)}$$

$$P_a \cdot V_{EXP} = n_{EXP} \cdot R \cdot T_a \qquad \text{(Eq. V.2)}$$

, where n is the number of moles of gas in the samples cell; R is the gas constant; T is temperature; P is pressure; and the sub-index $_a$ is referred to ambient conditions.

Then, the valve opens, and the pressure falls to an intermediate value. The new pressure equilibrium is defined as P_2:

$$P_2 \cdot \left(V_{CELL} - V_{Sample} + V_{EXP}\right) = n_{CELL} \cdot R \cdot T_a + n_{EXP} \cdot R \cdot T_a \qquad \text{(Eq. V.3)}$$

, which substituting results in:

$$P_2 \cdot \left(V_{CELL} - V_{Sample} + V_{EXP}\right) = P_1 \cdot \left(V_{CELL} - V_{Sample}\right) + P_a \cdot V_{EXP} \qquad \text{(Eq. V.4)}$$

$$(P_2 - P_1) \cdot \left(V_{CELL} - V_{Sample}\right) = (P_a - P_2) \cdot \left(V_{EXP} - V_{Sample}\right) \qquad \text{(Eq. V.5)}$$

, which ends with the working equation for the pycnometer:

$$V_{Sample} = V_{CELL} - \frac{V_{EXP}}{\frac{P_1 - P_a}{P_2 - P_a} - 1} \qquad \text{(Eq. V.6).}$$

Knowing the sample mass, the density can be derived automatically following the equation:

$$d_{solid\ phase} = \frac{mass}{V_{Sample}} \qquad \text{(Eq. V.7).}$$

5.1.2. Results and discussion

The results plotted in Figure 58 show the density variation for the surface samples. The granodioritic thrust sheet unit, results in densities between 2.57 and 2.67 g/cm^3. The borehole samples units, which are also from the granodioritic unit show similar results, with densities between 2.56 and 2.70 g/cm^3. However, and the metamorphic slates densities are quite higher, between 2.76 and 2.80 g/cm^3.

Therefore, although the density results are similar, there is a slight tendency of decreasing density towards the south, towards the VF trace.

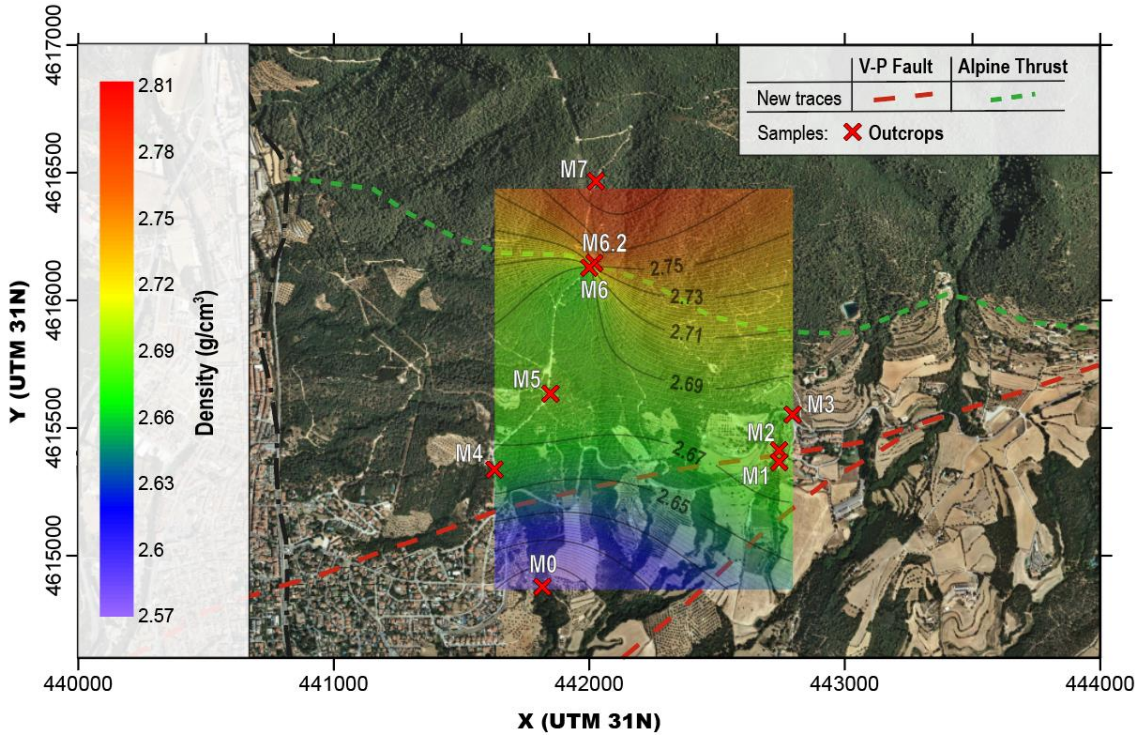

Figure 58. Density results plot on the La Garriga-Samalús map. The density decreases towards the Vallès Fault. The metamorphic samples, M6.2 and M7, have the highest density values.

5.2. Porosity

Porosity is defined as the summarized volume of pores, fractures, or non-solid containing parts of a sample (V_{pore}) related to the total volume of the sample (V_{bulk}):

$$\phi = \frac{V_{pore}}{V_{bulk}} = \frac{V_{bulk} - V_{solid}}{V_{bulk}} \qquad \text{(Eq. V. 8)}$$

, where V_{solid} is the volume of the solid mineral components, frequently called “grain volume” (Schön, 2015).

Porosity is a fundamental volumetric rock property that describes the potential storage volume of fluids and influences most physical rock properties (for example, electrical resistivity, elastic

wave velocity, and density) (Anovitz & Cole, 2015). Moreover, its connectivity and pore structure control the fluid flow. Therefore, this property is one of the critical factors in geothermal characterization, and its analysis can provide a better reservoir identification and characterization (i.e., Dobson et al., 2003; Stimac et al., 2004).

5.2.1. Methodology

In order to obtain the porosity values, the following parameters were measured for all the samples:

a) **Geometry**: All the samples were previously cut in a cylinder shape. Therefore, its geometry has been calculated by measuring the three dimensions of the samples several times in order to get a final average value.

b) **Density**: The matrix density measurements were carried out using an *AccuPyc 1330* helium pycnometer (*Micromeritics*), employing the gas displacement method. Prior to the analysis, the samples were dried by heating in an oven.

c) **Dry and wet mass**: For measuring the wet mass, samples were saturated with water under a vacuum for a minimum of 12 hours. The saturating water bore the same properties as the studied area groundwater. For the dry mass, the samples were dried in an oven at 120ºC for more than 12 hours. After the two processes, the samples were weighed using a high-resolution scale.

From the measured data, we calculated the following parameters for each sample:

1. **Solid or matrix volume** (V_{solid}): calculated using the dry mass and the density data.

$$V_{solid} = \frac{\text{mass}_{\text{dry}}}{\text{density}_{\text{matrix}}} \quad \text{(Eq. V. 9)}$$

2. **Pore volume** (V_{pore}): calculated using the water-filled volume and the previously-measured groundwater density (W_d = 997.91 kg/m^3).

$$V_{pore} = \frac{\text{mass}_{\text{water}}}{\text{density}_{\text{water}}} = \frac{\text{mass}_{\text{wet}} - \text{mass}_{\text{dry}}}{\text{density}_{\text{water}}} \quad \text{(Eq. V. 10)}$$

3. **Bulk volume:** calculated considering two methods of calculation and therefore, obtaining two results for the porosity analysis:

    a) Bulk volume calculated using the geometry, and therefore, independent from parameters 1. and 2.

$$V_{bulk1} = \text{length} \cdot \pi \cdot \text{radius}^2 \quad \text{(Eq. V. 11)}$$

    b) Bulk volume calculated using the water volume and matrix volume

$$V_{bulk2} = V_{pore} + V_{solid} \quad \text{(Eq. V. 12)}$$

Porosity has been calculated in three different ways in order to get a statistical result and detect result differences probably induced by big fractures and cavities, which might suffer from gravitative drainage during sample handling:

a) **Poro1:** "Water focus" calculation

$$\emptyset_1 = \frac{V_{pore}}{V_{bulk1}} \cdot 100\% \qquad \text{(Eq. V. 13)}$$

b) **Poro2:** "Matrix focus" calculation

$$\emptyset_2 = \left(1 - \frac{V_{solid}}{V_{bulk1}}\right) \cdot 100\% \qquad \text{(Eq. V. 14)}$$

c) **Poro3:** Porosity using 3.b as bulk volume.

$$\emptyset_3 = \frac{V_{pore}}{V_{bulk2}} \cdot 100\% \qquad \text{(Eq. V. 15)}$$

5.2.2. Results and discussion

Porosity results using the methods described earlier are presented in Figure 59. Samples *M6* and *M6.2* did not resist the analysis and had some affectations, so they are not included in the results. For this analysis, the *M5.2* sample was added, a dyke intrusion sample located next to *M5* (instead of a granodiorite). Moreover, these results include a sample from the Miocene sandstones of the Vallès Basin (*Mio*).

The *BH* granodioritic samples show a secondary porosity related to fractures and cavities that reaches 10-15%. The *M* samples are plotted considering the proximity towards the VF trace. They show rather individual porosity distributions between 5% and 30%, which seems to depend on the mineral composition of the rock rather than the proximity to the VF. These porosity differences may also be related to how the mineralogical differences of rock condition the weathering degree. Therefore, these results may not be representative of its porosity in depth.

Nevertheless, the heterogeneous nature of porosity in the near-surface range suggests the potential complexity of the flow system at multiple scales. It is, therefore, consistent with the general considerations of fracture and deformation-controlled fractured bedrock aquifers. So, the extreme diversity in the near-surface underground underlines this thesis's multi-methodology and multi-scale approach.

Regarding the different ways to calculate porosity, it is essential to comment on the standard deviation for some samples. The most considerable deviations (i.e., *M2* or *M5*) are related to samples with high weathering degrees; therefore, some sample losses during the measuring could have occurred.

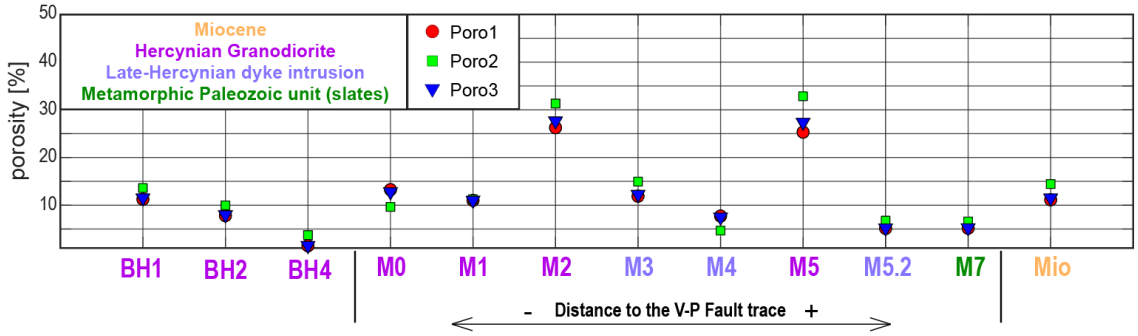

Figure 59. Porosity results for granodioritic borehole samples (BH); outcropping samples from the thrust sheet, which include granodioritic and dyke intrusion samples; an outcropping sample from the Paleozoic metamorphic series (M7), and a Miocene sandstone from the Vallès Basin (Mio). Results show a great variety of porosities which not seem to depend on the proximity to the faults. The different porosity calculation methods show similar results, with the biggest deviations in high-fractured and meteorized samples (M2 and M5).

5.3. Spectral Induced Polarization (SIP)

The electrical conductivity of a rock (σ^*) is generally a frequency-dependent (ω), complex-valued and anisotropic. It can be understood as the superposition of an electrolytic (real part, σ') and an interface conductivity (imaginary part, σ''), and can be expressed as amplitude and phase shift ($|\sigma^*|, e^{i\varphi}$) (Lockner & Byerlee, 1985; von Hippel, 1954):

$$\sigma^*(\omega) = \sigma'(\omega) + \boldsymbol{i}\sigma''(\omega) = |\sigma^*| \cdot e^{i\varphi} \qquad \text{(Eq. V. 16)}$$

The electrolytic conductivity includes conduction through the free water phase in a rock's pore space. Therefore, it depends on porosity, saturation, cementation characteristics, and pore water conductivity. Instead, a variety of mineral-surface-related polarization phenomena causes the interface conductivity, so it depends on grain toughness, pH, and weakly also on salinity.

The basis of polarization phenomena is the property of many minerals to develop a surface charge. When an external electric field is applied, conduction and polarization take place. Thereby, polarization occurs at metal or semiconductor–solution interfaces and along the charge surfaces of non-conducting grains. These diffusion-related polarization phenomena include several mechanisms, such as the polarization by the motion of charge carriers within the interface (electrochemical polarization) (Revil & Florsch, 2010; Schwartz & Zhang, 2003) and the polarization at narrow pore throats, where the neighboring interfaces come close (membrane polarization) (Marshall & Madden, 1959).

The spectral-induced polarization (SIP) method investigates both electrical conduction and polarization phenomena of rocks and other materials through laboratory and field measurements applied in the frequency domain (Schön, 2015). So, in other words, it measures the complex electrical conductivity of geo-materials.

This complex electrical conductivity is influenced by different physical properties, including the temperature. The differences in temperature near the surface are usually small, but it is also conceivable that induced polarization measurements may be used for geothermal exploration. In this context, a large temperature range is covered, and IP is particularly suitable for estimating the hydraulic conductivity of the subsurface (Bairlein et al., 2016).

5.3.1. Methodology

In the laboratory, a rock sample is placed in a sample holder, where a unidirectional, sinusoidal current of varying frequency is injected into the system via two electrodes (Figure 60). Then, at two more electrodes, the voltage drop is measured. Thereby, both amplitude and phase shift of the voltage are recorded. Finally, the complex conductivity is computed for each subsequent frequency from current, voltage, and measurement geometry.

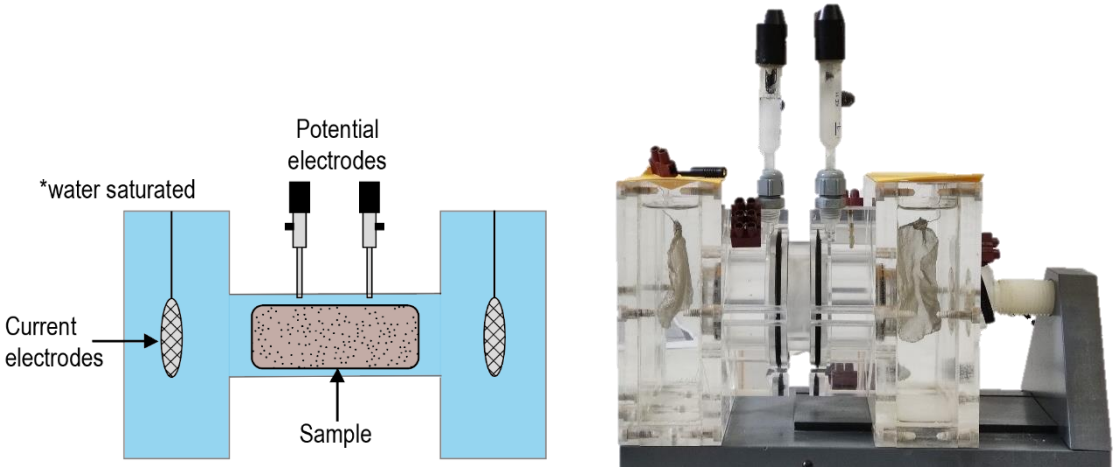

Figure 60. Schematic and real SIP device from the Institute of Geophysics and Geoinformatics of the Technical University of Bergakademie Freiberg.

Most of the samples used in this case are located in the granodioritic unit, therefore, between the AT and the VF, which is the 'key' unit in our geothermal system. The samples selected from this unit have different alteration and fracture degrees, as they are located at different distances from both faults, and at different depths of the borehole.

This method was applied in ambient conditions excepting one borehole sample, in which we did a SIP temperature dependence measurement. Temperature was increase from 25ºC to 65ºC in steps of 10ºC. The time between increasing the temperature and starting the measurement was around 24 hours to ensure that the sample was at the required temperature and chemical equilibrium during the measurement.

Although the results are still being analyzed, in the following chapters we present the preliminary results in ambient conditions and for the temperature dependent sample.

5.3.2. Results and discussion

The laboratory IP spectra for all samples are shown in Figure 61, presenting the conductivity in real (σ') and imaginary parts (σ'') in the frequency range between 10^{-3} and 10^{3} Hz. Results show how conductivity varies between samples over almost two decades. However, all of them show a weak frequency dependence.

Borehole sample results differ from the rest of the outcrop samples, resulting in low conductivities. These values would be caused by the low-porosity degree in the massive zone of the rock and the absence of clay minerals. Furthermore, these samples had large fractures and cavities that did not retain well the water inside, which could also cause a decrease in conductivity.

Apart from the resistivity range, all the spectra are relatively similar. All the samples show flat frequency dependencies, typical for clayey and fresh igneous rocks. The most different behavior is visible for the Paleozoic metamorphic slate (yellow curve), which shows a different slope. This sample, a part of being from another unit, was less meteorized than the others.

In conclusion, to identify different result types, more samples would be needed. However, the resistivity values can also be helpful for a better interpretation of the electric geophysical methods.

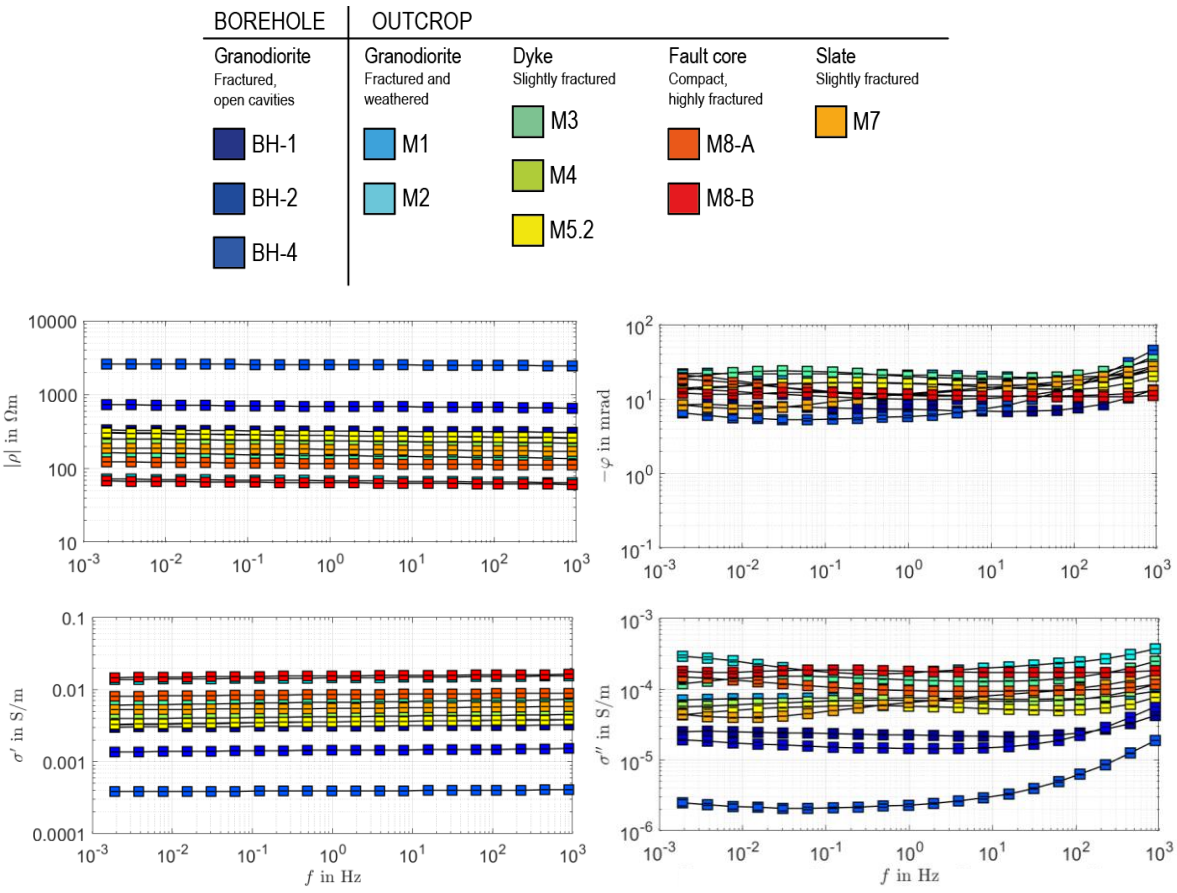

Figure 61. SIP results. Resistivity (ρ), phase (φ), real conductivity (σ') and imaginary conductivity (σ'') parts variation with the frequency (f).

In addition, a borehole sample was tested to see how the SIP results change with temperature. It should be noted that only one experimental test has been carried out, which is insufficient to draw any conclusions.

Figure 62-left shows the variation of the resistivity and complex conductivity of the sample considering the temperature and the time to get the equilibrium. The dashed lines indicate the average results when the sample is considered in equilibrium for each temperature, which have been separately plot in the Figure 62-right for its analysis.

Therefore, Figure 62-right shows how the resistivity is influenced by temperatures between 20-70ºC (which are in the temperature range of the geothermal system under study), showing resistivity variations around 150 Ωm and following an exponential function.

On the other hand, the imaginary part of the complex conductivity, which is highly related to a variety of mineral-surface-related polarization phenomena, shows a temperature dependence.

Although the SIP method has not been applied at all in this case of study, due to the lack of samples analyzed, there is an important relation between temperature and induced polarization which could have a future role in geothermal exploration. First, knowledge about the dependence of the SIP response on temperature is necessary to avoid possible misinterpretation of datasets conditioned by temperature. And second, the possibility to estimate permeability from the SIP response might be the most important benefit in this exploration context.

However, there are significant challenges to obtaining accurate and repeatable SIP measurements. Sample preparation procedures require considerable attention to detail if representative measurements of a material are to be obtained. This is a particularly challenging issue in this kind of samples where it is difficult to reliably reproduce the pores throats controlling the SIP effect.

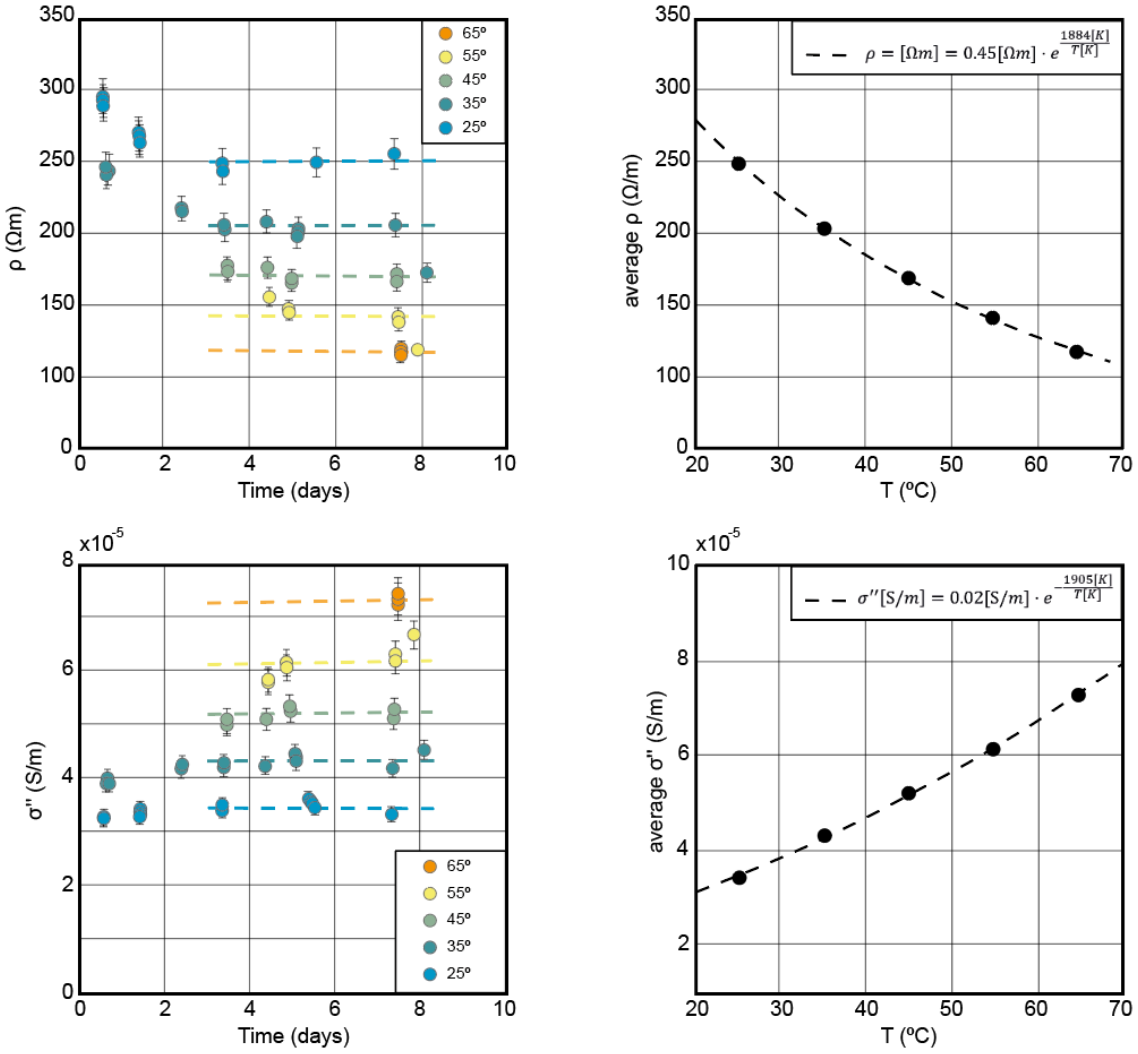

Figure 62. Left: Experimental variation of resistivity and imaginary part of complex conductivity with increasing temperatures. Every day the temperature was increased 10 ºC but registering all the temperatures in order to get a final equilibrium resistivity for each temperature. This equilibrium resistivity has been plotted (Right) to better represent the dependence of resistivity and complex conductivity (imaginary part) on temperature.

Chapter VI

Hydrogeological characterization

The anomalous temperatures of the geothermal hot springs found in La Garriga (G-S) and Caldes de Montbui (CdM) are the primary evidence of the presence of a deep geothermal system. Therefore, to complete its characterization, it is necessary to understand the hydraulic functioning and determine the causes of the localized hot springs.

The hydrological characterization involves the identification of the main hydraulic units, such as the reservoir, the recharge zone, and the discharge zone, together with quantifying some important hydraulic parameters such as permeability, temperature gradient, or thermal conductivity. Based on previous chapters' results and the reviewed bibliographic hydrological data, it has been possible to describe the Vallès Basin geothermal system. The main drawback of this chapter is that most of the information is located in the G-S area (IGME, 1977, 1982, 1984b, 1984a, 1986b; Mas-Pla, 2000; Santamaria, 2006). However, CdM will be referred to in the discussion section, as there is no consensus on whether thermal anomalies are part of the same system or independent (IGME, 1986a; Trilla, 1974).

The first critical hydrological reports of the Vallès Basin area were made by the geological survey of Spain (IGME) as a preliminary study before the geothermal exploration boreholes phase. These preliminary studies included a superficial and subterranean hydrological analysis (IGME, 1977). Later, during the exploration boreholes phase, they complement this information with an inventory of wells, natural springs, and water galleries analysis, ending with the first conceptual model of the G-S area (IGME, 1982, 1984b, 1984a, 1986b). This model set the bases of the subsequent publications (Canals et al., 1990; Fernàndez & Banda, 1988, 1990; Mas-Pla, 2000; Santamaria, 2006).

6.1. Thermal anomaly origin

Fernàndez & Banda (1988 & 1990) tested four different mechanisms as possible causes to explain the localized and relatively high geothermal anomalies found along the Vallès Fault (VF). They tested: (1) frictional heating due to the presence of the VF, since the anomaly coincides with the

fault trace; (2) magmatic intrusion due to the recent volcanism developed in nearby areas, like Hostalric, Maçanet, Olot, and Girona towns; (3) free convection, as the basement is at enough depth to be able to create convection cells; and (4), forced convection due to the high topography of the area, together with the geological structure, which may generate enough hydraulic gradient to create a deep convective circulation.

Finally, using isotopic data and the analytical solution developed by Domenico & Palciauskas (1973), forced convection was set as the only mechanism capable of explaining isolated high geothermal gradients in these areas where the temperature gradient should be on average.

In the following chapters, this forced convection process will be detailed by describing the different hydrologic units and the water circulation path.

6.2. Permeability from fractures

Permeability is one of the crucial parameters which can condition the geothermal flow in a forced convection system.

Estimating the hydraulic properties of fractured aquifers is particularly challenging due to the range of scales for measuring and applying the results. The three-dimensional nature of the fracture network characterizing the fault zones is a primary factor controlling the fault-related permeability. In this case study, the quantitative characterization of the structures has been used to estimate groundwater flow parameters using the methodology presented by Moore & Walsh (2021).

With this methodology, previously adapted from (Reiss, 1980), bulk permeability is derived from the cubic law (Eq. VI. 1) (Schwartz & Zhang, 2003), using average spacing (s) and average aperture (b); versus fracture porosity as a percentage (Eq. VI. 2) for fractures units in different parts of the granodioritic thrust sheet.

$$\mathrm{k} = \frac{\mathrm{b}^3}{12 \cdot \mathrm{s}^2} \quad \text{(Eq. VI. 1)} \qquad\qquad p = \frac{b}{s} \quad \text{(Eq. VI. 2)}$$

Furthermore, hydraulic conductivity was derived by multiplying the permeability values by the estimated values for the water properties, gravitation, density, and dynamic viscosity at ambient temperature (Schwartz & Zhang, 2003). Results presented in Figure 63 show significant permeabilities of the intrusive unit, presenting variables between 10^{-9} and 10^{-5} m^2. The granodioritic outcrops do not present a clear spatial relationship with the permeability, whereas the relay area is the most permeable and conductive zone overall. The permeability results are aperture-dependent, and despite the apparent relationship between the proximity to the VF and fracture density, the aperture does not correlate similarly. This occurs because accommodating

the same stress in fewer fractures provides a more transmissive system than one that distributes stress over many fractures. Consequently, permeabilities do not have to be more significant near the fault core.

Another factor that is not indexed in simple permeability calculations is that while carbonate infills demonstrate the circulation of geothermal fluid, they also reflect the ability of fractures to self-seal. This self-sealing could inhibit flow, but valving of fluids during multiple slip events or earthquakes often operates on the same fractures, which have, in any case, vuggy and, therefore, weaker infills (Cantarero et al., 2010; Facca and Tonani, 1967). Given the prolonged and ongoing activity of self-sealing fractures, there is no reason to expect self-sealing to be a transient phenomenon.

The porosity results presented in Chapters V had already set a first idea of the groundwater flow capacities of the granodioritic unit, considering the borehole samples to be the most reliable due to the low degree of weathering. Comparing both methodologies, a higher porosity was obtained in the laboratory, as the result was total porosity and not only the porosity generated by fracturing. Even so, the general trend is comparable, especially in the order of magnitude. This higher porosity due to weathering would be directly proportional to the degree of fracturing, as this can act as a pathway for weathering agents. Therefore, both porosity distributions – fracture porosity and total porosity – would correspond at the near-surface.

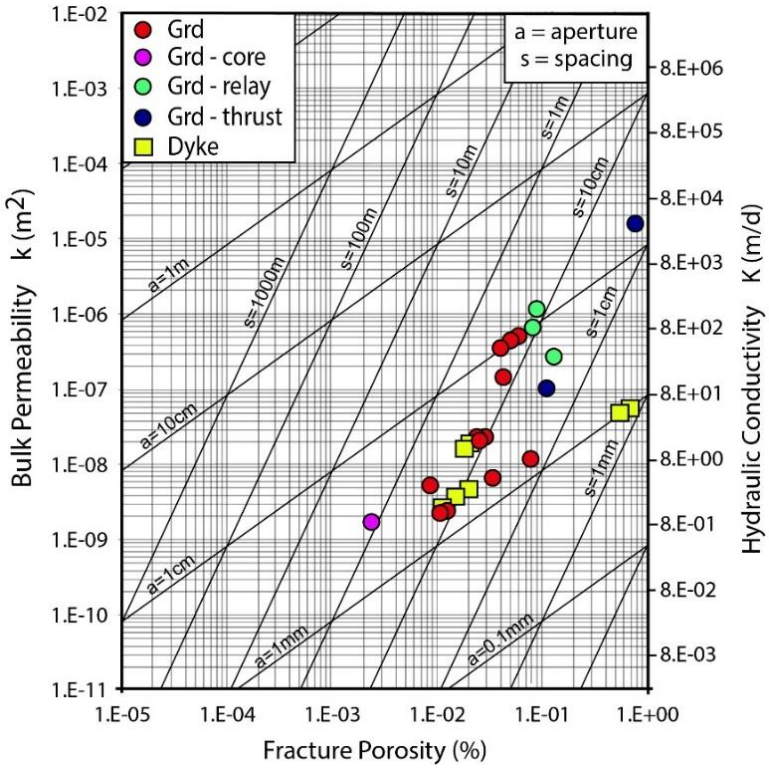

Figure 63. Bulk permeability, fractures porosity, and hydraulic conductivity derived from fracture and joint parameters (aperture and density). The colors of the granodioritic unit measurements locate the samples in the fault core, in the relay zone, and close to the Alpine Thrust. Original scheme from Moore & Walsh (2021), based on Reiss (1980).

6.3. The main aquifers

Considering the geological results discussed in Chapter IV and the permeability considerations, three units will be considered as the principal aquifers: The Quaternary sediments, the Miocene unit, and the fractured granodiorite.

The alluvial Quaternary unit is the main extraction aquifer of the Vallès Basin area, with overexploitation at certain times of year (Mas-Pla, 2000).

The Miocene deposits have been previously described as a unique hydrogeologic unit constituted by a thick clay formation of more than 1500 m (IGME, 1984b). This unit acts as an aquitard with detrital levels of variable permeability, directly connected with the surface and through the slow-recharge aquitard unit. So, it can be defined as a group of 'poor' aquifers, sub-exploited due to its low permeability and, therefore, its low productivity. The S3 borehole, which crosses the entire column of Miocene sediments, shows that the aquifers located in the sand and conglomerate levels also recorded high temperatures. Even so, this water would be hot due to thermic conduction and not due to its geothermal origin (IGME, 1984a).

The fractured granodioritic unit constitutes the thermal aquifer. The open fractures allow the presence of the geothermal reservoir, defining permeable zones that drive the overall water flow. The discharge of the granodioritic aquifer, and thus, thermal hot springs, would be conditioned by structurally even weaker zones with a high degree of fracturing and weathering. These zones correspond to those described in Chapter IV as relay zones and fault intersections. N-S structures perpendicular to the VF has been presented as potential structures that coincide with valleys and rivers. These fault intersection points would act as vertical conduits, also allowing the formation of hot springs. On the other hand, the fact that thermal evidence is only found on one side of the N-S fault could mean that these structures also act as hydraulic barriers.

6.4. The hydrogeological functioning

The recharge area of the system has been previously set in the Pla de la Calma, in the Montseny Massif (Prelitoral Range), at 1200 m high, where the water infiltrates downward with a mainly-vertical flux, reaching significant depth and temperatures (Fernàndez & Banda, 1990; Mas-Pla, 2000; Santamaria, 2006).

The Prelitoral Range formed mainly by metamorphic materials, should act as an impermeable unit. However, some fracturing has been characterized in previous chapters, although far from the faults, it is inconsistent. This low permeability generated by fracturing and the with high rainfall degree in the area (IGME, 1984b), results in a piezometric level close to the surface. This condition favors the recharge area, creating a high piezometric gradient.

As the water level analysis is fundamental for understanding the hydrogeological dynamics of a system, we have carried out an analysis of the spatial distribution of the hydraulic level following the previous work carried out by Mas-Pla (2000). In addition to this previous interpretation, 772 water point data with chemical analyses and other hydrological data measured between 1968-2016 have been used to analyze the hydrogeological functioning. The *Centro Internacional de Hidrología Subterránea* has provided this data, which is presented in Figure 64.

In Figure 64, groundwater heads and isolines can be used to interpret the flux direction and the discharge. On the one hand, in the G-S area, the isolines indicate flux towards the SW, geometry influenced by the regional topography and, therefore, by the Congost river. And in CdM surrounds, the groundwater heads show a local anomaly close to the intersection between the VF and the N-S valley, which could be interpreted as a water barrier.

So, although the hydrogeological functioning is influenced by the main geological structures, which are vertical and related to a vertical flow, at shallow depths, this flow can be influenced by the topography and the N-S-oriented valleys and river courses.

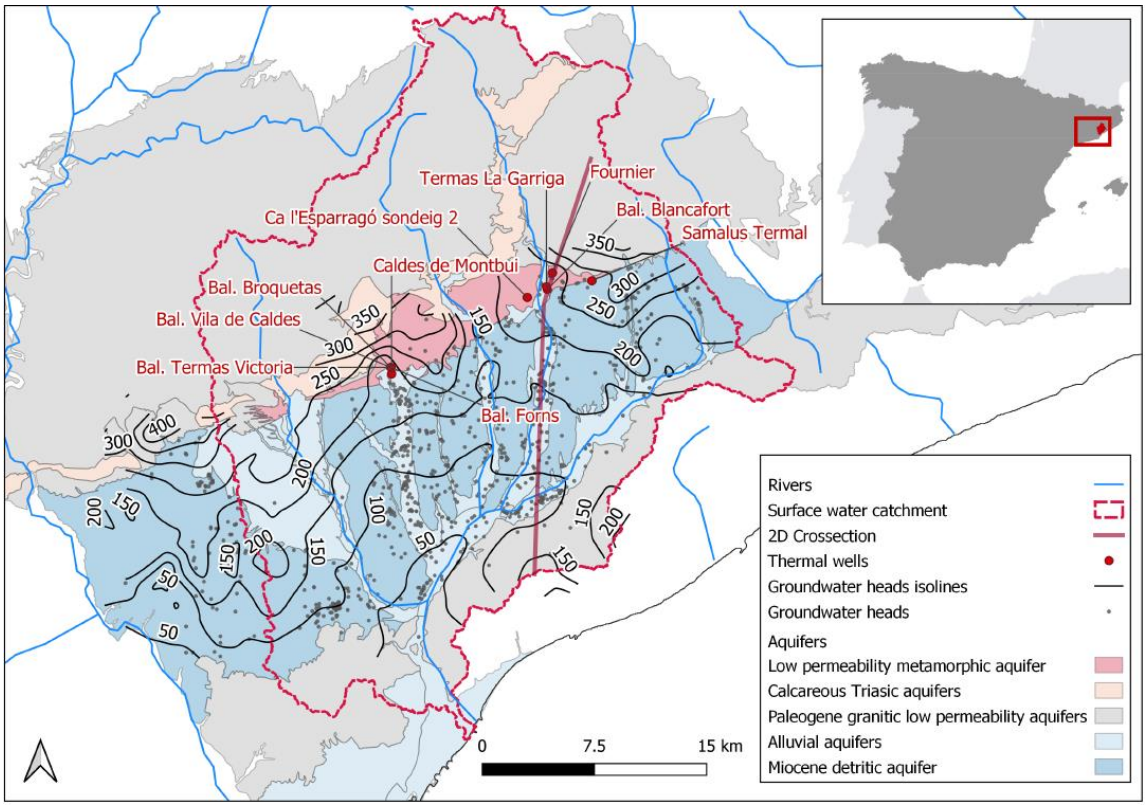

Figure 64. Groundwater heads and isolines in the Vallès Basin (Del Val et al., 2021).

6.5. Temperature analysis

In this section, the temperature gradient of the area and the system temperature are reviewed using the geothermal exploration boreholes data and their reports information (IGME, 1982, 1984a, 1986b).

Figure 65 shows the location of the boreholes in the new geological map and the temperatures measured. All the boreholes suggest anomalous temperature gradients. Even in the S3 borehole, which does not reach the basement unit, the temperature is high, which suggests that the proximity to the subjacent granodioritic unit could allow the heating of the Miocene aquifers.

The boreholes S1, S2, and S6 reach the highest temperatures and temperature gradients. These three boreholes are located in the relay zone's eastern margin, which was previously set as a maximum fracturing area.

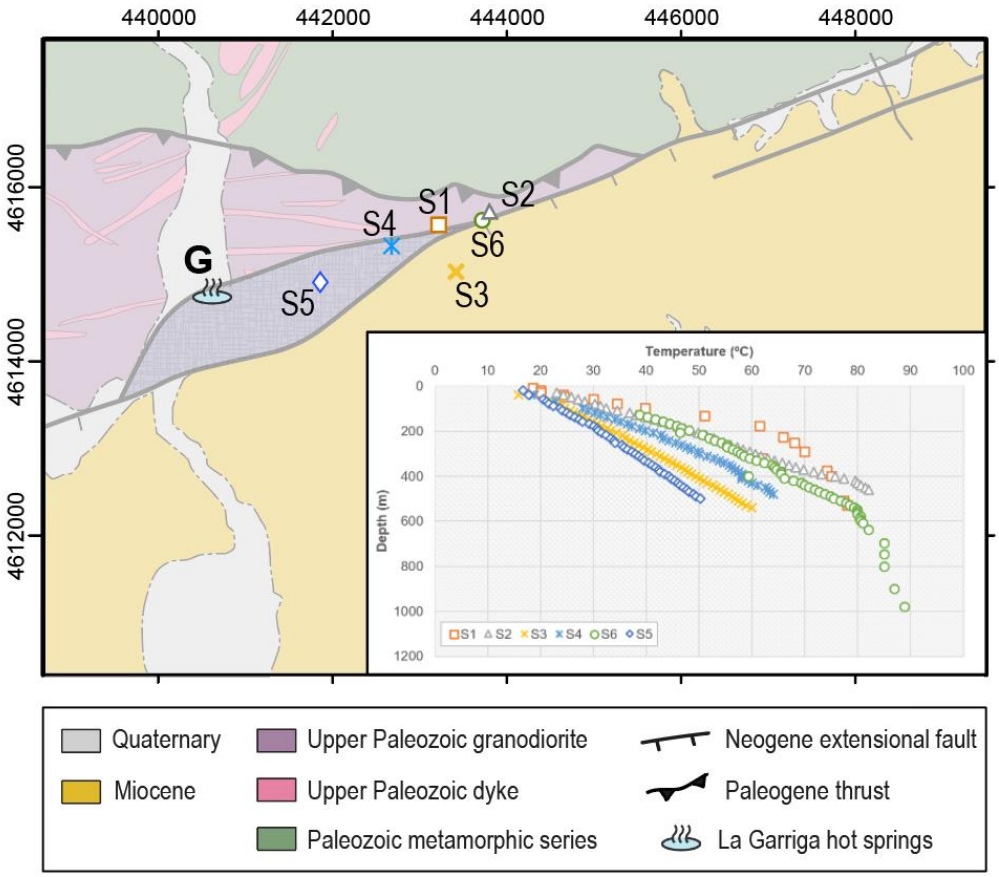

Figure 65. Geological map with the location of the IGME geothermal exploration boreholes and the graphs with the temperatures measured.

In Figure 66, the temperature data from the borehole's reports (IGME, 1982, 1984a, 1986b) have been plotted separately, distinguishing between basin and basement data. The differentiation of the data has allowed the detection that the temperature values fit a different type of regression line depending on the geological unit. For example, while the values measured within the Miocene

unit fit a linear regression, the values measured in the basement fit better to an exponential regression. However, the borehole S5, which has the lowest total gradient, also shows a better adjustment to a linear regression in the granodioritic unit.

Therefore, while the general heat flow may remain constant with depth, the thermal gradient is not necessarily linear. Moreover, nonlinearity in the geothermal gradient would be expected when there are variations in the thermal conductivity or permeability (Stranne & O'Regan, 2016).

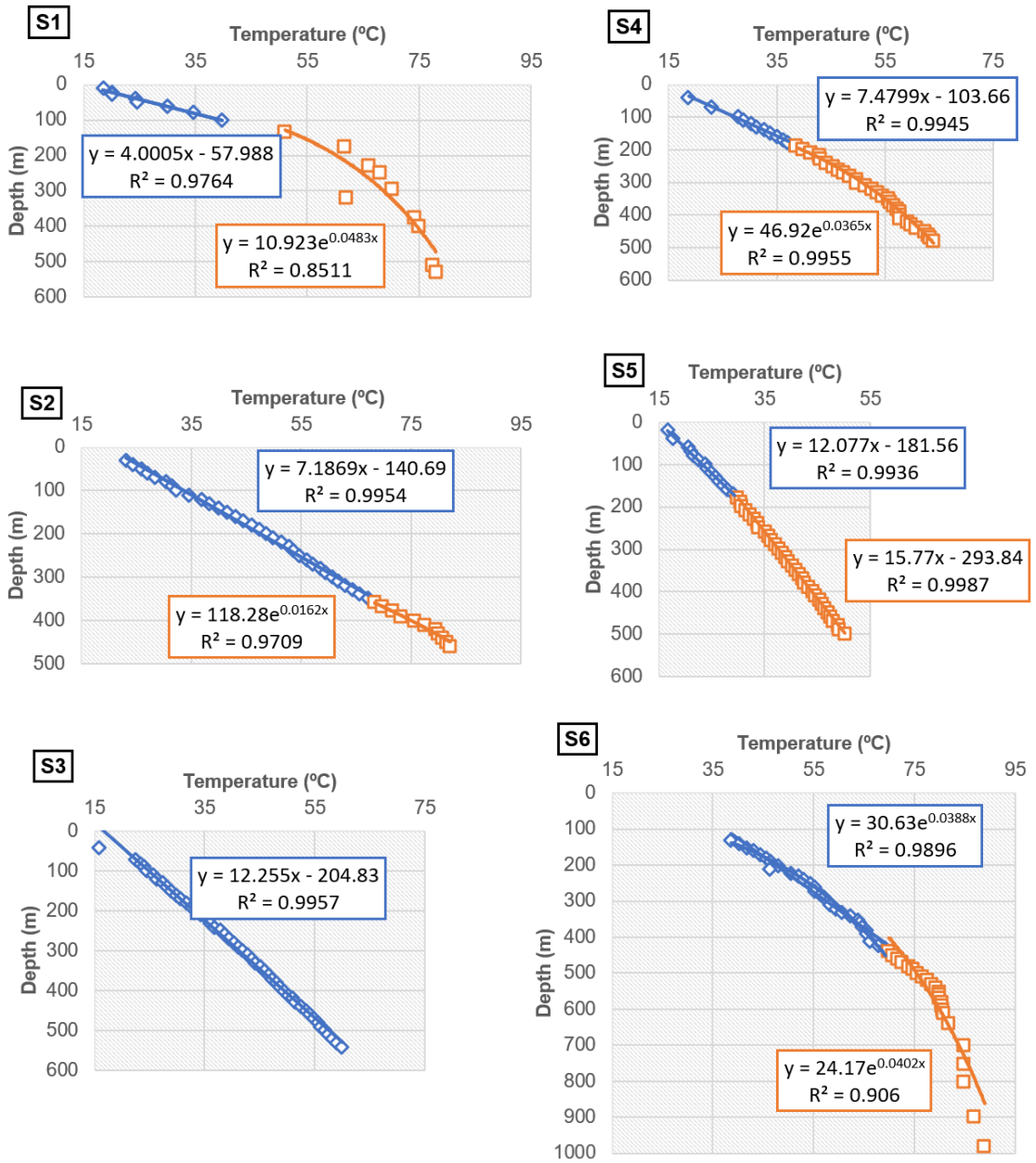

Figure 66. Temperature gradient for the IGME exploration boreholes (IGME, 1982, 1984a, 1986b). The blue data points are measured in the basin unit (mainly sandstones from the Miocene Vallès Basin) and the orange data points are measured in the basement unit (mainly fractured granodiorite and cataclasites from the late-Hercynian intrusion). Function parameters: y: depth, x: temperature.

The S6 borehole report also included a calculation of the system temperature using the fluid inclusions in fluorites and calcites (120-130ºC) (Figure 67), the thermodynamic study of the water-rock equilibrium (100-124ºC), and the analysis of the G-S thermal water solved gas (129ºC). All the results show similar values for the maximum reservoir temperature, which would be set between 120 and 130 ºC.

Considering the temperature gradient function for the basement part (orange data in Figure 66) of the S6 borehole, the system's maximum temperature would reach around 3500 m in depth, which could varies depending on permeability variations and ascend velocities of the water. However, the calculations made by Fernandez and Banda (1990), considering the forced convection system, match the results, setting the circulation of thermal water maximum depth around the 3000 m.

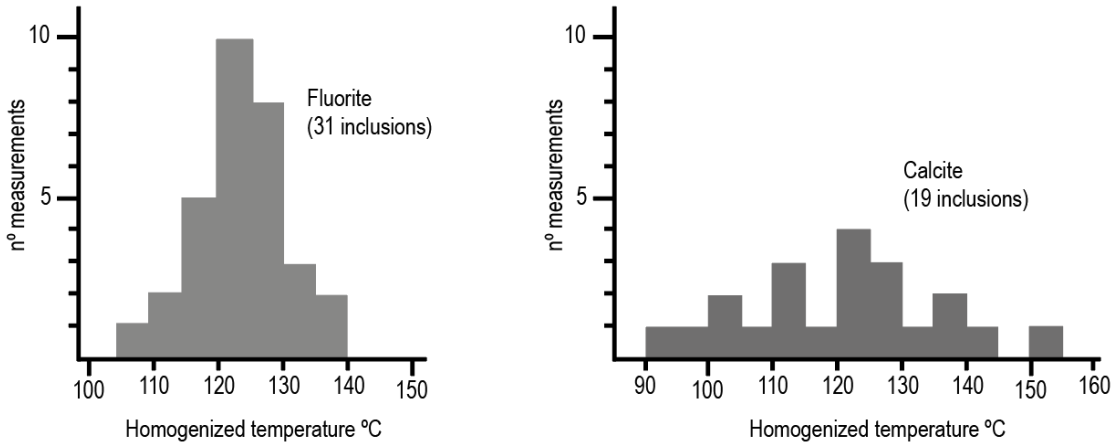

Figure 67. Homogenized temperature (liquid + vapor = liquid) of the fluids inclusions of the fluorite (left) and calcite (right) crystals from the borehole S6 (data from IGME, 1986) the homogenized temperatures of both phases (liquid and vapor) show a maximum in the fluorite inclusions between 120 and 130ºC. However, the calcite inclusions show bigger dispersions, with temperatures between 90 and 150ºC, probably due to the smaller number of measurements, but also attributed to the later recrystallizations of the crystals which may have modified the fluid density.

6.5.1. Thermal conductivity

During the S6 exploration borehole, the thermal conductivity of some samples was calculated (Figure 68). The results show a directly proportional tendency, with increasing thermal conductivities with increasing depths. However, there are some differences, mainly regarding the lithology of the analyzed unit. The extreme values correspond to the hydrothermal lamprophyre dyke unit (2.06 W/m·K) and the deep granodiorite (3.32 W/m·K).

Although at these depths, the thermal conductivity expected would be higher, previous works have shown how porosity (in this case, given by the degree of fracturing) can decrease these values (Schön, 2015).

These thermal conductivity results, which are quite homogeneous, confirm that the evolution of the thermal gradient would not be conditioned by notable changes in the granodioritic unit's thermal conductivity but by the hydrothermal system's convective dynamics.

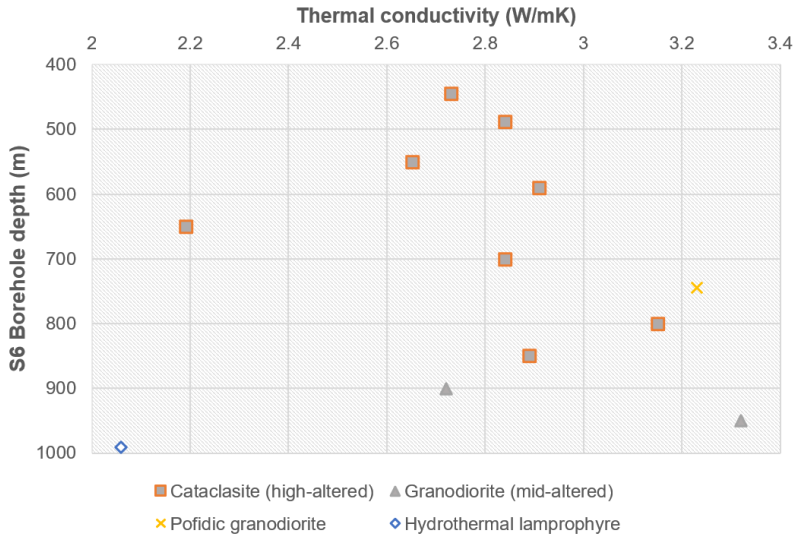

Figure 68. Thermal conductivity vs depth, for different lithological samples (data from IGME, 1986b).

6.6. Hydrochemistry

As mentioned in this chapter's introduction, the IGME project allowed the hydrogeological characterization of the system. Even so, later in 2006, Santamaria worked on the Vallès Basin geothermal systems, including a hydrochemistry characterization of the thermal waters.

The thermal waters of G-S are classified as soft waters, with sodium bicarbonate-chloride hydrochemical facies (Figure 69). They are weakly mineralized and have a high fluoride content. On the other hand, the waters of CdM are soft, with sodium chloride hydrochemical facies. These are classified as medium mineralized, and fluoride and lithium, among the minority components, are noteworthy.

The hydrochemistry described in the G-S area corresponds to the water-granitic rock equilibrium at temperatures equal to or higher than 100ºC (IGME, 1984b; Santamaria, 2006). On the other hand, the CdM waters would be affected by the infiltration or circulation through evaporitic materials. Therefore, these rock types could be related to the Triassic unit, which outcrops north of the granodioritic thrust sheet and exclusively in this western part.

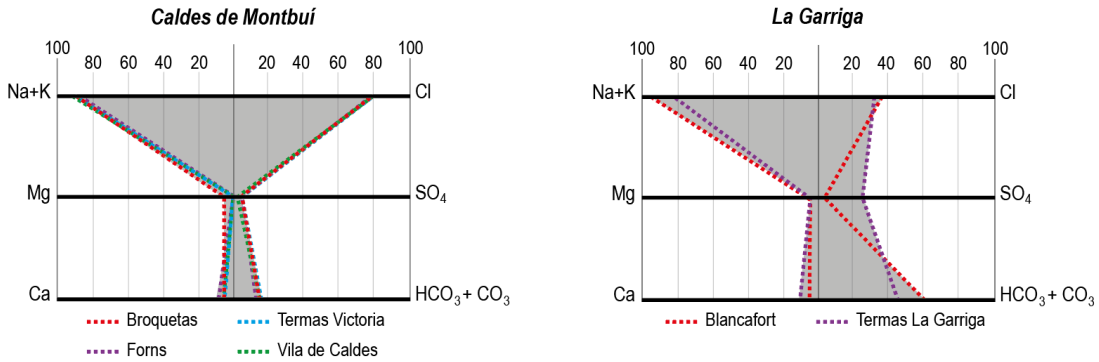

Figure 69. Hydrochemical facies from spas in the area of CdM (left) and (G-S) (right) (from López-Geta et al., 2002).

6.7. Discussion

The geothermal system behavior is similar to any other aquifer with related springs, but in this case, for groundwater heating, a deep circulation is needed. The differences in water temperature, and therefore, water density, causes the formation of a convective movement in the reservoir, which is the principal fluid movement controller. However, other parameters like porosity or fracturing can increase permeability and influence fluid circulation. This increased permeability is a key factor in normal-temperature gradient geothermal systems, as it favors the fast-upward flow circulation and also can favor the presence of thermal manifestations at the surface.

All the chapters in this thesis have highlighted the importance of the different geological units and the whole fracture system in the functioning of this geothermal system, but also in the presence of the hot springs in G-S and in CdM.

The circulation of the geothermal fluid would be conditioned by the main structures of the area, resulting in a main vertical water flux that takes advantage of the damage zone related to the VF. Locally, structurally weaker areas such as relay zones or fault intersections could favor the presence of fast conduits that allow higher temperature anomalies in both, CdM and G-S, breaking possible self-sealing caps and generating hot springs.

In addition, it has been observed that the N-S structures located in both subsystems, G-S and CdM, could also have an impermeable or retardant behavior (except for the intersection points with the VF); which could explain why the thermal evidence is only found on one side of the faults. Moreover, the chemical differences between the waters of the two subsystems could also indicate a differentiation during the ascent of the water, which is influenced by the local geology.

Near the surface, the flow may present some horizontal tendency controlled mainly by the topography, resulting in a hydraulic tilting towards the SW in the G-S area and the S-SE in CdM. This shallower flow would also be influenced by the N-S structures, as shown in the groundwater heads (Figure 64).

In conclusion, this chapter has defined the last parameters that allow to create the conceptual model of the Vallès Basin. Focused on the hydraulic system's functioning, it has also provided parameters to be considered for a future construction of a numerical flow model to test the conceptual model.

Part 4

Chapter VII
3D geological and geothermal models

Chapter VIII
Final discussions and conclusions

Chapter VII

3D geological and geothermal models

Chapter VII integrates all the previous data to build the conceptual geological and geothermal models that explain the thermal anomalies of the Vallès Basin region. Specifically, this section will show 3D representations of the geophysical and geological models created with *Leapfrog Geothermal*® software (*Seequent*) with some screenshot figures along the chapter. Moreover, a video with the 3D visualization of the data used and the final models is available at the following link: *https://youtu.be/CSkryuPnkIY*.

The 3D visualization of the models has allowed the experimental manipulation of the data to fit the model results better and finally interpret the geothermal system's functioning. Therefore, these models represent the first discussion and conclusions of the thesis, although some specific issues related to the main structure will be more widely detailed in the following chapter (Chapter VIII).

7.1. Conceptual model

The first step in creating the final geological and geothermal model is defining the imaging targets. Therefore, a preliminary conceptual scheme is essential to correctly image the area's geology and to choose meaningfully which geothermal units will define the system. So, in this first section, some of the geometries that may be relevant to creating the geological model will be discussed.

Considering the previous descriptions for the Vallès Fault (VF) in the MT-Vilamajor model, which is not distorted by the presence of two fault segments, we set the VF as a sub-vertical fault zone of a 65-70º dip. This fault is characterized by segmenting along the study area, where relay zones between segments are formed. These relay zones involve maximums of brittle deformation, which may have favored the formation of later structures, specifically, perpendicular structures (N-S) in the Caldes de Montbui and La Garriga river valleys. Even so, the whole granodioritic wedge is highly fractured and weathered, which is relevant to the functioning of the geothermal system, as this unit has been characterized as permeable.

In contrast, the metamorphic unit has different stress behavior. In contact with the VF and the AT, this geological unit forms a fault gouge in the fault cores and behaves more or less ductile away from the main structures. Therefore, it conditions the deep geothermal circulation, forming impermeable seals; and also, the recharge area characteristics, allowing the slow infiltration of meteoric water.

Figure 70 presents a simplified diagram of the Vallès Basin geothermal system functioning. In the Montseny massif's recharge zone, water infiltrates to great depths, taking advantage of the Prelitoral Range fracturing. The VF, previously defined as a cortical fault, acts as a deep connection with the surface, and the hot water from great depths takes advantage of the related damage zone to ascend. When this fluid reaches the intersection between the VF and the AT, which would have a joint root, it reaches the fault gouge, which acts as a seal-retardant. This seal causes the lateral detour of fluids, although there is also dispersed circulation upwards through the granodioritic unit. This lateral circulation would explain the increasing temperature towards the edges of the granodioritic unit in the borehole's records.

On the other hand, temperature maximum and hot springs are within the granodioritic unit, specifically in the highly deformed relay and fault intersection zones. These structures, caused by recent structural activity, would have broken the seal formed by the fault gouge, acting as vertical pipes. The fact that this system is seismically active is remarkably relevant to its functioning, as this causes the breaking of the hydrothermal self-sealing effect.

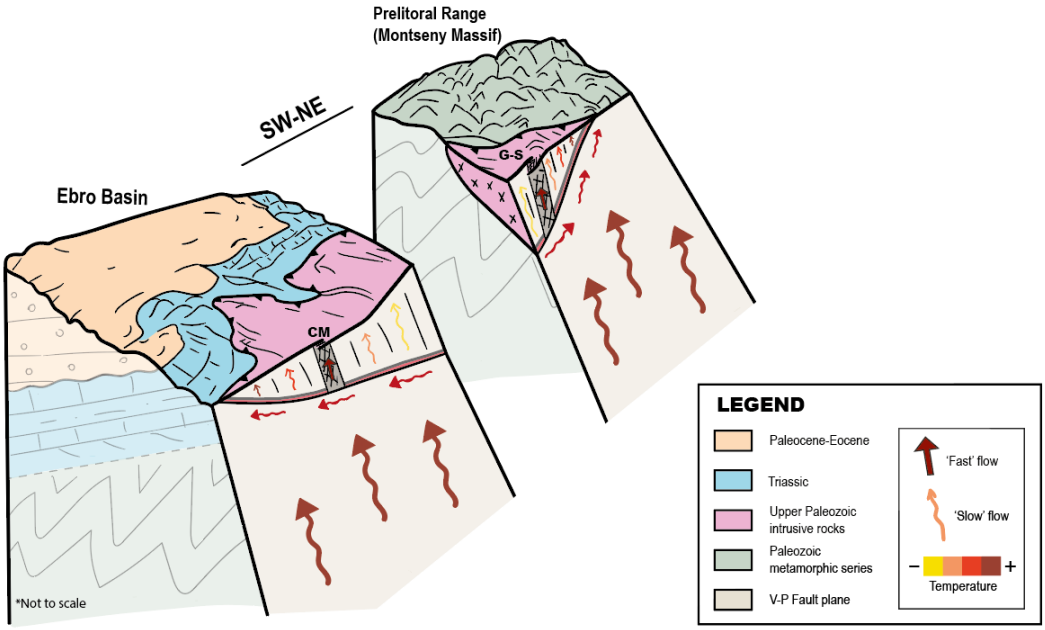

Figure 70. Vallès Basin geothermal conceptual model. The hot water ascends through the Vallès Fault's damage zone until it reaches the intersection between the Vallès Fault plane and the Alpine Thrust. In this intersection, the fault gouge act as a seal, causing the lateral detour of hot fluids. However, in some structural complexity areas, as in relay zones or where major faults intersect, these recent structures break the seal, acting as vertical pipes and allowing the upwelling of hot springs. This situation corresponds to the study locations, La Garriga-Samalús system (G-S) and Caldes de Montbui (CM).

7.2. Geophysical model

In this section, an integration of the geophysical data previously presented in Chapter III has been carried out. The residual gravity anomaly map, the MT resistivity profiles, and the HVSR basement depth data have been 3D-plotted together to observe how they correlate. These data are a significant starting point for creating the geological model, especially for defining the VF main surface and the basin-basement limit mesh.

Figure 71 shows a 3D view of the geophysical data. The gravity data is presented as the residual anomaly map plotted on the topography, although it could also have been represented with 3D points for a better qualitative analysis of the basin geometry. However, HVSR data results have been prioritized to create the final basin-basement mesh. This mesh represents the basal surface of the Miocene Vallès Basin.

The MT resistivity models could be imported as resistivity data or, as in this case, georeferenced cross-sections, allowing an easier and faster interpretation. Therefore, they have been used to constrain the basin-basement mesh, as the basin was also clearly imaged in the resistivity model; and as the deep primary information to define the VF plane and the related damage zone.

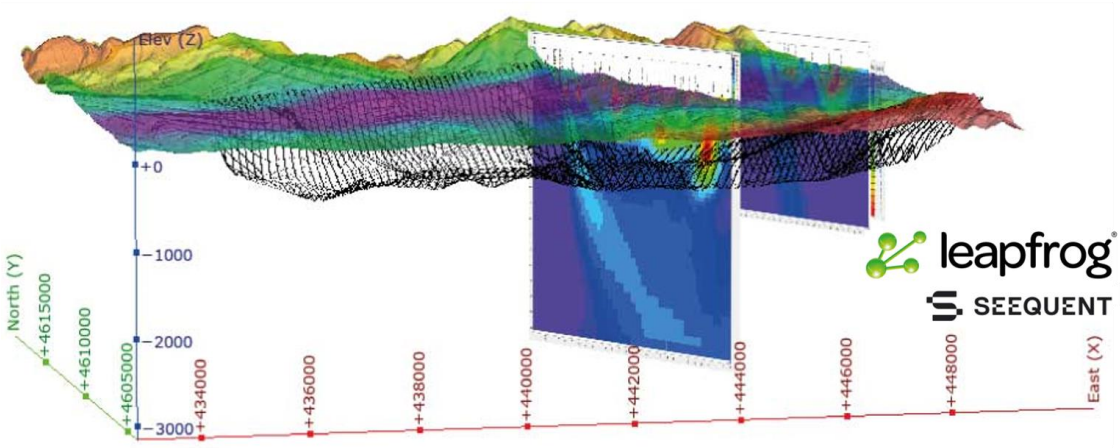

Figure 71. 3D representation of the geophysical data in Leapfrog Geothermal (by Seequent). The residual anomaly map is plotted above the topography; the MT profiles are presented as cross-section images, and the HVSR data is presented as an interpolated mesh.

7.3. Geological model

Three-dimensional geological modeling consists of inferring a realistic spatial representation of the lithological units of the studied domain and other relevant features, such as faults from sparse data and interpretations.

In this case study, 3D geological modeling has been carried out to visualize the Vallès Basin area. As seen in previous chapters, the geological units have an essential role in the geothermal system's functioning as they allow a better contextualization for the later thermal and hydrological interpretations.

In this thesis, the data used for the modeling mainly includes well data, GIS information, previous cross-section data, and the geophysical interpreted model.

First, the DEM mesh has been imported to limit the model at the top and to constrain the layout of geological structures and units in areas lacking information. As previously demonstrated, the topography analysis can give relevant information about the main structure's location and the geological unit’s limits. Moreover, all the previously available geological maps (ICGC, 2002, 2006; IGME, 1974; Santamaria, 2006) and the new interpretations have also been added to define the geological unit and structure's intersection with the topography.

For the subsurface modeling, the geophysical data has been set as the starting point, in addition to cross-sections and borehole data. The most profound borehole data is provided by the IGME geothermal exploration boreholes (IGME, 1982, 1984a, 1986a, 1986b); however, some other information from geotechnical reports has been included.

7.3.1. Geological/geothermal units

The different geological units have been defined, not only considering their lithology but rather considering their role in the functioning of the geothermal system (mainly conditioned by their hydraulic properties). To discern between units, the discussions presented in the geological, petrophysical, and hydrological chapters are considered.

From north to south, we will distinguish between the following units (Figure 72):

- ***Metamorphic series:*** These Paleozoic metamorphic rocks have been set as a low-permeable unit. Although there is some considerable fracturing in its proximity to the VF and the AT, it is quite heterogeneous and low-consistent. However, this low permeability is enough to condition the recharge area

- ***Metamorphic fault gouge:*** The Paleozoic metamorphic rocks, in contact with the main faults (VF and AT), generate a fault gouge. This fault gouge has been set as an impermeable unit.

- ***High-fractured granodiorite:*** Some areas of the granodioritic unit should not be underestimated, as they have an even higher fracturing rate than the rest of the bedrock. These zones are mainly located in fault intersections and relay zones. These complex structural zones are set as hydraulically competent, with permeability maximums. Therefore, they may be the leading cause of the functioning of the geothermal system and thermal hot springs at specific points in the area.

- ***Fractured granodiorite:*** The granodioritic unit (which includes the dykes intrusions) has a heterogenous hydraulic behavior, but it can be considered permeable. The fracturing variations concerning the primary fault distances, or the presence of non-weathered dykes, create different lenses with different permeabilities along the unit. However, the outcrops and the borehole samples evidence its high hydraulic capacities.

- ***Protocataclasite:*** the granodioritic unit in contact with the VF shows a 10 meters core of a protocataclasite described as a compact and impermeable rock. Although it does not have significant spatial relevance, this unit can be hydraulically critical, acting as a seal.

- ***Miocene-Quaternary sediments***: As mentioned in previous chapters, the Miocene and Quaternary sediments could be separated aquifers; however, in this model, we will consider that they have the same role in the geothermal system's functioning. The particularity of this unit is that the basal Miocene is formed by a retarding unit of clays that could almost be considered a seal. However, some shallow aquifers present higher temperatures close to the VF due to the temperature conduction effect close to the geothermal reservoir. So, although they are not thermal waters, their exploitation to harness the higher temperature areas could also be considered.

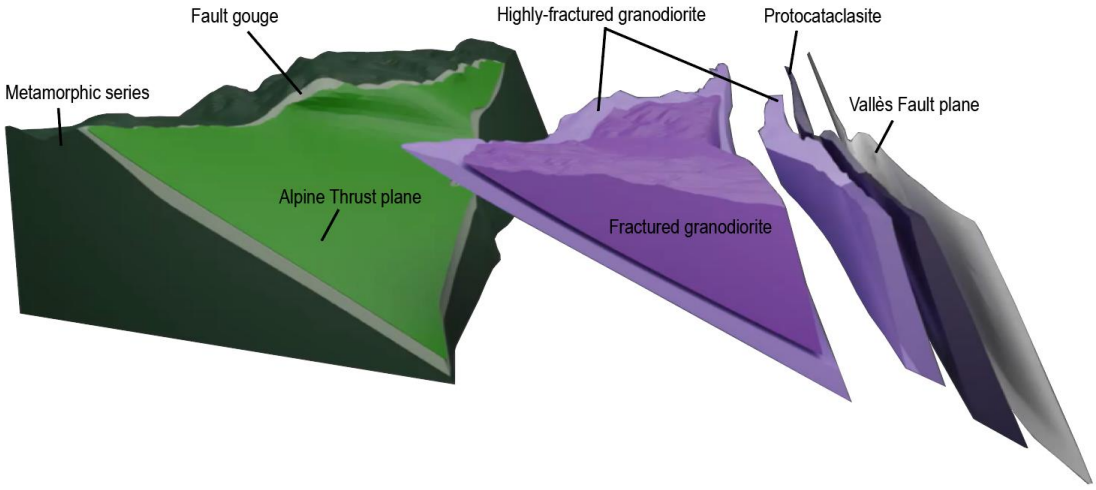

Figure 72. 3D model of the Vallès Fault footwall cut in a N-S section in La Garriga town. The main units that will define the geological model are set, together with the two main faults.

Therefore, the geological model has been built considering the geothermal role of each unit. The different geological and geophysical inputs used to discern between the main units (Figure 73), both at the surface and depth, are:

- ***Metamorphic series:*** Previous geological maps, the new geological fieldwork, and some geological sections of old reports. For the fault gouge limitation, we have used the thicknesses identified in the geological mapping fieldwork and the ERT-IP profiles.

- ***Granodiorite:*** Previous geological maps, new geological fieldwork, and borehole information. We have mainly used the fracture density characterization and the boreholes reports to differentiate between the sub-units (high-fractured/fractured/protocataclasite). For example, the relay zones have been set as a high-fractured granodiorite unit (see La Garriga relay ramp in Figure 73).

- ***Miocene-Quaternary sediments***: Previous geological maps and geophysical data. The primary data used comes from the HVSR data, the MT resistivity models, and the boreholes, which easily allows the generation of the mesh that defines the unit's base.

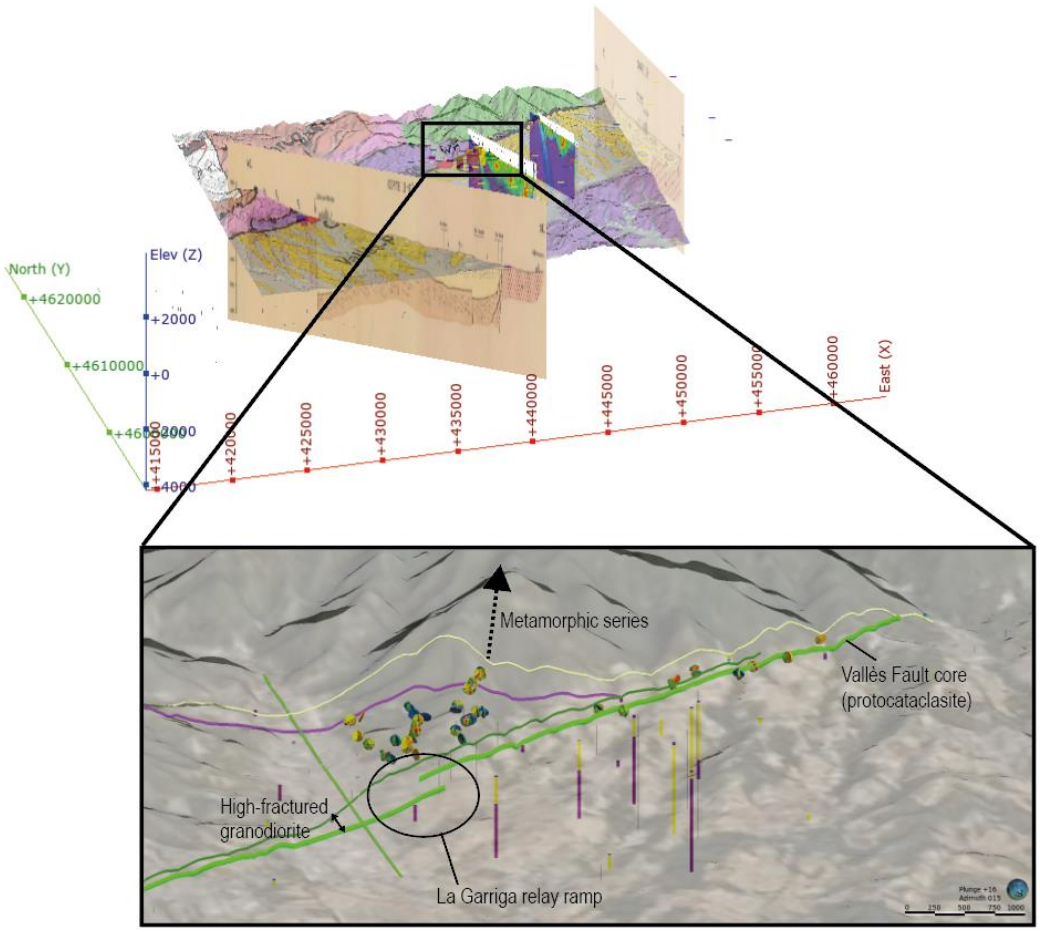

Figure 73. Some of the input data used for constraining the geothermal units (geological map, cross-sections, and geophysical model). The 'zoom-in' figure shows the La Garriga-Samalús area. Inputs like borehole information, fracture density limits, structural data, or lineament results, can be observed.

7.3.2. Geological structures

Faults are often complex, terminating in space rather than providing a reasonable domain boundary and surrounded by complex networks of brittle damage rather than being simple, neat planes. So, their accurate representation is one of the most challenging parts of geothermal modeling.

The interaction between faults and their chronology has to be defined for building a fault system. In this case, the two main geological structures, the AT and the VF have been modeled.

First, the previous geological map with the new variations has been used to generate the VF plane. Topographic elements such as slopes, valleys, or river course deviations have also been considered at the surface level. Moreover, MT models, boreholes, and earthquake hypocenters have been used for the in-depth extension of the plane.

The difficulty in modeling the VF is that it has been defined as a segmented fault. However, although some simplifications must be made, *Leapfrog* software provides a possible workflow to model finite faults with an interactive relay zone. In a simplified way, the creation of these segmented faults involves the construction of several finite meshes, extracting the points where the different segments overlap, and joining them together to form a final structure (Figure 74).

Second, geological maps, previous cross-sections, and structural data have been used to generate the AT plane. As there were some uncertainties about the trace orientation, we closely followed the data from previous geological maps and the topography interpretations.

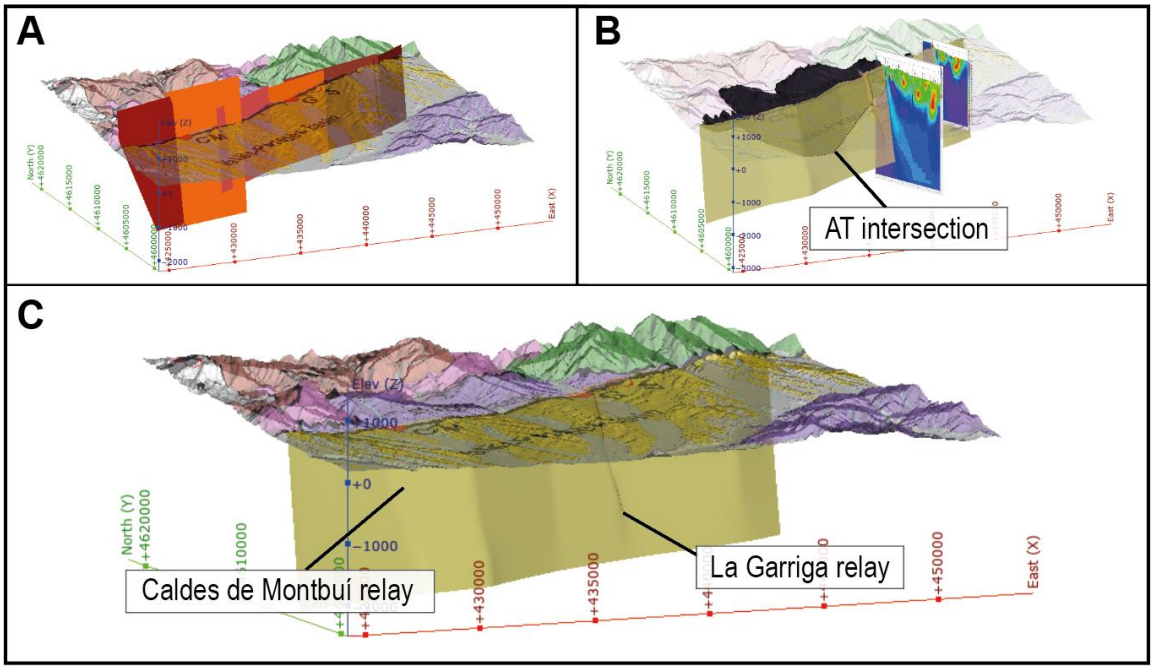

Figure 74. A) Finite faults segments to finally generate a unique fault plane. B) Final Vallès Fault (VF) and Alpine Thrust (AT) plane. The MT sections interpretation constraint the geometry of the VF mesh. C) Final VF, were the La Garriga and Caldes de Montbui relays can be appreciated in depth, as plane bends or irregularities.

7.3.3. Final geological model

Figure 75 shows the final volumes and surfaces created in a cut model through La Garriga town. This model presents the geothermal units described in section 7.3.1 with the main structures, the VF and the AT (7.3.2).

The main drawback of the geological modeling has been the need for more information in some parts of the study area. For example, although the input data covers the La Garriga-Samalús area, in the western part, close to Caldes de Montbui, there is a lack of information. However, the available results of this thesis have characterized the granodioritic thrust sheet as a relatively symmetrical structural unit. Therefore, the eastern part's geology and hydraulics data have been extrapolated to understand the system's functioning and build the complete geothermal model.

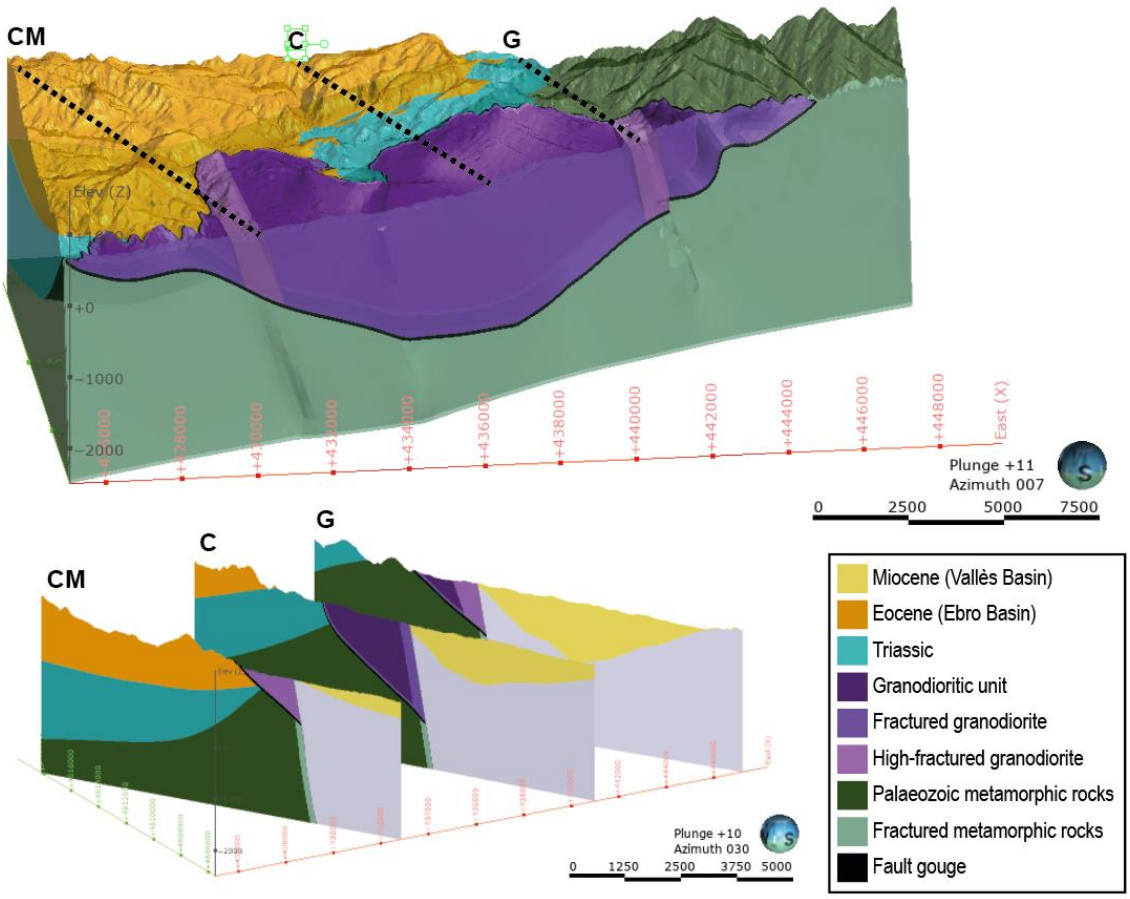

Figure 75. Geological model of the granodioritic thrust sheet area, between Caldes de Montbui and La Garriga towns. The 3D model only includes the footwall of the Vallès Fault, but in the cross sections the Vallès Basin is also represented.

7.4. Temperature model

In addition to the geological model, *Leapfrog Geothermal* can create numeric models from a wide array of data. In this case, borehole information has been used to create a temperature model. The main drawback of this chapter has been the availability of data and their irregular distribution. Most of the temperature information are quite shallow, except for the IGME geothermal exploration boreholes (IGME, 1982, 1984a, 1986a, 1986b), although they are only localized or in Caldes de Montbuí or in La Garriga-Samalús towns (Figure 76).

Leapfrog Geothermal uses the fast-radial basis function algorithm (FastRBFTM) to build numeric models. The interpolant function and the related parameters control the relationship between the known points values and the estimated ones so that each possibility will produce a different fitted model (Seequent Limited - a Bentley Company, 2021). Therefore, selecting an adequate interpolation function and parameters that make the more geological and geothermal sense is essential.

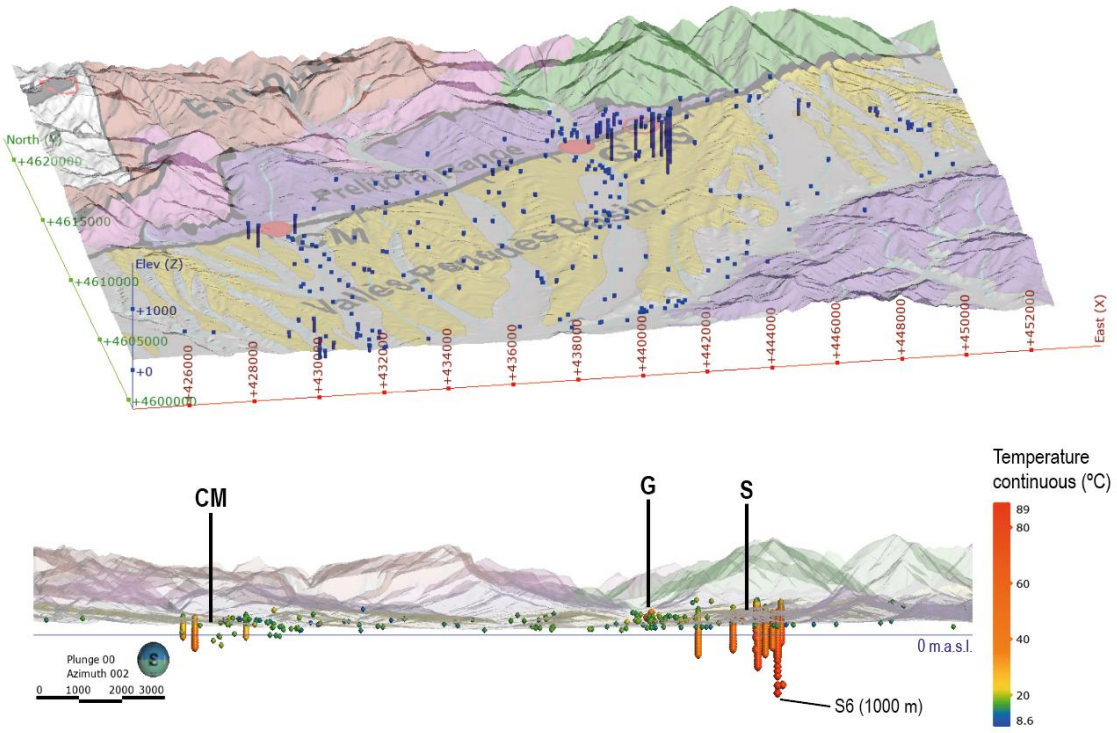

Figure 76. Schematic map and section with the temperature data from boreholes. The deepest information is from the geothermal exploration boreholes made by the geological survey of Spain during the 80's. These boreholes are located in Caldes de Montbui (CM) town, and in La Garriga (G) and Samalús (S) region.

In this case study, the conceptual model previously presented (7.1) can be relevant as a good understanding of how the geothermal system works and, therefore, will justify the correct selection of the different interpolant functions and parameters.

Leapfrog Geothermal uses two main interpolant functions, the linear interpolant, and the spherical interpolant. The linear interpolant function assumes that known values closer to an unknown point have a proportionally greater influence than points that are further away. As a result, the calculated estimations strongly reflect values at nearby points, which can be helpful for a general purpose or in cases with sparse and irregular sampling. In contrast, the spheroidal interpolant is for cases with a finite range beyond which the influence of data should fall to zero (Seequent Limited - a Bentley Company, 2021).

In this case study, we have chosen the linear interpolant as it will give the best results for temperature models and is also the easiest to use for this purpose.

7.4.1. Temperature units

In order to represent the temperature variations in the study area, the model has been divided into different temperature sub-volumes. This subdivision's main advantage is the possibility of adjusting the interpolation parameters to smaller areas and better fitting the interpretation presented in the conceptual model (7.1).

The volumes defined are conditioned by the different temperature interpolations, and they will be created as *Combined models* in *Leapfrog Geothermal*, which means that they will also be reliable to the geothermal units previously defined (7.3.1):

- **T1** and **T2**: VF damage zone related to the Paleozoic basement materials (T1) and the granodioritic unit (T2). For these volumes, a linear temperature increase will be used, with a higher temperature gradient than the not-fractured units.

- **T3:** Vertical pipes in structural complexity areas, represented by the high-fractured granodiorite. The main fault's intersection and relay zones favor the direct ascend of hot water and the seal break.

- **T4**: Fault gouge, which acts as a seal and separates the temperature model between T1 and T2.

- **T5**: Rest of the granodioritic unit, which is less fractured.

- **T6**: Rest of the Prelitoral Range units, which include the Paleozoic metamorphic unit, the Triassic unit, and the Eocene unit.

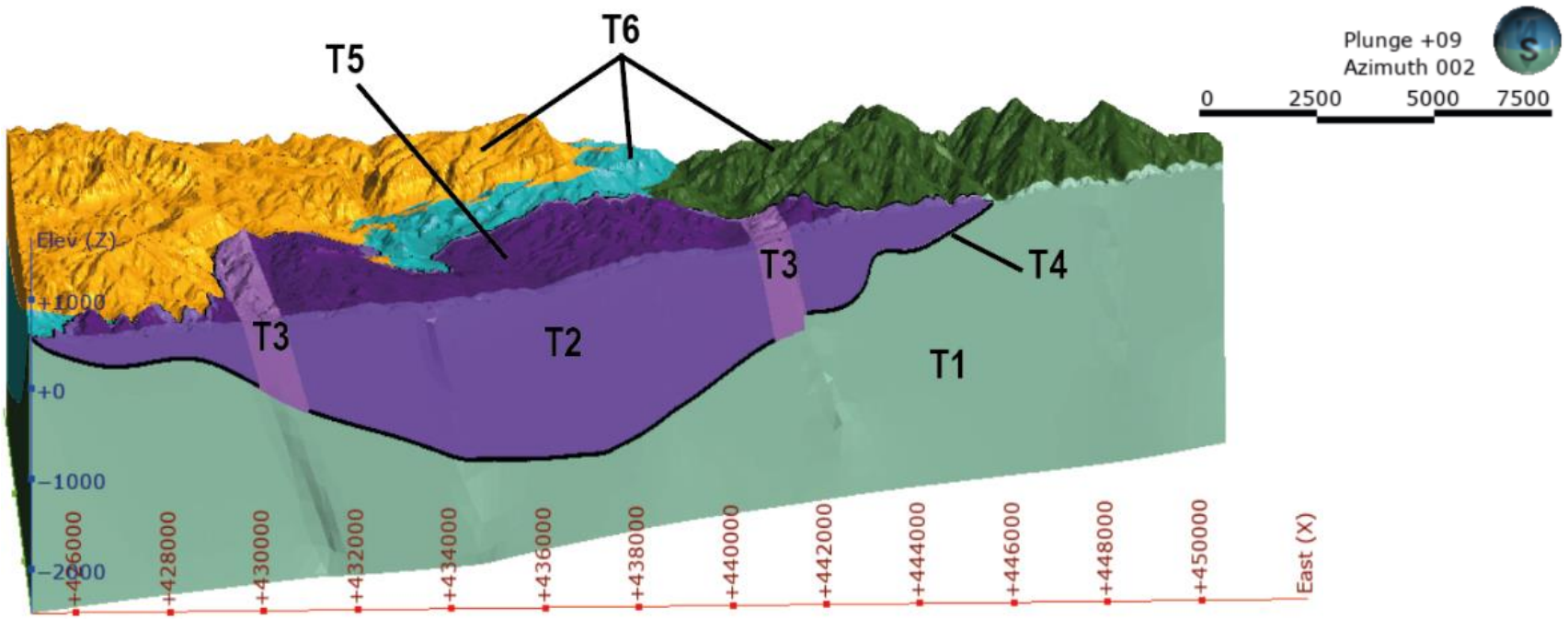

Figure 77. Geothermal units with the selected temperature volumes. T1: Damaged metamorphic Paleozoic; T2: Damaged granodiorite; T3: Highly-damaged vertical pipes in structurally complex zones; T4: Fault gouge; T5: Granodiorite; T6: Metamorphic Paleozoic unit (dark green), Triassic unit (blue), and Eocene unit (orange).

7.4.2. Final temperature model

Figure 78 presents the VF damage zone sub-volumes (T1, T2) and the structural complex zones (T3) with the interpolated temperature.

The general tendency shows a linear temperature increasing towards the surface; however, the isotherms change their geometry inside the granodioritic body. The differences between the isotherms inside the granodioritic thrust sheet evidence the effect of the fault gouge, which limits both zones. Moreover, inside the granodioritic unit, the two temperature peaks correspond to the relay zones and the hot springs locations, Caldes de Montbui and La Garriga.

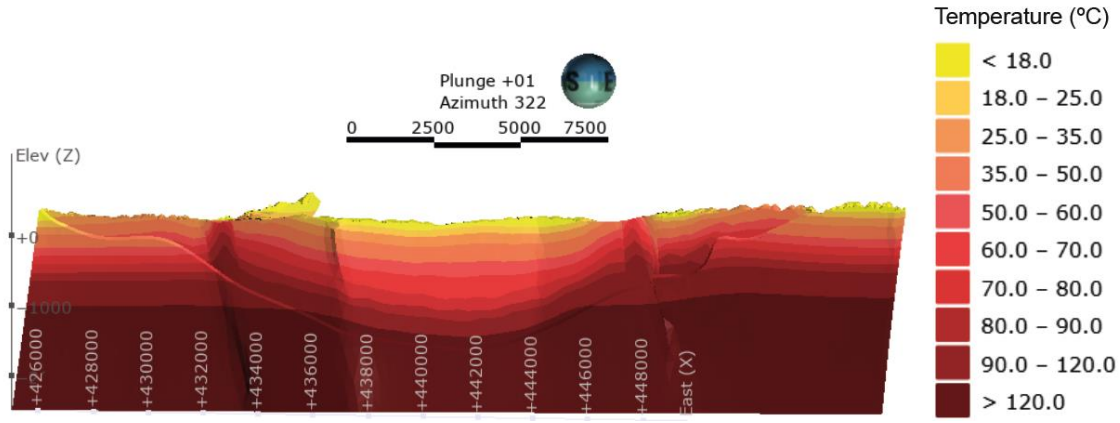

Figure 78. Temperature model of the Vallès Fault damage zone. This model is divided in three subzones: the granodioritic unit, the structural complex areas (vertical pipes in the granodioritic unit), and the metamorphic bedrock.

The rest of the granodioritic body, which corresponds to the temperature unit T5, has also been interpolated using a linear function but adding a structural trend, the VF. Therefore, although the isotherms will follow the boreholes data and the linear interpolation function, there will be a general tendency to increase temperatures toward the fault plane. This increasing tendency would be related to the dispersed circulation of thermal water and temperature conduction. Figure 79 shows the final temperature model with the two main tendencies. First, in an orientation parallel to the VF plane (A), the model shows increasing temperatures towards the principal hot spring locations, Caldes de Montbui and La Garriga. In the perpendicular section (C), the temperature gradient increases towards the VF plane.

For the resting unit (T6), the temperature interpolant has been set to linear without any modification or trend. However, some isotherms have been slightly corrected to coincide with the adjacent volumes. Therefore, the resulting model shows continuity between the temperature units without abrupt changes.

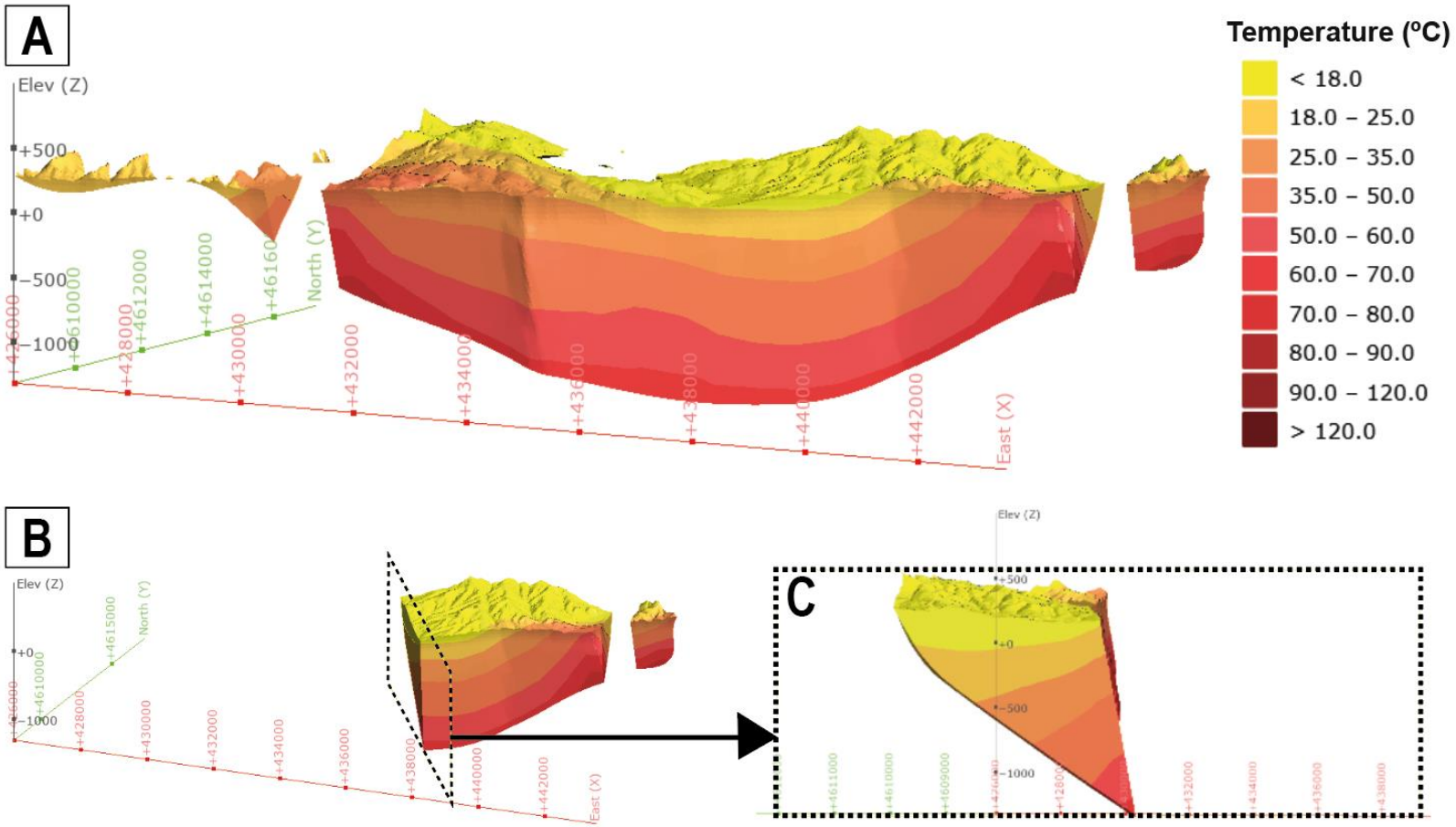

Figure 79. Temperature model for the granodioritic thrust sheet (less fractured) which corresponds to the sub-volume T5. A) Total volume, the gaps in the edges of the body are the vertical pipes volumes corresponding to Caldes de Montbui and La Garriga locations. The temperature increases towards these structural complexity zones. B) Granodioritic volume cut in the middle to show a cross section temperature model. C) Cross section in the middle of the volume which show the slight increasing towards the Vallès Fault plane.

7.4.3. Planned wells

An efficient well placement strategy requires detailed information about the reservoir's structure, geometry, and petrophysical and hydrothermal properties (Norrena & Deutsch, 2022). Preferential flow paths, such as faults and fractures, can influence the borehole placement strategy, as they often form effective fluid pathways that naturally enhance the thermal gradient and fluid flow. When faults are the main fluid pathways for fluid circulation, the characterization of permeability and permeability anisotropy directions are crucial for productivity (Daniilidis et al., 2021).

On the other hand, fault zones may have associated seismicity, which, although minimal and imperceptible, could cause social and political unconformity. In this structural context, incomplete knowledge of fault structures and stress heterogeneities within highly complex fault systems would challenge the degree of predictability of induced seismicity related to underground fluid injections or extractions.

Therefore, although there needs to be more information to choose where to position the geothermal exploitation boreholes, several tests have been performed using a *Leapfrog* tool for hypothetical imaging cases.

Figure 80 shows an example of two drilling prognoses in both locations with hot springs, Caldes de Montbui and La Garriga towns. Both localities show similar results, with slightly higher temperatures in Caldes de Montbui, as expected considering the temperature of hot springs.

In both cases, the boreholes could reach 100ºC at 1 km depth, which set them as exploitable areas. However, more confirmation studies like fluid flow numerical modeling or seismic risk studies should be performed.

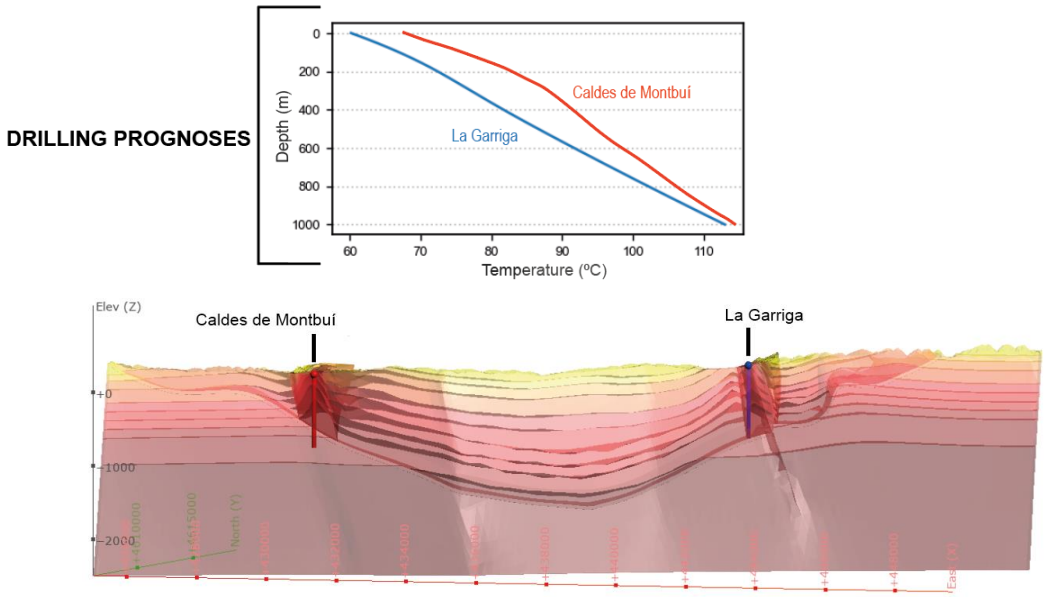

Figure 80. Drilling prognoses of two vertical wells located in La Garriga and Caldes de Montbui towns.

Chapter VIII

Final Discussions

The previous chapter has shown the results in the form of geothermal models, representing this thesis's first discussions and conclusions. However, in addition to that, other issues, mainly involving the structure of the study area, should be further discussed.

So, in the first section of this chapter, we present the integration of all the interdisciplinary results of the different thesis parts to discuss the main structural aspects ruling the functioning of the geothermal system under study. And finally, the conclusions presented, highlighting the fulfillment of the thesis goals through this multidisciplinary applied methodology and its potential to be extrapolated to similar structural context geothermal systems studies.

8.1. The Vallès Basin structural context

The present-day structure of the Catalan Coastal Ranges (CCR) predominantly reflects normal faulting arising from Neogene extensional tectonics, which post-dates and cuts Paleogene structures developed during compressional Alpine deformation (Marcén et al., 2018). Previous authors investigating the structural evolution of the CCR have suggested that the Vallès Fault is the result of the negative inversion of thrusts during Neogene extension (e.g., Anadón et al., 1979; Fontboté, 1954; Roca et al., 1999) but there is no consensus regarding the geometric relationship between the Alpine Thrust (AT) and the Vallès Fault (VF).

Although some geometric structural aspects have not been defined at great depths, the structural and deformation characteristics of the outcrops have allowed a better understanding of the functioning of the geothermal system, which is clearly influenced by the structural context of the area.

8.1.1. Vallès Fault geometry and related deformation

Constraints from mapping and geophysical data indicate that the VF has a trace length of 100 km and a maximum displacement of around 5 km (Bartrina et al., 1992; Gallart et al., 1997; Gaspar-

Escribano et al., 2004; Gómez & Guimerà, 1999; Juez-Larré & Andriessen, 2006; Roca et al., 1999; Roca & Guimerà, 1992; Sàbat et al., 1995; Vidal et al., 1995), scaling properties that are consistent with existing empirical constraints for normal fault (Nicol et al., 2020). The main fault dips, from geophysical and borehole results, are quite consistent, between 60º and 70º.

Lateral changes in displacement along the VF are supported by lower displacements in the study area (< 3 km), the presence of exposed fault tips at either end of the fault, the basin narrowing towards the NE and SW, and evidence on seismic profiles for a decrease in the basement depth towards the NE (Roca, 1992). Moreover, towards the eastern tip of the VF, the prevailing hangingwall topography also dips towards the SW, with associated river systems sourced directly from the footwall mountains in the north and curving towards the SW in the south.

Although the mapped trace of the VF is relatively simple on regional scale maps, closer examination indicates that it is characterized by fault bends and steps that are developed at and below km-scales. Specifically, at Caldes de Montbui town, towards the eastern limit of the VF, the trace is marked by non-aligned linear segments connected by fault bends. A very similar structure has been defined in the La Garriga relay zone, which has a width of 650 m and an overlap length of 2000 m, consistent with the scaling relationship of relays along large faults (Fossen & Rotevatn, 2016).

Combining the displacement and relay dimensions, and comparing them with empirical quantitative constraints of large published relay databases, strongly suggests that the relay is breached and, most likely, doubly breached to form a lenticular zone of fault-related deformation because the rapid transfer of 1.5 km scale displacements is not compatible with an intact relay at that 1-2 km scale. Our work also indicates that relay breaching promotes the fracturing of adjacent granodioritic host rocks, in particular, circumstances that provide a means of generating steeply inclined pathways along the relay axis (Fossen & Rotevatn, 2016; Walsh et al., 2018). Specifically, the analysis of the La Garriga relay highlights the intense fracturing associated with the fault zone, in which faults that are parallel and perpendicular to the main VF provide a basis for generating a fracture network which is the locus for fluid flow.

8.1.2. The Vallès Fault and Alpine Thrust geometrical relation

Based on the structural evolution of the area and the geometrical characterization of the main structures, we propose two alternatives for explaining the current spatial relationship between the AT and the VF.

First, the current configuration of both faults could simply arise from a later normal fault offsetting a previous shallow dipping thrust, which is therefore, only exposed within the footwall of the normal fault but would have a deeper expression within the hangingwall fault block. An

alternative model is that the AT is a footwall short-cut structure arising from the inversion of any pre-Tertiary expression of the VF.

Distinguishing between these models is not easy given the available constraints; however, as the AT does not appear to steepen and root into the VF, a cross-cutting relationship is favored, which has been the option used for the creation of the Chapter VII models.

Whichever of these models is correct, both involve a deeply rooted normal fault extending into the basement, circumstances which promote the emergence of high enthalpy geothermal systems developed along the VF.

8.1.3. The role of the seismic activity

Although the Paleogene and Neogene tectonic evolution of the CCR has been well studied, there are much fewer constraints on the Pliocene and Quaternary tectonic evolution of the region (Masana, 1996). The general consensus is that the main phase of normal faulting in the Vallès Basin began in Late Oligocene times, at the latest, and continued into the Late Miocene (Tortonian), particularly along the VF (Bartrina et al., 1992; Roca et al., 1999). Thereafter, decreases in across-fault sequence growth have been attributed to the predominance of late rift-related thermal subsidence and sedimentation, and the accommodation of lower rates of crustal extension, principally by the cessation of movement on most faults and a decreased level of fault activity along the larger faults, such as the VF and the Barcelona Fault, until the present day (Masana, 1994, 1995; Roca et al., 1999).

Despite this relatively low seismicity activity in the CCR, the VF earthquake history provides support for fault reactivation and associated fluid circulation, a scenario we must consider in the context of this geothermal system study. Specifically, these active fault characteristics are similar to faults from which seismic pumping models of fault-related fluid flow have been advanced (Muir-Wood & King, 1993).

Seismic pumping involves the inter-seismic accumulation of dilations due to fracturing and poro-elastic effects within host-rock volumes surrounding normal faults. Seismic deformation is then marked by the imposition of compressional strains subscribing to elastic dislocation theory which involves the expulsion of considerable volumes of fluid during individual earthquake events (Sibson, 1993). While this model could make an important potential contribution to the hydrodynamics of the Vallès Basin, it does not, on its own, provide a rationale for the localization of flow along the VF itself. However, the studies presented in this thesis could favor the hypothesis of a seismic pulsing fluid flow that is strongly localized along the main faults and relay zones, as proven by the characterization of the main deformation and its hydraulic behavior.

8.2. Further reasoning behind the Vallès Basin conceptual model

The development of geothermal systems adjacent to faults within extensional basins is a well-established phenomenon (Curewitz & Karson, 1997; Fairley & Hinds, 2004; Sibson, 1993; Walsh et al., 2018). Crustal thinning is accompanied by increases in geothermal gradient and the potential for the deeply penetrating convective flow systems with a hydrodynamic system supplied by the downward ingress of groundwater through faults, syn-rift, or hydrostatically pressured basement. However, while the sinking of fluids would be facilitated by increases in salinity, analysis of the thermal waters at the La Garriga region does not suggest the presence of heavy brines. Specifically, the Vallès Basin migration pathways in the recharge area are unclear, with south- to southwestward migration pathways from footwall Paleozoic metamorphism/granodioritic and Triassic units.

Even assuming the cessation of fault slip along the VF in Pliocene to recent times, the basin will retain much of the syn-rift hydrodynamic regime, including structural, thermal, and pore-fluid pressure drives. One of the principal mechanisms for up-fault flow is fault valving which is exclusively driven by the migration of higher pressure (i.e. deep and warmer) fluids when fluid pressures lead to mechanical failure of fault seals, a scenario that can occur within basins that are not tectonically active (Phillips, 1972; Sibson, 1993; Walsh et al., 2018). Another potential mechanism is even simpler insofar as it requires passive up-fault flow along preferred flow conduits at rates that match the build-up of fluids at depth. Whichever combination of models applies, the basic requirement for structurally controlled flow localization at particular sites is the complexity and heterogeneity of structure. What this study has shown is that hydrothermal fluid flow is developed preferentially towards the intersection of an AT and the VF. The basic configuration and trace of this thrust suggest that its intersection line with the normal fault will plunge towards the center of the fault away from the mapped branch points, a scenario that will lead to preferential flow towards the ends of the thrust. Perhaps more importantly for the La Garriga geothermal system, a major step in the VF is characterized by accentuated fault damage, veining, and fluid flow. This setup is consistent with evolutionary models for the growth and breaching of relays, which are often considered to be the locus for up-fault fluid flow (Fossen & Rotevatn, 2016; Kyne et al., 2019; Rotevatn et al., 2009). The importance of this structure is clearly reflected in the thermal structure of the area and accentuated porosity and permeability arising from higher density fracture systems and meshes, providing conduits for the upward flow of hydrothermal fluid, which in the study area provides groundwater of 60ºC, with recorded downhole temperatures of up to 90ºC at depths of 1 km (IGME, 1986).

Conclusions

The work presented in this thesis develops an innovative multidisciplinary methodology focused on exploring a fault-controlled geothermal system. This practice has been built around two central cores, geophysical exploration and fracture characterization.

In the first methodological part, the geophysical exploration (Chapter III) has allowed the identification of the main geological structures which form the study area and the main reservoir and fluid circulation channels. More specifically, it has been shown that electrical and electromagnetic methods can also play a crucial role in low- and mid-temperature systems.

Secondly, the geological investigations, mainly focused on a good characterization of the major and minor structures (Chapter IV), have been crucial in showing how structural complexity can influence the system's functioning. So, not only the presence of a crustal fault such as the Vallès Fault conditions the presence of this geothermal system, but the presence of other overlying structures, complex zones, and recent tectonic activity also favors it.

These initial results have allowed the carrying out of more detailed studies, which include petrophysical (Chapter V) and hydrological (Chapter VI) considerations, as well as the contextualization with previous data, to finally create the geological and geothermal models (Chapter VII).

8.3. Geophysical exploration

The integration of complementary geophysical methods has resulted in a good option for the preliminary stages of geothermal system exploration, especially due to its application in an urban area. In this thesis case of study, the integration of magnetotellurics, electrical resistivity tomography, passive seismic, gravity, and induced polarization methods have allowed the identification and characterization of the geological units and structures that control the geothermal system.

Specifically, the geophysical methods employed have been useful in delimitating the different geological units and setting the Vallès Fault zone as the main path for the hot fluids. Moreover, the geophysical characterization established a new geometry for the Miocene Vallès Basin, which presents a stepwise morphology with an increasing thickness towards the center of the basin.

These results have evidenced that, although warm water may create an insufficient physical contrast in some geothermal systems, the appropriate use of geophysical techniques can still be helpful for the structural characterization of medium and low-temperature geothermal systems.

8.4. Geological exploration

By developing a multiscale and multidisciplinary methodology, this thesis has put together traditional geoscientific techniques and new digital visualization tools to characterize each geothermal unit. Moreover, a good geological characterization, primarily focused on the outcrop fracturing study, has been a key point in understanding how the geothermal units can behave in-depth and influence the fluid flow circulation.

One of the main conclusions of this geological part has been identifying and highlighting the importance of structurally complex zones, such as relay zones or fault intersections, which can significantly influence the presence of a geothermal system.

This characterization could be improved for future perspectives by extending the study area to Caldes de Montbui and acquiring deeper borehole data. Even so, the urbanization of the area and the few outcrops difficult the procedures.

8.5. Integrated methodology and modeling

The whole thesis consists of an interdisciplinary assessment where each chapter is focused on a different geoscientific technique valuable for geothermal exploration, ending with the integration of the results, where the geological and geothermal models for the Vallès Basin case of study are presented (Figure 81).

This study's key point has been using different types of information and, at multiple scales, including traditional and new tools. The proper integration of all the results gives a better view of how the geothermal system works, helps to define the role of the different geological units in the system, and proposes a methodological example to be applied in systems of similar origin.

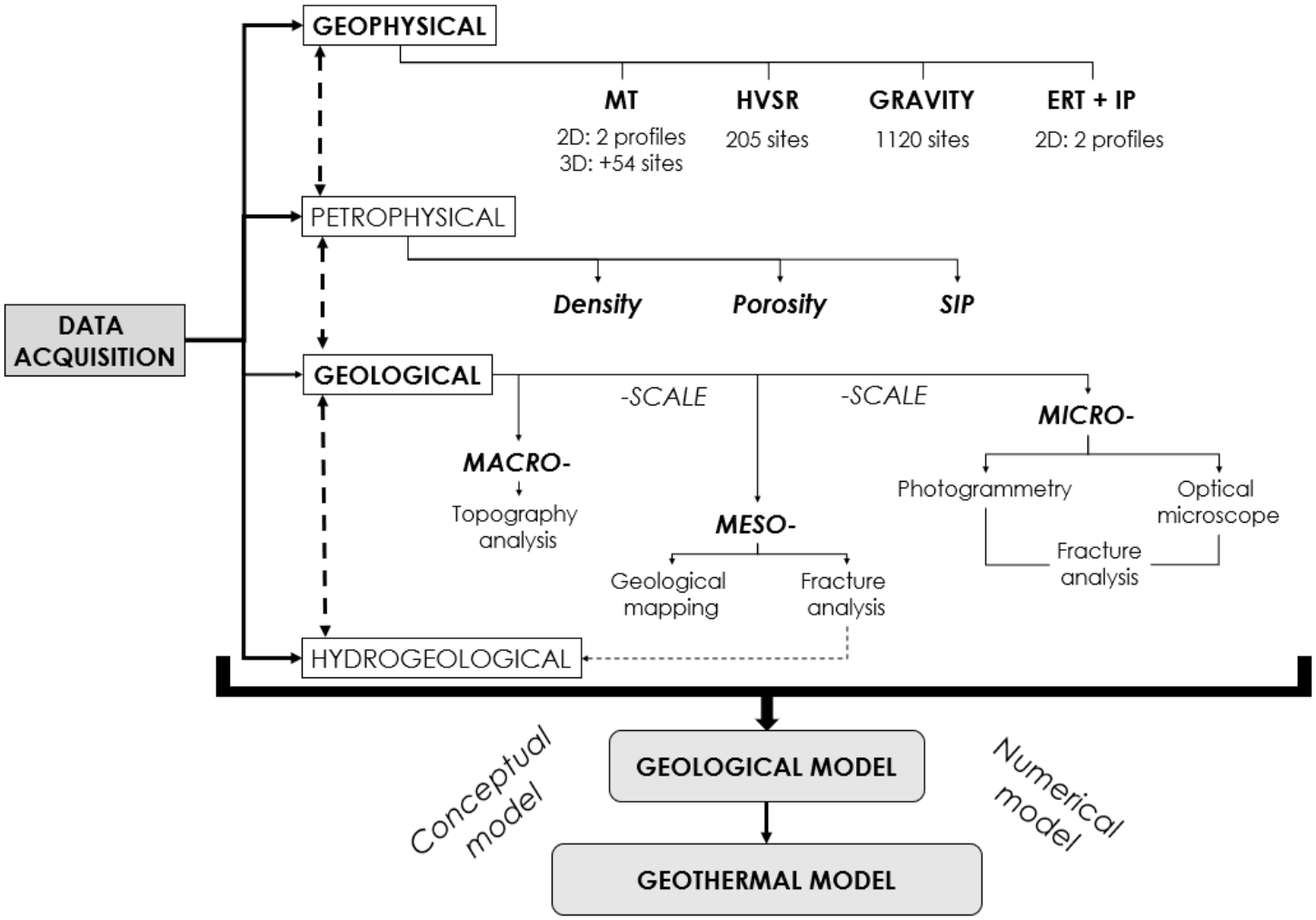

Figure 81. Summary of the methodology presented for the characterization of a fault-controlled geothermal system.

Part 5

References

Appendix

Scientific papers

References

Abdullah, A., Akhir, J. M., & Abdullah, I. (2010). Automatic mapping of lineaments using shaded relief images derived from digital elevation model (DEMs) in the Maran - Sungi Lembing area, Malaysia. *Electronic Journal of Geotechnical Engineering*, *15*, pp. 949–957.

Abdul Nassir, S. S. (1997). *A study of the use of different electrode array for electrical imaging surveys*. PhD Thesis. Universiti Sains, Malaysia.

Abdul Nassir, S. S., Loke, M. H., Lee, C. Y., & Nawawi, M. N. M. (2000). Salt-water intrusion mapping by geoelectrical imaging surveys. *Geophysical Prospecting*, *48* (4), pp. 647–661.

Agisoft Metashape. (2019). *User Manual - Professional Edition, Version 1.5*. p. 145.

Albert, J. F. (1988). *La Calor de la Terra: energia geotèrmica a Catalunya*. Generalitat de Catalunya. Departament d'Indústria i Energia. p. 88.

Albert, J. F., Corominas, J., & París, C. (1979). El estudio hidrogeológico de los manantiales y su aplicación geológica: caso de las aguas termales, carbónicas y sulfhídricas de Cataluña. *Acta Geológica Hispánica*, *14* (Homenatge a Lluís Solé i Sabarís), pp. 391–394.

Aldega, L., Viola, G., Casas-Sainz, A., Marcén, M., Román-Berdiel, T., & van der Lelij, R. (2019). Unraveling Multiple Thermotectonic Events Accommodated by Crustal-Scale Faults in Northern Iberia, Spain: Insights From K-Ar Dating of Clay Gouges. *Tectonics*, *38* (10), pp. 3629–3651.

AL-Hameedawi, M. M., & Thabit, J. M. (2017). Comparison between four electrode arrays in delineating sedimentary layers of alluvial fan deposits in eastern Iraq using a 2D imaging technique. *Environmental Earth Sciences*, *76* (525).

Anadón, P., Cabrera, L., Guimerà, J., & Santanach, P. (1985). Paleogene strike-slip deformation and sedimentation along the southeastern margin of the Ebro Basin. *Strike-Slip Deformation, Basin Formation, and Sedimentation, June 2018*, pp. 303–317.

Anadón, P., Colombo, F., Esteban, M., Marzo, M., & Robles, S. (1979). Evolución tectonoestratigráfica de los Catalánides. *Acta Geológica Hispánica*, *14* (1), pp. 242–270.

Andreassen, K., Nilssen, E. G., & Ødegaard, C. M. (2007). Analysis of shallow gas and fluid migration within the Plio-Pleistocene sedimentary succession of the SW Barents Sea continental margin using 3D seismic data. *Geo-Marine Letters*, *27* (2–4), pp. 155–171.

Anovitz, L. M., & Cole, D. R. (2015). Characterization and analysis of porosity and pore structures. *Reviews in Mineralogy and Geochemistry*, *80 (1)*, pp. 61–164.

An, P., Fang, K., Jiang, Q., Zhang, H., & Zhang, Y. (2021). Measurement of rock joint surfaces by using smartphone structure from motion (SFM) photogrammetry. *Sensors*, *21* (3:992).

Antics, M., & Sanner, B. (2007). Status of Geothermal Energy Use and Resources in Europe. *Proceedings European Geothermal Congress 2007*, Unterhaching (Germany), 30 May-1 June.

Árnason, K., Karlsdottir, R., Eysteinsson, H., Flóvenz, Ó. G., & Thor, S. (2000). The Resistivity Structure of High-Temperature Geothermal Systems in Iceland. *Proceedings World Geothermal Congress 2000, Kyushu-Tohoku, Japan*, pp. 923–928.

Ashton, N., Lewis, S. G., de Groote, I., Duffy, S. M., Bates, M., Bates, R., Hoare, P., Lewis, M., Parfitt, S. A., Peglar, S., Williams, C., & Stringer, C. (2014). Hominin footprints from Early Pleistocene deposits at Happisburgh, UK. *PLOS ONE (www.plosone.org)*, *9* (2), E88329.

Bairlein, K., Bücker, M., Hördt, A., & Hinze, B. (2016). Temperature dependence of spectral induced polarization data: Experimental results and membrane polarization theory. *Geophysical Journal International*, *205* (1), pp. 440–453.

Baqués, V., Travé, A., Roca, E., Marín, M., & Cantarero, I. (2012). Geofluid behaviour in successive extensional and compressional events: A case study from the southwestern end of the Vallès-Penedès fault (Catalan coastal ranges, NE Spain). *Petroleum Geoscience*, *18* (1), pp. 17–31.

Barazzetti, L., Binda, L., Scaioni, M., & Taranto, P. (2011). Photogrammetric survey of complex geometries with low-cost software: Application to the 'G1′ temple in Myson, Vietnam. *Journal of Cultural Heritage*, *12* (3), pp. 253–262.

Bard, P.-Y. (1985). Les effets de site d'origine structurale: Principaux résultats experimentaux et théoriques. In V. Davidovici (Ed.), *Genie Parasismique* (pp. 223–238). Presses de l'école nationale des ponts et chaussées.

Bard, P.-Y. (1998). Microtremor measurement: a tool for site effect estimation? *Second International Symposium on the Effects of Surface Geology on Seismic Motion*, *3*, pp. 1251–1279.

Bard, P.-Y., & SESAME-Team. (2005). *Guidelines for the implementation of the H/V spectral ratio technique on ambient vibrations-measurements, processing and interpretations. SESAME European research project EVG1-CT-2000-00026 - Deliverable D23.12*, p. 62. http://sesame-fp5.obs.ujf-grenoble.fr.

Bartrina, M. T., Cabrera, L., Guimerà, J., Roca, E., & Jurado, M. J. (1992). Evolution of the central Catalan margin of the Valencia trough (western Mediterranean). *Tectonophysics*, *203* (1–4), pp. 219–247.

Bauer, J. F., Meier, S., & Philipp, S. L. (2015). Architecture, fracture system, mechanical properties and permeability structure of a fault zone in Lower Triassic sandstone, Upper Rhine Graben. *Tectonophysics*, *647*, pp. 132–145.

Beamish, D., & Travassos, J. M. (1992). The use of the D+ solution in magnetotelluric interpretation. *Journal of Applied Geophysics*, *29* (1), pp. 1–19.

Benderitter, Y., & Cormy, G. (1990). Possible approach to geothermal research and relative cost estimate. In M. H. Dickson & M. Fanelli (Eds.), *Small Geothermal Resources* (pp. 67–71). UNITAR/UNDP Centre for Small Energy Resources.

Benjumea, B., Macau, A., Gabas, A., Bellmunt, F., Figueras, S., & Cirés, J. (2011). Integrated geophysical profiles and H/V microtremor measurements for subsoil characterization. *Near Surface Geophysics*, *9* (5), pp. 413–425.

Benjumea, B., Macau, A., Gabàs, A., Esquerda, M., & Figueras, S. (2014). Improving near surface characterization by combining reprocessed vintage seismic and geophysical passive datasets. *Near Surface Geoscience 2014 - 20th European Meeting of Environmental and Engineering Geophysics*, *September 2014*, pp. 14–18.

Bertrand, L. (2017). *Etude des réservoirs géothermiques développés dans le socle et à l'interface avec les formations sédimentaires.* PhD Thesis. Université de Lorraine.

Bertrand, L., Géraud, Y., & Diraison, M. (2021). Petrophysical properties in faulted basement rocks: Insights from outcropping analogues on the West European Rift shoulders. *Geothermics*, *95*, *102144*.

Betlem, P., Birchall, T., Ogata, K., Park, J., Skurtveit, E., & Senger, K. (2020). Digital drill core models: Structure-from-motion as a tool for the characterisation, orientation, and digital archiving of drill core samples. *Remote Sensing*, *12* (330).

Bistacchi, A., Massironi, M., & Menegon, L. (2010). Three-dimensional characterization of a crustal-scale fault zone: The Pusteria and Sprechenstein fault system (Eastern Alps). *Journal of Structural Geology*, *32* (12), pp. 2022–2041.

Boissavy, C., Rocher, P., Laplaige, P., & Brange, C. (2016). Geothermal Energy Use, Country update for France. *European Geothermal Congress*, pp. 1–19.

Burtman, V., & Zhdanov, M. S. (2015). Induced polarization effect in reservoir rocks and its modeling based on generalized effective-medium theory. *Resource-Efficient Technologies*, *1* (1), pp. 34–48.

Cagniard, L. (1953). Basic theory of the magneto-telluric method of geophysical prospecting. *Geophysics*, *18*, pp. 605–635.

Caine, J. S., Evans, J. P., & Forster, C. B. (1996). Fault zone architecture and permeability structure. *Geology*, *24*, pp. 1025–1028. http://oreilly.com/catalog/errata.csp?isbn=9781449340377

Canals, A., Albert, J., & Ayora, C. (1990). El sistema geotérmico de la Garriga-Samalús: comparaciones con sistemas hidrotermales fósiles. *Geogaceta*, *7*, pp. 88–90.

Cantarero, I. (2013). *Deformation-fluid multiphase interaction within the fractures of the Barcelona Plain and the Vallès Basin: influence on fault rocks and diagenesis*. PhD Thesis. Universitat de Barcelona. p. 304.

Cantarero, I., Lanari, P., Vidal, O., Alías, G., Travé, A., & Baqués, V. (2014). Long-term fluid circulation in extensional faults in the central Catalan Coastal Ranges: P-T constraints from neoformed chlorite and K-white mica. *International Journal of Earth Sciences*, *103* (1), pp. 165–188.

Cantarero, I., Zafra, C. J., Travé, A., & Martín-Martín, J. D. (2012). Diagénesis y fracturación de las rocas miocenas entre las subcuencas del Vallès y del Penedès: características y rellenos (Esparraguera, Baix Llobregat). Congreso Geológico de España, *Geotemas*, *13* (VIII), pp. 837–840.

Cardellach, E., Canals, A., & Grandia, F. (2002). Recurrent hydrothermal activity induced by successive extensional episodes: The case of the Berta F-(Pb-Zn) vein system (NE Spain). *Ore Geology Reviews*, *22* (1–2), pp. 133–141.

Casas, A., Torné, M., & Banda, E. (1987). *Mapa gravimètric de Catalunya 1:500.000*. Servei Geològic de Catalunya.

Chave, A. D., & Jones, A. G. (2012). *The Magnetotelluric Method: Theory and Practice*. Cambridge University Press. p. 551.

Chesnaux, R., Allen, D. M., & Jenni, S. (2009). Regional fracture network permeability using outcrop scale measurements. *Engineering Geology*, *108* (3–4), pp. 259–271.

Childs, C., Manzocchi, T., Walsh, J. J., Bonson, C. G., Nicol, A., & Schöpfer, M. P. J. (2009). A geometric model of fault zone and fault rock thickness variations. *Journal of Structural Geology*, *31* (2), pp. 117–127.

Compañía General de Sondeos S.A. (1977). *Fase preliminar de prospección de recursos geotérmicos de baja entalpía en el Vallés (Barcelona).* Instituto Geológico y Minero de España. p. 92.

Compañía General de Sondeos S.A. (1978). *Estudio termométrico del Valles Occidental (Barcelona)*. Instituto Geológico y Minero de España. p. 121.

Compañía General de Sondeos S.A. (1979a). *Estudio magnetotelúrico y Audio - MT de las anomalías geotérmicas de Caldes de Montbui y La Garriga*. Instituto Geológico y Minero de España. p. 88.

Compañía General de Sondeos S.A. (1979b). *Estudio mediante Dipole Mapping de las anomalías geotérmicas de Cáldes de Montbuí y La Garriga.* Instituto Geológico y Minero de España. p. 51.

Compañía General de Sondeos S.A. (1979c). *Estudio microsísmico y de rudio seísmico de la fosa del Valles (Barcelona)*. Instituto Geológico y Minero de España. p. 40.

COP-21. (2015). Paris agreement. *Report of the Conference of the Parties to the United Nations Framework Convention on Climate Change (21st Session)*.

Curewitz, D., & Karson, J. A. (1997). Structural settings of hydrothermal outflow: Fracture permeability maintained by fault propagation and interaction. *Journal of Volcanology and Geothermal Research*, *79*, pp. 149–168.

Daniilidis, A., Saeid, S., & Doonechaly, N. G. (2021). The fault plane as the main fluid pathway: Geothermal field development options under subsurface and operational uncertainty. *Renewable Energy*, *171*, pp. 927–946.

Del Val, L., Mitjanas, G., Ledo, J., & Queralt, P. (2021). Interdisciplinary characterization of La Garriga-Samalús (Barcelona, Spain) fault-controlled geothermal system. *48th IAH Congress*, Brussels, Belgium.

Dewez, T. J. B., Girardeau-Montaut, D., Allanic, C., & Rohmer, J. (2016). Facets: A cloudcompare plugin to extract geological planes from unstructured 3d point clouds. *International Archives of the Photogrammetry, Remote Sensing and Spatial Information Sciences - ISPRS Archives*, *41*, pp. 799–804.

Dobson, P. F., Kneafsey, T. J., Hulen, J., & Simmons, A. (2003). Porosity, permeability, and fluid flow in the Yellowstone geothermal system, Wyoming. *Journal of Volcanology and Geothermal Research*, *123* (3–4), pp. 313–324.

Domenico, P. A., & Palciauskas, V. v. (1973). Theoretical Analysis of Forced Convective Heat Transfer in Regional Ground-Water Flow. *Geological Society of America Bulletin*, *84* (12), pp. 3803–3814.

Dumas, P. (2016). A European perspective of the development of deep geothermal in urban areas: Smart thermal grids, geothermal integration into smart cities. *Geomechanik Und Tunnelbau*, *9* (5), pp. 447–450.

Ekren, E. B., Bucknam, R. C., Carr, W. J., Dixon, G. L., & Quinlivan, W. D. (1976). East-Trending Structural Lineaments in Central Nevada. In *Geological Survey Professional Paper* (Issue 986). https://pubs.er.usgs.gov/publication/pp986?currow=1372

Escalas, M., Queralt, P., Ledo, J., & Marcuello, A. (2013). Polarisation analysis of magnetotelluric time series using a wavelet-based scheme: A method for detection and characterisation of cultural noise sources. *Physics of the Earth and Planetary Interiors*, *218*, pp. 31–50.

Everett, Mark. E. (2013). *Near-Surface Applied Geophysics*. Cambridge University Press. p. 403.

Fäh, D., Kind, F., & Giardini, D. (2001). A theoretical investigation of average HIV ratios. *Geophysical Journal International*, *145* (2), pp. 535–549.

Fairley, J. P., & Hinds, J. J. (2004). Rapid transport pathways for geothermal fluids in an active Great Basin fault zone. *Geology*, *32* (9), pp. 825–828.

Fernàndez, M., & Banda, E. (1988). Aproximacion a la anomalia geotérmica de La Garriga - Samalus (Vallès - Penedès). *Acta Geológica Hispánica*, *23* (1), pp. 1–20.

Fernàndez, M., & Banda, E. (1990). Geothermal Anomalies in the Valles-Penedes graben master fault: convection through the horst as a possible mechanism. *Journal of Geophysical Research*, *95* (B4), pp. 4887–4894.

Fontboté, J. M. (1954). *Sobre la evolución tectónica de la depresión del Vallés-Penedès*. Publ. Museu Sabadell.

Fossen, H., & Rotevatn, A. (2016). Fault linkage and relay structures in extensional settings-A review. *Earth-Science Reviews*, *154*, pp. 14–28.

Gabàs, A., Macau, A., Benjumea, B., Queralt, P., Ledo, J., Figueras, S., & Marcuello, A. (2016). Joint Audio-Magnetotelluric and Passive Seismic Imaging of the Cerdanya Basin. *Surveys in Geophysics*, *37* (5), pp. 897–921.

Gallart, J., Dañobeitia, J. J., Rojas, H., & Diaz, J. (1990). Features of deep crustal structure and the onshore-offshore transition at the Iberian flank of the Valencia Trough (Western Mediterranean). *Journal of Geodynamics*, *12* (2–4), pp. 233–252.

Gallart, J., Vidal, N., & Daiiobeitia, J. J. (1997). The ESCI Valencia Trough vertical reflection experiment: a seismic image of the crust from the NE Iberian Peninsula to the Western Mediterranean. *Revista de la Sociedad Geológica de España, 8 (4),* pp. 401-415.

Gamble, T. D., Goubau, W. M., & Clarke, J. (1979). Magnetotellurics with a remote magnetic reference. *Geophysics*, *44* (1), pp. 53–68.

Gaspar-Escribano, J. M. (2003). *Tectonic modeling of the Catalan Coastal Ranges (NE Spain) and adjacent areas*. PhD Thesis. Vrije Univ. Amsterdam.

Gaspar-Escribano, J. M., Garcia-Castellanos, D., Roca, E., & Cloetingh, E. (2004). Cenozoic vertical motions of the Catalan Coastal Ranges (NE Spain): The role of tectonics, isostasy, and surface transport. *Tectonics*, *23* (1), pp. 1–18.

Georgsson, L. S. (2009). Geophysical methods used in geothermal exploration. *Short Course on Surface: Exploration for Geothermal Resources* organized by *UNU-GTP and LaGeo*, El Salvador, 17-30 October 2009.

Geosoft Inc. (2015). *Oasis montaj Gravity and Terrain Correction. How-To Guide*. http://updates.geosoft.com/downloads/files/how-to-guides/Gravity and Terrain Correction Formulas.pdf

Glyn-Morris, T., Mclean, K., & Brockband, K. (2011). *Proceedings of the New Zealand Geothermal Workshop*.

Golden Software LLC. (2016). *Surfer®* (version 13.6.618).

Gómez, M., & Guimerà, J. (1999). Estructura Alpina de la Serra de Miramar y del NE de Las Muntanyes de Prades (Cadena Costera Catalana). *Rev. Soc. Geol. Esp*, *12*, pp. 405–418.

Grohmann, C. H., Riccomini, C., & Chamani, M. A. C. (2011). Regional scale analysis of landform configuration with base-level (isobase) maps. *Hydrology and Earth System Sciences*, *15* (5), pp. 1493–1504.

Guimerà, J. (1984). Palaeogene evolution of deformation in the northeastern Iberian Peninsula. *Geological Magazine*, *121* (5), pp. 413–420.

Haenel, Ralph., & Staroste, E. (1988). *Atlas of geothermal resources in the European Community: Austria and Switzerland* (Ralph. Haenel & E. Staroste, Eds.). European Commission.

Haenel, R., Rybach, L., & Stegena, L. (1988). Fundamentals of geothermics. In R. Haenel, L. Rybach, & L. A. Stegena (Eds.), *Handbook of Terrestrial Heat-Flow Density Determination* (9–57). Kluwer, Academic.

Haklidir, M., Servin, F., & Haklidir, T. (2010). Hydrogen Production from Geothermal Sources in Turkey. *World Geothermal Congress*, *April*, 25–29.

Hammer, S. (1939). Terrain corrections for gravimeter stations. *Geophysics*, *4* (3), pp. 184–194.

Haug, C., Haug, J. T., Waloszek, D., Maas, A., Frattigiani, R., & Libeau, S. (2009). New methods to document fossils from lithographic limestones of southern Germany and Lebanon. *Paleontologia Electronica*, *12* (3), 6T: 12. http://palaeo-electronica.org/2009_3/193/index.html

Hinze, W. J., von Frese, R. R. B., & Saad, A. H. (2012). *Gravity and Magnetic Exploration*. Cambridge University Press.

Hochstein, M. P. (1988). Assessment and modelling of geothermal reservoirs (small utilization schemes). *Geothermics*, *17* (1), pp. 15–49.

Holmes, E. (2020). *A GIS-based method for archival and visualization of microstructural data from drill core samples.* Master's Thesis, University of Louisville.

Horo, D., Pal, S. K., Singh, S., & Srivastava, S. (2020). Combined self-potential, electrical resistivity tomography and induced polarisation for mapping of gold prospective zones over a part of Babaikundi-Birgaon Axis, North Singhbhum Mobile Belt, India. *Exploration Geophysics*, *51* (5), pp. 507–522.

Ibs-Von Seht, M., & Wohlenberg, J. (1999). Microtremor Measurements Used to Map Thickness of Soft Sediments. *Bulletin of the Seismological Society of America*, *89* (1), pp. 250–259.

ICGC. (2002). *Mapa Geològic de Catalunya 1:250.000*. Institut Cartogràfic i Geològic de Catalunya. www.icc.cat/vissir3/

ICGC. (2006). *Vallès Oriental. Mapa geològic comarcal de Catalunya 1:50.000*.

ICGC. (2011). *Base Topogràfica de Catalunya 1:5.000 (BT-5M) v2*. Institut Cartogràfic i Geològic de Catalunya.

ICGC. (2022, October 1). *Butlletí sismològic (1984-2022)*.

IGME. (1974). *La Garriga (364). Mapa geológico de España 1:50 000:*

IGME. (1977). *Fase preliminar de prospección de recursos geotérmicos de baja entalpía en el Vallés (Barcelona).*

IGME. (1982). *Informe sobre el seguimiento técnico del sondeo SAMALUS-1*.

IGME. (1984a). *Proyecto de investigación geotérmica en el Vallés mediante sondeos de reconocimiento y síntesis hidrogeotérmica. Control geotérmico de los sondeos SAMALUS-2, 3, 4 y 5*.

IGME. (1984b). *Proyecto de investigación geotérmica en el Valles mediante sondeos de reconocimiento y síntesis hidrogeotérmica. Volumen I: Síntesis hidrogeológica del Valles.* 355.

IGME. (1986a). *Informe sobre el seguimiento técnico de los sondeos de reconocimiento CM-2, CM-3 y CM-4 en Caldes de Montbui (Valles, Barcelona)*.

IGME. (1986b). *Proyecto de seguimiento geológico del sondeo de reconocimiento geotérmico SAMALUS-6 (1000 m) (Valles-Barcelona)*.

Jefferies, S. P., Holdsworth, R. E., Shimamoto, T., Takagi, H., Lloyd, G. E., & Spiers, C. J. (2006). Origin and mechanical significance of foliated cataclastic rocks in the cores of crustal-scale faults: Examples from the Median Tectonic Line, Japan. *Journal of Geophysical Research: Solid Earth*, *111* (12).

Jefferies, S. P., Holdsworth, R. E., Wibberley, C. A. J., Shimamoto, T., Spiers, C. J., Niemeijer, A. R., & Lloyd, G. E. (2006). The nature and importance of phyllonite development in crustal-scale fault cores: An example from the Median Tectonic Line, Japan. *Journal of Structural Geology*, *28* (2), pp. 220–235.

Johannesson, J., & Clowes, D. (2022). Energy Resources and Markets - Perspectives on the Russia-Ukraine War. *European Review*, *30* (1), pp. 4–23.

Jolie, E., Scott, S., Faulds, J., Chambefort, I., Axelsson, G., Gutiérrez-Negrín, L. C., Regenspurg, S., Ziegler, M., Ayling, B., Richter, A., & Zemedkun, M. T. (2021). Geological controls on geothermal resources for power generation. *Nature Reviews Earth and Environment*, *2* (5), pp. 324–339.

Jorand, R., Clauser, C., Marquart, G., & Pechnig, R. (2015). Statistically reliable petrophysical properties of potential reservoir rocks for geothermal energy use and their relation to lithostratigraphy and rock composition: The NE Rhenish Massif and the Lower Rhine Embayment (Germany). *Geothermics*, *53*, pp. 413–428.

Juez-Larré, J., & Andriessen, P. A. M. (2006). Tectonothermal evolution of the northeastern margin of Iberia since the break-up of Pangea to present, revealed by low-temperature fission-track and (U-Th)/He thermochronology: A case history of the Catalan Coastal Ranges. *Earth and Planetary Science Letters*, *243* (1–2), pp. 159–180.

Kane, M. F. (1962). A comprehensive system of terrain corrections using a digital computer. *Geophysics*, *27* (4), pp. 455–462.

Kearey, P., Brooks, M., & Hill, I. (2002). *An Introduction to Geophysical Exploration* (3rd Edition). Blackwell Science.

Keller, G. V., & Frischknecht, F. C. (1966). *Electrical methods in geophysical prospecting*. Pergamon Press, Oxford.

Kordić, B., Lužar-Oberiter, B., Pikelj, K., Matoš, B., & Vlastelica, G. (2019). Integration of terrestrial laser scanning and UAS photogrammetry in geological studies: Examples from Croatia. *Periodica Polytechnica Civil Engineering*, *63* (4), pp. 989–1003.

Kusumah, Y. I., Suryantini, & Wibowo, H. H. (2010). Horizontal Derivative from Gravity Data as a Tool for Drilling Target Guide in Wayang Windu Geothermal Field, Indonesia. *Proceedings World Geothermal Congress*, *April*, 25–29.

Kyne, R., Torremans, K., Güven, J., Doyle, R., & Walsh, J. (2019). 3-D modeling of the lisheen and silvermines deposits, County Tipperary, Ireland: insights into structural controls on the formation of Irish Zn-Pb deposits. *Economic Geology*, *114* (1), pp. 93–116.

Lachet, C., & Bard, P. Y. (1994). Numerical and Theoretical Investigations on the Possibilities and Limitations of Nakamura's Technique. *Journal of Physics of the Earth*, *42* (5), 377–397.

Ledo, J., Queralt, P., & Pous, J. (1998). *Three-Dimensional Regional Structure*. pp. 295–301.

Lee, W. H. K., & Stewart, S. W. (1981). Principles and Applications of Microearthquake Networks. In *Advances in Geophysics* (Vol. 2). Academic Press.

le Maitre, R. W., Streckeisen, A., Zanettin, B., le Bas, M. J., Bonin, B., & Bateman, P. (2002). *Igneous Rocks: A Classification and Glossary of Terms* (2nd ed.). Cambridge University Press.

Lin, J., Wang, R., Li, L., & Xiao, Z. (2019). A Workflow of SfM-Based Digital Outcrop Reconstruction Using Agisoft PhotoScan. *2019 IEEE 4th International Conference on Image, Vision and Computing, ICIVC 2019*, pp. 711–715.

Li, X., Xiong, B., Yuan, Z., He, K., Liu, X., Liu, Z., & Shen, Z. (2021). Evaluating the Potentiality of Using Control-free Images from a Mini Unmanned Aerial Vehicle (UAV) and Structure-from-Motion (SfM) Photogrammetry to Measure Paleoseismic Offsets. *International Journal of Remote Sensing*, *42* (7), pp. 2417–2439.

Lockner, D. A., & Byerlee, J. D. (1985). Complex resistivity measurements of confined rock. *Journal of Geophysical Research*, *90* (B9), 7837.

Loke, M. H. (2000). *Electrical imaging surveys for environmental and engineering studies. A practical guide to 2-D and 3-D surveys.*

López-Geta, J. A., Baeza, J., & Ramírez A. (2002). *Las aguas minerales en España. Visión histórica, contexto hidrogeológico y persepectiva.* (Instituto Geológico y Minero de España, Ed.). Ministerio de Ciencia y Teconología.

Lowrie, W. (2007). *Fundamentals of geophysics* (2nd ed.). Cambridge University Press.

Macau, A., Benjumea, B., Gabàs, A., Bellmunt, F., & Figueras, S. (2018). Geophysical measurements for site effects characterisation in the urban area of Girona, Spain. *Near Surface Geophysics*, *16* (3), pp. 340–355.

Macau, A., Juvenal, A., Bellmunt, F., & Gabàs, A. (2021). *Caracterització de la fossa del Vallès mitjançant tècniques de sísmica passiva: sector del Vallès Oriental*.

Maltby, T. (2013). European Union energy policy integration: A case of European Commission policy entrepreneurship and increasing supranationalism. *Energy Policy*, *55*, pp. 435–444.

Manzella, A. (1973). Geophysical methods in geothermal exploration. In *Geochemical and Geophysical Methodologies in Geothermal Exploration* (p. 41). Italian National Research Council. International Institute for Geothermal Research.

Marcén, M., Casas-Sainz, A. M., Román-Berdiel, T., Griera, A., Santanach, P., Pocoví, A., Gil-Imaz, A., Aldega, L., & Izquierdo-Llavall, E. (2018). Multiple movements recorded in a crustal weakness zone in NE Iberia: The Vallès-Penedès Fault revisited. *Journal of Geodynamics*, *121*, pp. 96–114.

Mariita, N. O. (2012). Strengths and weaknesses of gravity and magnetics as exploration tools for geothermal energy. *Short Course VII on Exploration for Geothermal Resources, Kenya, Oct. 27 – Nov. 18, 2012*, 8. https://orkustofnun.is/gogn/unu-gtp-sc/UNU-GTP-SC-15-0402.pdf

Marshall, D. J., & Madden, T. R. (1959). Induced polarization, a study of its causes. *Geophysics*, *24* (4), pp. 790–816.

Masana, E. (1994). Neotectonic features of the Catalan Coastal Ranges, northeastern Spain. *Acta Geologica Hispanica*, *29* (2–4), pp. 107–121.

Masana, E. (1995). *L'activitat neotectònica a les Cadenes Costaneres Catalanes*. Universitat de.

Masana, E. (1996). Evidence for past earthquakes in an area of low historical seismicity: the Catalan coastal ranges, NE Spain. *Annali Di Geofisica*, *39* (3), pp. 689–704.

Mas-Pla, J. (2000). *Avaluació dels recursos higrogeològics de l'aqüífer termal de La Garriga-Samalús (Vallès Oriental): Vol. PDF 2020 Version*.

Matonti, C., Lamarche, J., Guglielmi, Y., & Marié, L. (2012). Structural and petrophysical characterization of mixed conduit/seal fault zones in carbonates: Example from the Castellas fault (SE France). *Journal of Structural Geology*, *39*, pp. 103–121.

Matte, P. (2001). The Variscan collage and orogeny (480-290 Ma) and the tectonic desinition of the Armorica microplate: a review. *Terra Nova*, *13* (2), pp. 122–128.

McCarthy, D. D., & Petit, G. (2004). IERS conventions (2003). In *IERS Technical Note 32*. http://handle.dtic.mil/100.2/ADA430152

Mezghani, M. M., Fallatah, M. I., & AbuBshait, A. A. (2018). From Drone-Based Remote Sensing to Digital Outcrop Modeling: Integrated Workflow for Quantitative Outcrop Interpretation. *Journal of Remote Sensing & GIS*, *07* (02).

Micrometrics Instrument Corporation. (2005). *AccuPyc 1330 Pycnometer Operator's Manual. V3.03*.

Milbert, D. (2010). *Solid.exe* (Update 7/6/2018). Available at [www.geodesyworld.github.io/SOFTS/solid.htm].

Mitjanas, G., Ledo, J., Macau, A., Alías, G., Queralt, P., Bellmunt, F., Rivero, L., Gabàs, A., Marcuello, A., Benjumea, B., Martí, A., & Figueras, S. (2021). Integrated seismic ambient noise, magnetotellurics and gravity data for the 2D interpretation of the Vallès basin structure in the geothermal system of La Garriga-Samalús (NE Spain). *Geothermics*, *93* (March).

Moeck, I. S. (2014). Catalog of geothermal play types based on geologic controls. *Renewable and Sustainable Energy Reviews*, *37*, pp. 867–882.

Moore, J. P., & Walsh, J. (2021). Quantitative analysis of Cenozoic faults and fractures and their impact on groundwater flow in the bedrock aquifers of Ireland. *Hydrogeology Journal*, p. 20.

Morelli, C., Gantar, C., Honkasalo, T., McConnel, R. K., Tanner, J. G., Szabo, B., Uotila, U., & Whalen, C. T. (1972). The International Gravity Standardisation Net 1971 (I.G.S.N. 71). *Special Publication No. 4*.

Moret, G., Gold, D. P., & Rose, A. W. (2006). Detecting Hydrothermal Pyritic Zones along Bald Eagle Ridge Using Induced Polarization. In *Environmental & Engineering Geoscience: Vol. XII*, 4, pp. 377–384.

Moritz, H. (1980). Geodetic reference system 1980. *Bulletin Géodésique*, *54*(3), pp. 395–405.

Muffler, L. J. P. (1978). *Geological Survey Circular 790*. 163.

Muir-Wood, R., & King, G. C. P. (1993). Hydrological signatures of earthquake strain. *Journal of Geophysical Research*, *98* (B12).

Nagy, D. (1966). The gravitational attraction of a right rectangular prism. *Geophysics*, *31* (2), pp. 362–371.

Nakamura, Y. (1989). A method for dynamic characteristics estimations of subsurface using microtremors on the ground surface. *Railway Technical Research Institute, Quaterly Reports*, *30* (1), pp. 25–33.

Nance, R. D., Gutiérrez-Alonso, G., Keppie, J. D., Linnemann, U., Murphy, J. B., Quesada, C., Strachan, R. A., & Woodcock, N. H. (2010). Evolution of the Rheic Ocean. *Gondwana Research*, *17* (2–3), pp. 194–222.

Nesbit, P. R., Durkin, P. R., Hugenholtz, C. H., Hubbard, S. M., & Kucharczyk, M. (2018). 3-D stratigraphic mapping using a digital outcrop model derived from UAV images and structure-from-motion photogrammetry. *Geosphere*, *14* (6), pp. 2469–2486.

Nicol, A., Mouslopoulou, V., Begg, J., & Oncken, O. (2020). Displacement Accumulation and Sampling of Paleoearthquakes on Active Normal Faults of Crete in the Eastern Mediterranean. *Geochemistry, Geophysics, Geosystems*, *21* (11).

Norrena, K. P., & Deutsch, C. v. (2022). Automatic Determination of Well Placement Subject to Geostatistical and Economic Constraints. *SPE International Thermal Operations and Heavy Oil Symposium and International Horizontal Well Technology*.

Nowell, D. A. G. (1999). Gravity terrain corrections - an overview. *Journal of Applied Geophysics*, *42* (2), pp. 117–134.

Odling, N. E., Harris, S. D., & Knipe, R. J. (2004). Permeability scaling properties of fault damage zones in siliclastic rocks. *Journal of Structural Geology*, *26* (9), pp. 1727–1747.

Okay, G., Cosenza, P., Ghorbani, A., Camerlynck, C., Cabrera, J., Florsch, N., & Revil, A. (2013). Localization and characterization of cracks in clay-rocks using frequency and time-domain induced polarization. *Geophysical Prospecting*, *61* (1), pp. 134–152.

O'Leary, D. W., Friedman, J. D., & Pohn, H. A. (1978). Lineament, linear, lineation: Some proposed new standards for old terms. *Bulletin of the Geological Society of America*, *89* (1), pp. 159–159.

Palacky, G. J. (1987). Resistivity characteristics of geologic targets. In *Electromagnetic methods in applied geophysics* (pp. 53–129).

Palomo-Torrejón, E., Colmenar-Santos, A., Rosales-Asensio, E., & Mur-Pérez, F. (2021). Economic and environmental benefits of geothermal energy in industrial processes. *Renewable Energy*, *174*, pp. 134–146.

Parkinson, W. D. (1959). Directions of Rapid Geomagnetic Fluctuations. *Geophysical Journal International*, *2* (1), pp. 1–14.

Pellerin, L., Johnston, J. M., & Hohmann, G. W. (1992). Evaluation of electromagnetic methods in geothermal exploration. *1992 SEG Annual Meeting*, *61* (1), pp. 405–408.

Phillips, W. J. (1972). Hydraulic fracturing and mineralization. *Journal of the Geological Society*, *128* (4), pp. 337–359.

Piña-Varas, P. (2014). *Aplicación del método magnetotelúrico a la caracterización de reservorios: Anticlinal de El Hito (Cuenca) y Sistema Geotérmico de Tenerife*. p. 257.

Poggi, F., Firmino, A., & Amado, M. (2015). Moving Forward on Sustainable Energy Transitions: The Smart Rural Model. *European Journal of Sustainable Development*, *4* (2), pp. 43–50.

QGIS.org. (2021). *QGIS Geographic Information System*. QGIS Association.

Raguenel, M., Driesner, T., & Bonneau, F. (2019). Numerical modeling of the geothermal hydrology of the Volcanic Island of Basse-Terre, Guadeloupe. *Geothermal Energy*, *7* (1).

Ramos-Escudero, A., Gil-García, I. C., García-Cascales, M. S., & Molina-Garcia, A. (2021). Energy, economic and environmental GIS–based analysis of shallow geothermal potential in urban areas—A Spanish case example. In *Sustainable Cities and Society* (Vol. 75).

Reiss, L. H. (1980). *The reservoir engineering aspects of fractured formations* (p. 108).

Revil, A., & Florsch, N. (2010). Determination of permeability from spectral induced polarization in granular media. *Geophysical Journal International*, *181* (3), pp. 1480–1498.

Revil, A., & Gresse, M. (2021). Induced polarization as a tool to assess alteration in geothermal systems: A review. In *Minerals*, *11*, *9*. MDPI.

Revil, A., Karaoulis, M., Johnson, T., & Kemna, A. (2012). Review: Some low-frequency electrical methods for subsurface characterization and monitoring in hydrogeology. *Hydrogeology Journal*, *20* (4), pp. 617–658.

Revil, A., Qi, Y., Ghorbani, A., Coperey, A., Ahmed, A. S., Finizola, A., & Ricci, T. (2019). Induced polarization of volcanic rocks. 3. Imaging clay cap properties in geothermal fields. *Geophysical Journal International*, *218* (2), pp. 1398–1427.

Reynolds, J. M. (1997). *An introduction to Applied and Environmental Geophysics*. John Wiley & Sons.

Roca, E. (1992). *L'estructura de la conca Catalano-Balear: paper de la compressiò i de la distensió en la seva gènesi*. Universitat de Barcelona.

Roca, E. (1996). La evolucion geodinamica de la Cuenca Catalano-Balear y areas adyacentes desde el Mesozoico hasta la actualidad. *Acta Geologica Hispanica*, *29* (1), pp. 3–25.

Roca, E., & Guimerà, J. (1992). The Neogene structure of the eastern Iberian margin: Structural constraints on the crustal evolution of the Valencia trough (western Mediterranean). *Tectonophysics*, *203* (1–4), pp. 203–218.

Roca, E., Sans, M., Cabrera, L., & Marzo, M. (1999). Oligocene to Middle Miocene evolution of the central Catalan margin (northwestern Mediterranean). *Tectonophysics*, *315* (1–4), pp. 209–229.

Rodi, W., & Mackie, R. L. (2001). Nonlinear conjugate gradients algorithm for 2-D magnetotelluric inversion. *Geophysics*, *66* (1), pp. 174–187.

Rohmer, J., Nguyen, T. K., & Torabi, A. (2015). Off-fault shear failure potential enhanced by high-stiff/low-permeable damage zone during fluid injection in porous reservoirs. *Geophysical Journal International*, *202* (3), pp. 1566–1580.

Rotevatn, A., Tveranger, J., Howell, J. A., & Fossen, H. (2009). Dynamic investigation of the effect of a relay ramp on simulated fluid flow: Geocellular modelling of the Delicate Arch Ramp, Utah. *Petroleum Geoscience*, *15* (1), pp. 45–58.

Rybach, L., & Bunterbarth, G. (1982). Relationships between the petrophysical properties density, seismic velocity, heat generation, and mineralogical constitution. *Earth and Planetary Science Letters*, *57* (2), pp. 367–376.

Sàbat, F., Roca, E., Muñoz, J. A., Vergés, J., Santanach, P., Sans, M., Masana, E., Estévez, A., & Santisteban, C. (1995). Role of extension and compression in the evolution of the eastern margin of Iberia: the ESCI-València Trough seismic profile. *Rev. Soc. Geol. España*, *8* (4), pp. 431–448.

Santamaria, J. (2006). *Estudi de les manifestacions termals dels sistemes geotèrmics de la depressió del Vallès, Maresme i Baix Llobregat. Recull de La Garriga*.

Santanach, P., Casas, J. M., Gratacós, O., Liesa, M., Muñoz, J. A., & Sàbat, F. (2011). Variscan and Alpine structure of the hills of Barcelona: geology in an urban area. *Journal of Iberian Geology*, *37* (2), pp. 121–137.

Santoso, B., Prirahmayang, N., & Kirana, K. H. (2019). Identification of aquifer using geoelectric resistivity method of reciprocal schlumberger array (case study: Tanggamus, Lampung Province). *IOP Conference Series: Earth and Environmental Science*, *311* (1).

Sanz de Galdeano, C., Azañón, J. M., Cabral, J., Ruano, P., Alfaro, P., Canora, C., Ferrater, M., García Tortosa, F. J., García-Mayordomo, J., Gràcia, E., Insua-Arévalo, J. M., Jiménez Bonilla, A., Lacan, P. G., Marín-Lechado, C., Martín-Banda, R., Martín González, F., Martínez-Díaz, J. J., Martín-Rojas, I., Masana, E., … Simón, J. L. (2020). Active Faults in Iberia. In C. Quesada & J. T. Oliveira (Eds.), *The Geology of Iberia: A Geodynamic Approach. Regional Geology Reviews.* (pp. 33–75). Springer Nature.

Sari, M. (2018). Investigating Relationships between Engineering Properties of Various Rock Types. *Global Journal of Earth Science and Engineering*, *5*, 1–25.

Schlumberger. (1998). *Energy Glossary*. www.glossary.slb.com

Schön, J. H. (2015). Physical Properties of Rocks: Fundamentals and principles of petrophysics. In J. Cubitt (Ed.), *Developments in Petroleum Science* (2nd Editio, Vol. 65). Elsevier.

Schumacher, M. E. (2002). Upper Rhine Graben: Role of preexisting structures during rift evolution. *Tectonics*, *21* (1: 1006).

Schwartz, F. W., & Zhang, H. (2003). *Fundamentals of groundwater*. John Wiley & Sons.

Seequent Limited - a Bentley Company. (2021). *Leapfrog Geothermal* (5.0.4).

Seigel, H., Nabighian, M., Dattatray, S. P., & Keeva, V. (2007). The early history of the induced polarization method. *The Leading Edge*, *26* (3), pp. 312–321.

Seleem, T. A. (2013). Analysis and Tectonic Implication of DEM-Derived Structural Lineaments, Sinai Peninsula, Egypt. *International Journal of Geosciences*, *04* (01), pp. 183–201.

Sharma, P. v. (1997). *Environmental and engineering geophysics*. Cambridge University Press.

Sibson, R. H. (1993). Earthquake faulting, induced fluid flow, and fault-hosted gold- quartz mineralization. *Basement Tectonics 8*, pp. 603–614.

Simpson, F., & Bahr, K. (2005). Practical magnetotellurics. *Practical Magnetotellurics*, *9780521817*(February 2005), pp. 1–254.

Simpson, R. W., & Jachens, R. C. (1989). Chapter 3: Gravity methods in regional studies. *Memoir of the Geological Society of America*, *172* (1), pp. 35–44.

Slater, L. D., & Lesmes, D. (2002). IP interpretation in environmental investigations. *Geophysics*, *67* (1), pp. 77–88.

Spector, A., Neitzke Adamo, L., Miller, K., Browning, J. v., & Rowan, C. M. (2020). Use of Drone Technology and 3D Visualization Software for Virtual Field Trip Creation: Pebble Bluff Outcrop in the Newark Basin, New Jersey. In *American Geophysical Union, Fall Meeting 2020: Vol. Abstract #ED036-001*.

Spitzer, K. (2001). Magnetotelluric static shift and direct current sensitivity. *Geophysical Journal International*, *144* (2), pp. 289–299.

Stanton, G. P., Kress, W. H., Teeple, A. P., Greenslate, M. L., & Clarck, A. K. (2007). Geophysical analysis of the Salmon Peak Formation near Amistad Reservoir Dam, Val Verde County, Texas, and Coahuila, Mexico, March 2006, to aid in piezometer placement. In *Scientific Investigations Report, pp. 2007-5143*.

Stimac, J. A., Powell, T. S., & Golla, G. U. (2004). Porosity and permeability of the Tiwi geothermal field, Philippines, based on continuous and spot core measurements. *Geothermics*, *33* (1–2), pp. 87–107.

Stranne, C., & O'Regan, M. (2016). Conductive heat flow and nonlinear geothermal gradients in marine sediments—observations from Ocean Drilling Program boreholes. *Geo-Marine Letters*, *36* (1), pp. 25–33.

Summer, J. S. (1976). *Principles of Induced Polarization for Geophysical Exploration*. Elsevier Science Publ. Co.

Sundberg, J., Back, P. E., Ericsson, L. O., & Wrafter, J. (2009). Estimation of thermal conductivity and its spatial variability in igneous rocks from in situ density logging. *International Journal of Rock Mechanics and Mining Sciences*, *46* (6), pp. 1023–1028.

Szarka, L. (1988). Geophysical aspects of man-made electromagnetic noise in the Earth – A Review. *Surveys in Geophysics*, *9*, pp. 287–288.

Tchalenko, J. S., & Ambraseys, N. N. (1970). Structural Analysis of the Dasht-e Bayaz (Iran) Earthquake Fractures. *Geological Society of America Bulletin*, *81*, pp. 41–60.

Telford, W. M., Geldart, L. P., & Sheriff, R. E. (1990). *Applied Geophysics* (2nd ed.). Cambridge University Press.

Thiele, S. T., Grose, L., Samsu, A., Micklethwaite, S., Vollgger, S. A., & Cruden, A. R. (2017). Rapid, semi-automatic fracture and contact mapping for point clouds, images and geophysical data. *Solid Earth*, *8* (6), pp. 1241–1253.

Trilla, J. (1974). Sobre el origen de las aguas termales de Caldes de Montbui. *Acta Geológica Hispánica*, *IX* (4), pp. 144–148.

Uehara, S. ichi, & Shimamoto, T. (2004). Gas permeability evolution of cataclasite and fault gouge in triaxial compression and implications for changes in fault-zone permeability structure through the earthquake cycle. *Tectonophysics*, *378* (3–4), pp. 183–195.

Van Nostrand, R. G., & Cook, K. L. (1966). Interpretation of resistivity data. In *Geological Survey*.

Velde, B., & Meunier, A. (2008). *The Origin of Clay Minerals in Soils and Weathered Rocks*. Springer Berlin Heidelberg.

Vidal, N., Gallart, J., & Danobeitia, J. J. (1995). Contribution of the ESCI-Valéncia Trough Wide-Angle Data to a Crustal Transect in the NE Iberian Margin. In *Revista de la Sociedad Geologica de Espana: Vol. 8 (4)* (pp. 417–429).

Vinegar, H. J., & Waxman, M. H. (1984). Induced polarization of shaly sands. In *GEOPHYSICS* (Vol. 49, Issue 8). http://library.seg.org/

von Hippel, A. R. (1954). *Dielectric materials and applications*. Cambridge Technology Press of MIT.

Vozoff, K. (1991). The Magnetotelluric Method. In M. N. Nabighian (Ed.), *Electromagnetic Methods in Applied Geophysics - Applications: Vol. Chapter 8*. http://library.seg.org/

Walsh, J. J., Torremans, K., Güven, J., Kyne, R., Conneally, J., & Bonson, C. (2018). Fault-Controlled Fluid Flow Within Extensional Basins and Its Implications for Sedimentary Rock-Hosted Mineral Deposits. *Society of Economic Geologists Special Publications*, *21*, pp. 237–269.

Weise, H. (1962). Geomagnetische tiefentellurik teil II: Die streichrichtung der untergrundstrukturen des elektrischen widerstandes, erschlossen aus geomagnetischen variationen. *Geofisica Pura e Applicata*, *52* (1), pp. 83–103.

Ziegler, P. A., & Dèzes, P. (2006). Crustal Evolution of Western and Central Europe Introduction. In D. G. Gee & R. A. Stephenson (Eds.), *European Litosphere Dynamics*, 32, pp. 43–56. Geol. Soc. Mem.

APPENDIX

A.1. MT-Samalús. Raw data and model response

A.2. MT-Vilamajor. Raw data and model response

* Final model video: *https://youtu.be/CSkryuPnkIY*.

A.1. MT-Samalús. Raw data and model response

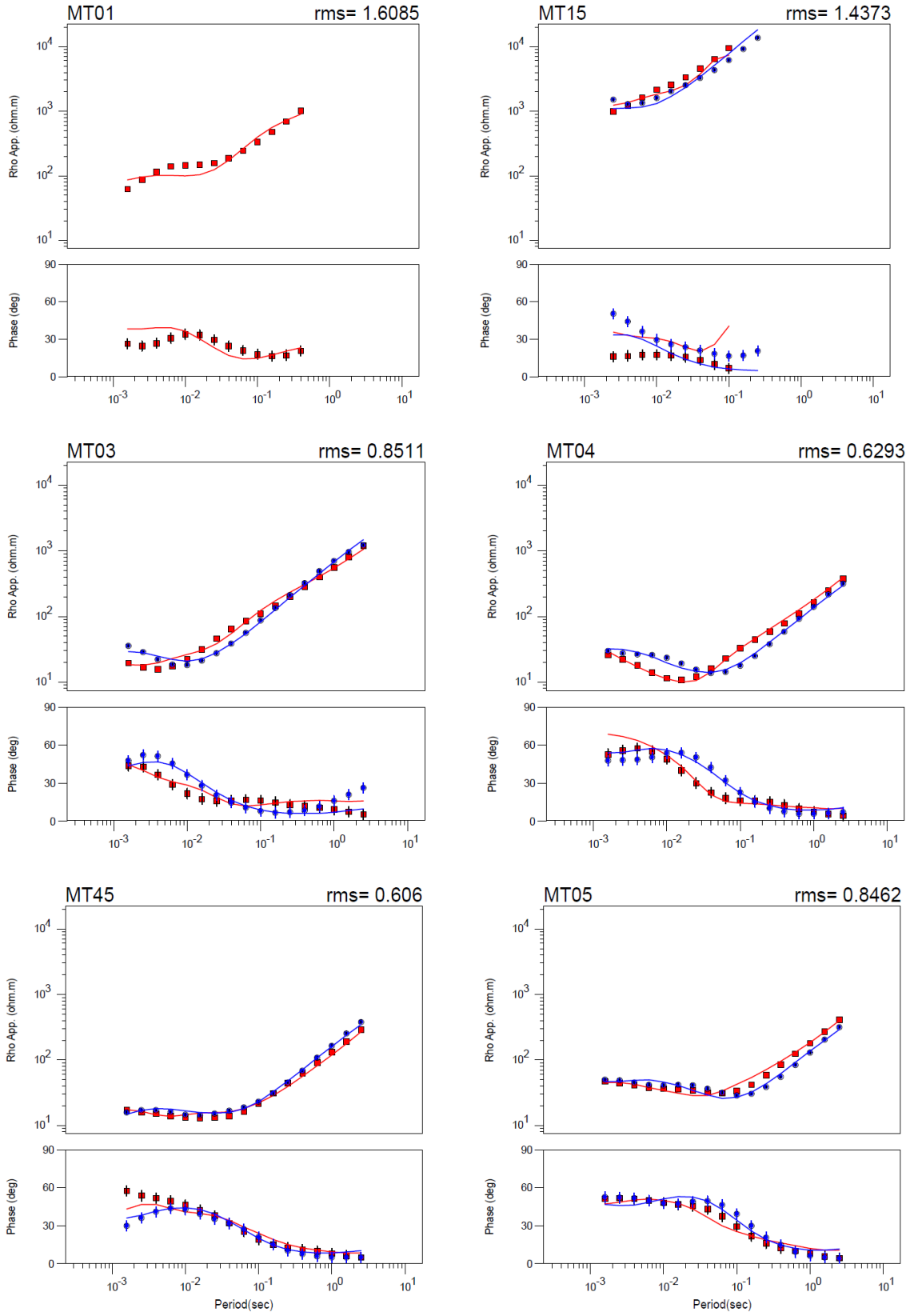

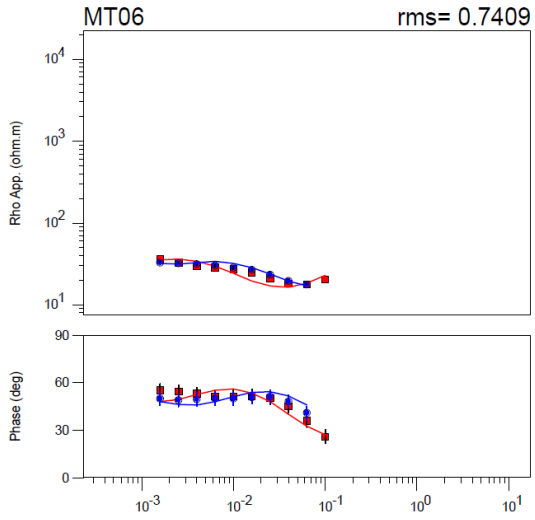
MT06
rms= 0.7409
Rho App. (ohm.m)
Phase (deg)

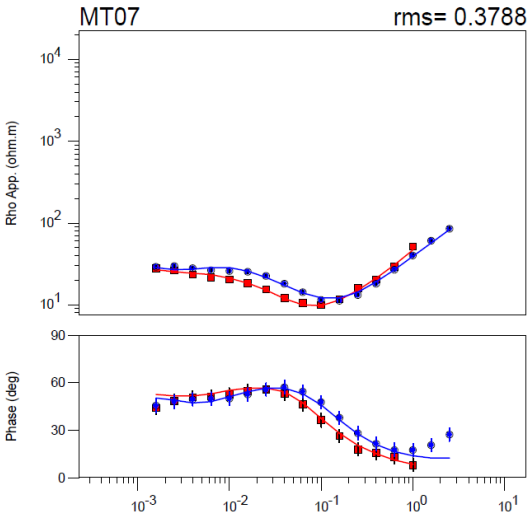
MT07
rms= 0.3788
Rho App. (ohm.m)
Phase (deg)

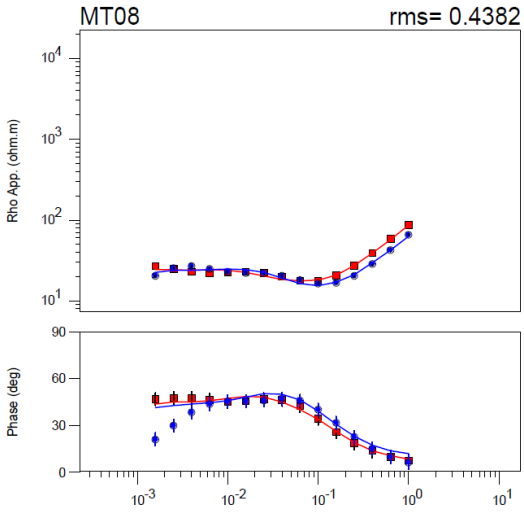
MT08
rms= 0.4382
Rho App. (ohm.m)
Phase (deg)

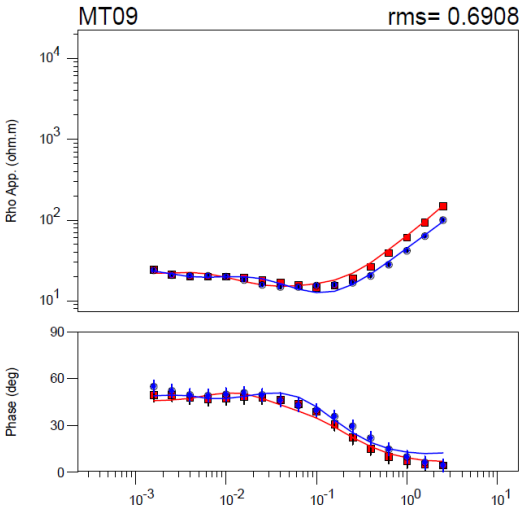
MT09
rms= 0.6908
Rho App. (ohm.m)
Phase (deg)

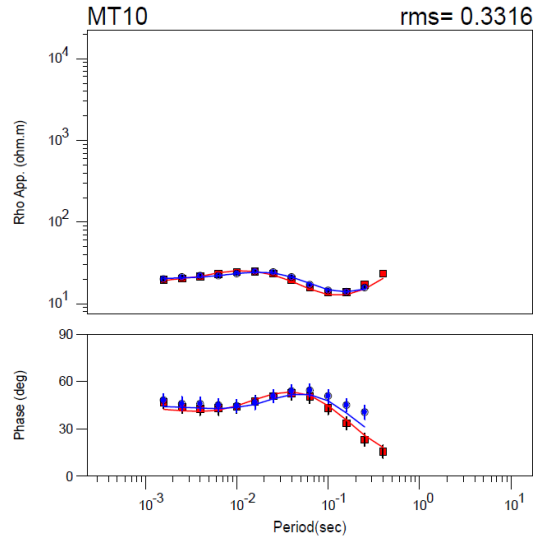
MT10
rms= 0.3316
Rho App. (ohm.m)
Phase (deg)
Period(sec)

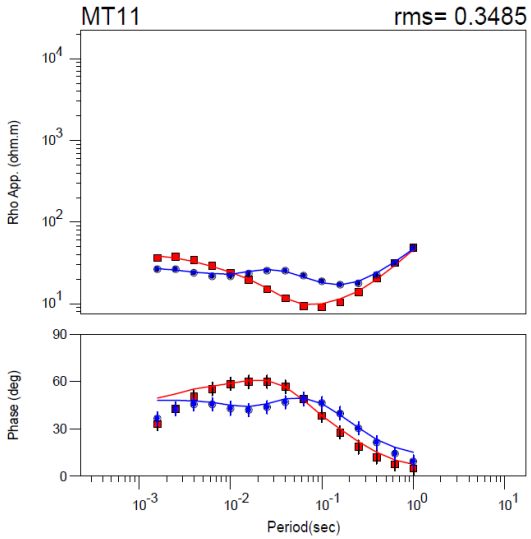
MT11
rms= 0.3485
Rho App. (ohm.m)
Phase (deg)
Period(sec)

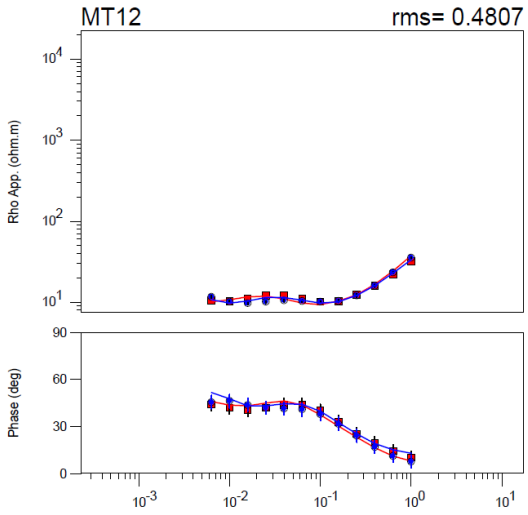

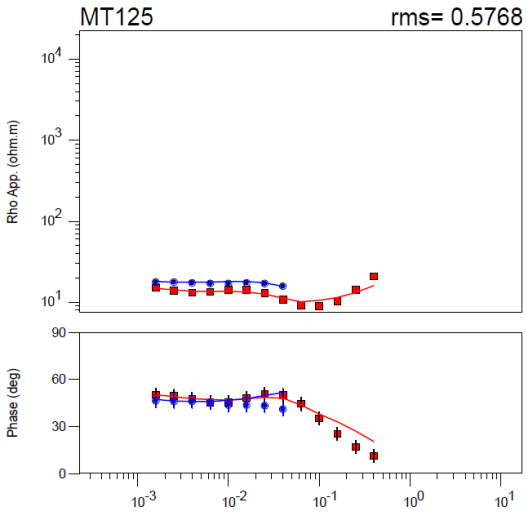

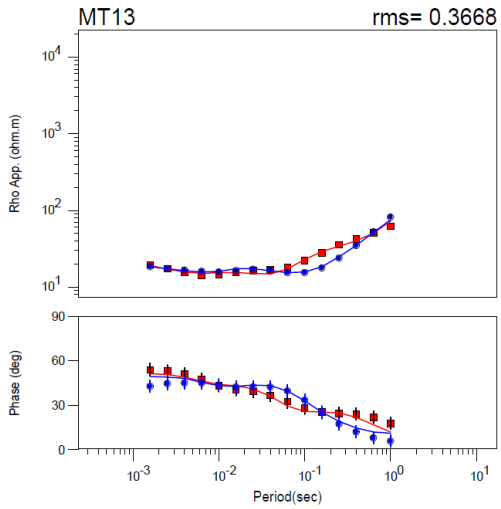

TE Original TE Calculated TM Original TM Calculated

A.2. MT-Vilamajor. Raw data and model response

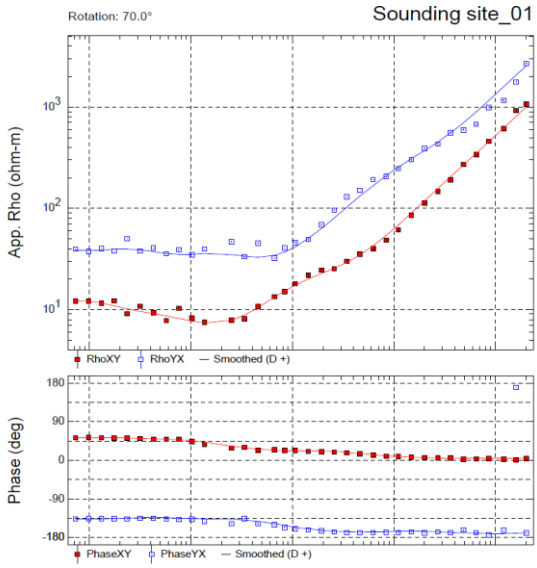

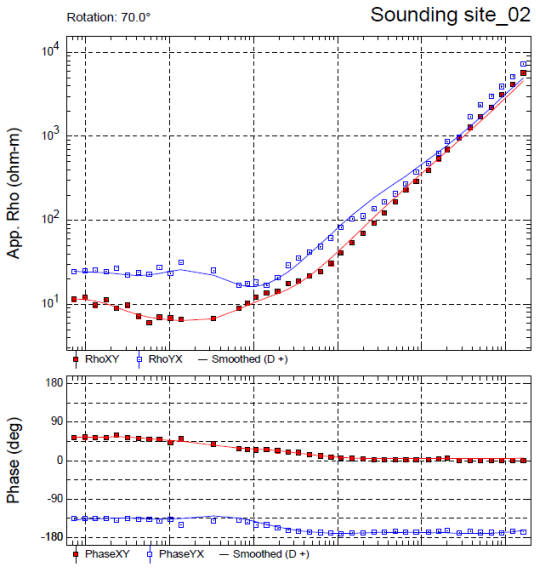

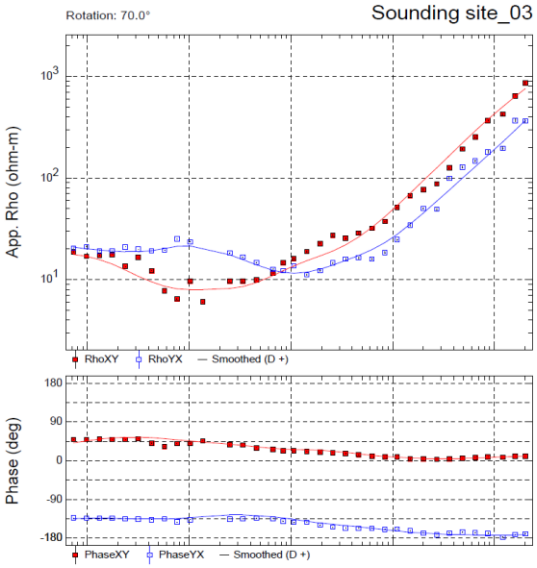

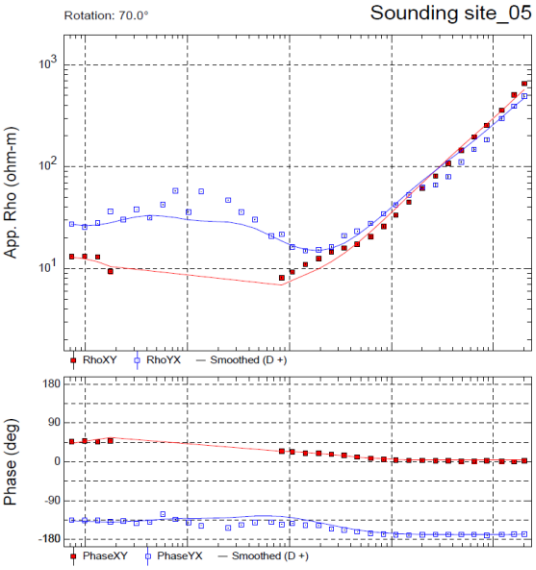

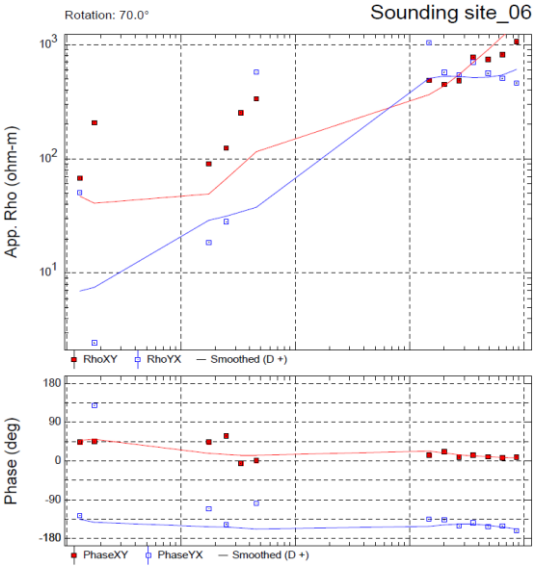

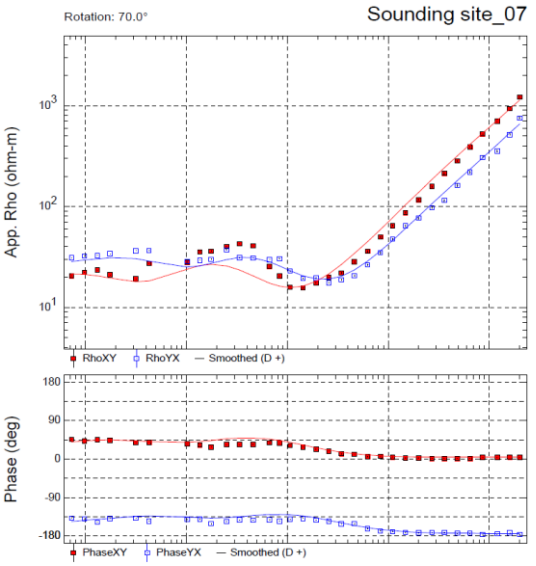

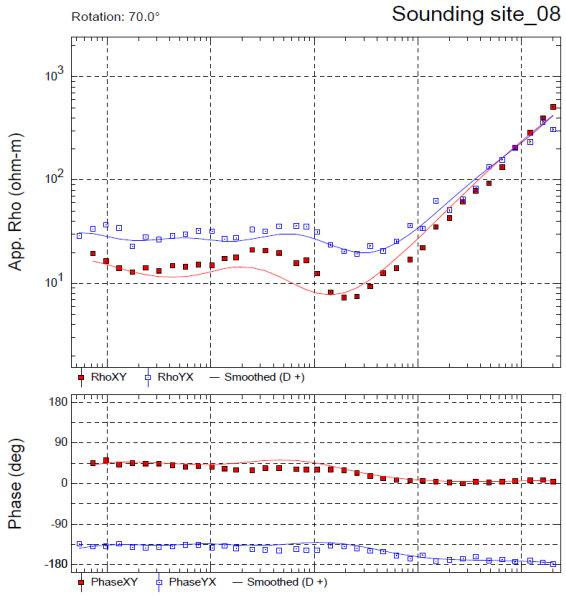
Rotation: 70.0°
Sounding site_08
App. Rho (ohm-m)
RhoXY
RhoYX
Smoothed (D +)
Phase (deg)
PhaseXY
PhaseYX
Smoothed (D +)

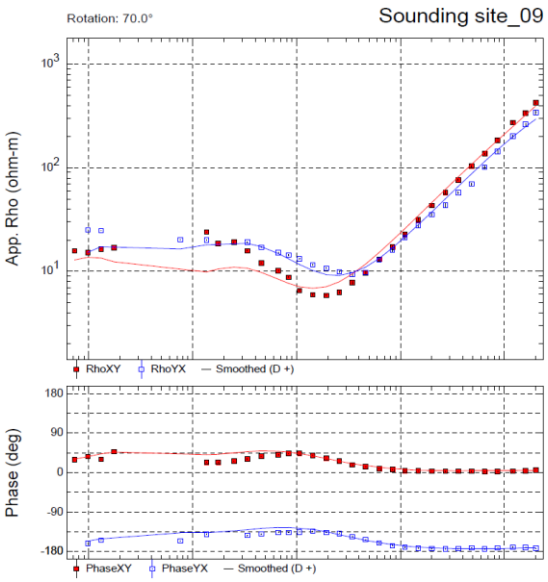
Rotation: 70.0°
Sounding site_09
App. Rho (ohm-m)
RhoXY
RhoYX
Smoothed (D +)
Phase (deg)
PhaseXY
PhaseYX
Smoothed (D +)

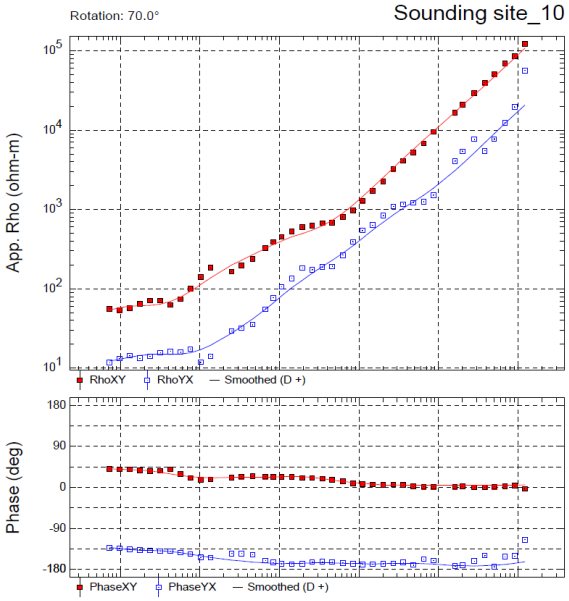
Rotation: 70.0°
Sounding site_10
App. Rho (ohm-m)
RhoXY
RhoYX
Smoothed (D +)
Phase (deg)
PhaseXY
PhaseYX
Smoothed (D +)

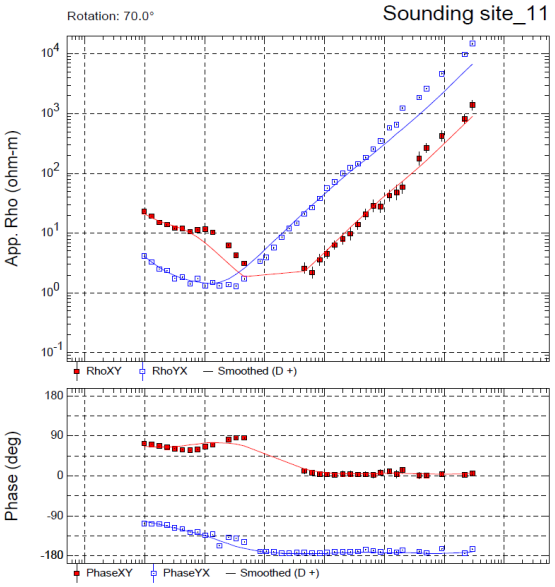
Rotation: 70.0°
Sounding site_11
App. Rho (ohm-m)
RhoXY
RhoYX
Smoothed (D +)
Phase (deg)
PhaseXY
PhaseYX
Smoothed (D +)

SCIENTIFIC PAPERS

(1) **G. Mitjanas, J. Ledo, A. Macau, G. Alías, P. Queralt, F. Bellmunt, Ll. Rivero, A. Gabàs, A. Marcuello, B. Benjumea, A. Martí, S. Figueras (2021).** *Integrated seismic ambient noise, magnetotellurics and gravity data for the 2D interpretation of the Vallès basin structure in the geothermal system of La Garriga-Samalús (NE Spain).* Geothermics, 93, 102067. *https://doi.org/10.1016/j.geothermics.2021.102067.*

(2) **G. Mitjanas, J. Walsh, E. Roca, G. Alías, P. Queralt, J. Ledo.** *The importance of structural complexity in locations of geothermal systems: a case of study in the Catalan Coastal Ranges (NE Spain).* Ready to be submitted to *Geothermics.*

Geothermics 93 (2021) 102067

Contents lists available at ScienceDirect

Geothermics

journal homepage: www.elsevier.com/locate/geothermics

Integrated seismic ambient noise, magnetotellurics and gravity data for the 2D interpretation of the Vallès basin structure in the geothermal system of La Garriga-Samalús (NE Spain)

G. Mitjanas [a,*], J. Ledo [a], A. Macau [c], G. Alías [b], P. Queralt [a], F. Bellmunt [c], Ll. Rivero [b], A. Gabàs [c], A. Marcuello [a], B. Benjumea [c], A. Martí [a], S. Figueras [c]

[a] Departament de Dinàmica de la Terra i de l'Oceà, Universitat de Barcelona, C/ Martí i Franquès s/n, 08028, Barcelona, Spain
[b] Departament de Mineralogia, Petrologia i Geologia Aplicada, Universitat de Barcelona, C/ Martí i Franquès s/n, 08028, Barcelona, Spain
[c] Institut Cartogràfic i Geològic de Catalunya (ICGC), Parc de Montjuïc, 08038, Barcelona, Spain

ARTICLE INFO

Keywords:
Geothermal exploration
Method combination
HVSR method
Magnetotelluric method
Gravity method

ABSTRACT

The integration of geophysical methods, together with the previous information of the Vallès basin area, has resulted in the creation of a new conceptual model that explains La Garriga-Samalús geothermal system. The integration of complementary geophysical methods seems to be a good option for the preliminary stages of a geothermal system exploration, especially in urban areas.

An integrated seismic ambient noise, magnetotellurics, and gravity methods were used to determine the geological units and structures which control the La Garriga-Samalús geothermal system. The 2D resistivity and density models have allowed the identification of the four main units which regulate the geothermal system: the Miocene basin, the Prelitoral Range unit, the Vallès Faut Zone, and the Paleozoic basement. The interpretation of our models set the Vallès Fault Zone, which is characterized by an anomalous low resistivity and low density, as the main path for the hot fluids. Moreover, the geophysical characterization established a new geometry for the Miocene basin. The Miocene basin presents a stepwise morphology, with the minor thickness towards the fault and an increasing thickness towards the center of the basin. This geometry seems to be related to synthetic normal faults.

These results have evidenced that, although, in some geothermal systems, the warm water may create an insufficient physical contrast; the appropriate use of some techniques can still be useful for the exploration of medium and low-temperature geothermal systems.

1. Introduction

The role of geophysics in the exploration of geothermal resources has been discussed in several review papers (Banwell, 1973, 1970; Bodvarsson, 1970; Manzella, 1973; Meidav and Tonani, 1976; Pálmason, 1976; Shah et al., 2015), and it has been definitely set among the main disciplines which allows the characterization and monitoring of a geothermal system (Abdelfettah et al., 2018; Chambefort et al., 2016; Hermans et al., 2014; Hunt et al., 2009; Kana et al., 2015; Peacock et al., 2013).

Geophysical exploration involves taking measurements at or near the Earth's surface that are influenced by the internal distribution of physical properties. The analysis of these measurements can reveal how the physical properties of the Earth's interior vary vertically and laterally, and consequently, interpret the geology and the structural features of the subsurface (Kearey et al., 2002). In a geothermal system context, the geophysical methods do not just allow the structural characterization of the subsurface, key parameters like temperature or fluid content, can be also indirectly estimated by their utilization (Georgsson, 2009; Leeuwen, 2016; Shah et al., 2015).

In recent years, geothermal exploration has put the spotlight on urban areas. (Di et al., 2006; Lüschen et al., 2014; Moeck et al., 2015; Yousefi et al., 2019; Zhang et al., 2012). This renewable energy has an enormous potential in populated regions, where the demand is continuously growing and there is a need of reducing the reliance on highly polluting energies (Kraft et al., 2009; Schiel et al., 2016). In this

* Corresponding author.
E-mail address: gmitjanas@ub.edu (G. Mitjanas).

https://doi.org/10.1016/j.geothermics.2021.102067
Received 9 June 2020; Received in revised form 10 February 2021; Accepted 14 February 2021
Available online 2 March 2021

geographical context, the development of geophysical surveying, properly applied, can optimize exploration programs by maximizing the rate of ground coverage and minimizing the drilling requirement (Kearey et al., 2002). Hence, urban areas are set as an important geographical context to apply the geophysical methods for geothermal exploration, but not in all the geological contexts their application would have great results. The physical property contrast in the subsurface of the study area would condition the quality of the geophysical results (Benson et al., 2003).

Most of the geophysical prospections in geothermal exploration are related to high-temperature geothermal systems (fluid temperature >150 °C), which are commonly found in exceptional geological areas, like volcanic or seismically active areas (Jousset et al., 2011; Khodayar and Björnsson, 2014). The hydrothermal alteration products or also the high-temperature contrast can allow an easy characterization of this kind of system by using geophysical methods (Maithya and Fujimitsu, 2019; Rodríguez et al., 2015). However, in medium and low-temperature systems, sometimes there is an insufficient physical contrast from the host rock to easily detect the geothermal reservoir or to detect its consequence alteration cap (Soengkono et al., 2013). Even that, geophysical methods are still useful to characterize the geothermal system by its geological characterization as well as the detection of some conditioning factors, for example, the fractured zones (Arango-Galván et al., 2011; Nieto et al., 2019; Thanassoulas and Xanthopoulos, 1991).

Two of the geological contexts in which geophysical methods can play an important role in medium-temperature geothermal systems are: systems related to sedimentary basins (Viseras, 2002) and systems related with fractured crystalline rocks (Lewis and Haeni, 1987). Previous studies (Calcagno et al., 2014; Mahajan et al., 2011; Rao, 1986) showed that different physical properties such as density or acoustic impedance reveal a great contrast between the basement and the sedimentary basin. Likewise, in fractured crystalline rocks, different physical properties, e.g. the electrical resistivity, can show a great contrast between the fractured and the fresh crystalline rock (Kirkby et al., 2016; Lewis and Haeni, 1987; Mandal et al., 2019; Thanassoulas and Xanthopoulos, 1991). In this way, geophysical methods allow a preliminary delimitation and characterization of the geothermal reservoir, which is essential for the determination of the system magnitude.

Moreover, the use of geophysical methods in heterogenous media may be particularly challenging. This is because the inversion process of geophysical data is inherently non-unique, hence, a variety of Earth models may fit the data equally well. Even so, as it has been demonstrated in previous studies (Ars et al., 2019; Gabàs et al., 2016; Gallardo et al., 2012; Garambois et al., 2002; García-Yeguas et al., 2017; Low et al., 2020; Mandal et al., 2019), the combination of different physical properties allows a better constraining of the models, and the interpretation can be greatly improved.

In the region of interest, the Catalan Coastal Ranges (NE Spain), several hot springs with different chemical composition and different sources can be found. Particularly, in La Garriga town there are several bicarbonate-sodic hot springs in which water comes out at temperatures of around 60 °C. A few kilometers from those hot springs (2−3 km), in Samalús village, a slight thermal anomaly (17−22 °C) was detected in some open shallow wells (10−26 m) (IGME, 1977). For this reason, during the 80's, and due to the growing interest in geothermal energy, six exploratory boreholes were made in Samalús area by the Geological Survey of Spain (IGME, 1986, 1984a, 1982). These boreholes allowed a first characterization of the lithologies as well as a temperature gradient estimation. Temperatures of around 90 °C were recorded at 1000 m depth (IGME, 1986). Currently in La Garriga-Samalús area, several spas benefit from these hot waters.

Although several works about this geothermal system were published after the boreholes construction (Canals et al., 1989; Cardellach et al., 2003; Fernàndez and Banda, 1990, 1988), many important aspects, such as the Vallès fault and the Miocene basin geometries, or the system which controls the circulation of hot water, are still poorly understood.

Thus, in order to bring new light to those questions we propose an integrated geophysical survey using H/V spectral ratio of seismic ambient noise (HVSR), magnetotelluric (MT) and gravity methods for the sub-surface characterization of La Garriga-Samalús geothermal system, in the Vallès basin (NE Spain). The derived physical properties, as the acoustic impedance, electrical resistivity, and density, will be used to characterize the basin geometry and the main fluid paths.

1.1. Geological setting

The Catalan Coastal Ranges (CCR), in the NE of Spain, constitute the onshore expression of the northeastern sector of the margin, which separates the thinned continental crust of the Valencia trough from the thickened crust of the Iberian plate (Gallart et al., 1990; Vidal et al., 1995). In this sector, the crust displays a well-developed horst and graben structure, composed of several NE-SW to ENE-WSW striking blocks. The two longitudinal mountainous chains of the CCR are the Prelitoral and Litoral ranges, which are separated by the Vallès-Penedès half-graben (Fig. 1).

Our study area is located in the CCR northeastern limit, where the Prelitoral range is limited from the Vallès basin by the Vallès normal fault. In this area, the main geological units are the Hercynian granodiorite which thrusts Paleozoic materials of the Montseny massif, and the Miocene deposits of the Vallès basin (Fig. 2). During the Paleogene extension, the Vallès fault was active and the basin was fed largely from the Prelitoral range, forming Miocene alluvial fans. In our study area, these deposits are the proximal facies of alluvial fans (Cabrera, 1981), constituted by conglomerates, sandstones and arkosic clays, which sometimes include granitic and Paleozoic boulders (IGME, 1985).

Few available seismic profiles exist around the major structure, the Vallès normal fault, but they are mostly located in the center of the

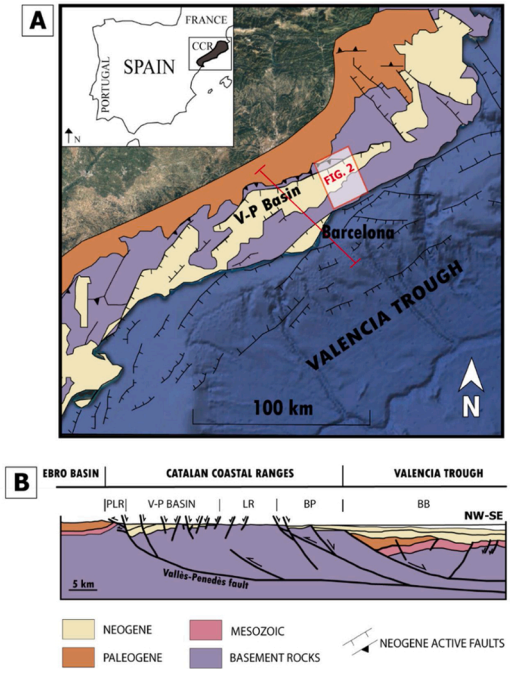

Fig. 1. A) Structural map of the Valencia trough, showing the Catalan-Valencian domain (modified from Martí et al., 1992). The red line indicates the location of the cross-section (B). The red square localizes the study area (see Fig. 2). B) Cross section of the Catalan Coastal Ranges and the Valencia trough (modified from Santanach et al., 2011). (V-P: Vallès-Penedès; PLR: Prelitoral range; LR: Litoral range; BP: Barcelona Plain; BB: Barcelona Basin). (For interpretation of the references to colour in this figure legend, the reader is referred to the web version of this article).

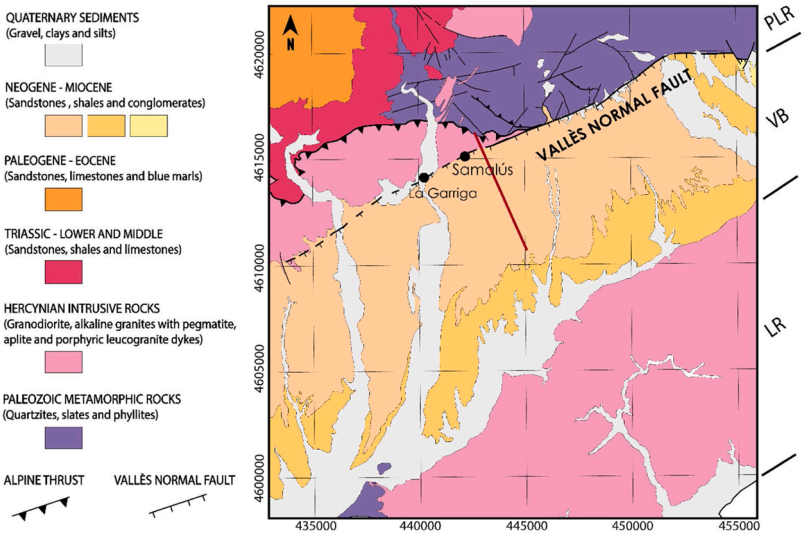

Fig. 2. Geological map of the studied area 1:50.000 (modified from ICGC, 2006) (PLR: Prelitoral range; VB: Vallès basin; LR: Litoral range).

Vallès-Penedès basin, significantly far from our study area (Gaspar-Escribano et al., 2004; Roca et al., 1999; Santanach et al., 2011). In these seismic interpretations, the Vallès fault is characterized by a listric geometry with the consequent roll-over in the Pliocene-Miocene hanging-wall (Roca et al., 1999; Sàbat et al., 1997); and also characterized by a detachment depth located in the lower/upper crust boundary (13–15 km) (Bartrina et al., 1992; Roca and Guimerà, 1992). All these previous authors identified the major thickness of the Miocene deposits next to the fault, which in some areas reaches up to 3000 m. Several later works extrapolated this roll-over geometry from the center of the Vallès-Penedès basin to the Vallès northeastern limit, near our study area (Canals et al., 1989; Cardellach et al., 2003; Fernàndez and Banda, 1990, 1988).

The main local knowledge of La Garriga-Samalús area comes from the geothermal prospection made by the Geological Survey of Spain (IGME) during the 70's and the 80's (IGME, 1986, 1985, 1984b, 1984a, 1982, 1977). Due to the presence of some hot springs which evidenced a geothermal reservoir, they constructed six exploration boreholes in Samalús village (Fig. 3). After that, they were able to characterize the sedimentary rocks of the Miocene basin as intercalations of arkosic sandstones and shales, and discordant conglomerates; as well as the basement rock, which was mainly a granitic column (IGME, 1986). They also intersected the Vallès fault, integrated by hydrothermal cataclasites, and with a fault plain dip between 73 and 75 degrees. Of all the boreholes reports, it is worth highlighting the S3 and S6 results.

The S3 borehole (600 m deep) (IGME, 1984a) was located a bit farther from the fault trace. It did not intersect the fault plain, and hence, neither the cataclastic basement rock. Nevertheless, it showed

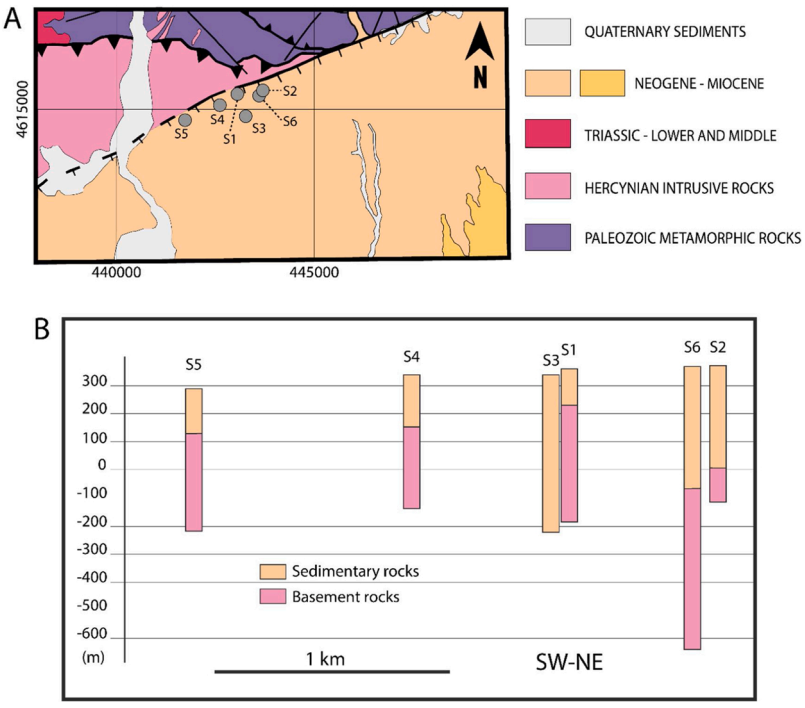

Fig. 3. A) Location of the geothermal exploration boreholes (IGME, 1986, 1984a, 1982). B) Basin-basement limit in some of the exploration boreholes. The S3 borehole (of 558 m) did not ridge the basement.

interesting results, noting that the deeper and permeable parts of the Miocene basin, were also saturated in hot water (60 °C). This hot water is not set as thermal water, it would be meteoric water warmed by thermal conduction (IGME, 1984a).

The S6 borehole was the deepest (IGME, 1986), and measured 90 °C at 1000 m depth. Studies of geothermometry and fluorite inclusion suggested that the maximum temperature of the geothermal system can be as high as 130 °C (IGME, 1986).

The actual geological model is characterized by a sub-vertical normal fault and a horst structure in the middle of the Vallès basin (Granollers horst) (Fig. 4A). This horst structure divides the basin in two parts: the northwestern sub-basin, which would have more than 3000 m thickness next to the Vallès fault, and the southeastern one, with 2000 m thickness (IGME, 1985). The preliminary study by the Geological Survey of Spain included a geoelectrical, gravity and seismic prospection in which they detected a resistive horizon between 200−500 m depth, in contact with the fault. This resistive layer was interpreted as compacted conglomerates (IGME, 1977) instead of crystalline basement. So in later works (IGME, 1986, 1984a) they assumed that the fault is an unique plain and that the resistive body is the conglomeratic layer, although any of the boreholes did not prove the model.

After the IGME studies, this geological model has been used to understand the geothermal system of La Garriga-Samalús, which is defined as a "forced convection" geothermal system (Fernàndez and Banda, 1988). In this kind of systems, where the thermal gradient is set as a "normal", the descending path needs to be deep and slow in order to provide high fluid temperatures. So, meteoric water would infiltrate down to several kilometers in the Prelitoral range (PLR), and then, the cataclastic granite zone in the Vallès fault core would allow a rapid ascent of the fluid (Fig. 4B), which is required to minimize conductive heat loss along the flow path. (Fernàndez and Banda, 1988; Sanchez-Guzman and Garcia De la Noceda-Marquez, 2005).

To sum up, both the general and local structural schemes of the area are characterized by a significant fault displacement (of at least 3 km), showing an important Miocene deposit thickness next to the fault. As explained below, our results challenge the current conceptual model of the system represented in Fig. 4.

2. Geophysical data acquisition and processing

Three complementary geophysical methods, H/V spectral ratio of seismic ambient noise (HVSR), magnetotellurics (MT), and gravity, have been used to characterize the subsurface structural geology which condition the geothermal system of La Garriga-Samalús. Each of these methods deals with different physical properties (acoustic impedance, electrical resistivity, and density), which allow us high detection capacities of different system elements. In Table 1 we present the three methods with the related physical parameter, and their main uses in geothermal exploration.

Table 1
Geophysical method, parameter of interest, and main uses in geothermal exploration (Georgsson, 2009; Hersir and Bjornsson, 1991; Kana et al., 2015).

HVSR Seismic velocity	MT Electrical resistivity	Gravity Density
• Basin-basement boundary • Faults delineation	• Rock composition • Fracturing and porosity • Alteration of the rocks • Water saturation • Salinity of the fluid • Temperature	• Rock composition • Subsurface structure • Porosity • Saturation of rocks

With the aim of constructing a new 2D conceptual model of the geothermal system and characterizing its structure, we have used these geophysical data and three deep exploratory boreholes (IGME, 1986, 1984a, 1982). Both MT and HVSR stations are located along the same profile (Fig. 2), which is 6 km long, and has an NNW-SSE orientation. Although the gravity stations cover an area, the final 2D density model will be also on the same profile.

2.1. H/V spectral ratio data

The horizontal-to-vertical spectral ratio technique applied to seismic ambient noise recordings (Bard, 1999; Nakamura, 1989) allows to identify large impedance contrasts between sediments and underlying bedrock, and determine the soil fundamental frequency. This frequency (f_0) is related to the average shear-wave velocity for the soil column (Vs) and the overburden thickness (H) using the following expression (Bard, 1985):

$$f_0 = \frac{V_S}{4 \cdot H} \quad (1)$$

Therefore, the soil fundamental frequency distribution is an indicator of the bedrock geometry in the area: a decrease in the soil fundamental frequency corresponds to an increase in the bedrock depth.

The main requirement in applying H/V method to calculate the sediments fundamental frequency (f_0) is that there must exist a sharp acoustic impedance contrast between sediments and bedrock, being the basement rock acoustic impedance at least twice than the sedimentary one (Fäh et al., 2001; Lachet and Bard, 1994). This method, originally used in seismic microzonation studies, can rapidly provide a robust estimate of the basement-basin limit depth and its geometry (Ibs-Von Seht and Wohlenberg, 1999).

For this experiment, 25 sites of HVSR measurements were recorded using a SARA SL06 datalogger connected to one Lennartz 0.2 Hz LE-3D/5 s three-component seismometer. The length of the seismic noise records ranges between 10 and 70 min, depending on the expected

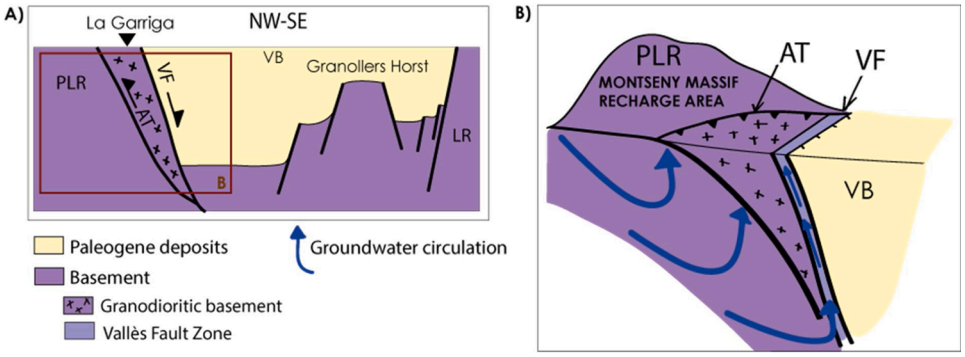

Fig. 4. Conceptual model of La Garriga-Samalús geothermal system. A) Structural model of the Vallès basin near La Garriga (modified from Fernàndez and Banda, 1988; Bertran and Tarragó, 1996). B) Hot-water circulation model (modified from Fernàndez and Banda, 1988) (PLR: Prelitoral range; LR: Litoral range; VB: Vallès basin; VF: Vallès fault; AT: Alpine thrust).

bedrock depth. The sampling frequency was fixed at 200 Hz. The average distance between the seismic noise measurement points was about 300 m. The H/V curves were calculated using the *Geopsy* software (http://www.geopsy.org), following this expression:

$$\frac{H}{V} = \frac{\sqrt{\frac{S_{NS}^2 + S_{EW}^2}{2}}}{S_v} \quad (2)$$

where S_{NS}, S_{EW} and S_V are the magnitudes of the spectrum Fourier method of north–south, east–west and vertical components, respectively. The Fourier spectrum for each component was smoothed in overlapped windows by 50 %. Anthropogenic noise was removed using a STA/LTA antitrigger algorithm (Lee and Stewart, 1981). The criteria used for the interpretation of the H/V peaks have followed the guidelines of the Site Effects Assessment using Ambient Excitations (SESAME) project (Bard and SESAME-Team, 2004).

2.2. Magnetotelluric data

The magnetotelluric method (MT) involves measuring the temporal fluctuations of the horizontal components of the natural electromagnetic field at the Earth's surface to infer the lateral and vertical variations of electrical conductivity of the Earth's interior (Chave et al., 2012). Magnetotelluric data were acquired at 16 sites along an NNW-SSE profile of approximately 6 km length from the Prelitoral range and across the Vallès basin in 2016, with the stations placed in rural areas, 2−3 km away from the main city, La Garriga. The site spacing ranges between 100 and 600 m. Measurements were carried out using the multichannel geophysical measurement system Metronix-ADU06 and Metronix-ADU07, using two induction coil magnetometers MFS-06 and four non-polarizable electrodes forming two dipoles in two orthogonal directions (N-S and E-W). The distance between electrodes of each dipole was around 50 m for all the stations. Natural electromagnetic field fluctuations were recorded at each site between 3 and 12 h, using sampling frequencies of 128 Hz and 4096 Hz.

The MT data was acquired near an urban area, with an intensive industrial and farming activity, what induces the presence of cultural noise. The most common sources of cultural noise are power lines and stations, electrified railways, electrified fences, power generators, and the corrosion protection systems used in oil and gas pipelines (Szarka, 1988); and all these sources are present in the Vallès basin. To detect and characterize this cultural noise, the time series were analyzed in the time-frequency domain. We considered that the cultural noise sources, in contrast to natural sources, generate an electromagnetic signal which is linearly polarized in a specific direction (Junge, 1996; Szarka, 1988; Zonge and Hugues, 1991), which allows us to distinguish between both kinds of signals. In order to work in the time-frequency domain, the data were processed using a Wavelet Transform-based scheme (Escalas et al., 2013). After the identification of the time and frequency intervals which are mostly affected by cultural noise, we discarded them from the temporal series, and thereby, reduced the noise sources effect. Figs. S1 and S2 (supplementary material) show a scalogram of the electric field at different times, and the comparison between apparent resistivities and phases with and without the noisy time series.

During data processing, we also used the remote reference technique (Gamble et al., 1979). For this technique, we used a magnetotelluric station that is less affected by cultural noise or that its cultural noise is not related to the measuring station's noise. Correlating the remote and measuring signals we obtained an increment in the signal-to-noise ratio. The final impedance tensor components were obtained for the period range 0.001–10 s. To retrieve the strike of the regional structures and the regional impedance tensor, we followed the scheme of McNeice and Jones (2002), based on the Groom and Bailey decomposition method (Groom and Bailey, 1989). Considering an error floor for the impedance components of 5%, we obtained a value of the regional strike of N60E. This value agrees with the main geological strike of the studied zone. Decomposition RMS misfits below 2 (Fig. 5) are considered reliable and indicative that a 2D model interpretation of the data is appropriate. Moreover, the regional strike of the multi-site multi-frequency impedance tensor decomposition is consistent with the strike of the main geological structures of the zone. The 2D impedance tensor was subject to stringent quality control. The aim of this control is removing low-quality points; therefore, they would not be included in the inversion process.

2.3. Gravity data

The gravity map covers an area of 110 km^2 with 354 gravity measurements, 214 of which were newly acquired (Fig. 6A). We used previous available Bouguer anomaly data from the Gravity Map of Catalunya 1:250 000 (IGC, 2012) (113 sites) and from a master's thesis coordinated by the Catalan Geological Survey (ICGC) (27 sites).

The new gravity sites were acquired during 2019, around La Garriga-Samalús area. The distances between all the measurement points range between 50 and 200 m, with most of the measuring stations located along forest roads. This irregular distribution was caused by the difficult access to some parts of the area. Even so, we got a high density of sites near the profile, where the HVSR and MT measurements were carried out.

For the acquisition, we used a Lacoste & Romberg gravity meter, and the bases employed belong to the Fundamental Gravimetric Network of Spain, originated from the International Gravity Standardization Network (IGSN 71) (Casas et al., 1987; Morelli et al., 1972).

Likewise, the most important correction made in this area with a significant topography is the terrain correction. Its procedure is based on the Hammer zones (Hammer, 1939) which in this case we have set to the standard distance, 167 km (Nowell, 1999). The terrain correction was made using the *Gravity and Terrain Correction extension of Geosoft Oasis Montaj Programs (2008)*, which allows the calculation of the regional terrain correction from a coarse regional Digital Elevation Model (DEM) draped over a more finely sampled local DEM. This produces a regional correction grid which represents terrain corrections beyond a local correction distance, and this can be re-used to calculate detailed corrections at each observed gravity location. This process uses a combination of the methods described by Kane (1962) and Nagy (1966).

Considering the great variety of lithologies present, each with a particular range of densities, it was decided to employ a single reduction density corresponding to the mean density of the upper crust (Simpson and Jachens, 1989). Thus, the Bouguer anomalies were computed using a reduction density of 2.67 g/cm^3. The ellipsoid adopted for the calculation of theoretical gravity was the WGS84, which includes corrections caused by attraction produced by atmospheric mass.

From the Bouguer anomaly value of every site, the Bouguer anomaly map was interpolated (Fig. 6B). This map contains all the gravity anomaly effects generated by the crustal structure and other effects generated by shallower local structures with enough density contrast. As our objective was to define the near surface structure, we decomposed the Bouguer anomaly into a regional component and a residual component. This separation was carried out by assimilating the regional

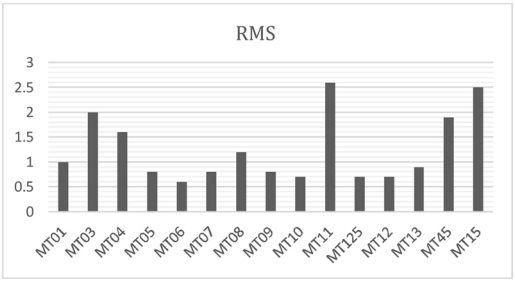

Fig. 5. RMS error of each individual MT site fitting the regional strike of N60E.

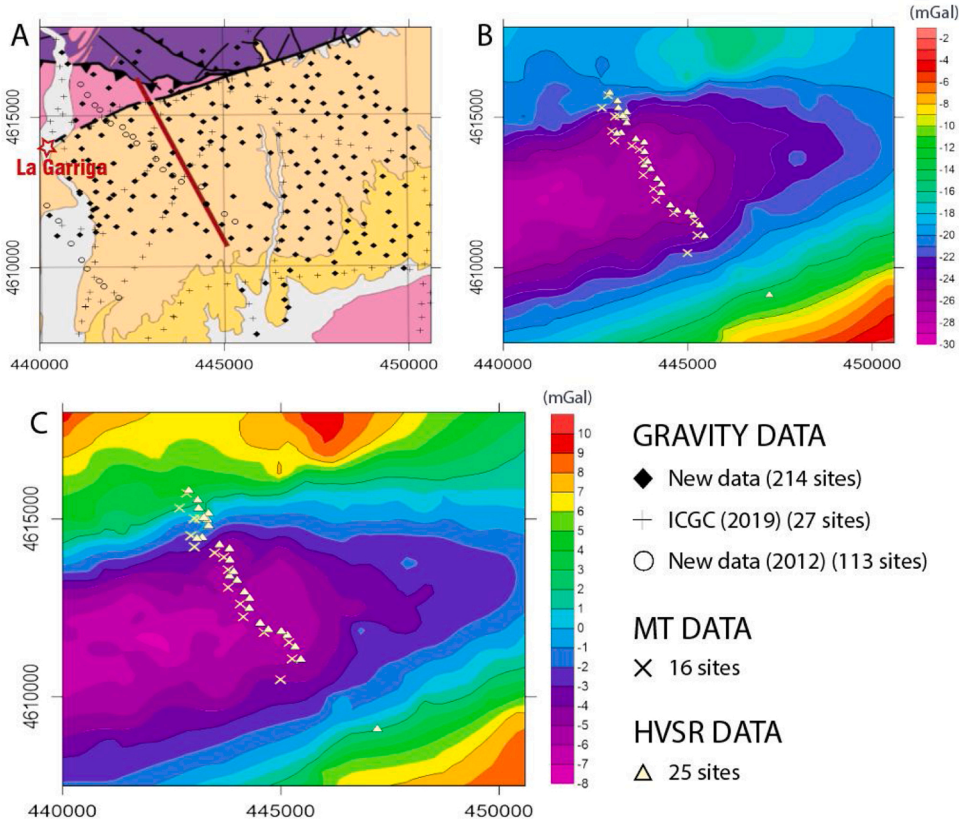

Fig. 6. A) Geological map with the gravity sites and the location of the profile. B) Bouguer anomaly map with the MT and HVSR sites. C) Residual anomaly map with the MT and HVSR sites.

anomaly to a first-degree polynomial surface, and therefore assuming the NE-SW trending of the Catalan Coastal Ranges.

The Residual Anomaly map (Fig. 6C) illustrates a large negative anomaly with an ENE-WSW direction. This anomaly reaches –8 mGal over the center of the Vallès basin. Towards the north, there is a high slope with higher values, reaching 10 mGal. From the negative anomaly to the south, the values increase slightly more gradually, as well as towards the NE.

3. Inversion and results

3.1. H/V spectral ratio

We have obtained the H/V ratio curves at each measurement point. Most of them (23 sites) show a clear peak related to the soil fundamental frequency at each site. However, in two cases the H/V spectral ratio shows a flat curve without any significant peak, indicating that the basement crops out or is very shallow. Fig. 7A shows the soil fundamental frequency values across the study profile, evidencing a clear distribution. The minimum of 0.21 Hz (red dots in Fig. 7A) is in the south-east of the profile, close to the center of the basin. From this point,

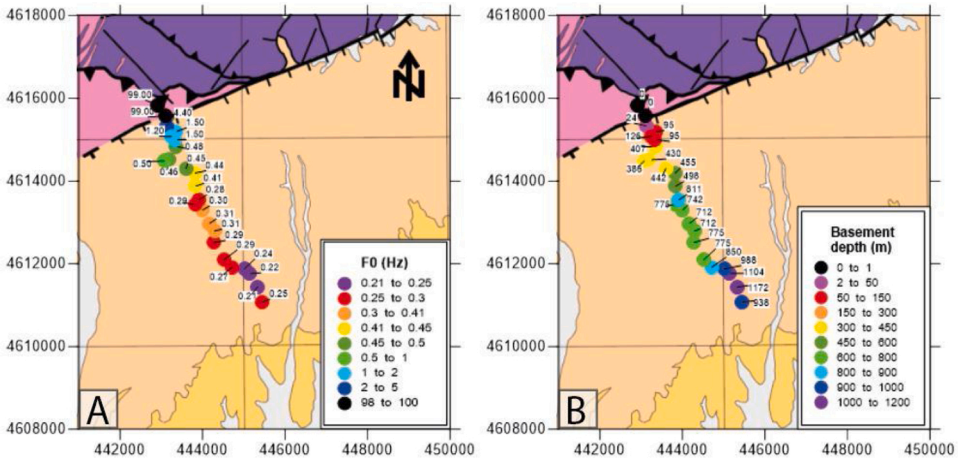

Fig. 7. A) Soil fundamental frequency values obtained from HVSR throughout the study area. B) Basement depth calculated from soil fundamental frequency using the relationship proposed by Ibs-Von Seht and Wohlenberg (1999).

the soil fundamental values increase towards the northwest, as we get closer to the Vallès fault, reaching a maximum of 4.4 Hz (blue dots in Fig. 7A). The sites without significant peaks (black points in Fig. 7A) are located northwest of the Vallès fault, in a probably rocky area. Thereby, we can get a first draft of the soil-rock boundary geometry based on the soil fundamental frequency values, which shows that the deepest basement would be in the center of the basin and the shallowest would appear near the Vallès fault.

The next step will be the conversion of the soil fundamental frequency (f_0) to basement depth (H). When shear-wave velocity information is available, the most straightforward method is to apply expression (1) to calculate sediment thickness. Usually, the shear-wave velocity profiles are not known. In this case, we can obtain basement depth using an empirical relationship between H and f_0 (Ibs-Von Seht and Wohlenberg, 1999):

$$H = a \cdot f_0^b \quad (3)$$

where *a* and *b* are empirical parameters strongly dependent on geological conditions, specifically on shear-wave velocity profiles. In most cases, bedrock depth was directly measured from boreholes, but it could also be calculated from the geophysical methods. The bibliography shows different empirical laws fitted in different geological environment: Ibs-Von Seht and Wohlenberg (1999) estimated in a deep Tertiary basin; Delgado et al. (2000) computed in a thin Quaternary deposits or Benjumea et al. (2011) calculated in a weathered granitic area.

This methodology has been applied in several Neogene basins near the Vallès basin (Benjumea et al., 2014; Gabàs et al., 2016; Macau et al., 2018). In these studies, the HVSR results have been compared with other geophysical exploration methods (seismic noise array technique, magnetotelluric method or even seismic refraction tomography). In all of them, it has been verified that the soil fundamental frequency is related to the contact between the bottom of the Neogene sediments and bedrock. The expression proposed by Ibs-Von Seht and Wohlenberg (1999) shows the best fit for a broad range of frequencies (Macau et al., 2018). Fig. 7B presents the bedrock topography from the values of the soil fundamental frequency and the equation proposed by Ibs-Von Seht and Wohlenberg (1999). Near the Vallès fault there is a sharp contrast of the soil fundamental frequencies. Thus, NW of the supposed Vallès fault trace there are no sediments and SE of the fault trace there is a step gradient reaching a sediment thickness of 400 m at 500 m from the fault. From this point the sediment thickness increases to the SE up to reaching 1200 m sediment thickness close to the end of the profile.

3.2. Magnetotelluric inversion and results

After rotating the MT data to the obtained strike angle of 60 °N, we

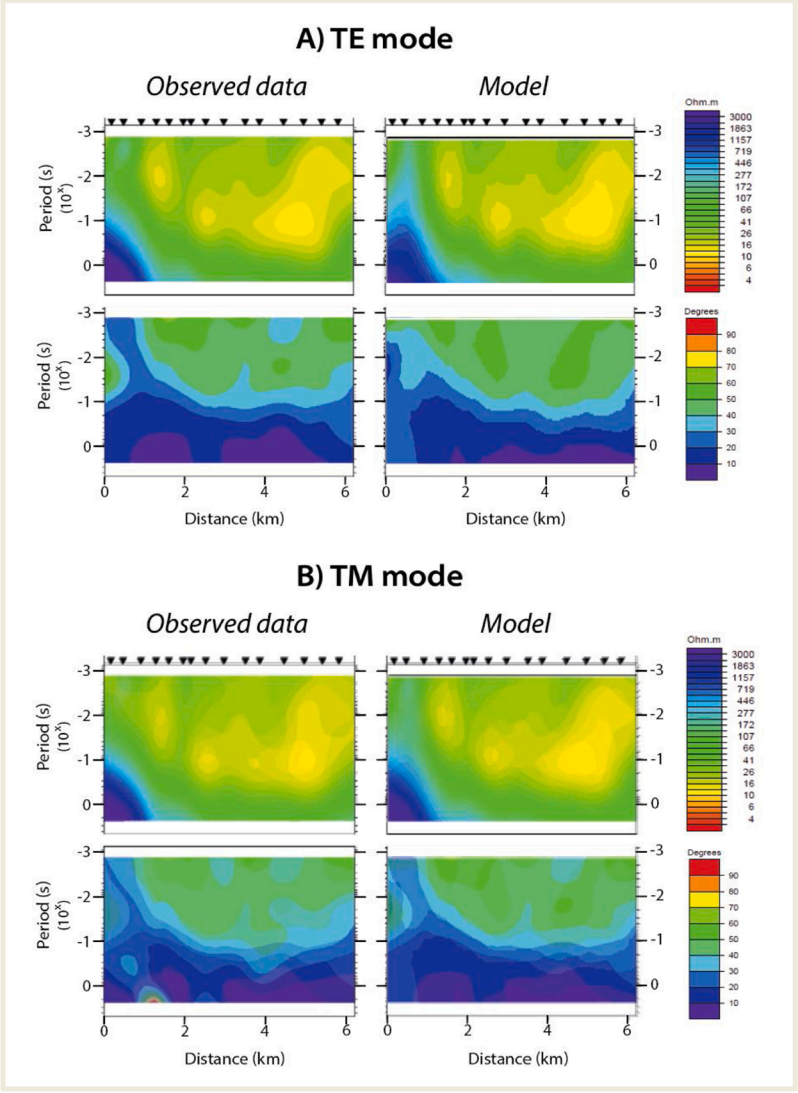

Fig. 8. Apparent resistivity (top) and phase (bottom) pseudosections of observed data and model responses for the TE (A) and TM (B) mode.

assigned the TE and TM modes to the main impedance components, and the related apparent resistivities and phases.

Simultaneous 2D inversions of TM and TE apparent resistivities and phases were undertaken using the nonlinear conjugate-gradient algorithm of Rodi and Mackie (2001), implemented in the Winglink software (Geosystem SRL). This algorithm simultaneously searches for the model which trades off the lowest overall RMS misfit with the smallest lateral and vertical conductivity gradients in a regularized manner. On average, we fit the logarithm of the apparent resistivity data to within 10 %, and the phases to within 2.9°. We used data from 15 MT stations – see Fig. S3 of Supplementary material (station MT2 was discarded because it was too near to the station MT3, and therefore, redundant). A final rms 1.2 was achieved. The initial model was a homogeneous half-space of 100 Ωm, with a mesh of 89 horizontal cells and 134 vertical cells, neither structural features nor conductivity discontinuities were imposed. Fig. 8A and B compare the resistivity and phase pseudosections of the observed data and model responses. Figure S4 of Supplementary material shows the apparent resistivity and phases curves comparison between the raw data and model responses for the whole dataset. The resulting final model is shown in Fig. 9, where the results of HVSR, as well as the boreholes information (IGME, 1986, 1984a, 1982), are also plotted. For the HVSR results, the maximum and the minimum limits of the bedrock depth have been calculated considering the standard deviation of the fit (black vertical lines in Fig. 9).

In the next lines, we present the description of the main geoelectrical bodies (Fig. 9: R1, C1, C2, and R2) and a general interpretation for these units. A more detailed interpretation will be presented in the Discussions section.

- **R1:** In the north-northwestern part of the model there is a geoelectrical unit which presents the highest resistivity values (>3000 Ωm). These values can be observed from the shallow structures to the deep parts of the model in his area. This high resistivity unit corresponds to the outcropping granitic materials of the Prelitoral range.
- **C1:** To the SE of R1, there is a subvertical band with lower resistivity values. The resistivity values increase gradually with depth, from 100 Ωm to 500 Ωm. This unit is assumed to be the fault plain and its associated fractured zone.
- **C2:** The model presents a near surface conductive geoelectrical unit. This unit has a wedge geometry, with its thickness increasing towards the SSE (from 500 m of thickness in the north-northwestern part to 1250 m in the southeastern part). The resistivity values vary from 1 Ωm to 200 Ωm. This upper unit is associated to the Miocene sediments which fill the basin (alluvial fans of shales sandstones and conglomerates).
- **R2:** Below the previous conductive unit (C2) there is a resistive zone with values between 500 Ωm and 3000 Ωm. In this case, we should consider that the high conductivity values of the C2 unit could affect the determination of the resistivity value underneath.

3.3. Gravity inversion and results

The residual anomaly map (Fig. 6C) shows a clear WSW-ENE geometry with negative values which are associated to the Vallès basin. Towards the NNW, the increasing values would be related to the Prelitoral range, which is characterized by denser materials (igneous and metamorphic Paleozoic rocks). The Vallès fault, which separates the Prelitoral range and the Vallès basin, should be traced in the steeper parts of the map, where the contour lines are closer. Towards the SSE the contour lines are not as close, so the contact between the Vallès basin and the Litoral range seems to be more gradual.

Fig. 6C also shows SW-NE variations in the negative anomaly, within the basin, which can be associated to lateral changes of basement depth. The lower values, and therefore, the major thickness of the basin are located close to our study area.

A 2-D forward model was constructed over the NNW-SEE profile, identical to the location of the MT-HVSR 2D model (Fig. 9). To create this geological model from the physical characteristics, we used the GM-SYS (Gemperle et al., 1991) profile modeling tool in Geosoft software. The procedure employed for forward modeling can be summarized in the following steps: (1) construction of a model from a priori geometry and density of the rock type; (2) fitting the model response to the observed data, and (3) refine the geometrical and physical parameters of the model. It is important to consider that this software results in a unique density value for each unit (instead of a range of density values), so the final densities should be regarded with caution.

As starting geometries to constrain the model we used the HVSR - MT profile (Fig. 9) and the three exploration boreholes S1, S3 and S6 (IGME, 1986, 1984a, 1982), dividing the model in the four main units (R1, C1, R2, C2). For the observed data, we extracted from the residual anomaly map (Fig. 6C), 42 representative points along the profile.

The first results of forward density modeling showed considerable differences between computed and observed gravity anomalies. These differences were minimized by adding more layers inside the C2 and a

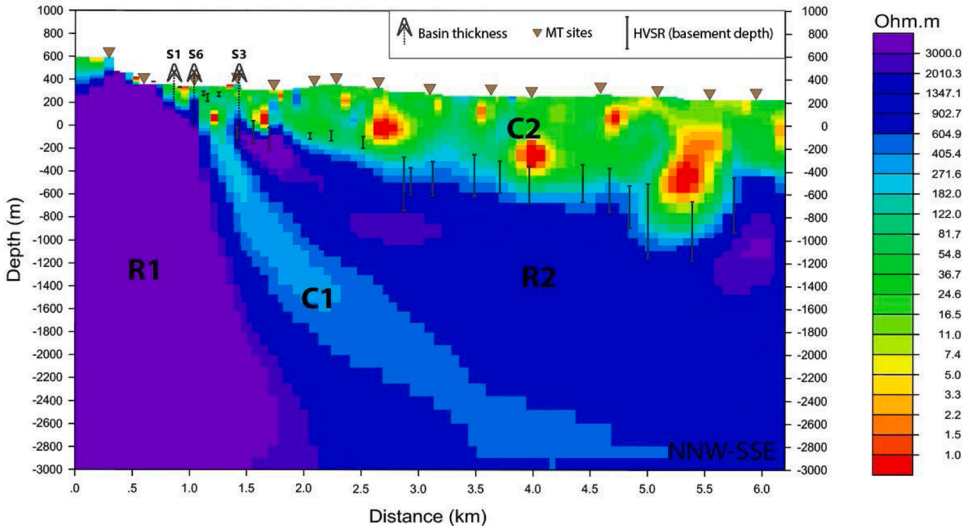

Fig. 9. Magnetotelluric model with the location of the MT and HVSR sites. The dashed lines represent the depth of the sedimentary unit - data from S1, S3 and S6 boreholes (IGME, 1986, 1984a, 1982). The vertical solid lines correspond to the range depth of the basin-basement limit obtained using the HVSR method and considering the standard deviation of the fit.

superficial layer in the upper left part of the R1. The criteria used for the differentiation of this new layers were the rounded low-resistivity bodies of the C2, and the low-resistivity anomaly in the left margin of the model (Fig. 9).

The final model was obtained through trial-and-error data fitting, partially fixing the geometry of the bodies, and inverting the density values. The final density model with the best fit (Fig. 10), and consistent with the previous geological and geophysical data (Figs. 2 and 9), shows a good tendance, with a low error value. Even that, in the northwestern part of the profile, some deviations between the observed data and the inversion curve can be observed. These adjustment issues correspond with the vertical presence of different density units, making it difficult to set a better fit for the calculated curve. This final density model presented in Fig. 10 can be divided into four major bodies:

- **D1**: this first major body comprises the D1_a, _b, _c, and _d minor bodies. These bodies have densities between 2.08 g/cm^3 and 2.84 g/cm^3. The high-density bodies (D1_b and D1_d), are related to the high conductivity parts of the basin (high-conductivity anomalies in C2, Fig. 9), and they appear as isolated bodies rather than in laterally continuous layers.
- **D2**: this second unit, located underneath the basin, has a density of 3.08 g/cm^3, the highest density value. Although in the MT-HVSR model (Fig. 9) there are some resistivity variations in this unit, the density model fits well with a unique density value. This homogeneity could be due to the low sensitivity of the density method at great depths or because there are not significant density changes.
- **D3**: this third unit has a density value of 2.55 g/cm^3. This body has a low-density value compared to the rest of units at these greater depths.
- **D4:** this forth major body includes the D4_a (2.25 g/cm^3) and D4_b (2.85 g/cm^3) minor bodies. In this case we have a high-density body with a small upper lower-density part in the north-northwestern margin.

4. Discussion

4.1. La Garriga-Samalús geological units

In this section we will combine all the obtained geophysical results in order to create a new geological model of the studied area. We have considered the compiled values of density and electrical resistivity (Manger and Nolan, 1963; Schon, 2015; Tenzer et al., 2011; Wald et al., 2013), as well as the geological map (Fig. 2), to assign the following geological units to our models: the Miocene basin, the Prelitoral range unit, the Vallès Fault Zone, and the Paleozoic basement (Table 2).

4.1.1. Miocene basin

In Fig. 11 we have compared the resistivity and density values of the sedimentary bodies (D1_*a*, *b*, *c*, and *d*, in Fig. 10) with compiled values of density and electrical resistivity for shales, sandstones, and conglomerates (Schon, 2015).

The D1_c and D1_d bodies are in the shales and sandstones ranges, but the D1_a and D1_b bodies are practically out of any range. Although their high-density values would link them with sandstones or conglomerates, the electrical resistivity values are very low. We have two proposals: deposits with high shales content, or water saturated sands and conglomerates. Considering the S3 exploration borehole (Fig. 3B), which recorded 560 m of Miocene basin without reaching the basement (IGME, 1984a), we could relate these bodies to sandy and conglomeratic lenses of the Miocene series. In the boreholes report (IGME, 1984a) the Miocene unit is described, in general, as a clayey-arkosic and conglomeratic unit, mostly impermeable; but beyond the 450 m, in S3, they detected sandy and conglomeratic lenses saturated in hot water (60 °C). Therefore, the low-resistivity values could be related to the presence of hot water in these permeable lenses.

In the Vallès-Penedès basin, all the sedimentary sequence of the Miocene consists mainly of proximal to distal-margin alluvial-fan sediments (Cabrera and Calvet, 1996; Gibert and Casanovas-Vilar, 2011; Roca et al., 1999). Specifically, our profile would be a section of the

Table 2
Summary of geological units and their electrical resistivity and density values.

GEOLOGICAL UNIT	Electrical resistivity (Ωm) (Fig. 9)	Density (g/cm^3) (Fig. 10)
Miocene basin (Mc)	C2: 1–200	D1a, b, c, d: 2.08–2.84
Prelitoral Range (PLR)	R1: >3000	D4: 2.67
Vallès fault zone (VZF)	C1: 100–500	D3: 2.27
Paleozoic basement (B)	R2: 500–3000	D2: 2.63

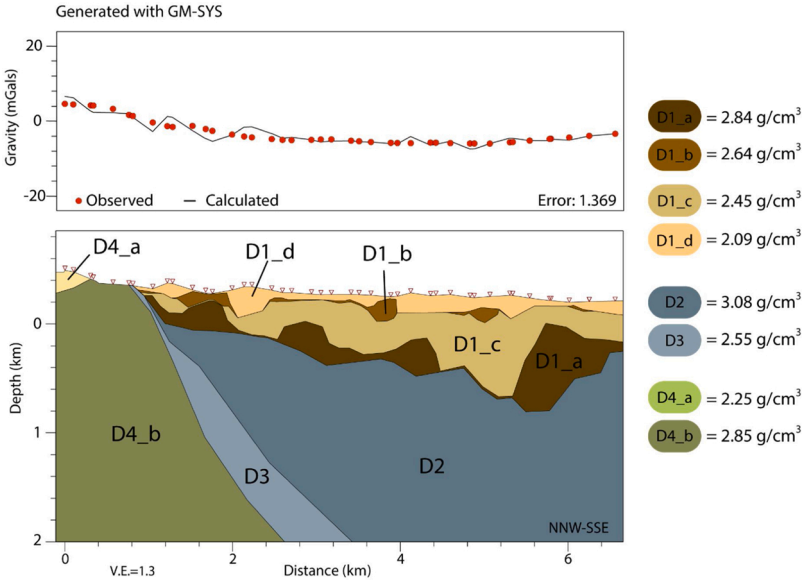

Fig. 10. Density model obtained from the gravity data inversion and constrained by the electrical resistivity model (Fig. 9), and the IGME exploration boreholes (IGME, 1986, 1984a, 1982).

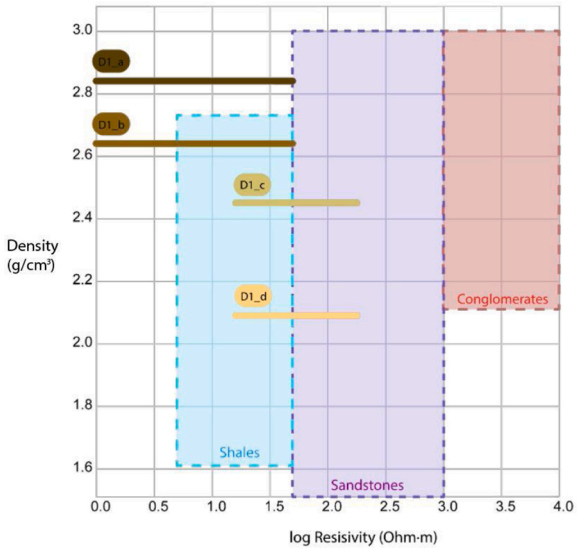

Fig. 11. Miocene sedimentary bodies of the density model (Fig. 10), plotted with the compiled density and resistivity values (Manger and Nolan, 1963; Schon, 2015; Tenzer et al., 2011; Wald et al., 2013) for shales (blue area), sandstones (purple area) and conglomerates (red area). (For interpretation of the references to colour in this figure legend, the reader is referred to the web version of this article).

proximal area of an alluvial fan, where the major supply direction comes from the northeast, perpendicular to our section (Roca et al., 1999). The geometry of this sedimentary unit is in line with the geometries of a typical alluvial fan depositional landform (Fig. 12). Precisely, the D1_a and D1_b bodies could be related to the coarse-grain deposits of the proximal area of an alluvial fan.

4.1.2. Prelitoral range unit

In Fig. 13 we have considered the rest of non-sedimentary units. In this figure we can associate the Prelitoral unit to the bodies D4_a and D4_b (R1 in Fig. 9), which correspond to the Paleozoic granodiorite and the altered Paleozoic metamorphic units, respectively. The granodiorite in the NNW part of the profile, with high resistivity and density values, thrusts the Paleozoic metamorphic materials as it can be observed in the geological map (Fig. 2).

4.1.3. Paleozoic basement

This unit corresponds to the R2 / D2 bodies, located under the Miocene basin. In Fig. 13 we can observe that this unit has a high-density value. In fact, the density value is 0.08 g/cm^3 higher than any of the ranges set. Obviously, this unit must have a high-density value since it is located at great depths. Even so, we should still consider that the unique value given by the software may have an error range.

This unit shows a broad range of electrical resistivity values, which could be due to the different rock composition, the porosity, the fracture degree, the temperature, the fluid content, and/or the mineral content. Even so, the low resistivity values of the Miocene basin could cause a screening effect on the underneath layers.

This basement body is an undifferentiated unit because it does not outcrop, therefore we do not know if it is formed by the Paleozoic metamorphic series, by the Paleozoic intrusive rocks (like the granodiorite), or both (Fig. 14A). Furthermore, if we take into account the exploration reports made by the Geological Survey of Spain (IGME, 1977), they considered that under the Miocene basin filling, there may be a thick conglomeratic unit related to the alluvial fans (Fig. 14B). Although the density and resistivity may not give us a clear differentiation between conglomerates and the Paleozoic rocks, we have interpreted that this high-resistivity and high-density body would be the Paleozoic basement. We consider that the electrical contrast between R2 and C2 (Fig. 9) is too high to be generated by the same sedimentary process and having similar grain sizes. Furthermore, our gravity map (Fig. 6) as well as the gravity inversion profile (Fig. 10) are consistent with our hypothesis.

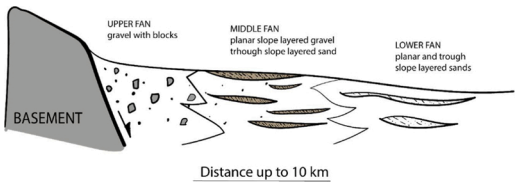

Fig. 12. Cross-section through a generalized alluvial fan. A large amount of gravel with rocks in the proximal range or upper fan whereby gravel, particularly in the distal fans, typically contain muddy matrix. There is a clear reduction in grain size toward the lower part of fans (Modified from Haldar and Tišljar, 2014; Moscariello, 2018).

4.1.4. Vallès Fault Zone (VFZ)

The D3 / C1 body is related to the Vallès Fault Zone (VFZ). Its low density and resistivity (C1 in Fig. 9) match with the results obtained in boreholes (IGME, 1986, 1984a, 1982), which detected a cataclastic zone with thermal circulation fluid evidences.

Fracturing and weathering increase the porosity of rock and consequently, reduces the bulk density; but also, if thermal water is present, the resistivity decrease. Therefore, this conductive body could act as the main path for the hot fluids.

4.2. A new geometry for the Vallès basin

One of the main results of this work is the determination of basin-basement limit geometry. The depth of the basement has been confirmed from the HVSR results and the MT model. We have also shown that the gravimetric anomaly is compatible with the observed geometry.

In previous studies of the Catalan Coastal Ranges, the maximum thickness of the Miocene deposits were imaged next to the Vallès fault (Gaspar-Escribano et al., 2004; Roca, 1994; Santanach et al., 2011), and some authors have extrapolated this geometry from southwestern parts of the basin to this study area (i.e. Fernàndez and Banda, 1988). In contrast, our results show a gradual increasing thickness of the Miocene unit, from the Vallès fault to the center of the basin. The geometry of the basin of our 2D model, which has a kind of stepwise morphology, could related this increasing thickness of the basin to other minor faults which dip in the same direction as the Vallès fault, in other words, it could be related to synthetic faults (Fig. 14A).

Our results confirm the existence of lateral changes along the Valles Fault Zone since this model differs from the previous ones made in other parts of the basin (Gaspar-Escribano et al., 2004; Roca et al., 1999; Santanach et al., 2011) (i.e. Figs. 1B and 4). As it is seen in the gravity data, the basin thickness changes laterally along the valley. This could reveal a more complex inner structure, with faults parallel to our profile direction. At the same time, this inner structure could condition the presence of the thermal anomalies in only some specific parts of the Vallès basin. So, although we have described this basin geometry in La Garriga-Samalús area, different models could coexist in different parts of the Vallès-Penedès basin.

4.3. La Garriga-Samalús geothermal system

An ideal geothermal system is formed by (1) an important heat source, (2) a geological formation which acts as a reservoir and (3) geological units or structures which act as seal layer (Gupta, 1980). A previous study (Fernàndez and Banda, 1990) demonstrated that force convection is the only mechanism capable of explaining this isolated

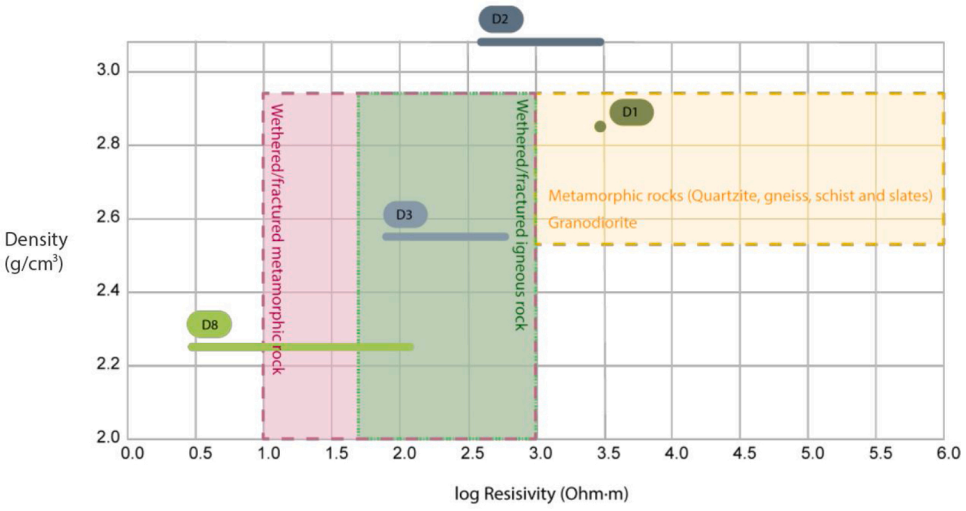

Fig. 13. Non-sedimentary bodies of the density model (Fig. 10), plotted with the compiled density and resistivity values (Manger and Nolan, 1963; Schon, 2015; Wald et al., 2013) for weathered/fractured metamorphic rocks (red area), weathered/fractured igneous rocks (green area), and granodiorite and metamorphic rocks which can be found near the study area (yellow area). (For interpretation of the references to colour in this figure legend, the reader is referred to the web version of this article).

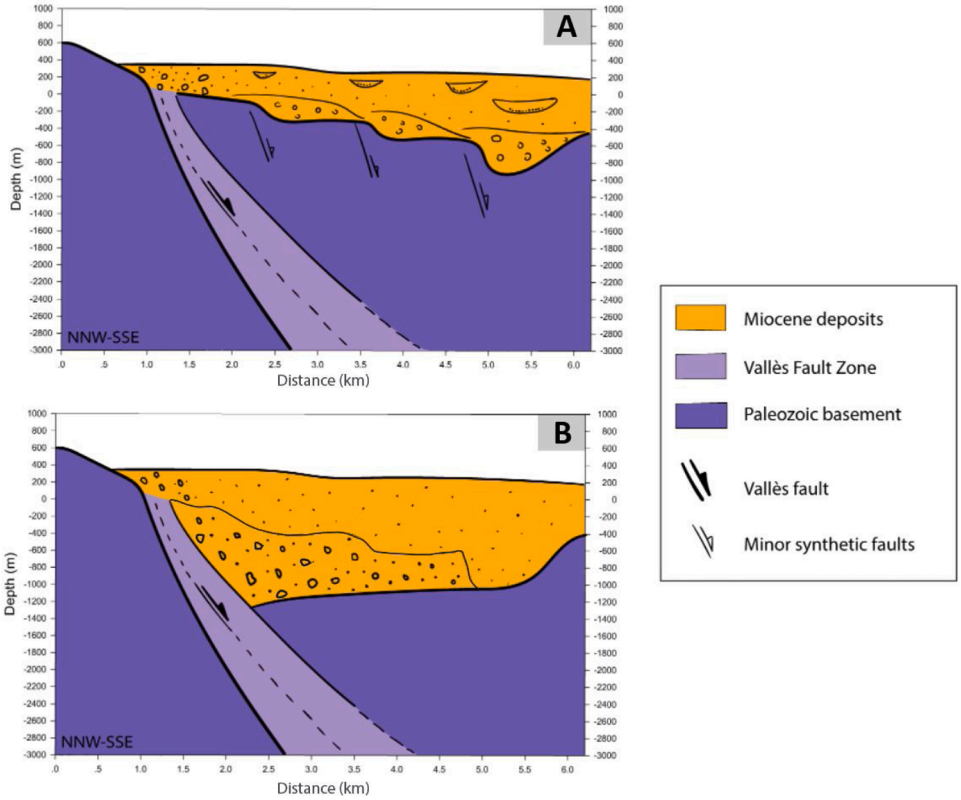

Fig. 14. Two possible interpretations of the MT-HVSR model. [A]: The R2 body (Fig. 9) interpreted as the Paleozoic basement unit. [B]: The R2 body (Fig. 9) interpreted as thick and compact conglomeratic deposits (IGME, 1977).

high geothermal gradient in La Garriga-Samalús area. The only condition would be a deep and slow descending path, and a conduit which allows a rapid ascent.

The structural characterization of this work is a key point for La Garriga-Samalús geothermal study, which has allowed the identification of this high-conductivity and low-density body, set as the Vallès Fault Zone (VFZ) (Fig. 15). The VFZ could act as a reservoir as well as the main ascending path for the hot fluids, and the impermeable layers of the Miocene basin could act as the seal layer in some parts of the system. On the other hand, the infiltration path has not been detected in our models, although in previous works was set in the Prelitoral Range (Fernàndez and Banda, 1990, 1988).

Furthermore, in terms of exploitation of geothermal energy, the permeable facies of the Miocene basin could not be ignored. In the electrical resistivity model (Fig. 9), potential saturated water zones have been detected, in addition to the hot meteoric water registered in the exploration boreholes (IGME, 1984a).

5. Conclusions

The present integrated geophysical study demonstrates that the combination of different geophysical methods, based on different physical properties, are an efficient option during the preliminary phase of the geothermal exploration.

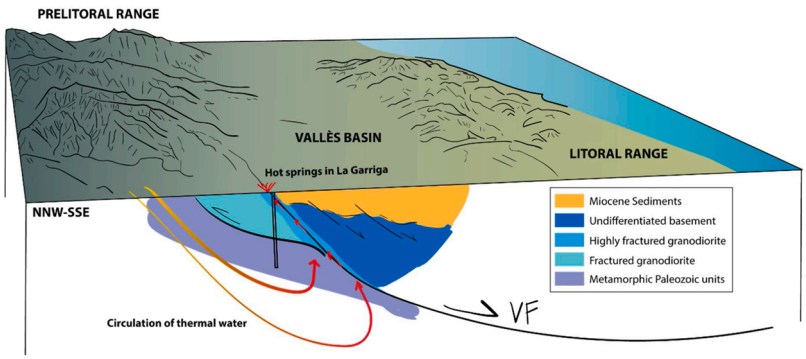

Fig. 15. Conceptual model of the La Garriga-Samalús geothermal system, with the new basin geometry. *Not to scale.

We have presented a multi-physics characterization of the La Garriga-Samalús geothermal system to create a new conceptual model. The HVSR, MT, and gravity results and the final joint interpretation have allowed the identification of four main bodies: (1) the Paleozoic basement, (2) the Vallès Fault Zone, (3) the Prelitoral range unit, and (4) the Miocene deposits. These results have also imaged a new geometry for the basin-basement limit located between 500 and 1250 m depth.

The final model is consistent with the available geological information of the area, although new structural and geological approaches have been defined. The new results indicate that in this area, the basin thickness increases gradually from the Vallès normal fault towards the south-east of the basin following a stepwise morphology, instead of having a roll-over geometry. At the same time, this new basin geometry could indicate the presence of minor synthetic faults. Although we propose this new geometry for the basin, the geology of the basement as well as the possible minor geological structures are not fully resolved. The interpretation of the R2 body remains in question because resistivity of compacted coarse grain conglomerates could be high enough (Schon, 2015), although the gravity and the HVSR interpretations do not corroborate the great fault displacement.

The geological and structural characterization of that geothermal system is the first step to try to understand the relevance of the geometry of the basin and its thickness in the geothermal fluid flow. The actual geothermal model fits with our geological model. The Vallès Fault Zone is confirmed as the main path as well as the reservoir for the hot fluids. Likewise, the coarse-grained permeable layers of the Miocene alluvial fans, which are in contact with this geothermal reservoir, should not be ignored as a potential secondary thermal reservoir.

Data availability

Datasets related to this article can be obtained asking to the corresponding author (gmitjanas@ub.edu).

CRediT authorship contribution statement

G. Mitjanas: Conceptualization, Methodology, Investigation, Writing - original draft, Visualization. **J. Ledo:** Conceptualization, Methodology, Investigation, Resources, Writing - original draft, Visualization. **A. Macau:** Methodology, Investigation, Writing - original draft, Visualization. **G. Alías:** Conceptualization, Methodology, Investigation, Writing - review & editing. **P. Queralt:** Conceptualization, Methodology, Investigation, Resources, Supervision, Writing - review & editing. **F. Bellmunt:** Investigation, Writing - review & editing. **Ll. Rivero:** Investigation, Writing - review & editing, Resources. **A. Gabàs:** Investigation, Writing - review & editing. **A. Marcuello:** Investigation, Resources, Writing - review & editing. **B. Benjumea:** Investigation, Writing - review & editing. **A. Martí:** Investigation, Writing - review & editing. **S. Figueras:** Investigation.

Declaration of Competing Interest

The authors declare that they have no known competing financial interests or personal relationships that could have appeared to influence the work reported in this paper.

Acknowledgements

This research was funded by the GEO-URBAN project (ERANET-GEOTHERMICA project no. 73117 and PCI2018-092943 Spanish Government - Ministerio de Ciencia, Innovación y Universidades); and the PIXIL project (project no. EFA362/19, co-financed by the INTERREG POCTEFA program of the European Regional Development Fund, and the University of Barcelona).

Mitjanas, G., also acknowledges the economic support from the University of Barcelona, for its pre-doctoral fellowship (APIF-2019).

Appendix A. Supplementary data

Supplementary material related to this article can be found, in the online version, at doi:https://doi.org/10.1016/j.geothermics.2021.102067.

References

Abdelfettah, Y., Sailhac, P., Larnier, H., Matthey, P.D., Schill, E., 2018. Continuous and time-lapse magnetotelluric monitoring of low volume injection at Rittershoffen geothermal project, northern Alsace – France. Geothermics 71, 1–11.

Arango-Galván, C., Prol-Ledesma, R.M., Flores-Márquez, E.L., Canet, C., Villanueva Estrada, R.E., 2011. Shallow submarine and subaerial, low-enthalpy hydrothermal manifestations in Punta Banda, Baja California, Mexico: geophysical and geochemical characterization. Geothermics 40, 102–111.

Ars, J.M., Tarits, P., Hautot, S., Bellanger, M., Coutant, O., Maia, M., 2019. Joint inversion of gravity and surface wave data constrained by magnetotelluric: application to deep geothermal exploration of crustal fault zone in felsic basement. Geothermics 80, 56–68.

Banwell, C.J., 1970. Geophysical techniques in geothermal exploration. United Nations Symposium on the Development and Utilization of Geothermal Resources, Pisa, Italy.

Banwell, C.J., 1973. Geophysical methods used in geothermal exploration. Geothermal Energy. Review of Research and Development. UNESCO, pp. 41–48.

Bard, P.-Y., 1985. Les effets de site d'origine structurale: Principaux résultats experimentaux et théoriques. In: Davidovici, V. (Ed.), Genie Parasismique, pp. 223–238.

Bard, P.-Y., 1999. In: Irikura, K., Kudo, K., Okada, H., Sasatami, T. (Eds.), Microtremor Measurement: A Tool for Site Effect Estimation?, pp. 1251–1279.

Bard, P.-Y., SESAME-Team, 2004. Guidelines for the Implementation of the H/V Spectral Ratio Technique on Ambient Vibrations-Measurements, Processing and Interpretations, SESAME European Research Project EVG1-CT-2000-00026. deliverable D23.12.

Bartrina, M.T., Cabrera, L., Guimerà, J., Roca, E., Jurado, M.J., 1992. Evolution of the central Catalan margin of the Valencia trough (western Mediterranean). Tectonophysics 203, 219–247.

Benjumea, B., Macau, A., Gabas, A., Bellmunt, F., Figueras, S., Cirés, J., 2011. Integrated geophysical profiles and H/V microtremor measurements for subsoil characterization. Near Surf. Geophys. 9, 413–425.

Benjumea, B., Macau, A., Gabàs, A., Esquerda, M., Figueras, S., 2014. Improving near surface characterization by combining reprocessed vintage seismic and geophysical

passive datasets. Near Surf. Geosci. 2014 - 20th Eur. Meet. Environ. Eng. Geophys. 14–18.
Benson, R., Yuhr, L., Kaufmann, R., 2003. Some considerations for selection and successful application of surface geophysical methods. 3rd Int. Conf. Geophys. 8–12.
Bertran, J., Tarragó, M., 1996. Síntesi estratigràfica del Vallès Oriental. Lauro 11, pp. 54–78.
Bodvarsson, G., 1970. Evaluation of geothermal prospects and the objectives of geothermal exploration. Geoexploration 8, 7–17.
Cabrera, L., 1981. Influencia de la tectónica en la sedimentación continental de la cuenca del Vallés-Penedés (provincia de Barcelona, España) durante el Mioceno inferior. Acta Geológica Hispánica 16, 165–171.
Cabrera, L., Calvet, F., 1996. Onshore Neogene record in NE Spain: Vallès–Penedès and El Camp half-grabens (NW Mediterranean). In: Friend, P., Dabrio, C. (Eds.), Tertiary Basins of Spain: The Stratigraphic Record of Crustal Kinematics. Cambridge University Press, pp. 97–105.
Calcagno, P., Baujard, C., Guillou-Frottier, L., Dagallier, A., Genter, A., 2014. Estimation of the deep geothermal potential within the Tertiary Limagne basin (French Massif Central): an integrated 3D geological and thermal approach. Geothermics 51, 496–508.
Canals, A., Albert, J., Ayora, C., 1989. El sistema geotérmico de la Garriga-Samalús: comparaciones con sistemas hidrotermales fósiles. Geogaceta.
Cardellach, E., Canals, À., Grandia, F., 2003. Recurrent hydrothermal activity induced by successive extensional episodes: the case of the Berta F-(Pb-Zn) vein system (NE Spain). Ore Geol. Rev. 22, 133–141.
Casas, A., Torné, M., Banda, E., 1987. Mapa gravimètric de Catalunya 1:500.000.
Chambefort, I., Buscarlet, E., Wallis, I.C., Sewell, S., Wilmarth, M., 2016. Ngatamariki Geothermal Field, New Zealand: Geology, geophysics, chemistry and conceptual model. Geothermics 59, 266–280.
Chave, A.D., Jones, A.G., Mackie, R., Rodi, W., 2012. The Magnetotelluric Method. Cambridge University Press, Cambridge.
Delgado, J., López Casado, C., Estévez, A., Giner, J., Cuenca, A., Molina, S., 2000. Mapping soft soils in the Segura river valley (SE Spain): a case study of microtremors as an exploration tool. J. Appl. Geophys. 45, 19–32.
Di, Q., Shi, K., Li, Y., Wang, R., Fu, C., An, Z., 2006. Successful applications of CSAMT for deep geothermal exploration in urban areas. In: 2006 SEG Annual Meeting. Society of Exploration Geophysicists, New Orleans, pp. 820–824.
Escalas, M., Queralt, P., Ledo, J., Marcuello, A., 2013. Polarisation analysis of magnetotelluric time series using a wavelet-based scheme: a method for detection and characterisation of cultural noise sources. Phys. Earth Planet. Inter. 218, 31–50.
Fäh, D., Kind, F., Giardini, D., 2001. A theoretical investigation of average HIV ratios. Geophys. J. Int. 145, 535–549.
Fernàndez, M., Banda, E., 1988. Aproximacion a la anomalia geotérmica de La Garriga - Samalus (Vallès - Penedès). Acta Geológica Hispánica 23, 1–20.
Fernàndez, M., Banda, E., 1990. Geothermal Anomalies in the Valles-Penedes graben master fault: convection through the horst as a possible mechanism. J. Geophys. Res. 95, 4887–4894.
Gabàs, A., Macau, A., Benjumea, B., Queralt, P., Ledo, J., Figueras, S., Marcuello, A., 2016. Joint audio-magnetotelluric and passive seismic imaging of the Cerdanya Basin. Surv. Geophys. 37, 897–921.
Gallardo, L.A., Fontes, S.L., Meju, M.A., Buonora, M.P., De Lugao, P.P., 2012. Robust geophysical integration through structure-coupled joint inversion and multispectral fusion of seismic reflection, magnetotelluric, magnetic, and gravity images: example from Santos Basin, offshore Brazil. Geophysics 77, 237–251.
Gallart, J., Dañobeitia, J.J., Rojas, H., Diaz, J., 1990. Features of deep crustal structure and the onshore-offshore transition at the Iberian flank of the Valencia trough (Western Mediterranean). J. Geodyn. 12, 233–252.
Gamble, T.D., Goubau, W.M., Clarke, J., 1979. Magnetotellurics with a remote magnetic reference. Geophysics 44, 53–68.
Garambois, S., Sénéchal, P., Perroud, H., 2002. On the use of combined geophysical methods to assess water content and water conductivity of near-surface formations. J. Hydrol. 259, 32–48.
García-Yeguas, A., Ledo, J., Piña-Varas, P., Prudencio, J., Queralt, P., Marcuello, A., Ibañez, J.M., Benjumea, B., Sánchez-Alzola, A., Pérez, N., 2017. A 3D joint interpretation of magnetotelluric and seismic tomographic models: the case of the volcanic island of Tenerife. Comput. Geosci.
Gaspar-Escribano, J.M., Garcia-Castellanos, D., Roca, E., Cloetingh, E., 2004. Cenozoic vertical motions of the Catalan Coastal ranges (NE Spain): the role of tectonics, isostasy, and surface transport. Tectonics 23, 1–18.
Gemperle, M., Conrad, G., Sargen, M.Y., Starr, S., 1991. Geosoft GM-SYS. Version 1.8. Northwest Geophys. Assoc. Inc., New York.
Georgsson, L.S., 2009. Geophysical Methods Used in Geothermal Exploration, 50, pp. 227–249.
Gibert, J.M., Casanovas-Vilar, I., 2011. Contexto geológico del Mioceno de la cuenca del Vallès-Penedès. Paleontol. i Evol. Memòria Espec. 6, 55–80.
Groom, R.W., Bailey, R.C., 1989. Decomposition of magnetotelluric impedance tensors in the presence of local three-dimensional galvanic distortion. J. Geophys. Res.
Gupta, H.K., 1980. Geothermal resources: an energy alternative. Geothermal Resources: An Energy Alternative. Elsevier Scientific Pub. Co.
Haldar, S.K., Tišljar, J., 2014. Precipitation systems of major sedimentary bodies—collector rocks of oil and gas. Introduction to Mineralogy and Petrology. Elsevier, pp. 233–260.
Hammer, S., 1939. Terrain corrections for gravimeter stations. Geophysics 4, 184–194.
Hermans, T., Nguyen, F., Robert, T., Revil, A., 2014. Geophysical methods for monitoring temperature changes in shallow low enthalpy geothermal systems. Energies 7, 5083–5118.
Hersir, G.P., Bjornsson, A., 1991. Geophysical Exploration for Geothermal Resources: Principles and Application, p. 94.
Hunt, T.M., Bromley, C.J., Risk, G.F., Sherburn, S., Soengkono, S., 2009. Geophysical investigations of the Wairakei Field. Geothermics 38, 85–97.
Ibs-Von Seht, M., Wohlenberg, J., 1999. Microtremor measurements used to map thickness of Soft sediments. Bull. Seismol. Soc. Am. 89, 250–259.
ICGC, 2006. Vallès Oriental. Mapa geològic comarcal de Catalunya 1:50.000.
IGC, 2012. Mapa gravimètric de Catalunya 1:250.000.
IGME, 1977. Fase preliminar de prospección de recursos geotérmicos de baja entalpía en el Vallés (Barcelona).
IGME, 1982. Informe sobre el seguimiento técnico del sondeo SAMALUS-1.
IGME, 1984a. Proyecto de investigación geotérmica en el Vallés mediante sondeos de reconocimiento y síntesis hidrogeotérmica. Control geotermico de los sondeos SAMALUS 2 (3), 4 y 5.
IGME, 1984b. Proyecto de investigación geotérmica en el Valles mediante sondeos de reconocimiento y síntesis hidrogeotérmica. Síntesis hidrogeológica del Vallés y La Selva.
IGME, 1985. Proyecto de investigación geotérmica en el Vallés mediante sondeos de reconocimiento y síntesis hidrogeotérmica, p. 355.
IGME, 1986. Proyecto de seguimiento geológico del sondeo de reconocimiento geotérmico SAMALUS-6 (1000 m) (Vallès - Barcelona).
Jousset, P., Haberland, C., Bauer, K., Arnason, K., 2011. Hengill geothermal volcanic complex (Iceland) characterized by integrated geophysical observations. Geothermics 40, 1–24.
Junge, A., 1996. Characterization of and correction for cultural noise. Surv. Geophys. 17, 361–391.
Kana, J.D., Djongyang, N., Raïdandi, D., Njandjock Nouck, P., Dadjé, A., 2015. A review of geophysical methods for geothermal exploration. Renew. Sustain. Energy Rev. 44, 87–95.
Kane, M.F., 1962. A comprehensive system of terrain corrections using a digital computer. Geophysics 27, 455–462.
Kearey, P., Brooks, M., Hill, I., 2002. An Introduction to Geophysical Exploration, 3rd editio. ed. Blackwell Science.
Khodayar, M., Björnsson, S., 2014. Fault ruptures and geothermal effects of the second earthquake, 29 May 2008, South Iceland Seismic Zone. Geothermics 50, 44–65.
Kirkby, A., Heinson, G., Holford, S., 2016. Imaging fracture permeability using magnetotellurics. ASEG Ext. Abstr. 2016, pp. 1–8.
Kraft, T., Mai, P.M., Wiemer, S., Deichmann, N., Ripperger, J., Kästu, P., Bachmann, C., Fäh, D., Wössner, J., Giardini, D., 2009. Enhanced geothermal systems: mitigating risk in urban areas. Eos (Washington DC) 90, 273–274.
Lachet, C., Bard, P.Y., 1994. Numerical and theoretical investigations on the possibilities and limitations of Nakamura's technique. J. Phys. Earth 42, 377–397.
Lee, W.H.K., Stewart, S.W., 1981. Principles and Applications of Networks. A G 1981.
Leeuwen, Wvan, 2016. Geothermal Exploration Using the Magnetotelluric Method. Faculty of Geosciences - Utrecht University.
Lewis, M.R., Haeni, F.P., 1987. Use of Surface Geophysical Techniques to Detect Fractures in Bedrock – An Annotated Bibliography. US Geol. Surv. Circ.
Low, U., Abşar, A., Duraiswami, R., Singh, A., 2020. Geophysical exploration of Tural-Rajwadi group of hot springs, West Coast Geothermal Province, Maharashtra, India and its implications. Geothermics 88, 101874.
Lüschen, E., Wolfgramm, M., Fritzer, T., Dussel, M., Thomas, R., Schulz, R., 2014. 3D seismic survey explores geothermal targets for reservoir characterization at Unterhaching, Munich, Germany. Geothermics 50, 167–179.
Macau, A., Benjumea, B., Gabàs, A., Bellmunt, F., Figueras, S., 2018. Geophysical measurements for site effects characterisation in the urban area of Girona, Spain. Near Surf. Geophys. 16, 340–355.
Mahajan, A.K., Galiana-Merino, J.J., Lindholm, C., Arora, B.R., Mundepi, A.K., Rai, N., Chauhan, N., 2011. Characterization of the sedimentary cover at the Himalayan foothills using active and passive seismic techniques. J. Appl. Geophys. 73, 196–206.
Maithya, J., Fujimitsu, Y., 2019. Analysis and interpretation of magnetotelluric data in characterization of geothermal resource in Eburru geothermal field, Kenya. Geothermics 81, 12–31.
Mandal, A., Basantaray, A.K., Chandroth, A., Mishra, U., 2019. Integrated geophysical investigation to map shallow surface alteration/fracture zones of Atri and Tarabalo hot springs, Odisha, India. Geothermics 77, 24–33.
Manger, G.E., Nolan, T.B., 1963. Porosity and Bulk Density of Sedimentary Rocks: Contributions to Geochemistry.
Manzella, A., 1973. Geophysical Methods in Geothermal Exploration. Italian National Research Council. International Institute for Geothermal Research, Pisa, Italy.
Martí, J., Mitjavila, J., Roca, E., Aparicio, A., 1992. Cenozoic magmatism of the valencia trough (western mediterranean): relationship between structural evolution and volcanism. Tectonophysics 203, 145–165.
McNeice, G.W., Jones, A.G., 2002. Multisite, multifrequency tensor decomposition of magnetotelluric data. Geophysics.
Meidav, T., Tonani, F., 1976. A critique of geothermal exploration techniques. Proceedings of the 2nd UN Symposium on the Development and Use of Geothermal Resources, pp. 1143–1154.
Moeck, I., Bloch, T., Graf, R., Heuberger, S., Kuhn, P., Naef, H., Sonderegger, M., Uhlig, S., Wolfgramm, M., 2015. The St. Gallen project: development of fault controlled geothermal systems in urban areas. Proc. World Geotherm. Congr. 2015, 1–5.
Morelli, C., Gantar, C., Honkasalo, T., McConnel, R.K., Tanner, J.G., Szabo, B., Uotila, U., Whalen, C.T., 1972. The International Gravity Standardisation Net 1971 (IGSN71). Spec. Publ. No. 4.

Moscariello, A., 2018. Alluvial fans and fluvial fans at the margins of continental sedimentary basins: geomorphic and sedimentological distinction for geo-energy exploration and development. Geol. Soc. Spec. Publ. 440, 215–243.
Nagy, D., 1966. The gravitational attraction of a right rectangular prism. Geophysics 31, 362–371.
Nakamura, Y., 1989. A method for dynamic characteristics estimations of subsurface using microtremors on the ground surface. Q. Rept. RTRI 30, 25–33.
Nieto, I.M., Martín, A.F., Blázquez, C.S., Aguilera, D.G., García, P.C., Vasco, E.F., García, J.C., 2019. Use of 3D electrical resistivity tomography to improve the design of low enthalpy geothermal systems. Geothermics 79, 1–13.
Nowell, D.A.G., 1999. Gravity terrain corrections - an overview. J. Appl. Geophys. 42, 117–134.
Pálmason, G., 1976. Geophysical methods in geothermal exploration. Proceedings of the 2nd UN Symposium on the Development and Use of Geothermal Resources 1175–1184.
Peacock, J.R., Thiel, S., Heinson, G.S., Reid, P., 2013. Time-lapse magnetotelluric monitoring of an enhanced geothermal system. Geophysics 78, 121–130.
Rao, D.B., 1986. Modelling of sedimentary basins from gravity anomalies with variable density contrast. Geophys. J. R. Astron. Soc. 84, 207–212.
Roca, E., 1994. La evolución geodinámica de la Cuenca Catalano-Balear y áreas adyacentes desde el Mesozoico hasta la actualidad. Acta Geológica Hispánica 29, 3–25.
Roca, E., Guimerà, J., 1992. The Neogene structure of the eastern Iberian margin: structural constraints on the crustal evolution of the Valencia trough (western Mediterranean). Tectonophysics 203, 203–218.
Roca, E., Sans, M., Cabrera, L., Marzo, M., 1999. Oligocene to Middle Miocene evolution of the central Catalan margin (northwestern Mediterranean). Tectonophysics 315, 209–229.
Rodi, W., Mackie, R.L., 2001. Nonlinear conjugate gradients algorithm for 2-D magnetotelluric inversion. Geophysics 66, 174–187.
Rodríguez, F., Pérez, N.M., Padrón, E., Melián, G., Piña-Varas, P., Dionis, S., Barrancos, J., Padilla, G.D., Hernández, P.A., Marrero, R., Ledo, J.J., Bellmunt, F., Queralt, P., Marcuello, A., Hidalgo, R., 2015. Surface geochemical and geophysical studies for geothermal exploration at the southern volcanic rift zone of Tenerife, Canary Islands, Spain. Geothermics 55, 195–206.
Sàbat, F., Roca, E., Muñoz, J.A., Vergés, J., Santanach, P., Sans, M., Masana, E., Estévez, A., Santisteban, C., 1997. Role of extension and compression in the evolution of the eastern margin of Iberia: the ESCI-València Trough seismic profile. Rev. Soc. Geol. España 8, 431–448.
Sanchez-Guzman, J., Garcia De la Noceda-Marquez, C., 2005. Geothermal energy development in Spain – country update report. Proceedings World Geothermal Congress, Antalya, Turkey, pp. 24–29.
Santanach, P., Casas, J.M., Gratacós, O., Liesa, M., Muñoz, J.A., Sàbat, F., 2011. Variscan and Alpine structure of the hills of Barcelona: geology in an urban area. J. Iber. Geol. 37, 121–137.
Schiel, K., Baume, O., Caruso, G., Leopold, U., 2016. GIS-based modelling of shallow geothermal energy potential for CO2 emission mitigation in urban areas. Renew. Energy 86, 1023–1036.
Schon, J.H., 2015. Physical properties of rocks. Fundamentals and principles of petrophysics. Developments in Petroleum Science, 2nd ed.
Shah, M., Sircar, A., Vaidya, D., Sahajpal, S., Chaudhary, A., Dhale, S., 2015. Overview of geothermal surface exploration methods. Ijariie 1, 55–64.
Simpson, R.W., Jachens, R.C., 1989. Chapter 3: gravity methods in regional studies. Mem. Geol. Soc. Am. 172, 35–44.
Soengkono, S., Bromley, C., Reeves, R., Bennie, S., 2013. Geophysical techniques for low enthalpy geothermal exploration in New Zealand. Explor. Geophys. 2011, 37–40.
Szarka, L., 1988. Geophysical aspects of man-made electromagnetic noise in the Earth – a review. Surv. Geophys. 9, 287–288.
Tenzer, R., Sirguey, P., Rattenbury, M., Nicolson, J., 2011. A digital rock density map of New Zealand. Comput. Geosci. 37, 1181–1191.
Thanassoulas, C., Xanthopoulos, N., 1991. Location of possibly productive geothermal fracture zones/faults using integrated geophysicals methods over lesvos island geothermal field, Greece. Geothermics 20, 355–368.
Vidal, N., Gallart, J., Danobeitia, J.J., 1995. Contribution of the ESCI-Valéncia trough wide-angle data to a crustal transect in the NE iberian margin. Rev. la Soc. Geol. Espana.
Viseras, C., 2002. Principles of sedimentary basin analysis (third edition). Sediment. Geol. 152, 327–328.
Wald, J.A., Graham, R.C., Schoeneberger, P.J., 2013. Distribution and properties of soft weathered bedrock at $\leq$ 1m depth in the contiguous United States. Earth Surf. Process. Landforms 38, 614–626.
Yousefi, H., Roumi, S., Ármannsson, H., Noorollahi, Y., 2019. Cascading uses of geothermal energy for a sustainable energy supply for Meshkinshahr City, Northwest, Iran. Geothermics 79, 152–163.
Zhang, N., Qin, Q., He, L., Jiang, H., 2012. Remote sensing and GIS based geothermal exploration in southwest Tengchong, China. Int. Geosci. Remote Sens. Symp. 5364–5367.
Zonge, K.L., Hugues, L.J., 1991. Controlled source audio-frequency magnetotellurics. Electromagn. Methods Appl. Geophys., p. 2.

The importance of structural complexity in locations of geothermal systems: a case study along the Vallès-Penedès Fault in the Catalan Coastal Ranges (NE Spain)

Mitjanas, G.; Walsh, J.; Roca, E.; Alías, G.; Queralt, P. & Ledo, J.

Abstract

The Vallès-Penedès Fault is a Neogene normal fault marked by the presence of two established geothermal systems at La Garriga-Samalús and Caldes de Montbuí within the Catalan Coastal Ranges of NE Spain. The analysis and collation of existing and new geological and geophysical datasets provide the basis for the development of an improved conceptual model for the presence and localization of hot geothermal fluid systems at relatively shallow depths (e.g., 60^0C at surface and 90^0C at 1 km). Geothermal flow is concentrated within Paleozoic granodiorites of the immediate footwall of the V-P Fault, host rocks that are susceptible to fault-related fracturing, and the generation of both extension and hybrid fracture systems in association with active fault displacements. Flow localization is enhanced further by the presence of fault-related structural complexities, with both systems marked by 300 m wide steps in the main fault trace. These are attributed to relay development and breaching characterizing host rocks by high fracture intensities and fault rock development on a fault that locally has a vertical displacement of over 1.5 km. Accentuated fracturing and deformation are consistent with strain localization predicted by existing models for the development of fault zones along normal faults. The plumbing of the geothermal systems is attributed to up-fault flow in combination with lateral flow controlled by the intersection of the V-P fault with a low-angled Paleogene thrust defining the base of the host-rock granodiorites, with the geothermal systems localized at distil end of the thrust. Sustainable geothermal flow is attributed to groundwater flow circulation associated with seismic pumping and valving of warmer and deeper fluids, and the ingress of groundwater either along faults and fractured basement rocks.

1. Introduction

Faults have long been known to significantly influence on the migration of fluids within the crust, often acting as the principal conduits and traps for groundwater, hydrocarbon, and mineral flow systems (Sibson 1987, Faulkner et al. 2010, Walsh et al. 2018). Recent work has highlighted their importance in the formation of low-high enthalpy geothermal reservoirs (Bellanger et al., 2019; Duwiquet et al., 2019, 2021), providing the conduits and storage for hydrothermal fluids and playing a pivotal role in the emergence of sustainable flow circulation systems. Within otherwise relatively impermeable rock volumes, such as granites, basement rocks or massive limestones, faults often comprise zones of more permeable fault rocks bounded by highly fractured host rocks, together representing the essential flow components of multiple fault networks (Achtziger-Zupančič et al.,

2017; Bellanger et al., 2019; Duan et al., 2017; Haines et al., 2016; Sibson, 1996; Siebenaller et al., 2013; Süer et al., 2008). By contrast, within higher porosity-permeability host rocks, such as clastic sediments, fault rock can represent seals or baffles to across-fault flow (e.g. Fisher & Knipe 1998; Manzocchi et al. 2010; Yielding 2002), but can also act as pathways for along-fault flow (e.g. Rowe and Burley 1997; Selley et al. 2005; Walsh et al. 2018; Wibberley et al. 2008). This duality of flow behaviour, depending on host rock properties and flow direction, means that faults and fractures often exercise a major control on the plumbing of flow systems in the subsurface (Sibson 1987, 1998; Faulkner et al. 2010; Walsh et al. 2018).

Previous studies have highlighted how the complexities of fault zone structure arising from fault propagation and localization can often provide important pathways for fluid flow. The formation and evolution of major faults are associated with the nucleation and growth of fault segments during the deformation (Cartwright et al., 1996). The overlap and linkage of such fault segments is often marked by zones of accentuated deformation associated with the formation of relay ramps (Camanni et al., 2019; Cartwright et al., 1996; Childs et al., 1995; Fossen and Rotevatn, 2016; Mansfield and Cartwright, 2001; Peacock and Sanderson, 1994). Increases in faulting, fracturing and fault rock development adjacent to these fault zones (fault zones) can have a controlling influence on the migration of fluids, acting as a fluid conduit, barrier, or combined conduit-barrier system (Faulds and Hinz, 2015; Manzocchi et al., 2008; Rotevatn et al., 2009b, 2009a).

The general conceptual model for fault zones involves high-strain localizations of fault rock and slip surfaces, often referred to as the fault core, surrounded by fractures and faulting in a lower-strain damage zone (Faulkner et al., 2010; Passchier and Trouw, 2005). In practice, the distribution of damage is very heterogeneous, often reflecting the 3D segmentation and bifurcation of fault surfaces (Childs et al. 2009), and it is this heterogeneity of structure which localizes fluid flow. Fault zones comprise cataclastically deformed host rocks, including brecciated, indurated, and geochemically altered host rocks, unconsolidated clay-rich gouge zones and internal multiple slip surfaces (Anderson et al., 1983; Lindsay et al. 1993; Sibson 2000; Caine et al., 1996; Childs et al. 1996). This fault core is mainly characterized by lower porosity and permeability, and is generally considered to act as a flow barrier to across-fault flow (e.g., Manzocchi et al. 1999, 2010; Wibberley and Shimamoto, 2002), but can, at the same time, act as a conduit for along-fault flow (Sibson 2000; Walsh et al. 2018). The surrounding lower-strain damage zone can be very heterogenous in structure, comprising faults and fractures (including hybrid and extension structures) over a wide range of length scales, often generating high permeability conductive networks within otherwise low permeability host rocks (Sibson 1990, 1996; Caine et al. 1996; Wibberley and Shimamoto, 2002; Childs et al. 2009; Faulkner et al., 2010; Seebeck et al. 2014).

Whilst fault zones have been extensively studied in geothermal exploration studies (i.e., Géraud et al., 2010; Loveless et al., 2014; Siler et al., 2018), previous work has less often investigated the significance of structural complexity for a geothermal system. For example, the geometry and nature of fault intersections, splays, relays, and associated damage-related fractures, are usually not considered in the context of flow localization and host-rock alteration. Nevertheless, earlier studies on West European Rift Systems have demonstrated that high thermal gradient locations along fault

zones on normal faults are very prospective as high enthalpy geothermal targets (i.e. Bertrand et al., 2013; Duwiquet et al., 2019; Loveless et al., 2014; Rhén et al., 2007). In this paper, we describe the geometry, deformation and flow indicators (e.g., alteration patterns and vein infills), and investigate the relationship between key structural parameters and the localization of a geothermal system. The study is within the Catalan Coastal Ranges (CCR) and along the Vallès-Penedès Fault, a major crustal fault bounding the NW margin of the Vallès-Penedès Basin (Fig. 1). The NE end of this major basement fault has been established as the main locus for the hot fluids of the La Garriga, Samalús, and the Caldes de Montbui geothermal systems. Our study focusses on the La Garriga-Samalús geothermal system (Fig. 2), which has been the subject of several previous studies (Canals et al., 1989; Cardellach et al., 2002; Fernàndez and Banda, 1990, 1988; Mitjanas et al., 2021). We present a geological and structural characterization of the controlling structures of this geothermal system, utilising the geophysical data presented in Mitjanas et al. (2021). In addition, a 3D geothermal model is presented of the northeastern part of the Vallès basin, highlighting the pivotal role of structural complexity in the functioning of the geothermal system.

2. Geological and geothermal setting

2.1. Vallès-Penedès Fault

The Vallès-Penedès (V-P) Fault, an ENE-trending major crustal normal fault more than 100 km in length, is located in the Catalan Coastal Ranges (CCR), in the NE of the Iberian Peninsula (Fig. 1). The CCR are the onshore southern extension of the Catalan margin, comprising the Prelitoral and Litoral ranges that are separated by the Vallès-Penedès half-graben basin. The V-P Fault, which limits the Prelitoral Range from the Vallès-Penedès Basin, has a cumulative displacement of up to 4 km, which developed from approximately Oligocene to Present times (Bartrina et al., 1992; Gaspar-Escribano et al., 2004; Roca et al., 1999; Santanach et al., 2011). The present configuration of the CCR mainly arises from the late Oligocene-early Miocene opening of the Valencia Trough (Western Mediterranean) (Bartrina et al., 1992; Roca, 2001). This trough comprises several ENE- to NE-striking basement blocks bounded by 50 to 150 km-long normal faults (Gaspar-Escribano et al., 2004). These major normal faults dip towards the SE and define a system of major half-graben filled by Miocene deposits. Previous work suggests that some of these faults are long-lived structures, which, before their most recent Neogene activity, could have originally formed during the Mesozoic opening of the Tethys (Martín-Martín et al., 2021) and later accommodated contractional inversion during the Paleogene collision between Iberia and Eurasia (Fontboté et al., 1990; Roca et al., 1999).

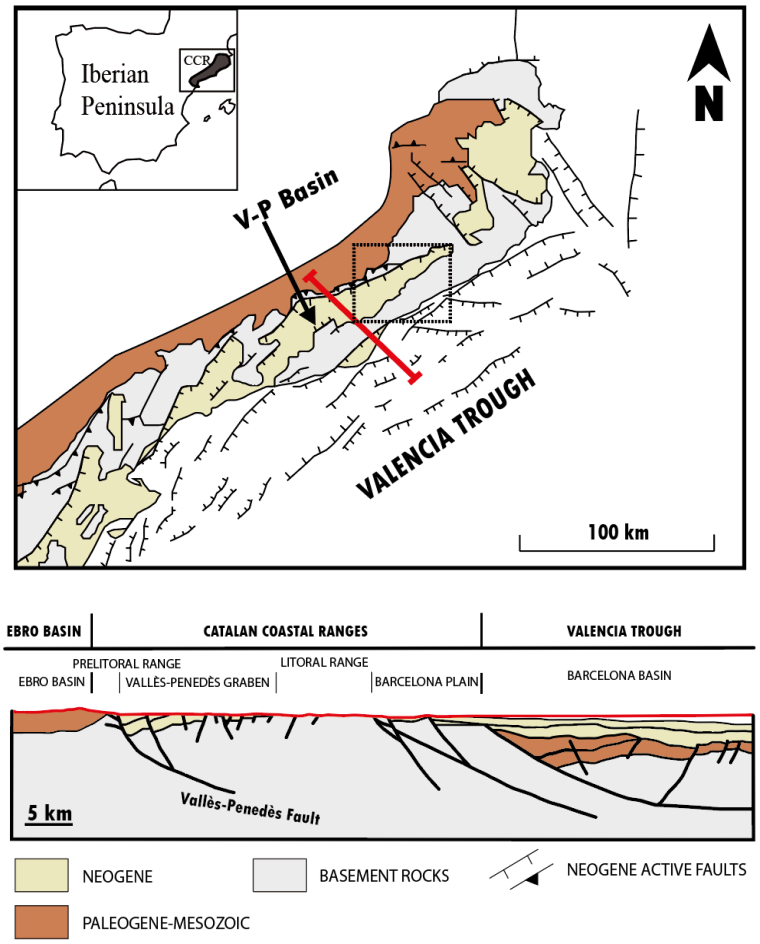

Figure 1. *(UP) Structural map of the Valencia trough, showing the Catalan-Valencian domain (modified from Marti et al., 1992). This map highlights the orientation of the main NE-SW trending normal faults providing onshore Neogene basins (yellow), including the Valles-Penedes (V-P) basin. Towards the west, the V-P fault fault bends into an NNE-SSW orientation, whereas towards the northeast, the fault dies out and is replaced by a NW-SE fault system which in turn transfers to another NW-SE trending normal fault system in the north. (DOWN) Cross-section derived from interpreted seismic data (Roca et al. 1999) highlighting the rotated fault blocks and hangingwall syn-rift infill of the V-P Basin and the Barcelona Basin.*

The V-P Fault separates a basin filled with Miocene sediments in the SE from an outcropping Variscan basement in the NW. The footwall basement forms a mountain range up to 1700 m high, referred to as the Prelitoral Range, which has been attributed to isostatic footwall uplift of 2 km during the Neogene activity of the V-P Fault (Gaspar-Escribano, 2003). The immediate footwall to the V-P Fault comprises a NNW-directed granodioritic Paleogene thrust sheet, which overthrusts a series of Cambro-Ordovician to Carboniferous metamorphic rocks. The Paleogene thrust sheet is a major reverse fault system with a component of sinistral horizontal displacement oblique to the direction of maximum shortening of the Pyrenean zone (Anadon et al., 1985; Gaspar-Escribano et al., 2004; Guimerá, 1984; Roca, 1996; Roca et al., 1999). The footwall metamorphic series comprises slates, quartzites, and minor limestones (ICGC, 2006; IGME, 1974), and the post-Variscan intrusive unit comprising granodiorites intruded by E-W aplite, pegmatite and granitic porphyry dykes (ICGC, 2006). By contrast, the basin infill of the V-P Fault comprises conglomerates, arkosic sandstones, and mudstones, forming an alluvial fan sequence containing big boulders of the Prelitoral Range igneous and metamorphic rocks (ICGC, 2006, 2002; IGME, 1974) immediately adjacent to the V-P

Fault. The precise thickness of the V-P Basin is not well established, as demonstrated by the differing thicknesses shown on previously published geological cross-sections (Fernàndez and Banda, 1990, 1988; Fontboté, 1954; IGME, 1977; Mitjanas et al., 2021; Roca, 1992).

2.2. La Garriga-Samalús geothermal system

Two localities are marked by geothermal activity along the V-P Fault trace (Fig. 2): La Garriga-Samalús (G-S) and Caldes de Montbuí (CM). Both have similar structural configurations insofar as they are in the vicinity of the NE and SW branch points, respectively, between the NNW-directed Paleogene thrust and the V-P Fault (Figure 1). They are, however, marked by different thermal waters, with the La Garriga water springs having sodium bicarbonate compositions and a surface temperature of ca 60ºC, and those of Caldes de Montbui having sodium chloride compositions with the temperature of ca 70ºC (IGME, 1986). Previous studies were mainly focused on the Caldes de Montbui hot spring, where the onset of the geothermal activity was dated as middle/late Miocene and the thermal waters are characterized by the mixing of hydrothermal fluids and meteoric waters, and the precipitation of pedogenic products along faults (Cantarero et al., 2014a, 2014b). Our study is focused in the G-S geothermal system where the structure is better known from geological and geophysical data collected in previous studies. Later we will consider aspects of both geothermal systems in an effort to define a unified model for their formation

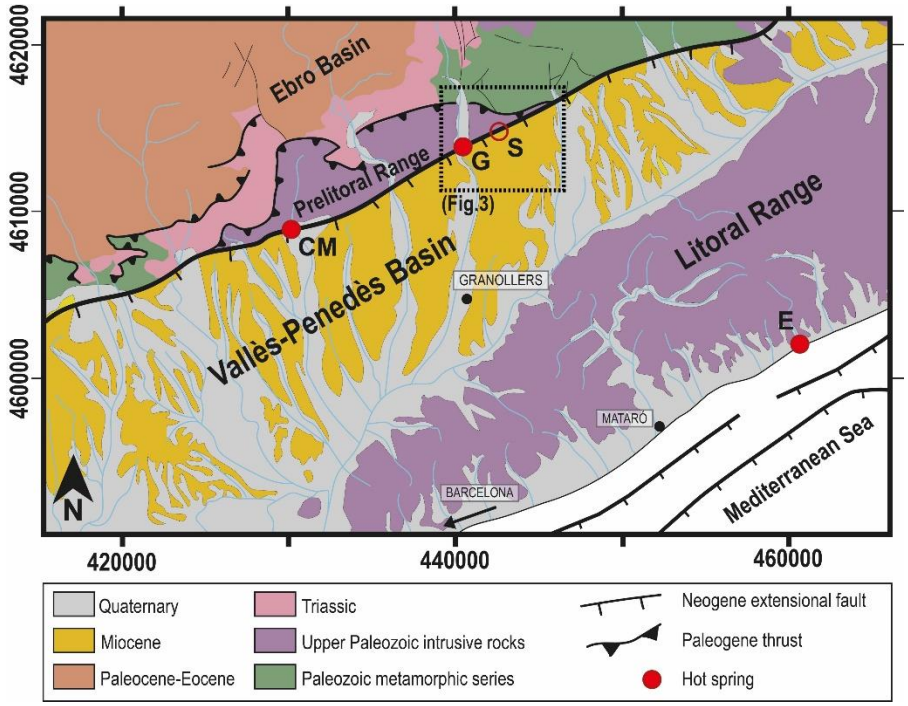

Figure 2. *Geological map (UTM coordinates) of the central to eastern part of the Catalan Coastal Ranges, highlighting the Valles-Penedès Basin and its bounding southward-dipping Valles-Penedès (V-P) fault. Normal faulting of Neogene age has generated a Miocene filled half-graben, which deepens and widens along-strike towards the west and gives way to the south to similar southward-dipping normal faults which bound the offshore Valencia Trough. Hot springs along the V-P Fault are located where the footwall rocks are Upper Paleozoic granitic intrusive in the hangingwall of a southward dipping Paleogene thrust study area (red square; need to make sure the location box is the correct shape and location relative to next figure) and the location of the towns with thermal hot springs:* ***CM*** *- Caldes de Montbuí (70ºC);* ***G*** *- La Garriga (60ºC);* ***E*** *- Caldes d'Estrac (38ºC); and other indicators of thermal activity:* ***S*** *- Samalús (90ºC at 1000 m depth). The study area is indicated by the red outlined square (Modified from ICGC, 2002 and (Martí et al., 1992).*

The G-S geothermal system was previously studied during the 1980's, when the geological survey of Spain investigated the geothermal potential of Spain (IGME, 1982, 1984, 1986). At this time, six exploration boreholes S1 (IGME, 1982), S2-S5 (IGME, 1984), and S6 (IGME, 1986), were drilled in Samalús town, with the last one recording 90ºC at 1000 m depth. These boreholes were also complemented with some temperature profiles close to La Garriga town (Fig. 3). Later studies worked on the origin of the geothermal system and its broad conceptual framework (Canals et al., 1989; Cardellach et al., 2002; Fernàndez and Banda, 1990, 1988; Mitjanas et al., 2021). The derived geothermal model for the G-S system advocates convection through the uplifted footwall (Fernàndez and Banda, 1990), with a slow downward circulation of meteoric water until it reaches the V-P Fault, with later geophysical characterization interpreted to indicate completion of the cycle with fast ascending hot fluids migrating along the fault zone (Mitjanas et al., 2021).

3. Methods

In order to understand the La Garriga-Samalús geothermal system, this study integrates structural and petrographic analysis of the main fault and associated meso- and micro-scale faults/fractures, together with an evaluation of the hydraulic properties of the different units. Our work complements earlier geophysical data (Mitjanas et al., 2021), with the acquisition of a new magnetotelluric (MT) profile and additional ambient seismic noise (HVSR) sites (Fig. 3).

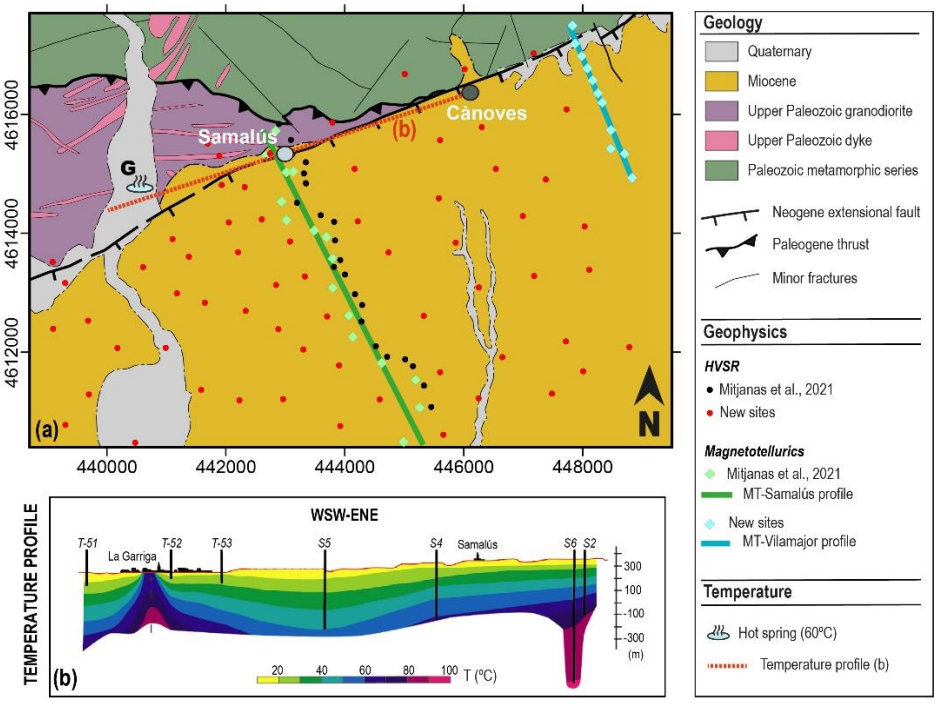

Figure 3. *(a) Geological map of the La Garriga-Cànoves region in which the location of the main towns and the temperature profile. The biggest town of the area, La Garriga (G), is the only with hot springs (60ºC), but the main exploration boreholes were made close to Samalús town. The location of the along-fault temperature variation cross-section shown in (b) is marked by red broken line. The sites for previous (Mitjanas et al., 2021) and newly acquired geophysical data (see legend for details) are shown, highlighting that this study provides HVSR data covering a 3D zone instead of just a profile and that an additional MT profile is now available outside of the granodioritic thrust sheet. (b) Temperature variations along cross-section parallel to the V-P fault (scale 1:1, see (a) for line location), derived from considerations of different temperature profiles (T) and borehole data (S) (Modified from IGME (1984, 1986).*

3.1. H/V spectral ratio data

The horizontal-to-vertical spectral ratio (HVSR) technique applied to seismic ambient noise recordings, allows identification of large-impedance contrasts between sediments and underlying bedrock and is, therefore, an indicator of the bedrock hangingwall geometry (Bard, 1998, 1985; Nakamura, 1989). Our work includes more data sites than previous studies (Mitjanas et al., 2021), in order to provide better 3D definition of the La Garriga-Samalús footwall (Fig. 4). The HVSR data acquisition and processing of 97 sites was carried out by the *Geophysical Techniques Department* of the *Catalan Cartographic and Geological Institute* (ICGC), following the same procedure described in Mitjanas et al. (2021). This methodology has already been applied in other Neogene basins near the Vallès basin (Benjumea et al., 2014, 2011; Gabàs et al., 2016; Macau et al., 2018; Mitjanas et al., 2021).

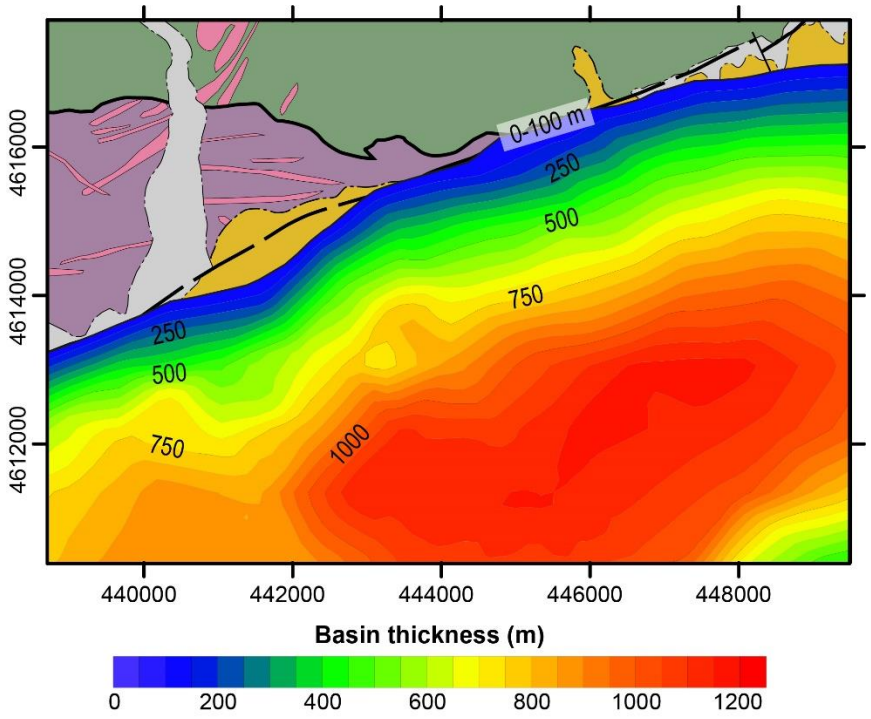

***Figure 4**. Sediment thickness along the region of study, between La Garriga and Cànoves towns, derived from the horizontal-to-vertical (H/V) spectral ratio. The first contour (0-100 m) is set as a range since the accuracy of the final extrapolation from the measurement points does not allow to obtain an accurate limit this close to the topographic surface. Its thickness is up to a maximum of 1200 m towards the center of the basin (SE), and the intersection of the presented surface and the topography seems to represent the V-P fault trace.*

3.2. Magnetotelluric data

This study presents a new across-fault magnetotelluric profile (MT-Vilamajor) comprising 11 sites along an NNE-SSE profile of approximately 3 km length, from the footwall Prelitoral range into the hangingwall Vallès-Penedès basin sediments. This MT profile is located to the east of Canovas town, where the granodiorite thrust sheet no longer outcrops, and to that extent, it complements an earlier published profile from Samalús town (MT-Samalús) spatially associated with the granodiorite-hosted geothermal system (Figs 3 & 5; Mitjanas et al., 2021). The acquisition and processing procedure for this new MT profile is the same as described in Mitjanas et al. (2021). The calculated

apparent resistivity and phase curves for the stations used in the modeling process can be accessed in the ***Supplementary Material (S.1)***.

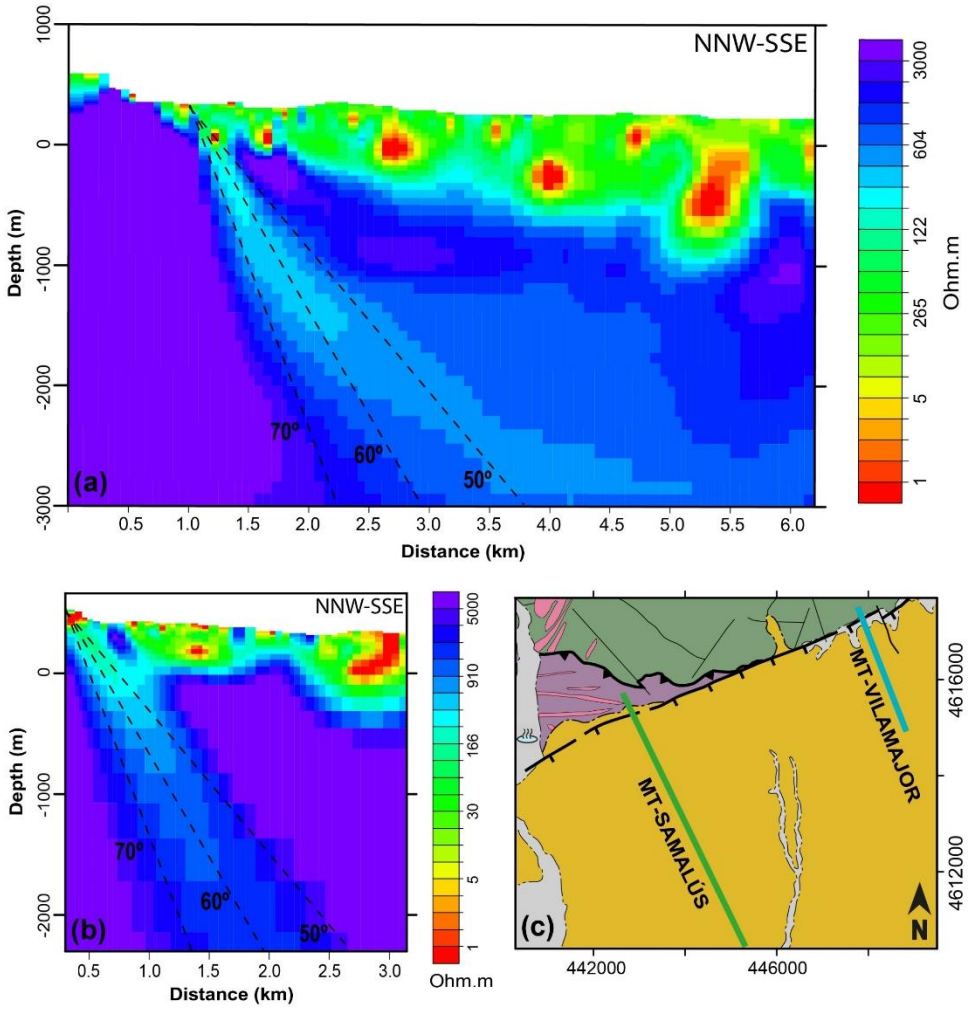

Figure 5. *Resistivity models for sections across the V-P fault showing along strike changes in the fault zone structure. (a) Western section indicating that the bounding fault has steep-moderate dips (70^0-50^0) towards the south, perhaps consistent with widening and shallowing in the west at the boundary to the fault bend at La Garriga. (b) Eastern section suggesting a steeper dipping fault zone (ca 70^0) which could be as wide as 500-750m.*

3.3. Geological fieldwork

The geological fieldwork has been designed to improve the geological map of the area and, in particular, define the fault trace geometry of both the V-P Fault and the Paleogene thrust (Fig. 3). The V-P fault trace, a critical determinant of the geometry and the potential plumbing of the system, has been defined from mapping the distribution of hangingwall Miocene sediments and footwall granites (Fig. 6), on the one hand, and from across-fault terrain changes particularly those reflected in deflections of river systems (Fig. 7), on the other. The locus of faulting has also been investigated from quantitative fracture analysis of footwall Variscan granodiorites immediately adjacent to the V-P Fault. Fracture geometry (dip and strike), and where possible fracture aperture, were measured for each fracture, with the spatial distribution of fractures analysed using the linear scanline sampling method (Figs 8 & 9; Priest, 1993; Priest and Hudson, 1981; Schön, 2015; Watkins et al., 2015). This

method permits the recording and analysis of a wide range of fracture attributes, though care needs to be taken about potential susceptibility to orientation bias when variably orientated fractures are sampled in a single scanline (Park and West, 2002). This methodology was applied to 50 footwall outcrops, providing an adequate means of investigating the spatial variations of fractures and of quantifying fracture density as a function of proximity to the V-P Fault trace: for the latter, distance against fracture density was estimated using the Natural Neighbour gridding method within *Surfer*® software (Golden Software LLC, 2016).

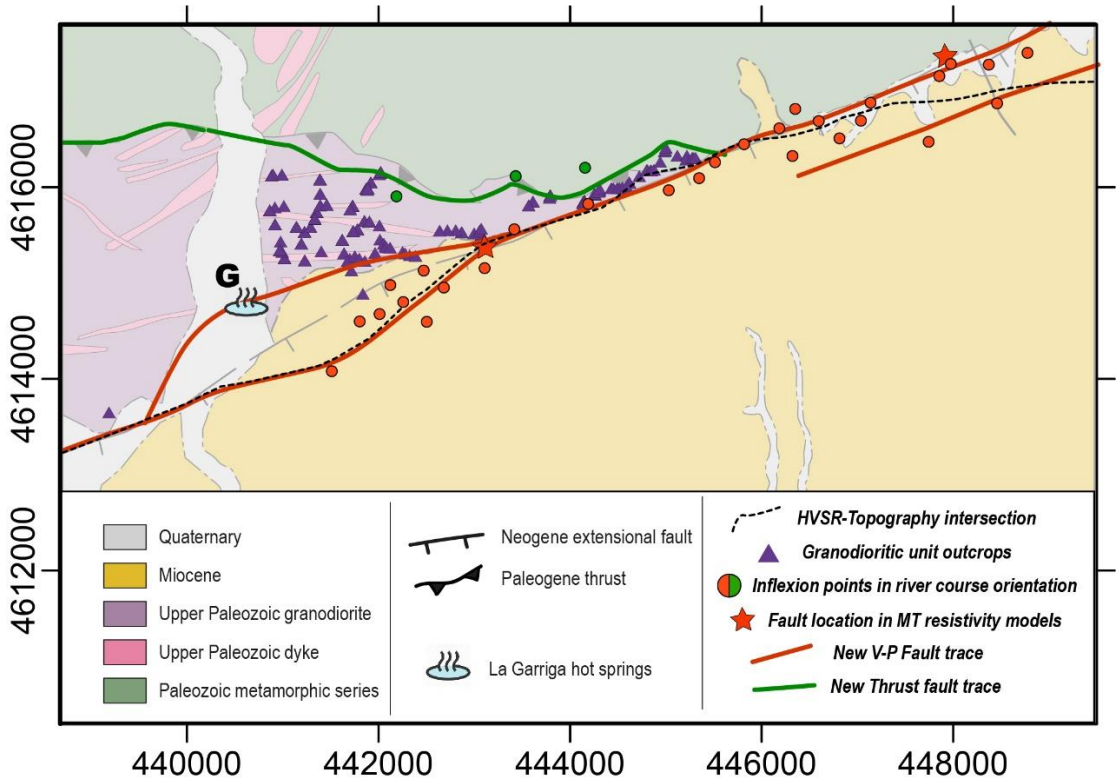

Figure 6. *Map showing constraints on the fault trace geometry of the V-P fault relative to earlier geological map (modified from ICGC, 2016). Evidence is derived from the following data: (i) the HVSR-Topography intersection line (green line; see also Fig. 3), (ii) the disposition of granodiorite outcrops, (iii) river inflection points (see Fig. 7), (iv) fault locations on MT resistivity models. The La Garriga river valley has occasionally been interpreted to contain a N-S fault of unknown origin, though its existence is not supported by any offsets of the V-F or the footwall Palaeogene thrust. A new interpretation of the main V-P fault zone envisages a fault lens arising from the breaching of a left-stepping relay.*

3.4. Petrographic characterization

Detailed petrographic analysis of secondary minerals and deformation textures has been performed on thin sections from outcrop and borehole samples (Fig. 9) to define the nature of deformation and fluid circulation within the damage zone of host rocks and the footwall granites, in particular. Our characterization of rock microstructure and the main mineral associations follows the procedure of Bertrand (2017) and Velde and Meunier (2008) on the following minerals to provide constraints on a variety of processes:

- Plagioclase and K-feldspars, to verify the alteration to clay minerals.
- Biotite, to investigate deformation and chlorite retrogression.

- Quartz, to identify micro-fractures, crystal deformation (e.g. undulate extinctions) and sub-grain recrystallization.
-

3.5. Structure-from-motion photogrammetry

Structure-from-motion photogrammetry (SfM) (Betlem et al., 2020) has been used to analyze fractures within 5 borehole core samples, in terms of their 3D nature and geometry, prior to thin section studies and further analysis (Fig. 11). SfM processing was performed from digital images acquired using a remote-controlled system camera *Lumix G7* coupled with a *14-42 mm Lumix* lens, and following the workflow illustrated in the***Supplementary material (S.2)***. The resulting point cloud for fractures has been analyzed using the open-source software *CloudCompare* (*2021*).

3.6. Porosity measurements

Twelve samples from outcrops and the S1 borehole (IGME, 1982) have been analyzed in order to get porosity values of the granodioritic unit and the metamorphic Paleozoic unit (Fig. 12). Porosity is a fundamental volumetric rock property that describes the potential storage volume of fluids and influences most physical rock properties (for example, electrical resistivity, elastic wave velocity, and density) (Anovitz & Cole, 2015). Moreover, its connectivity and pore structure control the fluid flow. Therefore, this property is one of the critical factors in geothermal characterization, and its analysis can provide a better reservoir identification and characterization (i.e., Dobson et al., 2003; Stimac et al., 2004).

The analysis of the selected samples was conducted in the *Institute of Geophysics and Geoinformatics* of the *Technical University of Bergakademie Freiberg* (Germany) following the procedure outlined in the ***Supplementary material (S.3)***.

4. Results

4.1. V-P Fault geometry

The map geometry of fault traces is an important means of defining the location of structural complexities along normal faults. Various constraints are available for the study area, providing a high-resolution areal definition.

H/V spectral ratio data suggest a left-hand hangingwall bend in the vicinity of the La Garriga town, as defined by hangingwall sediment thicknesses of < 100 m (Fig. 4) approaching the surface trace of the sediment to basement contact. This bend is consistent with geological maps indicating a similar left-hand footwall bend or step bounding thin (< 100 m) Miocene sediments and footwall granite exposures (Fig. 3). Taken together, these bends suggest the presence a fault-bounded lens (Fig. 5 & 6) straddling what is mapped as the principal fault trace. This lenticular configuration is also consistent with terrain changes reflected in the trajectories of rivers cutting across the fault (Fig. 7),

with single sharp deflections of rivers aligning with the approximately straight fault trace and with multiple deflections associated with the hangingwall and footwall bends enclosing an apparent lens in La Garriga town. Across the fault, the main river systems are approximately N-S or NNW-trending within the footwall of, and at a high angle to, the V-P Fault. However, they gradually turn towards more NNE-trending trajectories further to the south within the hangingwall basin fill (Fig. 2), particularly on regional scales as the southern footwall basement block is approached.

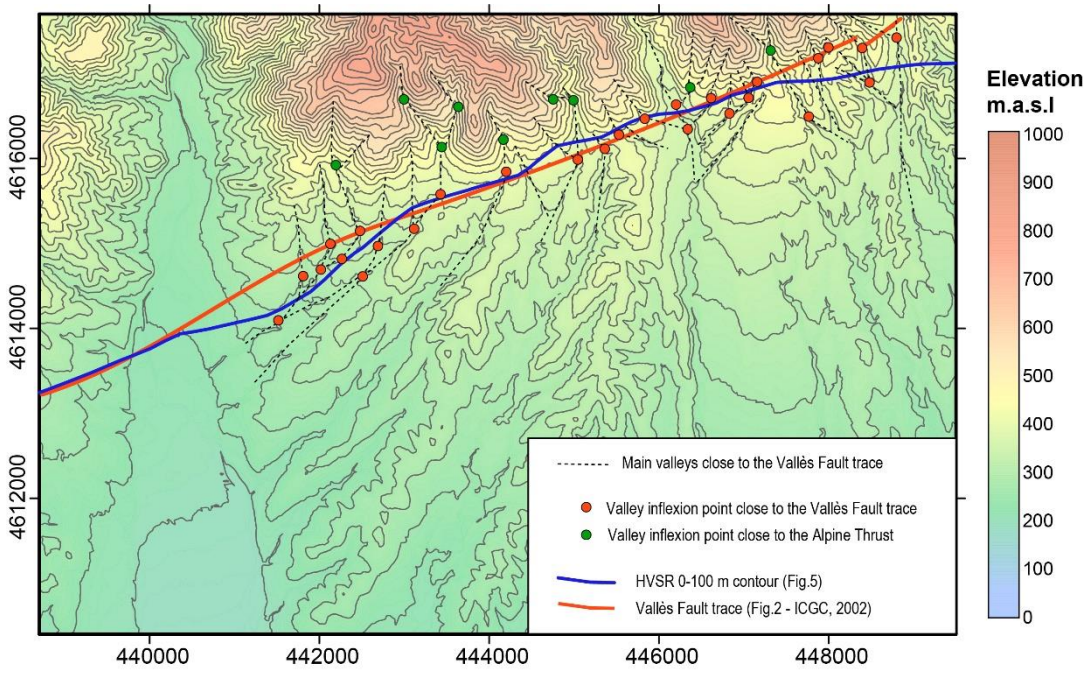

***Figure 7**. Location of the main streams, rivers and ravines of the drainage network between La Garriga an Cànoves towns, together with the sediment-footwall map contact. Red points indicate inflexion points in the river course orientation.*

The resistivity models for two cross-sections across the V-P Fault are consistent with the mapped locations of the fault trace, but they also provide excellent constraints on the deep geometry of the V-P Fault zone and Miocene basin (Fig. 4). On both cross-sections, the footwall basement rocks of the V-P Fault have very high resistivities (> ca 3000 Ωm) and bound fault zones up to ca 1km wide comprising lower resistivity rocks (< ca 300 Ωm) extending to depths of greater than ca 2 km below sea level. Within the hangingwall of the V-P Fault, near-surface Miocene sediments define a heterogeneous geo-electric unit characterized by resistivity values between 1 and 200 Ωm. This syn-kinematic Miocene unit increases to ca 1 km thick within about 3 km of the V-P Fault and towards the center of the Neogene basin (Figs 4 & 5), a change which could be accommodated by successive synthetic normal faults given the resolution of the available data.

Both MT cross-sections suggest that the footwall fault is steeply dipping (ca 70ºC) and approximately planar, but with a slightly shallowing (to 60ºC) on the MT-Samalús profile. The most significant departure from planarity is, however, the hangingwall side of the fault zone on the MT-Samalús profile, which dips at closer to ca 45ºC. This shallowing is considered a local artifact of the MT modeling, as conventional seismic suggests that a shallow dipping listric geometry should be developed at greater depths of between 5-10 km (Gaspar-Escribano et al., 2004; Roca et al., 1999).

Therefore, slightly shallower fault dips could be tentatively attributed to the eastward plunging of the La Garriga left-hand bend or the presence of synthetic normal faults not easily observed beneath the Miocene syn-rift sediments (Figs 4 & 5). The potential for synthetic faults within a few kilometers of the V-P Fault is supported by stepping off the imaged Miocene unit, with the extensive development of mapped river terrace deposits perhaps coinciding with the main fault zone of the eastern cross-section. In that sense, the mapped trace of the V-P Fault is simply the footwall-bounding structure of the fault zone, with the potential for additional synthetics within a few kilometers wide zone, which accommodates the syn-rift thickening suggested by H/V spectral ratio data.

Resistivity modelling also provides some indication of the displacement on the V-P Fault. Previous work has suggested a vertical displacement of ca 4 km based on a conventional seismic line that transects the fault about 30-40 km to the west of La Garriga (Roca et al. 1999). Within the study area, Miocene syn-rift sediments are no greater than ca 1.25 km thick, a scenario which is attributed to an eastward decrease in displacement along the fault, with previous work indicating a fault tip and the end of the V-P hangingwall basin a further 25 km to the east (Fig. 1). Regional maps support the discontinuous nature of the V-P Fault and its hangingwall basin, with an overall mapped length of ca 120 km and a maximum displacement of 5 km (accounting for fault dip), scaling properties which are consistent with previously published normal fault databases (e.g., Nicol et al. 2020).

4.2. Paleogene Prelitoral Thrust Geometry

The upper Paleozoic granodiorites within the footwall of the V-P Fault are contained in a thrust sheet overlying variably deformed Paleozoic metamorphic rocks. These units together are geographically referred to as the Prelitoral Range. At the surface, the thrust defines a broad bow-and-arrow geometry indicating an ENE-striking and SSE-dipping surface consistent with the characteristic NNW-directed Paleogene shortening. The fault trace geometry of the thrust is locally irregular, indicating a shallow-moderate dipping surface (ca 15º and 50º) compared to the steeply dipping V-P fault. Although the available geophysical data do not permit 3D definition of the Prelitoral Thrust, previous exploration boreholes located in Samalús town, which extend to depths of up to ca 1 km (e.g. S6 borehole; IGME, 1986), do not cross the granodiorite-metamorphic contact, therefore suggesting prevailing thrust dips of ca 45º or greater. Such moderate fault dips provide some support for the notion that the thrust may have been derived from the inversion of pre-existing normal faults along the site of the V-P Fault. However, they could also derive from associated footwall drag or minor synthetic fault displacements during Neogene extensional faulting. Whatever its precise geometry, the basic configuration of the thrust surface suggests a southward dipping thrust with the branch line between thrust and normal fault plunging towards the west in the La Garriga-Samalús study area and towards the east in the Caldes de Montbuí area. This geometrical arrangement is considered to be of first- order significance for the geothermal system's plumbing, an issue which is considered later.

4.3. Deformation features of the thrust sheet unit

The deformation of the granodiorite rocks of the Paleogene thrust sheet unit has been characterized in terms of its fault rock development, fracture types, fracture intensity, and porosities. The host rock has been defined using the essential minerals of a granodiorite, quartz (25%), potassic feldspar (20%), plagioclase (40%), biotite (10%), and lesser proportions of accessory minerals (+5%); in addition to the always affecting fracturing and alteration, which often show a sympathetic relationship and are spatially linked to the V-P Fault and, to a lesser extent, the Paleogene thrust.

a) Deformation of host rock granodiorites

The granodiorite host rocks are always highly fractured irrespective of their proximity to the major faults. Background fracture densities are generally less than 0.1/meter on sample lines across the fracture system, with the average fracture network occupying up to 20% of the rock volume. These rocks show moderate degrees of replacement of orthoclase and plagioclase by kaolinite and sericite, with some deformation, kinking, and chlorite retrogression of biotite and the localised presentation of calcite (Fig. 8). Fracture networks normally comprise two preferred fracture orientations, with the development of more anastomosing systems with an increase in strain and fracture intensity. Fracture apertures visible at outcrop vary from 0.05 to 2 mm, and in some cases, they are infilled by calcite and iron oxides (Fig. 8).

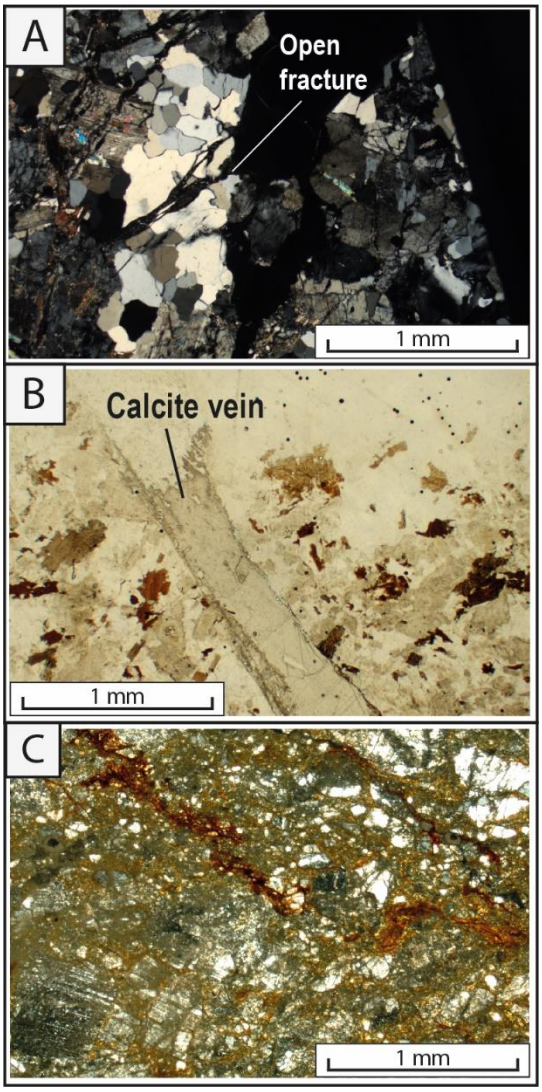

Figure 8. *A) Fractured granodiorite with open fractures. Sample shows undulant extinction, biotite deformation and subgrain recrystallization (XP). B) Granodiorite with carbonate vein (PP). C) Protocataclasite and highly fractured rock in which it is possible to identify an associated matrix (XP).*

Approaching the V-P Fault plane, the granodiorite host rocks can become harder and more compact, increasing the difficulty of sampling. Petrographic analysis indicates a high degree of particle crushing contained within an aphanitic matrix enriched in quartz and calcite cement that is heterogeneously distributed but rarely represents more than 50% by volume. This protocataclasite comprises rounded-angular clasts (Fig. 8c), with cataclasis and straining of quartz and feldspar

grains, and moderate to total alteration of feldspars. This development of protoclasite constitutes a fault core comprising up to ca 10 m thick of recrystallized and slickensided fault rock that appears in borehole cores to be hard, impermeable, and devoid of fractures. This fault rock is, in turn, bounded by a fault damage zone of high-intensity fracturing of the granodiorites that reaches ca 300 m beyond the fault surface.

Deformation adjacent to the Prelitoral thrust plane is more difficult to characterize however, it appears to be marked by the development of up to 4 m of incohesive impermeable gouge mainly derived from Ordovician slates in its footwall, a type of fault rock that has been previously identified in other parts of the CCR (i. e., Ribes Blaves fault gouge (Marcén et al., 2018)). Deformation of the footwall of the thrust is marked by ca 25 meters of fractured metamorphic unit below the main fault gouge, but the fracturing of the overlying hangingwall granodiorites unit is more pervasive (ca 50m) and intense.

b) Fracture systems within granodiorites

Fracture characterization within the host rock granodiorites has resulted in the identification of 6 sets of outcrop-scale fractures with the characteristics outlined in **Error! No s'ha trobat l'origen de la referència.** and Fig. 9. Moreover, the main orientations of fractures identified in boreholes point clouds (Fig. 10) match with those sets of fractures defined in the outcrops, with the most common fractures being F_A, followed by N-S steep (F_B) and shallow dipping (F_c) fractures. Although it has not been possible to determine the orientation of all of the borehole samples, together they permit fracture characterization without weathering and an assessment of the fracture apertures (2-4 cm) which can be both open and connected.

Table 1. *Fracture sets identified in the granodiorite of the Prelitoral thrust sheet.*

ID	Strike	Dip	Aperture	Infillings
F_A	NE-SW	50º – 88º	1 mm – 4 cm	Mostly unfilled (not-determined)
F_B	N-S to NNE-SSW	66º – 90º	4 mm – 2 cm	Unfilled
F_C	N-S	16º – 55º	0 mm – 2 mm	Filled (kaolin)
F_D	E-W	28º – 84º	2 mm – 1 cm	Filled (not-determined)
F_E	NW-SE to NNW-SSE	57º – 89º	1 mm – 3 mm	Mostly unfilled (carbonated)
F_F	WNW-ESE	73º – 86º	0 mm – 2 mm	Unfilled

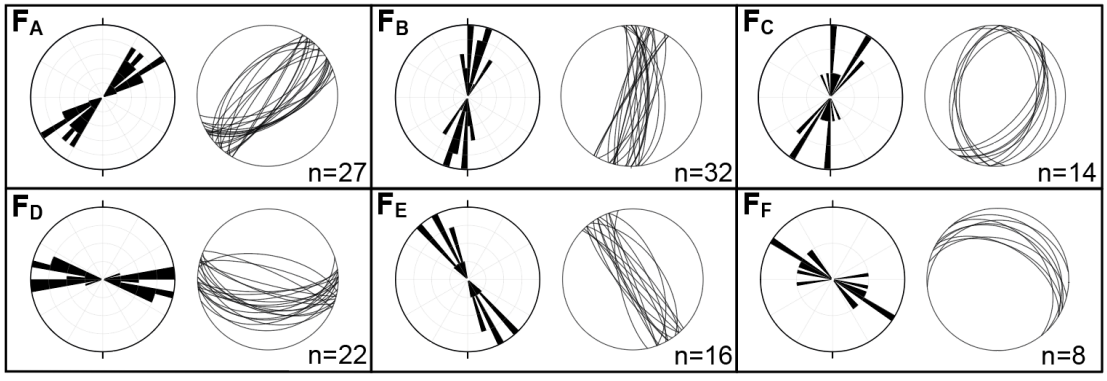

Figure 9. *Lower-hemisphere Schmidt stereonet and rose diagrams of the measured fractures grouped in the 6 fracture families distinguished in the granodiorite of the Prelitoral thrust sheet.*

From the few observable outcrops crosscutting relationships, the following chronology of the distinguished fracture families has been established: 1) F_F; 2) F_E; 3) F_D; 4) F_B and F_C; and, finally, 5) the F_A. Since no radiometric ages of veins are available in this area, there are no direct chronological constraints on the timing of fracture sets. Despite that shortcoming, potential geometric correlations (e.g., dip and strike) can be made between fracture sets and the main tectonic events, the relative timing of which is better defined from previous studies. On geometrical and kinematic grounds, we consider the F_D, F_E, and F_F fractures as the oldest fracture sets developed during the later stages of magma cooling related to the Variscan Orogeny. Cooling joints in magmatic intrusions are very frequently displaying a characteristic pattern of vertical (F_E) and sub-horizontal fractures (F_F) (Cloos, 1922; Mattsson et al., 2020; Price and Cosgrove, 1989). F_D fractures have the same orientation as the E-W dyke swarm of aplites and pegmatites, suggesting that they may be cooling fractures following the ascent of late granitic intrusions. Whilst fractures related to Mesozoic deformation have previously been described in the western part of the Vallès basin (Cantarero et al., 2014), our study has not identified fractures attributable to this deformation. Instead, the temporal activity of F_B and F_C fracture sets is unclear but is tentatively attributed to the Tertiary. Previous work has suggested that the Alpine orogeny (Eocene-Oligocene) was marked by NW-SE and N-S compression during earlier phases to be replaced by later NE-SW (Guimerá and Santanach, 1978). The main expression of Alpine deformation in the study area is the Prelitoral Thrust, with minor fractures previously considered to be strike-slip fractures with NW-SE and E-W orientations (Guimerá, 1984; Guimerá and Santanach, 1978), perhaps involving the reactivation of the previously fracture sets. Instead F_B, and F_C fracture sets are attributed to post-Alpine deformation as follows. The V-P Fault is the main expression of the Neogene rifting event (Bartrina et al., 1992; Cabrera and Calvet, 1996; Fontboté et al., 1990; Roca and Guimerà, 1992), with the F_A fracture set striking and dipping in the same orientation, with greater intensities adjacent to the fault trace, but with borehole samples indicating dip-slip slickenlines. Whilst cross-cutting relationship suggests that F_B and F_C are cross-cut by F_A, they are spatially distributed across the study but are densely localized close to the V-P Fault trace at La Garriga town and the branch point between the Prelitoral thrust and the V-P Fault. In the circumstances, their origin is tentatively attributed to localized deformation that is accentuated adjacent to structural complexities associated with the V-P Fault, including branch points and the breached relays.

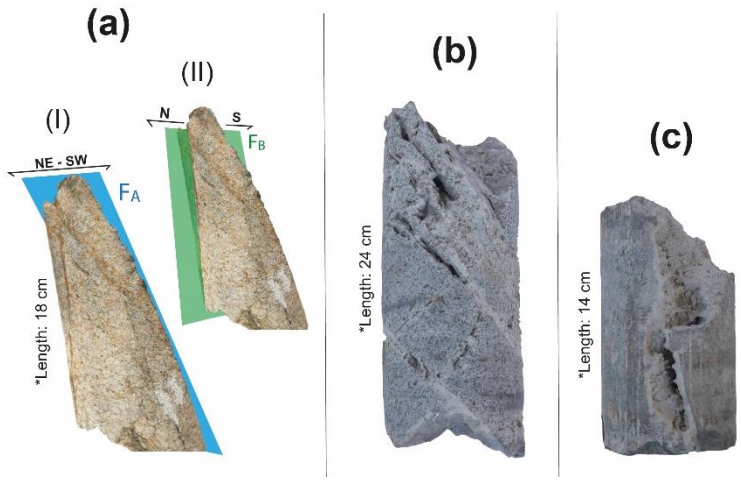

Figure 10. S1 borehole core samples. (a) Oriented sample used to relate the family sets described in outcrops with the deep

fractures. (b & c) Not oriented samples of a granodiorite (left) and a leucogranite (right) with open fractures partially filled by hydrothermal carbonated precipitates.

c) Fracture intensities

Quantitative characterisation of the V-P damage zone has been performed by measuring fracture density (8) from nearly 50 outcrops of 5 meters long average size. The resulting intensity map highlights an increase in fracture intensity towards the V-P Fault and, to a lesser extent, the Prelitoral Thrust. Average fracture intensities can reach values as high as 0.5/m approaching the V-P Fault, though the heterogeneous nature of fracture spatial distributions is typical at all scales. High intensities are typical of outcrops within ca 200 m of the V-P Fault, an observation which is consistent with open and connected fractures seen in both outcrops and boreholes. Taken together the fracture intensity data support the notion of a damage zone marked by enhanced fracturing within the immediate footwall of the V-P Fault (Fig. 11).

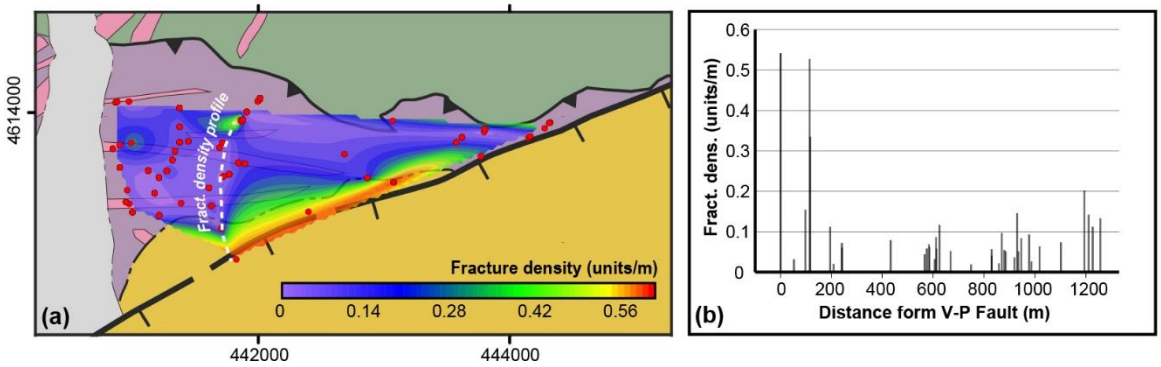

Figure 11. *Fracture intensity map and graph for the granodiorites within the footwall of the V-P fault. (a) Map with contours of the average fracture intensity (/m) for different outcrops (red dots). (b) Graph presents the average fracture density per meter sampled for individual outcrops in (a) projected onto a sample line (white broken line) extending from the V-P fault to the Prelitoral thrust; each outcrop is marked by a vertical line denoting the average fracture intensity.*

d) Porosity characteristics and distribution

Porosity measurements have been defined for granodiorite, dyke and metamorphic rocks sampled from outcrops, and for granodiorites sampled from the S1 borehole adjacent to Samalús. Outcrop samples for the granodiorite and dyke samples have porosities of between 5% and 30%, with the finer grained dykes providing lower porosity samples (5-15%). Petrographic analysis of these samples indicates the importance on weathering with varying degrees of alteration likely to dominate the associated porosity measurements, which are relatively high for conventional granites. By contrast borehole-derived porosities are both lower (1-10%) and are usually marked by fracture-related porosity as opposed to secondary porosities arising from weathering, values which are therefore considered to be more representative of the deeper subsurface (see below). Samples of metamorphic rocks underlying the Paleogene thrust have much lower and more consistent porosities of ca 5%, values we attribute to fracturing considering the unweathered nature of those host rocks compared to the overlying granodiorites. Existing constraints are relatively sparse at present but they do not suggest a direct relationship between the sample porosity and proximity to the V-P fault plane, a feature we attribute to the heterogeneous nature of deformation and alteration.

e) Estimation of groundwater flow parameters

Whilst porosity measurements for the host-rock granodiorite within the sub-surface suggest that weathering can generate porosity within the host-rock granodiorites, examination of borehole data indicates that deep sub-surface processes are dominated by fracture-controlled porosity arising from vuggy and high-intensity arrays of fractures and by associated cementation. In principle, more diffuse flow within weathered granites could contribute to groundwater flow in the near subsurface, but the heterogeneous nature of weathering and the outflow of geothermal fluids indicate that up-fault flow connectivity, either within the V-P Fault rocks or damage zone, is effectively a pre-requisite of the La Garriga geothermal system. The best examples of these are from the S1 borehole (IGME, 1982), which extends to depths of nearly 1 km, and given the vertical orientation of the borehole and the steep dip of the V-P Fault (ca 70º), must be within ca 200 m of the main fault surface and well within the intensely deformed damage zone of the fault. The presence of vuggy vein infills attests to the flow connectivity of the associated fracture system, but in the absence of flow data (e.g., flow rate, hydraulic conductivity), there is no means of directly defining the flow properties of the system.

Therefore, we use a method in which groundwater parameters are defined analytically from empirically derived measures of fracture aperture (perpendicular opening) and spacing (perpendicular distance). This approach assumes that the concepts of equivalent permeability and representative elementary volume (REV) are tenable at the scale of the flow and transport volume of interest (Zimmerman and Bodvarrson 1996; Odling et al. 1999; Müller et al. 2010). Porosity (p), permeability (k), and hydraulic conductivity (K) are estimated using the cubic flow law (e.g., NRC 1996; Zimmerman and Bodvarsson 1996; Schwartz and Zhang 2003), assuming horizontal flow through regular spaced fractures with constant aperture (Reiss 1980; Motyka 1998; Müller et al. 2010 and refs therein; Fig. 12). This method utilises the cubic flow law, in which flow velocities relate to the cube of the aperture and are only linearly dependent on spacing. Whilst this approach is a gross simplification of the structural complexity of the fracture networks concerned, it provides a very general approximation of the potential flow parameters of different components of the fracture system, not including the weathering-related poro-perm contributions discussed earlier.

The available data used in this study derive from estimates of fracture spacing and aperture, with the latter derived from vein aperture and/or vein thickness measurements, a potential shortcoming we will consider later. Taken together, these data indicate very significant combinations of apertures or thicknesses and densities of fractures adjacent to the fault. The cumulative fracture porosity (including filled and infilled fractures) is, however, very modest with values of between 1%-0.1% porosity. The highest values of fracture porosity are recorded within the lenticular fault zone in the centre of the study area, which is interpreted to have previously been a relay. Progressively lower fracture porosities are recorded within the damage zones and the fault core, in particular, with some dykes marked by high fracture porosities, but with very low apertures.

Translating these geometric measures of aperture/thickness and fracture spacing into flow properties such as bulk permeability (m^2) and hydraulic conductivity (m/d), suggests that flow is likely to be localized within the V-P relay zone and adjacent to the Paleogene thrust, an outcome which highlights the importance of both structures in controlling up-fault and along-fault flow. The

granodioritic outcrops provide a very broad spread in derived permeability, whereas the relay area is the most permeable and conductive zone overall. Despite the relationship between fracture density and proximity to the V-P Fault, the importance of the relay zone and thrust surface reflects the pre-eminence of dilatancy and aperture in estimating flow properties. Whilst these estimates provide some indication of the localization of flow within different components of the fracture system, the flow properties estimated have utilized the combined aperture and infill rather than the prevailing aperture at any given moment in time. Insofar as the thickness of fractures could conceivably derive from many hundreds or more increments of opening or valving of fractures, perhaps related to individual earthquakes, the flow properties should not be taken as representative of the prevailing flow properties. Estimates of 2-3 orders of magnitude lower are perhaps much more likely, but would, nevertheless, still indicate fracture permeabilities in excess of 1 Darcy (equivalent to bulk permeabilities of 10^{-12} m^2). Another factor that is not indexed in these simple calculations of permeability is that whilst carbonate infills demonstrate the circulation of geothermal fluid, they also reflect the ability of fractures to self-seal. This self-sealing could inhibit flow, but valving of fluids during multiple slip events or earthquakes often operates on the same fractures, which have, in any case, vuggy, and therefore weaker infills (Cantarero et al., 2010; Facca and Tonani, 1967). Given the prolonged and ongoing activity of self-sealing fractures, there is every reason to expect self-sealing to be a transient phenomenon.

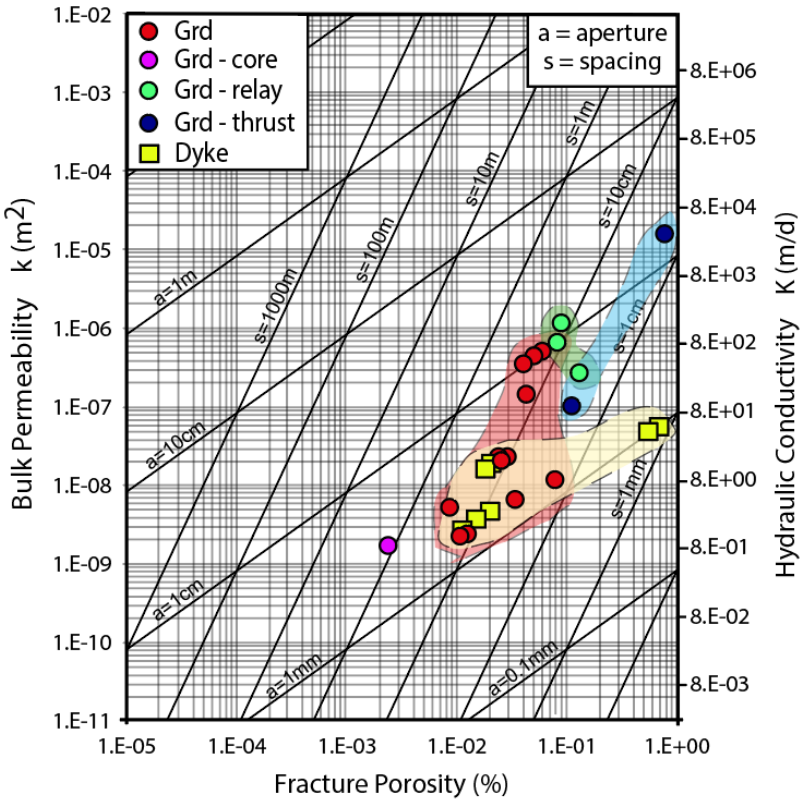

Figure 12. *Fracture spacing (s) vs fracture aperture (a) data for the study area, in which aperture is taken to be the cumulative fracture porosity (including filled and infilled fractures). The colors of the granodioritic unit measurements locate the samples in the fault core, in the relay zone, and close to the Alpine thrust. These data are also plotted within estimated bulk permeability, fracture porosity and hydraulic conductivity, using the method of Reiss (1980) assuming horizontal flow through regular spaced fractures with constant aperture. This approach provides very general estimates of fracture-controlled flow properties, which are, however, subject to very significant uncertainties (see text for details).*

5. Discussion

5.1. Alpine structure of the eastern margin of the Vallès-Penedès Basin.

The present-day structure of the Catalan Coastal Ranges predominantly reflects normal faulting arising from Neogene extensional tectonics, which post-dates and cuts Paleogene structures developed during compressional Alpine deformation (Marcén et al., 2018). Previous authors investigating the structural evolution of the Catalan Coastal Ranges have suggested that the V-P Fault is the result of the negative inversion of thrusts during Neogene extension (e.g., Anadón et al., 1979; Fontboté, 1954; Roca et al., 1999), but there is no consensus regarding the geometric relationship between the Prelitoral Thrust and the V-P Fault.

Our analysis of the available data confirms that the V-P Fault is a steeply dipping structure, with dips generally between 60^0 and 70^0 apart from more inclined surfaces associated with a relay at La Garriga town. This geometry is compatible with that of a bifurcating upwards normal fault marked by a breached relay at the surface (Giba et al. 2012; Roche et al. 2021).

Seismic evidence indicates approximately planar faults, albeit with some limited shallowing in the upper 10 km of the crust (Roca et al. 1999). The presence of hangingwall rollover has been interpreted to suggest a detachment at depths of 13-15 km (Roca and Guimera, 1992), but direct evidence from depth-converted seismic sections is lacking and similar deformations are also typical of established flexural-isostatic models of planar faults (e.g. Roberts & Yielding 1994). In this background context, we favour a planar fault model down to depths exceeding 10 km, a scenario that is commonplace in most low-strain intra-cratonic rift systems, such as the North Sea and the Basin and Range (e.g. King et al. 1988; Kusznir and Ziegler 1992), and is capable of generating the tilted fault blocks of the Catalan Coastal Ranges (Roca et al. 1999), together with the hangingwall subsidence and footwall uplift associated with individual faults.

In these circumstances, we propose two alternatives for explaining the current spatial relationship between the Paleogene thrust and the V-P Fault. First, the geometrical current configuration could simply arise from a normal fault offsetting a previous shallow dipping thrust which is therefore only exposed within the footwall of the normal fault but would have a deeper expression within the hangingwall fault block. An alternative model is that the Paleogene thrust is a footwall short-cut structure arising from the inversion of any pre-Tertiary expression of the V-P normal fault. Distinguishing between these models is not easy given the available constraints but insofar as the thrust does not appear to steepen and root into the V-P Fault, a cross-cutting relationship is favored. Whichever of these models is correct, both involve a deeply rooted normal fault extending into basement, circumstances which promote the emergence of a high enthalpy geothermal systems developed along the V-P Fault.

Although the Paleogene and Neogene tectonic evolution of the Catalan Coastal Ranges has been well studied, there are much fewer constraints on the Pliocene and Quaternary tectonic evolution of the region (Masana, 1996). The general consensus is that the main phase of normal faulting in the

V-P Basin began in Late Oligocene times, at the latest, and continued into the Late Miocene (Tortonian), particularly along the V-P Fault (e.g. Bartrina et al. 1992; Roca et al. 1999). Thereafter, decreases in across-fault sequence growth have been attributed to the predominance of late rift-related thermal subsidence and sedimentation, and the accommodation of lower rates of crustal extension, principally by the cessation of movement on most faults and a decreased level of fault activity along the larger faults, such as the V-P Fault and the Barcelona Fault (Masana, 1995, 1994; Roca et al. 1999). Small faults within the Pliocene and Lower Quaternary are sparse, attesting to the decreased intensity and activity of normal faulting in that period. Associated seismicity within the Catalan Coastal Range is considered to be low (Massana, 1994), with several earthquakes of M < 4 every year, and whilst there have been no recorded earthquakes greater than M5, two historical earthquakes with intensities of VII and VII-VIII (corresponding to M6.0-6.8) have occurred on or adjacent to the V-P Fault (de Galdeano et al. 2020). Despite this relatively low level of activity, these earthquakes and the protracted history of the V-P Fault provide support for fault reactivation and associated fluid circulation, a scenario we consider later in the context of the geothermal systems of La Garriga and Caldes de Montbui.

5.2. Fault trace and displacement geometry of the V-P Fault.

Constraints from mapping and geophysical data indicate that the V-P Fault has a maximum displacement of ca 5 km and a trace length of 100 km (Bartrina et al., 1992; Gallart et al., 1997; Gaspar-Escribano et al., 2004; Gómez and Guimerà, 1999; Juez-Larré and Andriessen, 2006; Roca and Guimerà, 1992; Roca et al., 1999; Sàbat et al., 1995; Vidal et al., 1995), scaling properties that are consistent with existing empirical constraints for normal faults (Nicol et al. 2020).

Lateral changes in displacement along the V-P Fault are supported by lower displacements (<3 km) in the study area, the presence of exposed fault tips at either end of the fault, the narrowing of the V-P Basin towards the NE and SW, and evidence on seismic profiles for a decrease in the basement depth of the V-P Basin towards the NE (Roca, 1992). Towards the eastern tip of the fault, the prevailing hangingwall topography also dips towards the SW, with associated river systems sourced directly from the footwall mountains in the north and curving towards the SW in the south.

Although the mapped trace of the V-P Fault is relatively simple on regional scale maps (Fig. 1), closer examination indicates that it is marked by fault bends and steps that are developed at and below km-scales. At Caldes de Montbui, towards the eastern limit of the V-P Fault, the trace is marked by non-aligned linear segments connected by fault bends. A very similar structure has been defined in the study area as the La Garriga relay zone, which has a width of 650 m and an overlap length of 2000 m, consistent with the scaling relationship of relays along large faults (Fossen and Rotevatn, 2016).

Combining the displacement and relay dimensions, and comparing them with empirical quantitative constraints of large published relay databases, strongly suggests that the relay is breached and, most likely, doubly breached to form a lenticular zone of fault-related deformation because the rapid transfer of 1.5 km scale displacements is not compatible with an intact relay at that 1-2 km scale (Fig. 13).

Our work also indicates that relay breaching promotes the fracturing of adjacent granite host rocks, in particular, circumstances that provide a means of generating steeply inclined potential pathways along the mapped relay axis (e.g. Bonson et al. 2007; Fossen and Rotevatn, 2016; Walsh et al. 2018). Analysis of the relay within La Garriga highlights the intense fracturing associated with the fault zone, in which faults that are parallel and perpendicular to the main V-F Fault provide a basis for generating a fracture network which is the locus for fluid flow, an issue we consider below.

Very indirect support for the presence of a relay adjacent to both the La Garriga and Caldes de Montbui geothermal systems is provided by the transecting rivers at those locations, an association that has been advocated in other active continental rifts, such as the Sperchios Basin, Central Greece (Eliet and Gawthorpe 1995), and the Gedz Graben, Western Turkey (Dart et al. 1995). The presence of river systems associated with relays, therefore, comes with the potential of dispersing geothermal fluids within Quaternary river sediments, a scenario which is known to have occurred at La Garriga.

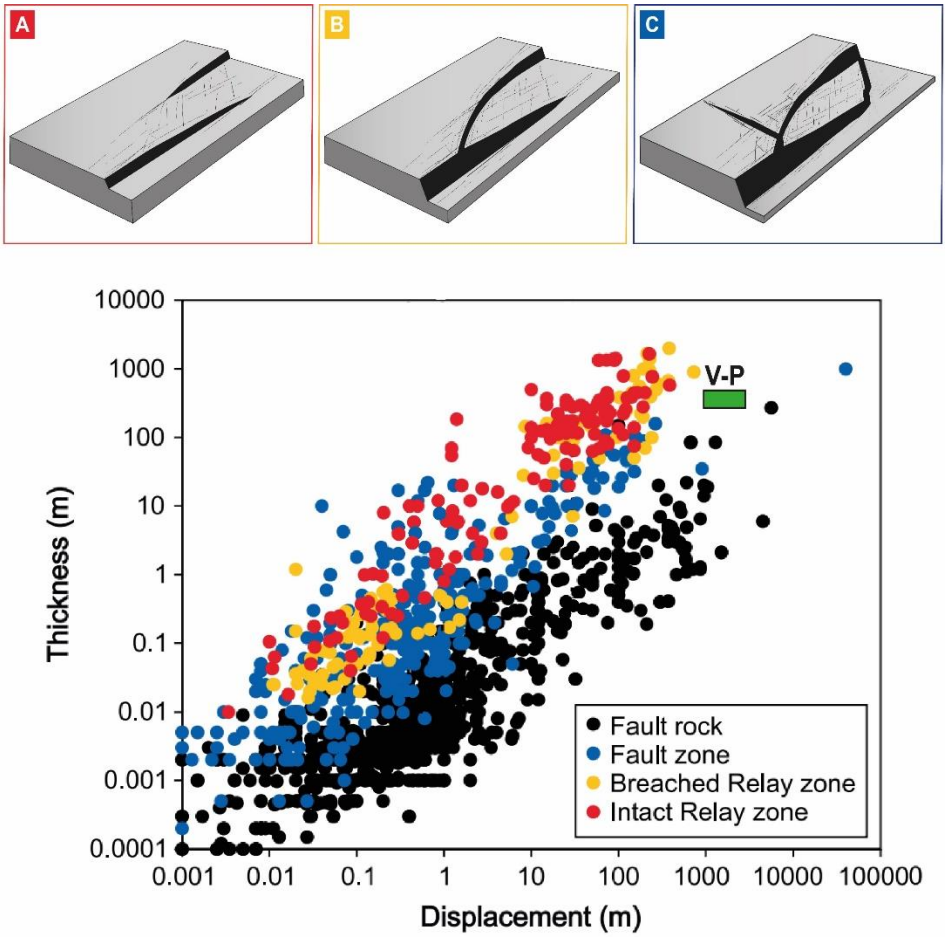

Figure 13. *A) Unbreached relay ramp displaying ramp-related fracturing and deformation. The thickness (T), or segment perpendicular separation, is shown. (B) Breached relay ramp in which continuous (i.e. ramp-related) deformations still accommodate much of the displacement transfer between segments. (C) Doubly-breached relay ramp, with strongly deformed fault lens. (D) Displacement vs thickness plot for different components of fault zones, including intact relay zones (red), breached relay zones (orange), fault zones (blue; including intact relays through to fault lenses) and fault rock (black). The scaling of the V-P fault zone at La Garriga is consistent with the presence of strongly fractured host rock and fault rock.*

5.3. Basinal context for geothermal systems within Vallès-Penedès Basin

Located within the Oligocene-early Miocene to recent Vallès-Penedès Basin, the Vallès site benefits from the presence of a relatively thick basin fill (up to 3 km) deposited upon mainly Hercynian metasediments and granites. Development of this 50 km wide half-graben is in the context of a much wider fault system extending across the Catalan Coastal Ranges (CCR) into the Valencia Trough (Fig. 6). The NE-trending graben is marked by emergent and faulted basin margins bounding domino-style faulting, with internal deformation of individual dominoes generating hangingwall rollover, footwall uplift, and the rotation of fault blocks.

The generation of the basin- and range--type terrains, and the deposition of siliciclastic sediments containing substantial thicknesses of sometimes relatively high poro-perm alluvial/fluvial sandstones (up to ca 2.5 km thick), provides a basis for the ingress of groundwater and its retention within basinal sequences. On the other hand, basement rocks underlying the V-P Basin Miocene infill are, however, volumetrically more significant than the basin fill sequence and could, therefore, represent the best means of both recharging the basinal fluid system and sourcing hotter fluids. For example, Mesozoic carbonate-dominated sequences are up to 2 km thick and comprise fractured and karstified limestone sequences in the southern and southwestern part of the V-P basins (ca 30 km from the study area) and within the Garraf-Montenegre, which separates the V-P and the Barcelona Basins (Baqués et al. 2012; Marin et al. 2021). Previous work has indicated multiple phases of meteoric percolation and fracturing processes within these limestones, with karst development extending from the pre-rift to late-rift phases of Neogene rifting (Baques et al. 2012; Marin et al. 2021). Underlying Variscan basement comprises Cambrian to Carboniferous slates together with Carboniferous to Permian granitoids (Marin et al. 2021), broadly corresponding to the metamorphic and granitoid basement rocks of the study area. Ongoing deformation arising from continued extension and associated earthquake activity also provides a means of driving fluids during seismic cycles through a variety of mechanisms including seismic valving or pumping. The accommodation of groundwater flow to significant depths is facilitated by the extensional nature of the basin, the porous nature of much of the basin fill and the fractured and karstified nature of underlying Mesozoic and Variscan basement rocks. These circumstances together with the tectonically and, to the north of the study area, volcanically active setting of the area provides an excellent basis for a system characterized by high geothermal gradients and hydrodynamic drives with hot springs providing groundwater temperatures of up to ca 60^0C and recorded downhole temperatures of up to 90^0C at depths of 1 km.

Localization of hot springs with elevated temperatures within the CCR is always associated with faulting (Canals et al., 1989; Cardellach et al., 2002; Fernàndez and Banda, 1988; Mitjanas et al., 2021). Faults evidently provide the optimal means of transporting hot aqueous fluids from depth up to the surface. The along-fault migration of fluids is sufficiently rapid to preserve high temperatures, circumstances which are not satisfied by slower fluid migration through syn-rift sediments or basement rocks. Therefore, fluid flow is promoted by the tectonically active nature of the system and by the associated deformation processes.

The response of different host rocks to the accommodation of displacement is very distinct, with adjacent granites marked by cataclastic fault rocks and damage zones that are dilational in nature but with more porous syn-rift sediments expected to be marked by deformation bands and compactive fault rocks that are usually detrimental to across-fault flow but can nevertheless be pathways for up-fault flow. Support for these prevailing fault rock distributions is provided by the presence of cataclastic gouge adjacent to syn-rift host rocks within boreholes and the prevalence of fracture-controlled flow within the granitic footwall.

The longevity of the flow system is very difficult to define, but the pervasive nature of the alteration of the granite host rocks is marked by the sericitization of feldspar, the retrogression of biotite to chlorite and by the precipitation of a variety of other alteration minerals. Another feature supporting the prolonged activity of the hydrothermal system is the intensity of vein filled fractures that have multiple orientations and are often vuggy. These types of fracture system attest to the overpressured nature of the associated thermal waters and strongly elevated downhole temperatures suggesting along fault geothermal gradients of nearly 100^0C/km.

5.4. 3D conceptual model of the Vallès geothermal system

The development of geothermal systems adjacent to faults within extensional basins is a well-established phenomenon (Curewitz and Karson, 1997; Sibson, 2001; Fairley and Hinds, 2004a, b; Walsh et al. 2018 and references therein). Crustal thinning is accompanied by increases in geothermal gradient and the potential for the deeply penetrating convective flow systems with a hydrodynamic system supplied by the downward ingress of groundwater through faults, syn-rift, or hydrostatically pressured basement. Whilst the sinking of fluids will be facilitated by increases in salinity, analysis of the thermal waters at La Garriga spa does not suggest the presence of heavy brines (REFERENCE). Within the Vallès-Penedes basin, the migration pathways are unclear, with the potential for north- and northwestward migration into the basin via hangingwall syn-rift sequences and karstified Mesozoic limestones or via uplifted footwall, mainly granitic, blocks in the southeast, or with south- to southwestward migration pathways from footwall Paleozoic metamorphic/granites, Triassic sediments or perhaps even volcanics much further to the NE. Given the prevalence of clastic syn-rift sequences and underlying fractured/karstified pre-rift rocks in the V-P basin, there are strong grounds for the sourcing of groundwater for the very localized geothermal systems along the V-P Fault. The main concerns thereafter are the hydrodynamic drive and localization of fluids within the system.

The available evidence suggests that whilst the V-P fault system basin was not as tectonically active in Pliocene-recent times, compared to its main period of activity in late Oligocene to late Miocene times, historical earthquakes with magnitudes of up to 6.8 have occurred, and the fault is considered active. Recent estimates of the seismic parameters of the so-called Montseny Fault (de Galdeano et al. 2020), which is the northern end of the V-P Fault, suggest slip rates of 0.05-0.13 mm/year arising from earthquakes with maximum magnitudes of 6.7-6.8 and mean recurrence intervals of ca

26,000 years. These characteristics are very similar to faults within the Basin and Range, from which seismic pumping models of fault-related fluid flow have been advanced (Muir-Wood & King 1993).

Seismic pumping involves the interseismic accumulation of dilations due to fracturing and poro-elastic effects within host-rock volumes surrounding normal faults. Co-seismic deformation is then marked by the imposition of compressional strains subscribing to elastic dislocation theory which involve the expulsion of considerable volumes of fluid during individual earthquake events (Sibson et al. 1975; Blundell 2002). Muir-Wood and King (1993) showed that predicted co-seismic porosity losses are consistent with accentuated surface flow during major earthquakes in the Basin and Range province, with, for example, volumetric changes of 0.3 km^3 of water expelled during the Borah Peak 1983 earthquake (M~6.9). This earthquake occurred on the Lost River Fault which has a maximum displacement of >4km requiring ca 1000 similar-sized events for regional recurrence intervals of 20,000 years over the lifetime of the Basin and Range. This scenario provides a basis for the draw-down and driving of fluid volumes of ca 3 x $10^2 km^3$ within the host rocks surrounding a normal fault which is very similar to that of the V-P Fault. Whilst this model could make an important potential contribution to the hydrodynamics of the V-P Basin it does not, on its own, provide a rationale for the localization of flow along the V-P fault itself. For this we advocate a model for fault-driven fluid flow referred to as seismic pulsing, in which earthquake slip and frictional sliding causes transient dilation (i.e., opening) and the pulsing of fluids up the fault surface (Wilkins and Naruk, 2007), a process that is similar to the seismic suction pump model described by others (Rudnicki and Chen, 1988; Grueschow et al., 2003). Estimates of transient dilation for the V-P Fault, a 100 km long structure with a time-averaged slip rate of 0.1 to 1mm/year, range between 10 km^3 to 100 km^3, corresponding to large flow volumes which could be even more strongly localized because of along-fault relays and lenses.

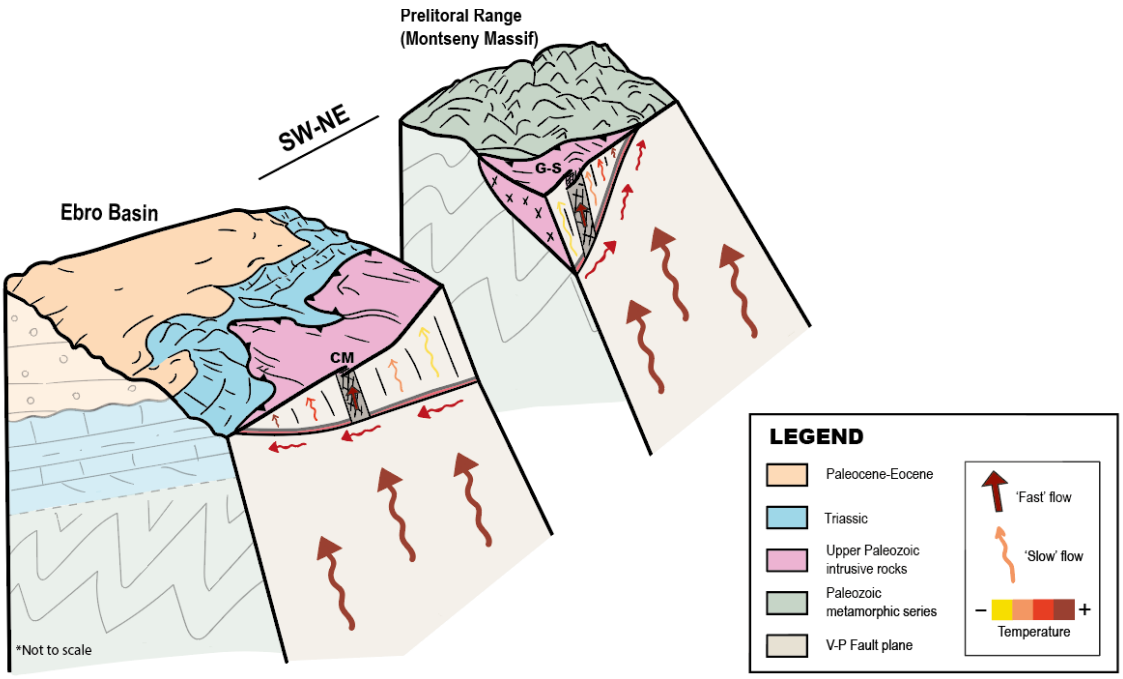

***Figure 14**. Geothermal conceptual model of the Caldes de Montbui (CM) – La Garriga and Samalús (G-S) system. Curvilinear arrows indicate the slower ascend of fluids, and their color, their relative temperature. The red straight arrows indicate the preferential channels for hydrothermal fluid upwelling. See text for details.*

Even assuming the cessation of fault slip along the V-P Fault in Pliocene to recent times, the basin will retain much of the syn-rift hydrodynamic regime, including structural, thermal and pore-fluid pressure drives. One of the principal mechanisms for up-fault flow is fault valving which is exclusively driven by the migration of higher pressure (i.e. deep and warmer) fluids when fluid pressures lead to mechanical failure of fault seals, a scenario which can occur within basins that are not tectonically active (Phillips 1972, Sibson 1990, 1992; Walsh et al. 2018). Another potential mechanism is even simpler, insofar as it requires passive up-fault flow along preferred flow conduits at rates which match the buildup of fluids at depth. Whichever combination of models applies, the basic requirement for structurally controlled flow localization at particular sites is complexity and heterogeneity of structure. What this study has shown is that hydrothermal fluid flow is developed preferentially towards the intersection of a Paleogene thrust and the V-P Fault. The basic configuration and trace of this thrust suggests that its intersection line with the normal fault will plunge towards the center of the fault away from the mapped branch points, a scenario which will lead to preferential flow towards the ends of the thrust. Perhaps more importantly for the La Garriga geothermal system, a major step in the Vallès Fault is characterized by accentuated fault damage, veining, and fluid flow. This scenario is consistent with evolutionary models for the growth and breaching of relays, which are often considered to be the locus for up-fault fluid flow (e.g. Rotevatn & Bastesen 2012; Fossen & Rotevatn, 2016; Kyne et al. 2019). The importance of this structure is clearly reflected in the thermal structure of the area and accentuated porosity and permeability arising from higher density fracture systems and meshes, providing conduits for the upward flow of hydrothermal fluid, which in the study area provides groundwater of ca 60^0C, with recorded downhole temperatures of up to 90^0C at depths of 1 km.

6. Conclusions

The integration of new and previous geological and geophysical data has allowed an improvement of the conceptual model which describes the Vallès Basin geothermal system's functioning. This improvement is mainly based on a better characterization of the main structures and the related deformation features. Some of the main outcomes are specified below:

A direct relationship has been observed between the shallow thermal anomaly manifestations and the maximums of structural complexity in the area.

Although the geometrical arrangement of the main structures, the V-P Fault and the Paleogene Thrust, at great depth remains unclear, the presented model establishes that the thrust is cut by the subsequent action of the Vallès Fault. However, this specific deep arrangement does not influence the functioning of the geothermal system under study.

The fracturing type conditioned by the major structure's proximity but also by the nature of the rock, affects both the recharge and discharge zones, as well as condition the fluid pathways.

The constant earthquake activity during time has a key role on the geothermal system functioning, driving fluids and breaking hydrothermal self-sealings.

7. References

Achtziger-Zupančič, P., Loew, S., Hiller, A., 2017. Factors controlling the permeability distribution in fault vein zones surrounding granitic intrusions (Ore Mountains/Germany). J. Geophys. Res. Solid Earth 122, 1876–1899.

Anadon, P., Cabrera, L., Guimera, J., Santanach, P., 1985. Paleogene strike-slip deformation and sedimentation along the southeastern margin of the Ebro Basin. Strike-slip Deform. basin Form. Sediment. 303–317.

Anadón, P., Colombo, F., Esteban, M., Marzo, M., Robles, S., 1979. Evolución tectonoestratigráfica de los Catalánides. Acta geológica hispánica 14, 242–270.

Anderson, J.L., Osborne, R.H., Palmer, D.F., 1983. Cataclastic rocks of the San Gabriel fault - An expression of deformation at deep crustal levels in the San Andreas fault zone. Tectonophysics 98, 209–251.

Vinyet Baqués AlmirallVinyet Baqués AlmirallA. TravéA. TravéEduard RocaEduard RocaShow all 5 authorsIrene CantareroIrene CantareroGeofluid behaviour in successive extensional and compressional events: a case study from the southwestern end of the Vallès-Penedès Fault (Catalan Coastal Ranges, NE Spain).

Baques, V., Trave, A., Roca, E., Marín, M., Cantarero, I., 2012. Geofluid behaviour in successive extensional and compressional events: a case study from the southwestern end of the Vall`es-Pened`es Fault (Catalan Coastal Ranges, NE Spain). Petroleum Geoscience 18, 17–31.

Baques, V., Trave, A., Cantarero, I., 2013. Development of successive karstic systems within the Baix Penedes Fault zone (onshore of the Valencia Trough, NW Mediterranean). Geofluids 14, 75–94.

Bard, P.-Y., 1998. Microtremor measurement : a tool for site effect estimation?, in: Second International Symposium on the Effects of Surface Geology on Seismic Motion. Yokohama, Japan, pp. 1251–1279.

Bard, P.-Y., 1985. Les effets de site d'origine structurale: Principaux résultats experimentaux et théoriques., in: Davidovici, V. (Ed.), Genie Parasismique. Presses de l'école nationale des ponts et chaussées., pp. 223–238.

Bartrina, M.T., Cabrera, L., Guimerà, J., Roca, E., Jurado, M.J., 1992. Evolution of the central Catalan margin of the Valencia trough (western Mediterranean). Tectonophysics 203, 219–247.

Bastesen, E., Rotevatn, A. 2012. Evolution and structural style of relay zones in layered limestone–shale sequences: insights from the Hammam Faraun Fault Block, Suez rift, Egypt. Journal of the Geological Society London 169, 477-488.

Bellanger, M., Hermant, B., Galibert, S., Auxiètre, J., 2019. Fault-controlled hydrothermal system associated with major Crustal Fault Zone : future drilling target to assess the deep geothermal potential – The Sioule license project. Eur. Geotherm. Congr. 2019, Den Haag, Netherlands, 11-14 June 2019 1–10.

Benjumea, B., Macau, A., Gabas, A., Bellmunt, F., Figueras, S., Cirés, J., 2011. Integrated geophysical profiles and H/V microtremor measurements for subsoil characterization. Near Surf. Geophys. 9, 413–425.

Benjumea, B., Macau, A., Gabàs, A., Esquerda, M., Figueras, S., 2014. Improving near surface characterization by combining reprocessed vintage seismic and geophysical passive datasets. Near Surf. Geosci. 2014 - 20th Eur. Meet. Environ. Eng. Geophys. 14–18.

Bertrand, L., Le Garzic, E., Géraud, Y., Diraison, M., 2013. Fractured crystalline reservoir: A field analog analysis on Tamariu's granite (Catalonian Coastal Ranges). 2nd EAGE Work. Nat. Fract. Reserv. Nat. Fract. Reserv. Real Life. https://doi.org/10.3997/2214-4609.20132004

Betlem, P., Birchall, T., Ogata, K., Park, J., Skurtveit, E., Senger, K., 2020. Digital drill core models: Structure-from-motion as a tool for the characterisation, orientation, and digital archiving of drill core samples. Remote Sens. 12. https://doi.org/10.3390/rs12020330

Blundell, D.J., 2002. The timing and location of major ore deposits in an evolving orogen: The geodynamic context. Geological Society, London, Special Publication 204, 1–12.

Bonson, C.G., Childs, C., Walsh, J.J., Schöpfer, M.P.J., Carboni, V. 2007. Geometric and

kinematic controls on the internal structure of a large normal fault in massive limestones: the Maghlaq Fault, Malta. Journal of Structural Geology 29, 336-354.

Cabrera, L., Calvet, F., 1996. Onshore Neogene record in NE Spain: Vallès–Penedès and El Camp half-grabens (NW Mediterranean), in: In P. Friend & C. Dabrio (Ed.), Tertiary Basins of Spain: The Stratigraphic Record of Crustal Kinematics. Cambridge University Press, pp. 97–105.

Caine, J.S., Evans, J.P., Forster, C.B., 1996. Fault zone architecture and permeability structure. Geology 24, 1025–1028.

Camanni, G., Roche, V., Childs, C., Manzocchi, T., Walsh, J., Conneally, J., Saqab, M.M., Delogkos, E., 2019. The three-dimensional geometry of relay zones within segmented normal faults. J. Struct. Geol. 129, 103895.

Canals, A., Albert, J., Ayora, C., 1989. El sistema geotérmico de la Garriga-Samalús: : comparaciones con sistemas hidrotermales fósiles. Geogaceta.

Cantarero, I., Lanari, P., Vidal, O., Alías, G., Travé, A., Baqués, V., 2014. Long-term fluid circulation in extensional faults in the central Catalan Coastal Ranges: P-T constraints from neoformed chlorite and K-white mica. Int. J. Earth Sci. 103, 165–188. https://doi.org/10.1007/s00531-013-0963-8

Cantarero, I., Travé, A., Alías, G., Baqués, V., 2010. Pedogenic products sealing normal faults (Barcelona Plain, NE Spain). J. Geochemical Explor. 106, 44–52. https://doi.org/10.1016/j.gexplo.2010.02.004

Cardellach, E., Canals, A., Grandia, F., 2002. Recurrent hydrothermal activity induced by successive extensional episodes: The case of the Berta F-(Pb-Zn) vein system (NE Spain). Ore Geol. Rev. 22, 133–141.

Cartwright, J.A., Mansfield, C., Trudgill, B., 1996. The growth of normal faults by segment linkage. Geol. Soc. Spec. Publ. 99, 163–177.

Childs, C., Manzocchi, T., Walsh, J.J., Bonson, C.G., Nicol, A., Schöpfer, M.P.J., 2009. A geometric model of fault zone and fault rock thickness variations. J. Struct. Geol. 31, 117–127.

Childs, C., Watterson, J., Walsh, J.J., 1995. Fault overlap zones within developing normal fault systems. J. - Geol. Soc. 152, 535–549.

Cloos, H., 1922. Tektonik und Magma: Untersuchungen zur Geologie der Tiefen.

CloudCompare [GPL software], 2021.

Curewitz, D., and Karson, J.A., 1997. Structural settings of hydrothermal outflow: Fracture permeability maintained by fault propagation and interaction: Journal of Volcanology and Geothermal Research 79, 149–168.

Dart, C, Cohen, H.A., Akyuz, H.S., Barka, A. 1995. Basinward migration of rift-border faults: implications for facies distributions and preservation potential. Geology 23, 69 –72.

de Galdeano, C.S., Azañón, J.M., Cabral,J., Ruano,P., Alfaro,P., Canora,C., Ferrater,M., García Tortosa, F.J., García-Mayordomo, J., Gràcia, E., Insua-Arévalo, J.M., Jiménez Bonilla, A., Lacan, P.L., Marín-Lechado, C., Martín-Banda, R., Martín González, F., Martínez-Díaz, J.J., Martín-Rojas, I., Masana, E., Ortuño, M., Pedrera, A., Perea, H., Simón, J.L. 2019. Active faults in Iberia. In: C. Quesada, J. T. Oliveira (eds.), The Geology of Iberia: A Geodynamic Approach, Regional Geology Reviews, 33-75.

Dobson, P. F., Kneafsey, T. J., Hulen, J., & Simmons, A. (2003). Porosity, permeability, and fluid flow in the Yellowstone geothermal system, Wyoming. *Journal of Volcanology and Geothermal Research*, *123*(3–4), 313–324.

Duan, Q., Yang, X., Chen, J., 2017. Hydraulic properties of a low permeable rupture zone on the Yingxiu-Beichuan Fault activated during the Wenchuan earthquake, China: Implications for fluid conduction, fault sealing, and dynamic weakening mechanisms. Tectonophysics 721, 123–142.

Duwiquet, H., Arbaret, L., Guillou-Frottier, L., Heap, M.J., Bellanger, M., 2019. On the geothermal potential of crustal fault zones: a case study from the Pontgibaud area (French Massif Central, France). Geotherm. Energy 7.

Duwiquet, H., Guillou-Frottier, L., Arbaret, L., Bellanger, M., Guillon, T., Heap, M.J., 2021. Crustal Fault Zones (CFZ) as Geothermal Power Systems: A

Preliminary 3D THM Model Constrained by a Multidisciplinary Approach. Geofluids 2021.

Eliet, P. P., Gawthopre, R.L. 2007. Drainage development and sediment supply within rifts, examples from the Sperchios basin, central Greece. Journal of the Geological Society, 152, 883-893.

Facca, G., Tonani, F., 1967. The self-sealing geothermal field. Bull. Volcanol. 30, 271–273. https://doi.org/10.1007/BF02597674

Fairley, J.P., and Hinds, J.L., 2004a. Rapid transport pathways for geothermal fluids in an active Great Basin fault zone: Geology 32, 825–828.

Fairley, J.P., and Hinds, J.L., 2004b. Field observation of fluid circulation patterns in a normal fault system: Geophysical Research Letters 31, L19502, doi: 10.1029/2004GL020812.

Faulds, J.E., Hinz, N.H., 2015. Favorable Tectonic and Structural Settings of Geothermal Systems in the Great Basin Region , Western USA: Proxies for Discovering Blind Geothermal Systems. World Geotherm. Congr. 2015 1–6.

Faulkner, D.R., Jackson, C.A.L., Lunn, R.J., Schlische, R.W., Shipton, Z.K., Wibberley, C.A.J., Withjack, M.O., 2010. A review of recent developments concerning the structure, mechanics and fluid flow properties of fault zones. J. Struct. Geol. 32, 1557–1575.

Fernàndez, M., Banda, E., 1988. Aproximacion a la anomalia geotérmica de La Garriga - Samalus (Vallès - Penedès). Acta Geológica Hispánica 23, 1–20.

Fernàndez, M., Banda, E., 1990. Geothermal Anomalies in the Valles-Penedes graben master fault: convection through the horst as a possible mechanism. J. Geophys. Res. 95, 4887–4894.

Fisher Q.J., Knipe R.J., 1998. Fault sealing processes in siliciclastic sediments. In: Faulting and Fault Sealing in Hydrocarbon Reservoirs (eds Jones G, Fisher QJ, Knipe RJ), Geological Society of London Special Publication 147, 117–34.

Fontboté, J.M., 1954. Sobre la evolución tectónica de la depresión del Vallés-Pened-es. Publ. Museu Sabadell, Sabadell.

Fontboté, J.M., Guimerà, J., Roca, E., Sàbat, F., Santanach, P., Fernández-Ortigosa, F., 1990. The Cenozoic geodynamic evolution of the Valencia trough (Western mediterranean). Rev. Soc. Geol. Esp 3, 249–259.

Fossen, H., Rotevatn, A., 2016. Fault linkage and relay structures in extensional settings-A review. Earth-Science Rev. 154, 14–28.

Gabàs, A., Macau, A., Benjumea, B., Queralt, P., Ledo, J., Figueras, S., Marcuello, A., 2016. Joint Audio-Magnetotelluric and Passive Seismic Imaging of the Cerdanya Basin. Surv. Geophys. 37, 897–921.

Gallart, J., Vidal, N., Daiiobeitia, J.J., 1997. The ESCI Valencia Trough vertical reflection experiment : a seismic image of the crust from the NE Iberian Peninsula to the Western Lateral variations in the deep crustal structure at the Iberian margin of the Valencia trough imaged from seismic reflectio.

Gaspar-Escribano, J.M., 2003. Tectonic modeling of the Catalan Coastal Ranges (NE Spain) and adjacent areas. Vrije Univ. Amsterdam.

Gaspar-Escribano, J.M., Garcia-Castellanos, D., Roca, E., Cloetingh, E., 2004. Cenozoic vertical motions of the Catalan Coastal Ranges (NE Spain): The role of tectonics, isostasy, and surface transport. Tectonics 23, 1–18.

Géraud, Y., Rosener, M., Surma, F., Place, J., Le Garzic, É., Diraison, M., 2010. Physical properties of fault zones within a granite body: Example of the Soultz-sous-Forêts geothermal site. Comptes Rendus - Geosci. 342, 566–574. https://doi.org/10.1016/j.crte.2010.02.002

Giba, M., Walsh, J.J., Nicol, A., 2012. Segmentation and growth of an obliquely reactivated normal fault. J. Struct. Geol. 39, 253–267.

Gómez, M., Guimerà, J., 1999. Estructura Alpina de la Serra de Miramar y del NE de Las Muntanyes de Prades (Cadena Costera Catalana). Rev. Soc. Geol. Esp 12, 405–418.

Grueschow, E., Kwon, O., Main, I.G., and Rudnicki, J.W., 2003, Observation and modeling of the suction pump effect during rapid dilatant slip: Geophysical Research Letters 30, 4 p.

Guimerá, J., 1984. Palaeogene evolution of deformation in the northeastern Iberian

Peninsula. Geol. Mag. 121, 413–420.

Guimerá, J., Santanach, P., 1978. Sobre la compresión alpina en el sector central de las Cadenas Costeras Catalanas. Acta geológica hispánica 13, 33–42.

Haines, S., Lynch, E., Mulch, A., Valley, J.W., van der Pluijm, B., 2016. Meteoric fluid infiltration in crustal-scale normal fault systems as indicated by δ18O and δ2H geochemistry and 40Ar/39Ar dating of neoformed clays in brittle fault rocks. Lithosphere 8, 587–600.

ICGC, 2016. Mapa Geològic de Catalunya 1:50.000.

ICGC, 2011. Base Topogràfica de Catalunya 1:5.000 (BT-5M) v2.

ICGC, 2006. Vallès Oriental. Mapa geològic comarcal de Catalunya 1:50.000.

ICGC, 2002. Mapa Geològic de Catalunya 1:250.000.

ICGC, 1984. Butlletí sismològic. Generalitat de Catalunya. Departament de territori i sostenibilitat.

IGME, 1986. Proyecto de seguimiento geológico del sonde de reconocimiento geotérmico SAMALUS-6 (1000 m) (Valles-Barcelona).

IGME, 1984. Proyecto de investigación geotérmica en el Vallés mediante sondeos de reconocimiento y síntesis hidrogeotérmica. Control geotermico de los sondeos SAMALUS 2, 3, 4 y 5.

IGME, 1982. Informe sobre el seguimiento técnico del sondeo SAMALUS-1.

IGME, 1977. Fase preliminar de prospección de recursos geotérmicos de baja entalpía en el Vallés (Barcelona).

IGME, 1974. La Garriga (364). Mapa geológico de España 1:50 000:

Juez-Larré, J., Andriessen, P.A.M., 2006. Tectonothermal evolution of the northeastern margin of Iberia since the break-up of Pangea to present, revealed by low-temperature fission-track and (U-Th)/He thermochronology: A case history of the Catalan Coastal Ranges. Earth Planet. Sci. Lett. 243, 159–180.

King, G.C.P., Stein, R.S., Rundle, J.B., 1988. The growth of geological structures by repeated earthquakes. 1. Conceptual framework: Journal of Geophysical Research: Solid Earth 93, 13307–13318.

Kusznir, N.J., Ziegler, P.A. 1992. The mechanics of continental extension and sedimentary basin formation: A simple-shear/pure-shear flexural cantilever model. Tectonophysics 215, 117-131.

Kyne, R., Torremans, K., Güven, J., Doyle, R., Walsh, J. 2019. 3-D modeling of the lisheen and silvermines deposits, County Tipperary, Ireland: insights into structural controls on the formation of Irish Zn-Pb deposits. Economic Geology 114, 93-116.

Lindsay, N.G., Murphy, F.C., Walsh, J.J., and Watterson, J., 1993. Outcrop studies of shale smears on fault surfaces. International Association of Sedimentologists, Special Publication 15, 113–123.

Loveless, S., Pluymaekers, M., Lagrou, D., Boever, E. De, Doornenbal, H., Laenen, B., 2014. Mapping the geothermal potential of fault zones in the Belgium-Netherlands border region. Energy Procedia 59, 351–358.

Macau, A., Benjumea, B., Gabàs, A., Bellmunt, F., Figueras, S., 2018. Geophysical measurements for site effects characterisation in the urban area of Girona, Spain. Near Surf. Geophys. 16, 340–355.

Mansfield, C., Cartwright, J., 2001. Fault growth by linkage: Observations and implications from analogue models. J. Struct. Geol. 23, 745–763.

Manzocchi, T., Walsh, J.J., Nell, P.A.R., and Yielding, G., 1999. Fault transmissibility multipliers for flow simulation models. Petroleum Geoscience 5, 53–63.

Manzocchi, T., Heath, A.E., Palananthakumar, B., Childs, C., Walsh, J.J., 2008. Faults in conventional flow simulation models: A consideration of representational assumptions and geological uncertainties. Pet. Geosci. 14, 91–110.

Manzocchi, T., Childs, C., Walsh, J. J., 2010. Faults and fault properties in hydrocarbon flow models. Geofluids 10, 94-113.

Marcén, M., Casas-Sainz, A.M., Román-Berdiel, T., Griera, A., Santanach, P., Pocoví, A., Gil-Imaz, A., Aldega, L., Izquierdo-Llavall, E., 2018. Multiple movements recorded in a crustal weakness zone in NE Iberia: The Vallès-Penedès Fault revisited. J. Geodyn. 121, 96–114.

Martí, J., Mitjavila, J., Roca, E., Aparicio, A., 1992. Cenozoic magmatism of the valencia trough (western mediterranean): Relationship between structural evolution and volcanism. Tectonophysics 203, 145–165.

Martín-Martín, M., Guerrera, F., Tosquella, J., Tramontana, M., 2021. Middle Eocene carbonate platforms of the westernmost Tethys. Sediment. Geol. 415, 105861.

Masana, E., 1996. Evidence for past earthquakes in an area of low historical seismicity: the Catalan coastal ranges, NE Spain. Ann. Di Geofis. 39, 689–704.

Masana, E., 1995. L'activitat neotectònica a les Cadenes Costaneres Catalanes. Universitat de.

Masana, E., 1994. Neotectonic features of the Catalan Coastal Ranges, northeastern Spain. Acta Geol. Hisp. 29, 107–121.

Marín, M., Roca, E., Marcuello, A., Cabrera, L., Ferrer, O. 2021. Mesozoic structural inheritance in the Cenozoic evolution of the central Catalan Coastal Ranges (western Mediterranean): Structural and magnetotelluric analysis in the Gai`a-Montmell High. Tectonophysics 814, 228970.

Mattsson, T., Burchardt, S., Mair, K., Place, J., 2020. Host-rock deformation during the emplacement of the Mourne Mountains granite pluton: Insights from the regional fracture pattern. Geosphere 16, 182–209.

Mitjanas, G., Ledo, J., Macau, A., Alías, G., Queralt, P., Bellmunt, F., Rivero, L., Gabàs, A., Marcuello, A., Benjumea, B., Martí, A., Figueras, S., 2021. Integrated seismic ambient noise, magnetotellurics and gravity data for the 2D interpretation of the Vallès basin structure in the geothermal system of La Garriga-Samalús (NE Spain). Geothermics 93.

Motyka, J. 1998. A conceptual model of hydraulic networks in carbonate rocks, illustrated by examples from Poland. Hydrogeology Journal 6, 469–482.

Muir-Wood, R., and King, G.C.P., 1993, Hydrological signatures of earthquake strain: Journal of Geophysical Research 98, 22,035–22,068.

Müller, C., Siegesmund, S., Blum, P. 2010. Evaluation of the representative elementary volume (REV) of a fractured geothermal sandstone reservoir. Environmental Earth Science 61, 1713–1724. https://doi.org/10.1007/s12665-010-0485-7

Nakamura, Y., 1989. A method for dynamic characteristics estimations of subsurface using microtremors on the ground surface. Railw. Tech. Res. Institute, Quaterly Reports 30, 25–33.

Nicol, A., Walsh, J.J., Childs, C., Manzocchi, T. 2020. The growth of faults. In: Understanding Faults: Detecting, Dating, and Modeling. (Edited by Tanner, D. & Brandes, C.). Elsevier.

Odling, N.E., Gillespie, P., Bourgine, B., Castaing, C., Chilés, J-P., Christensen, N.P., Fillion, E., Genter, A., Olsen, C., Thrane, L., Trice, R., Aarseth, E., Walsh, J.J., Watterson, J. 1999. Variations in fracture system geometry and their implications for fluid flow in fractured hydrocarbon reservoirs.Petroleum Geoscience 5, 374-384.

Park, H.J., West, T.R., 2002. Sampling bias of discontinuity orientation caused by linear sampling technique. Eng. Geol. 66, 99–110.

Passchier, C.W., Trouw, R.A.J., 2005. Microtectonics, 2nd Editio. ed.

Peacock, D.C.P., Sanderson, D.J., 1994. Geometry and development of relay ramps in normal fault systems. Am. Assoc. Pet. Geol. Bull. 78, 147–165. https://doi.org/10.1306/bdff9046-1718-11d7-8645000102c1865d.

Phillips, W.J., 1972. Hydraulic fracturing and mineralization: Journal of the Geological Society, London 8, 337–359.

Price, N.J., Cosgrove, J.W., 1989. Analysis ot geological structures. Cambridge University Press.

Priest, S.D., 1993. Discontinuity Analysis for Rock Engineering. Chapman & Hall, London, UK.

Priest, S.D., Hudson, J.A., 1981. Estimation of discontinuity spacing and trace length using scanline surveys. Int. J. Rock Mech. Min. Sci. 18, 183–197.

Reiss, L.H. 1980. The reservoir engineering aspects of fractured formations. Editions Technip, Paris

Rhén, I., Thunehed, H., Triumf, C.A., Follin, S., Hartley, L., Hermansson, J., Wahlgren, C.H., 2007. Development of a

hydrogeological model description of intrusive rock at different investigation scales: An example from south-eastern Sweden. Hydrogeol. J. 15, 47–69.

Roberts, A., and Yielding, G., 1994. Continental extensional tectonics, in: Hancock, P. (Ed.), Continental Deformation: Pergamon Press, Oxford, 223-250.

Roca, E., 2001. The Northwest Mediterranean Basin (Valencia Trough, Gulf of Lions and Liguro-Provençal basins): structure and geodynamic evolution, in: Ziegler, P.A., Cavazza, W., Roberson, A.H.F., Crasquin-Soleau, S. (Eds.), Peri-Tethys Memoir 6: Peri-Tethyan Rift / Wrench Basins and Passive Margins. Memoires Du Museum National D'Histoire Naturelle, pp. 671–706.

Roca, E., 1996. La evolucion geodinamica de la Cuenca Catalano-Balear y areas adyacentes desde el Mesozoico hasta la actualidad. Acta Geol. Hisp. 29, 3–25.

Roca, E., 1992. L'estructura de la conca Catalano-Balear: paper de la compressiò i de la distensió en la seva gènesi. Universitat de Barcelona.

Roca, E., Guimerà, J., 1992. The Neogene structure of the eastern Iberian margin: Structural constraints on the crustal evolution of the Valencia trough (western Mediterranean). Tectonophysics 203, 203–218.

Roca, E., Sans, M., Cabrera, L., Marzo, M., 1999. Oligocene to Middle Miocene evolution of the central Catalan margin (northwestern Mediterranean). Tectonophysics 315, 209–229.

Roche, V., Camani, G., Childs, C., Manzocchi, T., Walsh, J.J., Conneally, J., Saqab, M.M., Delogkos, E. 2021. Variability in the three-dimensional geometry of segmented normal fault surfaces. Earth Science Reviews 216, 103523, doi:

Rotevatn, A., Buckley, S.J., Howell, J.A., Fossen, H., 2009a. Overlapping faults and their effect on fluid flow in different reservoir types: A LIDAR-based outcrop modeling and flow simulation study. Am. Assoc. Pet. Geol. Bull. 93, 407–427.

Rotevatn, A., Tveranger, J., Howell, J.A., Fossen, H., 2009b. Dynamic investigation of the effect of a relay ramp on simulated fluid flow: Geocellular modelling of the Delicate Arch Ramp, Utah. Pet. Geosci. 15, 45–58.

Rowe, J., Burley, S.D., 1997. Faulting and porosity modification in the Sherwood Sandstone at Alderley Edge, northeastern Cheshire: An exhumed example of fault-related diagenesis: Geological Society, London, Special Publication 124, 325–352.

Rudnicki, J.W., Chen, C.-H., 1988. Stabilization of rapid frictional slip on a weakening fault by dilatant hardening: Journal of Geophysical Research 93, 4745–4757.

Sàbat, F., Roca, E., Muñoz, J.A., Vergés, J., Santanach, P., Sans, M., Masana, E., Estévez, A., Santisteban, C., 1995. Role of extension and compression in the evolution of the eastern margin of Iberia: the ESCI-València Trough seismic profile. Rev. Soc. Geol. España 8, 431–448.

Santanach, P., Casas, J.M., Gratacós, O., Liesa, M., Muñoz, J.A., Sàbat, F., 2011. Variscan and Alpine structure of the hills of Barcelona: geology in an urban area. J. Iber. Geol. 37, 121–137.

Schön, J.H., 2015. Physical properties of rocks. Fundamentals and principles of petrophysics., 2nd ed. Developments in Petroleum Science.

Schwartz, F.W., Zhang, H., 2003. Fundamentals of groundwater. Wiley, New York.

Seebeck, H., Nicol, A., Walsh, J.J., Childs, C., Beetham, R.D., and Pettinga, J., 2014. Fluid flow in fault zones from an active rift: Journal of Structural Geology 62, 52–64

Selley, D., Broughton, D., Scott, R.J., Hitzman, M., Bull, S.W., Large, R.R., McGoldrick, P.J., Croaker, M., and Pollington, N., 2005. A new look at the geology of the Zambian Copperbelt: Economic Geology 100th Anniversary Volume, 965–1000.

Sibson, R.H., 1987. Earthquake rupturing as a mineralizing agent in hydrothermal systems. Geology 15, 701–704.

Sibson, R.H., 1990. Conditions for fault valve behavior. Geological Society, London, Special Publication 54, 15–28.

Sibson, R.H., 1992. Implications of fault-valve behaviour for rupture nucleation and recurrence. Tectonophysics 211, 283–293.

Sibson, R.H., 1996. Structural permeability of fluid-driven fault-fracture meshes: Journal of Structural Geology 18, 1031–1042.

Sibson, R.H. 2000. Fluid involvement in normal faulting. Journal of Geodynamics 29, 469–499.

Sibson, R.H., 2001. Seismogenic framework for hydrothermal transport and ore deposition. Reviews in Economic Geology 14, 25–50.

Sibson, R.H., Moore, J.M.M., Rankin, A.H., 1975. Seismic pumping—a hydrothermal fluid transport mechanism: Journal of the Geological Society, London 131, 653–659.

Siebenaller, L., Boiron, M.C., Vanderhaeghe, O., Hibsch, C., Jessell, M.W., Andre-Mayer, A.S., France-Lanord, C., Photiades, A., 2013. Fluid record of rock exhumation across the brittle-ductile transition during formation of a Metamorphic Core Complex (Naxos Island, Cyclades, Greece). J. Metamorph. Geol. 31, 313–338.

Siler, D.L., Hinz, N.H., Faulds, J.E., 2018. Stress concentrations at structural discontinuities in active fault zones in the western United States: Implications for permeability and fluid flow in geothermal fields. Bull. Geol. Soc. Am. 130, 1273–1288. https://doi.org/10.1130/B31729.1

Stimac, J. A., Powell, T. S., & Golla, G. U. (2004). Porosity and permeability of the Tiwi geothermal field, Philippines, based on continuous and spot core measurements. *Geothermics*, *33*(1–2), 87–107.

Süer, S., Güleç, N., Mutlu, H., Hilton, D.R., Çifter, C., Sayin, M., 2008. Geochemical monitoring of geothermal waters (2002-2004) along the North Anatolian fault zone, Turkey: Spatial and temporal variations and relationship to seismic activity. Pure Appl. Geophys. 165, 17–43.

Tullborg, E.L., Larson, S.Å., 2006. Porosity in crystalline rocks - A matter of scale. Eng. Geol. 84, 75–83.

Velde, B., & Meunier, A. (2008). *The Origin of Clay Minerals in Soils and Weathered Rocks*. Springer Berlin Heidelberg.

Vidal, N., Gallart, J., Danobeitia, J.J., 1995. Contribution of the ESCI-Valéncia Trough Wide-Angle Data to a Crustal Transect in the NE Iberian Margin. Rev. la Soc. Geol. Espana.

Walsh, J.J., Torremans, K., Güven, J., Kyne, R., Conneally, J., Bonson, C., 2018. Fault-Controlled Fluid Flow Within Extensional Basins and Its Implications for Sedimentary Rock-Hosted Mineral Deposits. Soc. Econ. Geol. Spec. Publ. 237–269.

Watkins, H., Bond, C.E., Healy, D., Butler, R.W.H., 2015. Appraisal of fracture sampling methods and a new workflow tocharacterise heterogeneous fracture networks at outcrop. J. Struct. Geol. 72, 67–82.

Wibberley, C.A.J, Yielding, G., Di Toro G. 2008. Recent advances in the understanding of fault zone internal structure: a review. In: The Internal Structure of Fault Zones: Implications for Mechanical and Fluid-Flow Properties (eds Wibberley CAJ, Kurz W, Imber J, Holdsworth RE, Collettini C), Geological Society of London Special Publication 299, 5–33.

Wibberley, C.A.J, Shimamoto, T. 2003. Internal strucutre and permeability of major strike-slip fault zones: the Median Tectonic Line in Mie Prefecture, Southwest Japan. Journal of Structural Geology 25, 59-78.

Wilkins, S.J., Naruk, S.J., 2007. Quantitative analysis of slip-induced dilation with application to fault seal: AAPG Bulletin 91, 97–113.

Yielding, G. 2002. Shale Gouge Ratio – calibration by geohistory. In: Hydrocarbon Seal Quantification (eds Koestler AG, Hunsdale R), Norwegian Petroleum Society Special Publication, 11, 1–15.

Zimmerman, R.W., Bodvarsson, G.S. 1996. Hydraulic conductivity of rock fractures. Transport in Porous Media 23, 1-30.